
Nonclassical States and Quantum Synchronization of Dissipative Nonlinear Oscillators

Inauguraldissertation

zur

Erlangung der Würde eines Doktors der Philosophie
vorgelegt der
Philosophisch-Naturwissenschaftlichen Fakultät
der Universität Basel

von

Martin KOPPENHÖFER

aus Karlsruhe, Deutschland

Basel, 2020

Genehmigt von der Philosophisch-Naturwissenschaftlichen Fakultät

auf Antrag von

Prof. Dr. C. BRUDER

Prof. Dr. P. TREUTLEIN

Prof. Dr. R. FAZIO

Basel, den 26. Mai 2020

Prof. Dr. Martin SPIESS, Dekan

*Nature isn't classical, dammit,
and if you want to make a simulation of Nature,
you'd better make it quantum mechanical,
and by golly it's a wonderful problem,
because it doesn't look so easy.*

Richard P. Feynman (1918 – 1988)

Summary

In recent years, significant progress has been made to push micro-, nano-, and optomechanical systems into the quantum regime. The common goal is to demonstrate and control quantum effects in these systems, which enable applications in quantum metrology and quantum information processing. This process is hampered by dissipation, *i.e.*, the interaction of these systems with their environment.

In this thesis, we focus on two different aspects of dissipative nonlinear systems in the quantum regime. In the first part, we study how states with genuinely quantum properties can be generated by a continuous measurement of the interaction between the quantum system and its environment. This approach turns dissipation into a useful tool to generate nonclassical states of light and matter, which have been identified as important resources for quantum-enhanced sensing, quantum communication, and quantum error processing. We discuss the generation of mechanical states with a sub-Poissonian phonon-number distribution in an optomechanical phonon laser beyond the resolved-sideband regime, and we propose a heralded protocol to generate nonclassical states by photon-counting measurements. We apply this protocol to a Kerr nonlinear oscillator and show that it enables the creation of states with a negative Wigner function although the steady-state Wigner function of this system is strictly positive.

In the second part of this thesis, we focus on self-sustained oscillators in the quantum regime. If a weak perturbation is applied to a self-sustained oscillator, the oscillator can adjust its frequency of oscillation. This effect is called synchronization and has been identified as a universal feature of many different complex classical systems, *e.g.*, electrical circuits, biological systems, and power grids. In recent years, several theoretical proposals have been put forward to study synchronization in the quantum regime. However, an experimental demonstration of quantum effects in synchronization has still been missing.

We develop an analytical framework to study the synchronization of a quantum self-sustained oscillator to an external signal. This framework establishes a unified description of the above-mentioned proposals and allows us to identify the quantum-mechanical resource of synchronization. Based on these findings, we discover a novel interference-based quantum synchronization blockade effect and we derive a bound on the maximum degree of synchronization that can be achieved in the quantum regime. The framework also reveals a large freedom in tailoring a quantum system that is able to synchronize. Taking advantage of this freedom, we propose alternative implementations of quantum self-sustained oscillators that reduce the experimental challenges.

Finally, we use digital quantum simulation to implement a quantum self-sustained oscillator on a current quantum computer. Applying an external signal to the oscillator, we verify typical features of quantum synchronization, and we demonstrate interference-based quantum synchronization blockade. Our results are the first experimental demonstration of genuinely quantum effects in synchronization and they show that state-of-the-art noisy intermediate-scale quantum computers are powerful enough to implement and study realistic dissipative quantum systems.

Contents

Summary	v
Contents	vii
List of Abbreviations	xi
1 Introduction	1
2 Theoretical Background	5
2.1 Modeling dissipative quantum systems	5
2.2 Continuously monitored dissipative quantum systems	9
2.2.1 Positive-operator-valued measurements	9
2.2.2 Photon counting	11
2.2.3 Unbalanced homodyne detection	14
2.2.4 Balanced homodyne detection	16
2.2.5 Stochastic master equation vs. stochastic Schrödinger equation	18
2.2.6 Conditional vs. unconditional dynamics	18
2.3 Phase-space quasiprobability distributions	19
2.3.1 Harmonic oscillator	19
2.3.2 Spin	21
2.4 Optomechanical system	22
2.4.1 Optomechanical Hamiltonian	22
2.4.2 Optomechanical instability	25
2.5 Kerr oscillator	29
2.5.1 Harmonic drive	30
2.5.2 Parametric drive	32
2.6 Synchronization	33
2.6.1 Classical limit-cycle oscillator	33
2.6.2 Classical synchronization phenomena	35
2.6.3 Quantum limit-cycle oscillators	39
2.6.4 Quantum synchronization measures	40
2.7 Quantum computing	42
2.7.1 Elements of quantum computing	43
2.7.2 Quantum simulation	45
3 Nonclassical States of Motion in an Optomechanical Limit Cycle	49
3.1 Motivation	49
3.2 Optomechanical system	50
3.3 Methods and parameters	52
3.4 Nonclassical mechanical limit-cycle motion	55
3.5 Discussion and experimental implementation	58
3.6 Summary	62

4	Heralded Dissipative Generation of Nonclassical States in Nonlinear Systems	63
4.1	Motivation	63
4.2	Continuously monitored dissipative quantum system	64
4.3	Heralded state preparation protocol	66
4.4	Pseudosteady state and relaxation rate	67
4.4.1	Stochastic quantum master equation	67
4.4.2	Stochastic Schrödinger equation	70
4.5	Nonclassical states in a Kerr oscillator	72
4.5.1	Harmonic drive	73
4.5.2	Unraveling different pseudosteady states	75
4.5.3	Parametric drive	76
4.6	Finite temperature and imperfect photon detection	78
4.7	Experimental implementation	79
4.8	Summary	80
5	Quantum Synchronization	81
5.1	Motivation	81
5.2	Framework	83
5.2.1	Phase space and phase variable	83
5.2.2	Limit-cycle stabilization	84
5.2.3	External signal	87
5.2.4	Perturbation theory	87
5.2.5	Synchronization measure	89
5.2.6	Determining the signal strength	91
5.3	Extended Arnold tongue	96
5.4	Van der Pol limit cycle	98
5.4.1	Harmonic oscillator vs. spin 1	98
5.4.2	Semiclassical and squeezing signal	100
5.4.3	Optimized signal	102
5.5	Equatorial limit cycle	104
5.5.1	Limit-cycle stabilization	104
5.5.2	Semiclassical signal	105
5.5.3	Optimized signal	106
5.6	Maximum synchronization in the quantum regime	106
5.6.1	Upper bound on quantum synchronization	106
5.6.2	Tightness of the bound	109
5.6.3	Discussion	110
5.7	Interference-based quantum synchronization blockade	111
5.8	Experimental implementation of quantum synchronization	113
5.9	Summary	115
6	Digital Quantum Simulation of Quantum Synchronization	117
6.1	Motivation	117
6.2	Spin-1 limit-cycle oscillator	118
6.3	Mapping to a quantum computer	119
6.3.1	Unitary time evolution	120
6.3.2	Dissipative time evolution	123
6.4	Methods	126
6.5	Device characterization	130
6.6	Dealing with hardware constraints	132

6.7	Experimental demonstration of quantum synchronization	134
6.8	Summary	137
7	Conclusion and Outlook	139
	Acknowledgements	145
A	Definitions and Conventions	147
A.1	Quantum harmonic oscillator	147
A.1.1	Operators	147
A.1.2	Coherent states	148
A.2	Spin system	149
A.2.1	Operators	149
A.2.2	Spin-coherent states	150
B	Quantum Synchronization Formalism for Oscillator-Based Systems	153
C	Basis Gates of the IBM Q System	157
	List of Symbols	159
	Bibliography	164

List of Abbreviations

ABBREVIATION	MEANING	INTRODUCED IN
LO	L ocal O scillator	Sec. 2.2.2, p. 12
NISQ	N oisy I ntermediate- S cale Q uantum	Sec. 6.1, p. 118
POVM	P ositive- O perator- V alued M easurement	Sec. 2.2.1, p. 10
QME	Q uantum M aster E quation	Sec. 2.1, p. 5
qubit	q uantum b it	Sec. 2.7.1, p. 43
SME	S tochastic quantum M aster E quation	Sec. 2.2.2, p. 11
SSE	S tochastic S chrödinger E quation	Sec. 2.2.2, p. 14
vdP	v an d er P ol	Sec. 2.6.1, p. 34

Chapter 1

Introduction

Since the beginnings of quantum physics about one hundred years ago, quantum technologies have revolutionized human life and society. The development of the first transistor [Bardeen and Brattain, 1948] combined with the invention of integrated circuits laid the foundations of modern information processing. Lasers [Maiman, 1960] have become an indispensable resource not only for scientific research, but also for medicine, industry, and fast telecommunication. The development of light-emitting diodes operating in the visible spectral range [Holonyak and Bevacqua, 1962] prepared the ground for novel energy-efficient illumination concepts that gradually replace conventional light bulbs. Finally, solar cells are an important pillar of renewable energy production [Würfel and Würfel, 2016]. Large semiconductor and optical industries emerged that keep refining their production techniques to fabricate artificial structures at the micro- and nanoscale.

In parallel, various subfields of physics developed that focus on particular aspects of micro- and nanoscale devices, such as micro- or nanoelectromechanical systems [Ekinci and Roukes, 2005], optomechanical systems [Aspelmeyer *et al.*, 2014], superconducting electrical circuits [Makhlin *et al.*, 2001], and semiconductor quantum dots [Hanson *et al.*, 2007]. The Holy Grail of research activities in these fields is to demonstrate and control quantum effects in micro- and nanoscale structures. This is hampered by the fact that these structures interact with their environment, *i.e.*, they are *dissipative* systems. In general, dissipative processes carry away information on the quantum state of a system and reduce quantum states to classical ones in a process called *decoherence* [Zurek, 2003].

In the last years, increased understanding and meticulous reduction of decoherence mechanisms led to impressive experimental demonstrations of quantum effects: Superpositions of charge, flux, and spin states have been demonstrated [Nakamura *et al.*, 1999; Chiorescu *et al.*, 2003; Koppens *et al.*, 2006], which paved the way to the development of quantum information processing devices based on superconducting circuits and quantum dots [Wendin, 2017; Zwanenburg *et al.*, 2013]. In optomechanical systems, coherent state transfer between the optical and the mechanical subsystems has been demonstrated [Verhagen *et al.*, 2012; Palomaki *et al.*, 2013] and mechanical oscillations have been cooled down to the mechanical ground state [Teufel *et al.*, 2011; Chan *et al.*, 2011]. This experimental progress paves the way towards the generation of *nonclassical states* of light and matter, *i.e.*, states with genuinely quantum properties, which have been identified as an important resource for quantum sensing [Degen *et al.*, 2017; Pezzè *et al.*, 2018] and quantum information processing [Nielsen and Chuang, 2011].

Although dissipation usually degrades quantum states, it can also be turned into a useful tool to generate nonclassical states. This is the subject of the first part of this thesis, which is devoted to the generation of quantum states by measuring the interaction between a dissipative system and its environment.

An important subclass of dissipative systems are self-sustained oscillators. These systems possess an internal source of energy that counteracts damping and excites a periodic motion. The phase of this oscillation is free and can be influenced by a weak external perturbation. This leads to an adjustment of the natural frequency of oscillation of the self-sustained oscillator, which is called *synchronization* [Pikovsky *et al.*, 2003]. Synchronization has been discovered already in the 17th century, when the Dutch physicist Huygens [1673] observed that pendulum clocks mounted on a common wooden bar tick in unison. Since then, synchronization has been found to be a universal feature of many very different nonlinear dynamical systems, *e.g.*, electrical circuits [Adler, 1946], biological systems [Aschoff, 1965; Buck and Buck, 1968; Néda *et al.*, 2000], and power grids [Dörfler *et al.*, 2013].

Nonlinear systems at the micro- and nanoscale provide the exciting possibility to study synchronization in the quantum regime. An important difference between quantum and classical self-sustained oscillators is the unavoidable presence of noise due to quantum fluctuations. In general, adding noise to a classical self-sustained oscillator decreases its ability to synchronize [Pikovsky *et al.*, 2003], therefore, it is not *a priori* clear whether synchronization phenomena will persist in the quantum regime. Consequently, several proposals have been made to investigate this question using superconducting circuits [Zhironov and Shepelyansky, 2006], optomechanical systems [Ludwig and Marquardt, 2013; Walter *et al.*, 2014], trapped ions [Lee and Sadeghpour, 2013], and nanomechanical oscillators [Holmes *et al.*, 2012]. These theoretical studies predicted that quantum synchronization will survive the detrimental effect of quantum noise. However, an experimental demonstration of quantum synchronization has been missing so far because of the challenge to engineer and control both nonlinear dissipation and coherent interactions in a single experimental platform in the quantum regime.

In the second part of this thesis, a mathematical framework for quantum synchronization is developed that establishes a unified description of various experimental platforms. This framework reveals a large freedom in tailoring a quantum system that is able to synchronize. Alternative implementations of a quantum self-sustained oscillator are proposed, which take advantage of this freedom to reduce experimental challenges, and methods of quantum computing are used to implement quantum synchronization experimentally.

The continuous miniaturization of classical information-processing devices naturally triggered question whether information processing would still be possible with structures that are governed by the laws of quantum mechanics. Benioff [1980] answered this question affirmatively and showed that the mathematical model of any classical computation – the Turing machine – can be implemented in a quantum system. Therefore, every calculation that can be performed efficiently on a classical computer can also be performed efficiently on a quantum computer. Feynman [1982] pointed out that the converse statement is not true: Classical computers cannot efficiently calculate the time evolution of a large quantum system, but Feynman conjectured that this time evolution could be efficiently simulated using a quantum-mechanical model of computation. Nowadays, this approach is called *quantum simulation* and, more than ten years after Feynman’s conjecture, Lloyd [1996] finally proved that a universal quantum computer can indeed efficiently simulate any other quantum system that evolves according to local interactions.

Feynman’s conjecture and other predictions of advantages of quantum computers over classical ones [Bennett and Brassard, 2014; Deutsch and Jozsa, 1992; Shor, 1997; Grover, 1997] fueled a rapid development of quantum-information-processing devices [Nielsen and Chuang, 2011]. Today, small quantum computers with up to 72 quantum

bits are available [Kelly, 2018; Arute *et al.*, 2019; McClure and Gambetta, 2019; Chow and Gambetta, 2020; Rigetti, 2019], and some of them can even be controlled remotely via the internet by any interested person. These devices are commonly referred to as *noisy intermediate-scale quantum computers* [Preskill, 2018], since there is still a long way to go towards the goal of a fully error-corrected universal quantum computer. Despite all imperfections of these devices, impressive results have already been obtained, for instance, the first experimental demonstration of a significant quantum speedup for a specific task that cannot be efficiently solved on classical hardware [Arute *et al.*, 2019; Pednault *et al.*, 2019].

In this thesis, we will use quantum simulation techniques to implement quantum synchronization dynamics on a current quantum computer. In this way, we will give the first experimental demonstration of quantum synchronization and we will demonstrate that current quantum hardware is powerful enough to implement and study the dynamics of realistic dissipative quantum systems.

Overview of this thesis

Chapter 2 We will start by reviewing theoretical methods and techniques that are necessary to understand the calculations presented in this thesis. Markovian quantum master equations will be introduced as a powerful tool to describe dissipative quantum systems.

As a preparation for the chapters on nonclassical state generation, we will describe common experimental approaches to monitor the interaction of a quantum system with its environment. We will derive a theoretical description of these continuous measurements based on stochastic differential equations. Next, we will introduce phase-space quasiprobability distributions as a tool to illustrate the state of a quantum system and to quantify its degree of nonclassicality. We will also review the optomechanical system and the Kerr nonlinear oscillator, which are two paradigmatic models of nonlinear quantum systems that will be used in this thesis.

In preparation for the discussion of quantum synchronization, we will introduce important concepts of classical synchronization and we will review the literature on quantum synchronization measures. Finally, we will give an introduction to quantum computing with a focus on digital quantum simulation.

Chapter 3 Having introduced the theoretical foundations, we will discuss methods to generate nonclassical states in nonlinear dissipative quantum systems.

First, we will focus on the generation of mechanical states with a sub-Poissonian phonon-number distribution in an optomechanical system. If an optomechanical system is driven by a laser drive above resonance, mechanical oscillations arise. This effect is called *phonon lasing*. It has been predicted that the steady-state phonon distribution of a phonon laser is sub-Poissonian if the system is operated in the resolved-sideband regime, *i.e.*, if the optical decay rate κ is much smaller than the mechanical resonance frequency Ω_{mech} . We will show that a continuous measurement of the photons leaking out of the optical cavity can be used to generate nonclassical sub-Poissonian mechanical states even outside the resolved-sideband regime, and we will give a physical explanation for this effect.

Chapter 4 Next, we will shift our attention to another class of nonclassical states, namely, quantum states with negative values in their Wigner phase-space quasiprobability distribution. We will show that there are distinguished quantum states in the time evolution induced by a photon-counting measurement. In a suitable parameter

regime, the system will repeatedly converge towards these states despite the intrinsically stochastic dynamics due to the measurement process. We will use this effect to define a quantum state preparation protocol. Applying this protocol to a Kerr nonlinear oscillator, we will show that the generated states can be nonclassical despite the fact that the unconditional steady-state solution of a Kerr oscillator is strictly positive.

Chapter 5 In the second half of this thesis, we will focus on quantum synchronization.

We will start by developing a mathematical framework that provides a unified description of the synchronization of a quantum self-sustained oscillator to an external signal. This framework will allow us to identify the quantum-mechanical resource of synchronization and to discover a novel genuinely quantum effect in synchronization, namely, interference-based quantum synchronization blockade. A key element of the framework will be a general rule how to determine the signal strength such that the signal is only a weak perturbation to the self-sustained oscillation. This result will open a panoply of new applications: First, it defines the hitherto unknown upper limit of the synchronization region – the so-called Arnold tongue – in terms of the signal strength. At the same time, it extends the range of definition of the Arnold tongue and reveals that this tongue has actually a snake-like split structure. Second, this rule can be used to compare the synchronization of different self-sustained oscillators and signals. This will finally lead to the derivation of a tight upper bound on the maximum synchronization that is possible in quantum regime. Along the way, we will discover a variety of self-sustained oscillators that are presumably less challenging to implement experimentally than the quantum van der Pol oscillator.

Chapter 6 Finally, we will take advantage of the results of Chapter 5 to demonstrate quantum synchronization experimentally on a quantum computer. Focusing on a simple self-sustained oscillator, we will construct a quantum algorithm that implements a digital quantum simulation of quantum synchronization dynamics. Testing this algorithm on a state-of-the-art quantum computer, we will identify technical restrictions of current quantum hardware that hinder its use for the simulation of arbitrary dissipative quantum systems. However, the perturbative structure of the quantum synchronization problem will allow us to modify the algorithm to circumvent these restrictions and to give the first experimental demonstration of quantum synchronization. Our results show that state-of-the-art noisy intermediate-scale quantum computers are able to study realistic dissipative quantum systems that have not been realized experimentally before.

Chapter 7 Finally, we will give a summary of the main results of this thesis and we will identify open questions for future research projects. This will relate our research to other current problems in the fields of quantum optics and quantum computing.

Chapter 2

Theoretical Background

In this chapter, we will introduce concepts of quantum optics and quantum computing that are necessary to understand the calculations presented in this thesis. In Section 2.1, we will introduce Markovian quantum master equations as a description of dissipative quantum systems. Quantum master equations are obtained by embedding the dissipative quantum system of interest into a larger closed quantum system. The additional degrees of freedom describe the system's environment and are integrated out. In this step, all details of the interaction between the quantum system and its environment are discarded. However, continuous measurements allow one to obtain information on this interaction process. To account for this information, we will derive stochastic quantum master equations in Section 2.2. Both in the discussion of non-classical states and in the derivation of a framework for quantum synchronization, we will have to illustrate quantum states. A convenient tool to accomplish this task are phase-space quasiprobability distributions, which will be introduced in Section 2.3. Subsequently, we will review the basic properties of the optomechanical system and of the Kerr nonlinear oscillator in Sections 2.4 and 2.5, respectively. To put the discussion of quantum synchronization on solid ground, we will introduce the concept of classical synchronization in Section 2.6 and we will review quantum synchronization measures previously used in the literature. We end this chapter with an introduction to quantum computing in Section 2.7, with a particular focus on digital quantum simulation.

2.1 Modeling dissipative quantum systems

The theory of quantum mechanics has been developed to describe so-called closed quantum systems, *i.e.*, systems that conserve energy and evolve according to a unitary time-evolution operator. However, a realistic quantum system is never perfectly isolated from its environment. Instead, the quantum system typically exchanges energy or particles with its environment, which leads to a non-unitary time evolution describing dissipation and decoherence. Often, the environment has many more degrees of freedom than the quantum system of interest and it can be assumed that the quantum system interacts weakly with a very large number of densely-spaced environmental modes. Such a situation is called a *dissipative quantum system* interacting with a *bath* or *reservoir*. Each environmental mode is barely affected by the system, but Caldeira and Leggett [1981] pointed out that the combined effect of the entire environment on the quantum system may still be strong. The effective dynamics of the dissipative quantum system can be modeled by a quantum master equation (QME). Following standard textbooks [Wiseman and Milburn, 2009; Carmichael, 2002; Breuer and Petruccione, 2002], we will now sketch the main steps of the derivation of a QME and we will discuss the underlying assumptions and approximations.

To derive a QME, we consider an enlarged system that consists of the quantum system S and its environment E, *i.e.*, all environmental modes that interact with S. This combined system S+E is considered to be a closed system, described by a density matrix $\hat{\rho}_{SE}$. The unitary time evolution of $\hat{\rho}_{SE}$ is

$$\frac{d}{dt}\hat{\rho}_{SE}(t) = -\frac{i}{\hbar} \left[\hat{H}_S + \hat{H}_E + \hat{H}_C, \hat{\rho}_{SE}(t) \right] ,$$

where \hat{H}_S and \hat{H}_E are the Hamiltonians of the quantum system and its environment, respectively, and \hat{H}_C describes the coupling between S and E. Our goal is to derive an effective equation of motion for the reduced density matrix of the system $\hat{\rho}_S(t) = \text{Tr}_E [\hat{\rho}_{SE}(t)]$. For simplicity, we will work in the interaction picture with respect to $\hat{H}_S + \hat{H}_E$,

$$\tilde{\rho}_{SE}(t) = e^{i(\hat{H}_S + \hat{H}_E)(t-t_0)/\hbar} \hat{\rho}_{SE}(t) e^{-i(\hat{H}_S + \hat{H}_E)(t-t_0)/\hbar} , \quad (2.1)$$

$$\tilde{H}_C(t) = e^{i(\hat{H}_S + \hat{H}_E)(t-t_0)/\hbar} \hat{H}_C e^{-i(\hat{H}_S + \hat{H}_E)(t-t_0)/\hbar} , \quad (2.2)$$

where the unitary time evolution takes the more compact form

$$\frac{d}{dt}\tilde{\rho}_{SE}(t) = -\frac{i}{\hbar} \left[\tilde{H}_C(t), \tilde{\rho}_{SE}(t) \right] . \quad (2.3)$$

Equation (2.3) can be rewritten as an integro-differential equation,

$$\frac{d}{dt}\tilde{\rho}_{SE}(t) = -\frac{i}{\hbar} \left[\tilde{H}_C(t), \tilde{\rho}_{SE}(t_0) \right] - \frac{1}{\hbar^2} \int_{t_0}^t dt' \left[\tilde{H}_C(t), \left[\tilde{H}_C(t'), \tilde{\rho}_{SE}(t') \right] \right] . \quad (2.4)$$

We now use the assumption that the system S and its environment E interact only weakly. Therefore, if S and E are uncorrelated at some reference time t_0 ,

$$\tilde{\rho}_{SE}(t_0) = \tilde{\rho}_S(t_0) \otimes \tilde{\rho}_E(t_0) ,$$

the state of the environment is not changed by the system to lowest order in the interaction \tilde{H}_C , *i.e.*, the combined state at a later time $t > t_0$ is given by

$$\tilde{\rho}_{SE}(t) \approx \tilde{\rho}_S(t) \otimes \tilde{\rho}_E(t_0) .$$

This is the so-called *Born approximation*.

Despite the Born approximation, Equation (2.4) is still hard to solve because its right-hand side is a convolution involving a time integration over the system state $\tilde{\rho}_S(t')$. To obtain a form that is local in time, we assume that the environmental modes at the relevant frequencies of the system are dense and that the system couples roughly equally to all of them. Under these conditions, we can assume that the bath correlation time is much smaller than the typical timescale of the system's time evolution, *i.e.*, perturbations of the environment due to the interaction with the system decay quickly and do not affect the system at later times. This implies that the integrand in Equation (2.4) is sharply peaked at $t' \approx t$ and tends to zero elsewhere. Hence, we can approximate $\tilde{\rho}_S(t') \approx \tilde{\rho}_S(t)$ under the integral and we can safely extend

the lower limit of integration to $-\infty$,

$$\begin{aligned} \frac{d}{dt}\tilde{\rho}_{\text{SE}}(t) = & -\frac{i}{\hbar} \left[\tilde{H}_{\text{C}}(t), \tilde{\rho}_{\text{S}}(t_0) \otimes \tilde{\rho}_{\text{E}}(t_0) \right] \\ & - \frac{1}{\hbar^2} \int_{-\infty}^t dt' \left[\tilde{H}_{\text{C}}(t), \left[\tilde{H}_{\text{C}}(t'), \tilde{\rho}_{\text{S}}(t) \otimes \tilde{\rho}_{\text{E}}(t_0) \right] \right]. \end{aligned} \quad (2.5)$$

This is the so-called *Markov approximation*.

Finally, we have obtained a time-local differential equation and we can trace out the environment to obtain an effective equation of motion for the reduced density matrix $\tilde{\rho}_{\text{S}}$ of the system,

$$\frac{d}{dt}\tilde{\rho}_{\text{S}}(t) = -\frac{1}{\hbar^2} \int_{-\infty}^t dt' \text{Tr}_{\text{E}} \left(\left[\tilde{H}_{\text{C}}(t), \left[\tilde{H}_{\text{C}}(t'), \tilde{\rho}_{\text{S}}(t) \otimes \tilde{\rho}_{\text{E}}(t_0) \right] \right] \right). \quad (2.6)$$

Without loss of generality, we assume that the condition $\text{Tr}_{\text{E}}[\tilde{H}_{\text{C}}(t)\tilde{\rho}_{\text{S}}(t_0)\otimes\tilde{\rho}_{\text{E}}(t_0)] = 0$ holds, which can always be ensured by redefining $\hat{H}_{\text{S}} + \hat{H}_{\text{E}}$ appropriately.

To simplify Equation (2.6) further, we assume the generic situation that the system S is coupled to an environment E consisting of a set of harmonic oscillator modes,

$$\hat{H}_{\text{E}} = \sum_l \hbar\omega_l \hat{r}_l^\dagger \hat{r}_l,$$

where we ignored the constant contribution due to the zero-point energy of each mode. The environment is assumed to be in thermal equilibrium at a temperature T , *i.e.*, the initial state of the environment is

$$\hat{\rho}_{\text{E}}(t_0) = \prod_l \frac{e^{-\hbar\omega_l \hat{r}_l^\dagger \hat{r}_l / k_{\text{B}}T}}{1 - e^{-\hbar\omega_l / k_{\text{B}}T}}. \quad (2.7)$$

The coupling is considered to be of the form $\hat{H}_{\text{C}} = \hbar(\hat{s} \otimes \hat{e}^\dagger + \hat{s}^\dagger \otimes \hat{e})$, where $\hat{e} = \sum_l \kappa_l \hat{r}_l$ is a time-independent Schrödinger operator acting on E and \hat{s} is a ladder operator acting on S. The distribution of the frequencies ω_l and the coupling strengths κ_l are free parameters to model specific environments.

The interaction Hamiltonian can be rewritten in a more general form

$$\hat{H}_{\text{C}} = \hbar \sum_{j=1}^2 \hat{s}_j \otimes \hat{e}_j, \quad (2.8)$$

where we set $\hat{s}_1 = \hat{s}$, $\hat{s}_2 = \hat{s}^\dagger$, $\hat{e}_1 = \hat{e}^\dagger$, and $\hat{e}_2 = \hat{e}$. Since the \hat{s}_j are ladder operators acting on S, they fulfill the commutation relation $[\hat{H}_{\text{S}}, \hat{s}_j] = \delta_j \hat{s}_j$. The constant δ_j is the energy difference between the final and initial state of the transition, *i.e.*, $\delta_1 = -\delta$ and $\delta_2 = +\delta$. Inserting Equation (2.8) into Equation (2.6), we obtain

$$\begin{aligned} \frac{d}{dt}\tilde{\rho}_{\text{S}}(t) = & - \sum_{j,k=1}^2 \int_{-\infty}^t dt' \left(\left[\tilde{s}_j(t)\tilde{s}_k(t')\tilde{\rho}_{\text{S}}(t) - \tilde{s}_k(t')\tilde{\rho}_{\text{S}}(t)\tilde{s}_j(t) \right] \langle \tilde{e}_j(t)\tilde{e}_k(t') \rangle_{\text{E}} \right. \\ & \left. + \left[\tilde{\rho}_{\text{S}}(t)\tilde{s}_k(t')\tilde{s}_j(t) - \tilde{s}_j(t)\tilde{\rho}_{\text{S}}(t)\tilde{s}_k(t') \right] \langle \tilde{e}_k(t')\tilde{e}_j(t) \rangle_{\text{E}} \right), \end{aligned}$$

where we introduced the notation $\langle \tilde{e}_j(t)\tilde{e}_k(t') \rangle_{\text{E}} = \text{Tr}_{\text{E}}[\tilde{e}_j(t)\tilde{e}_k(t')\tilde{\rho}_{\text{E}}(t_0)]$ for the correlation functions of the environment. Since the operators \tilde{e}_j are time-independent operators in the Schrödinger picture, the correlation functions are invariant under time translation and only the time difference $\tau = t' - t$ matters. Going back to the

Schrödinger picture, we find

$$\frac{d}{dt}\hat{\rho}_S(t) = -\frac{i}{\hbar} [\hat{H}_S, \hat{\rho}_S(t)] - \sum_{j,k=1}^2 \left(\begin{aligned} & [\hat{s}_j \hat{s}_k \hat{\rho}_S(t) - \hat{s}_k \hat{\rho}_S(t) \hat{s}_j] S_{\hat{e}_j \hat{e}_k}^+(-\delta_k) \\ & + [\hat{\rho}_S(t) \hat{s}_k \hat{s}_j - \hat{s}_j \hat{\rho}_S(t) \hat{s}_k] S_{\hat{e}_k \hat{e}_j}^-(\delta_k) \end{aligned} \right), \quad (2.9)$$

where the properties of the environment are captured by the half-sided Fourier transforms of the environmental correlation functions,

$$S_{\hat{e}_j \hat{e}_k}^+(\omega) = \int_{-\infty}^0 d\tau \langle \hat{e}_j(0) \hat{e}_k(\tau) \rangle_E e^{-i\omega\tau}, \quad (2.10a)$$

$$S_{\hat{e}_j \hat{e}_k}^-(\omega) = \int_0^{\infty} d\tau \langle \hat{e}_j(0) \hat{e}_k(\tau) \rangle_E e^{-i\omega\tau}. \quad (2.10b)$$

The superscripts \pm reflect the property

$$S_{\hat{e}_j \hat{e}_k}^{\pm}(\omega) = \frac{1}{2} S_{\hat{e}_j \hat{e}_k}(\omega) \pm i\mathcal{PV} \int_0^{\infty} \frac{d\epsilon}{2\pi} \frac{S_{\hat{e}_j \hat{e}_k}(\epsilon)}{\omega - \epsilon},$$

where \mathcal{PV} \int denotes the Cauchy principal value of the integral and

$$S_{\hat{e}_j \hat{e}_k}(\omega) = S_{\hat{e}_j \hat{e}_k}^+(\omega) + S_{\hat{e}_j \hat{e}_k}^-(\omega) = \int_{-\infty}^{\infty} d\tau \langle \hat{e}_j(0) \hat{e}_k(\tau) \rangle_E e^{-i\omega\tau} \quad (2.11)$$

is the power spectrum of the environment.

For a thermal environment, described by the state (2.7), the correlation function vanishes for identical operators, $\langle \hat{e}_j(0) \hat{e}_j(\tau) \rangle_E = 0$, $j \in \{1, 2\}$, and the remaining terms in the sum of Equation (2.9) can be regrouped as follows:

$$\frac{d}{dt}\hat{\rho}_S(t) = -\frac{i}{\hbar} [\hat{H}_S + \Delta\hat{H}, \hat{\rho}_S(t)] + S_{\hat{e}_1 \hat{e}_2}(-\delta) \mathcal{D}[\hat{s}^\dagger] \hat{\rho}_S(t) + S_{\hat{e}_2 \hat{e}_1}(\delta) \mathcal{D}[\hat{s}] \hat{\rho}_S(t),$$

where we introduced the so-called *Lindblad dissipator*

$$\mathcal{D}[\hat{O}] \hat{\rho} = \hat{O} \hat{\rho} \hat{O}^\dagger - \frac{1}{2} \hat{O}^\dagger \hat{O} \hat{\rho} - \frac{1}{2} \hat{\rho} \hat{O}^\dagger \hat{O}. \quad (2.12)$$

Following Breuer and Petruccione [2002], we will call the operators \hat{O} *Lindblad operators*. The term $\Delta\hat{H}$ is a correction to the system Hamiltonian \hat{H}_S that stems from the principle-value integrals. It can be absorbed in the Hamiltonian by a suitable redefinition of the system parameters and we will omit it in the following. In the Markov approximation, sums over discrete environmental modes ω_l can be replaced by an integral $\int_0^{\infty} d\omega g(\omega)/2\pi$ over a continuum of modes weighted with the mode density $g(\omega)$. Likewise, the discrete coupling parameters κ_l are replaced by a continuous coupling function $\kappa(\omega)$. The spectral functions evaluated at the transition frequencies $\pm\delta$ of the system take the form

$$\begin{aligned} S_{\hat{e}_1 \hat{e}_2}(-\delta) &= \gamma n_{\text{th}}(\delta, T), \\ S_{\hat{e}_2 \hat{e}_1}(\delta) &= \gamma [n_{\text{th}}(\delta, T) + 1], \end{aligned}$$

where we defined the rate

$$\gamma = g(\delta) |\kappa(\delta)|^2 \quad (2.13)$$

and introduced the thermal occupation number

$$n_{\text{th}}(\omega, T) = \frac{e^{-\hbar\omega/k_{\text{B}}T}}{1 - e^{-\hbar\omega/k_{\text{B}}T}} \quad (2.14)$$

of a mode of energy ω at temperature T .

In summary, in the Born-Markov approximation, an environment of harmonic oscillators with linear coupling (2.8) is described by Lindblad dissipators of the form Equation (2.12) that are weighted with rates defined by the environmental spectral function $S_{\hat{e}_j \hat{e}_k}$ evaluated at the corresponding transition frequency of the system,

$$\frac{d}{dt} \hat{\rho}_{\text{S}}(t) = -\frac{i}{\hbar} [\hat{H}_{\text{S}}, \hat{\rho}_{\text{S}}(t)] + \gamma n_{\text{th}} \mathcal{D}[\hat{s}^\dagger] \hat{\rho}_{\text{S}}(t) + \gamma (n_{\text{th}} + 1) \mathcal{D}[\hat{s}] \hat{\rho}_{\text{S}}(t). \quad (2.15)$$

The Lindblad dissipators preserve the complete positivity $\hat{\rho}_{\text{S}}(t) \geq 0$ of the density matrix and its normalization $\text{Tr}[\hat{\rho}_{\text{S}}(t)] = 1$, but they introduce dissipative effects such as relaxation or dephasing. More specifically, the Lindblad dissipator $\mathcal{D}[\hat{s}^\dagger] \hat{\rho}_{\text{S}}(t)$ models an excitation of the system by absorbing a quantum from the environment, whereas the Lindblad dissipator $\mathcal{D}[\hat{s}] \hat{\rho}_{\text{S}}(t)$ models a relaxation of the system by emitting a quantum into the environment. This form of the quantum master equation in the Born-Markov approximation will be our starting point for the description of dissipative quantum systems. From now on, we will suppress the subscript S, *i.e.*, we will write $\hat{\rho}(t)$ and \hat{H} , respectively.

2.2 Continuously monitored dissipative quantum systems

The QME (2.15) describes the so-called *unconditional* state of the quantum system S interacting with its environment E. Excitations are emitted or absorbed by the system at rates $\gamma(n_{\text{th}} + 1)$ and γn_{th} , respectively, but the exact emission or absorption times are unknown. In contrast, one can imagine a situation where the system S is completely surrounded by detectors that track every exchange of excitations between S and E. In this case, the system is found to emit and absorb quanta at random times and its state evolves stochastically. Now, the instantaneous state of the system is *conditional* because it depends on a random sequence of previous detection events. Each repetition of the experiment corresponds to a random realization of a stochastic process and is called a *quantum trajectory*. Importantly, monitoring the interaction between S and E does not change the average dynamics, *i.e.*, an ensemble average over many quantum trajectories starting from the same initial state will reproduce the unconditional evolution given by the QME (2.15). For this reason, Alsing and Carmichael [1991] called the quantum trajectory approach an *unraveling* of the QME.

Photon counting and *homodyne detection* are two experimental methods to implement a continuous measurement that approximates the idealized picture described above. In Sections 2.2.2 and 2.2.3, we will derive stochastic differential equations that describe the time evolution of the system under these two measurement schemes. Before, we introduce the concept of a positive-operator-valued measurement as a model of the detection process.

2.2.1 Positive-operator-valued measurements

The postulates of quantum mechanics propose the so-called projective measurement as a theoretical model of the measurement process. Each physically measurable quantity is associated with a Hermitian observable \hat{A} with a set of eigenvalues α . If one

measures the observable \hat{A} with respect to a quantum state $|\psi\rangle$, one randomly obtains one of the eigenvalues α of \hat{A} as the measurement result. The probability to obtain a particular eigenvalue α_0 is given by $\langle\psi|\hat{\Pi}_{\alpha_0}|\psi\rangle$, where $\hat{\Pi}_{\alpha_0}$ denotes the projector on the subspace spanned by the eigenvectors associated with the eigenvalue α_0 . The final state after the measurement is the normalized projection of the state $|\psi\rangle$ before the measurement onto the subspace associated with α_0 .

However, this model of the quantum measurement process is highly idealized. In a more realistic model, the quantum system to be measured interacts with another quantum system serving as a measurement apparatus. The interaction entangles system and apparatus until, finally, the state of the measurement apparatus is determined in a projective measurement. Since system and measurement apparatus are entangled, the projective measurement of the apparatus also affects the system's state. A positive-operator-valued measurement (POVM) is an effective description of the impact of this measurement on the system if the degrees of freedom of the measurement apparatus have been eliminated. The following definition of POVMs is based on the textbooks by Breuer and Petruccione [2002] and Wiseman and Milburn [2009].

A POVM is defined by

- the set of possible measurement results r ,
- a map $\mathcal{O}_r(\hat{\rho})$, called *operation*, that defines the effective change of the system's state $\hat{\rho}$ if the measurement result r is obtained, and
- an operator \hat{E}_r , called *effect*, that defines the probability $P(r) = \text{Tr}[\hat{E}_r\hat{\rho}]$ to obtain the corresponding measurement result.

It can be shown that the effects must have the general form

$$\hat{E}_r = \sum_k \hat{O}_{r,k}^\dagger \hat{O}_{r,k} , \quad (2.16)$$

where the linear operators $\hat{O}_{r,k}$ are called *measurement operators*. To ensure that $P(r)$ is a probability, the effects must be positive semidefinite, $\hat{E}_r \geq 0$, and sum up to the identity,

$$\sum_r \hat{E}_r = \hat{\mathbb{1}} . \quad (2.17)$$

If a certain measurement result r is obtained, the normalized state of the system after the measurement is given by

$$\hat{\rho}'|_r = \frac{\mathcal{O}_r(\hat{\rho})}{P(r)} .$$

The operation \mathcal{O}_r must be

1. completely positive, *i.e.*, it maps positive operators onto positive operators even if \mathcal{O}_r is part of a combined operation $\mathcal{O}_r \otimes \mathbb{1}$ acting on a tensor product of Hilbert spaces $\mathcal{H} \otimes \mathcal{H}'$,
2. trace-preserving or decreasing, *i.e.*, $0 \leq \text{Tr}[\mathcal{O}_r(\hat{\rho})] \leq 1$, and
3. convex linear, *i.e.*, the relation $\mathcal{O}_r\left(\sum_j p_j \hat{\rho}_j\right) = \sum_j p_j \mathcal{O}_r(\hat{\rho}_j)$ holds for probabilities $0 \leq p_j \leq 1$ with $\sum_j p_j = 1$.

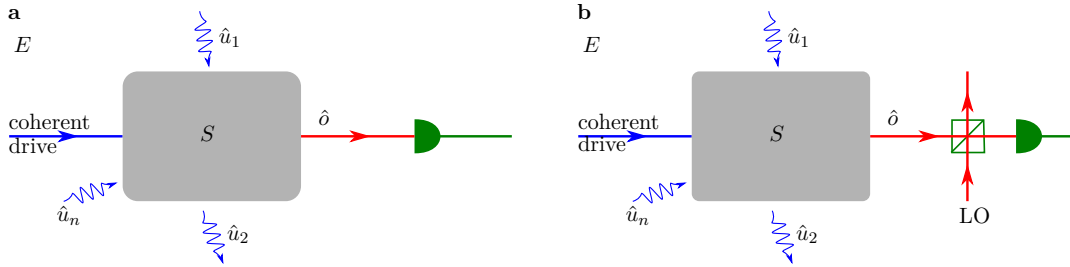


FIGURE 2.1: Sketch of a dissipative quantum system S whose interaction with the environment E via the mode \hat{o} is continuously monitored. **(a)** In the case of photon counting, the photons emitted in the mode \hat{o} are directly detected. **(b)** In the case of homodyne detection, the mode \hat{o} is displaced by a local oscillator (LO) signal at a beam splitter before detection. The sketch shows the so-called *imbalanced* homodyne detection scheme.

It can be shown that the only form that satisfies all of these conditions is

$$\mathcal{O}_r(\hat{\rho}) = \sum_k \hat{O}_{r,k} \hat{\rho} \hat{O}_{r,k}^\dagger. \quad (2.18)$$

The POVM obviously reduces to the conventional projective measurement of an observable \hat{A} if we choose the set of results r to be the set of eigenvalues α of \hat{A} and if we identify the measurement operators $\hat{O}_{r,k}$ with the projectors onto the corresponding eigenspaces $\hat{\Pi}_\alpha$. However, the results r in a POVM do not have to be related to the eigenvalues of an observable. Instead, they can label completely different abstract measurement outcomes, and there could be even only two distinct outcomes.

2.2.2 Photon counting

Stochastic quantum master equation

Following the treatment in Wiseman and Milburn [2009] and Breuer and Petruccione [2002], we now derive a stochastic master equation (SME) for photon counting. As discussed at the beginning of this chapter, this SME defines a stochastic process that is fully equivalent to its corresponding QME (2.15) if an ensemble average over many realizations of the stochastic process is taken.

As a starting point of the derivation, we consider a quantum master equation of the form (2.15),

$$\frac{d}{dt} \hat{\rho} = -\frac{i}{\hbar} [\hat{H}, \hat{\rho}] + \sum_{j=1}^{N_u} \mathcal{D}[\hat{u}_j] \hat{\rho} + \mathcal{D}[\hat{o}] \hat{\rho}, \quad (2.19)$$

with N_u+1 Lindblad terms. The Lindblad operators \hat{u}_j are associated with unobserved interactions between system and environment, whereas the emission of quanta via the transition associated with the Lindblad operator \hat{o} is continuously monitored, as shown in Figure 2.1(a). For simplicity, we absorbed the decay rates and the thermal prefactors into the Lindblad operators. Equation (2.15) is recovered by setting $N_u = 1$ and by defining $\hat{u}_1 = \sqrt{\gamma n_{\text{th}}} \hat{s}^\dagger$ and $\hat{o} = \sqrt{\gamma(n_{\text{th}} + 1)} \hat{s}$. To be prepared for the derivation of homodyne detection in Section 2.2.3, we assume that the output mode

\hat{o} is displaced by a complex amplitude ξ before detection,

$$\hat{o} \rightarrow \hat{o}_{\rightarrow} = \hat{o} + \xi . \quad (2.20)$$

The case of a pure photon counting measurement is recovered in the limit $\xi \rightarrow 0$. The displacement transformation (2.20) can be achieved by the setup shown in Figure 2.1(b), where the output mode \hat{o} of the system is mixed with a second mode \hat{o}_{LO} at a beam splitter of transmittivity p [Wiseman and Milburn, 1993],

$$\begin{aligned} \hat{o}_{\rightarrow} &= \sqrt{p}\hat{o} + i\sqrt{1-p}\hat{o}_{\text{LO}} , \\ \hat{o}_{\uparrow} &= -i\sqrt{1-p}\hat{o} - \sqrt{p}\hat{o}_{\text{LO}} . \end{aligned}$$

The quantity ξ depends on the local oscillator (LO) field \hat{o}_{LO} that is generated by a laser at the frequency of the output mode \hat{o} . It can be decomposed into a classical coherent field and quantum fluctuations, $\hat{o}_{\text{LO}} = -i\xi/\sqrt{1-p} + \hat{v}$. We now consider the limit $p \rightarrow 1$ of a high-transmittivity beam splitter and a strong laser. Then, the two output modes of the beam splitter are given by $\hat{o}_{\rightarrow} = \hat{o} + \xi$ and $\hat{o}_{\uparrow} = -\hat{o}_{\text{LO}}$.

Using the relation

$$\mathcal{D}[\hat{o} + \xi]\hat{\rho} = \mathcal{D}[\hat{o}]\hat{\rho} - i \left[\frac{i}{2}(\xi^*\hat{o} - \xi\hat{o}^\dagger), \hat{\rho} \right] ,$$

we can rewrite the Lindblad dissipator $\mathcal{D}[\hat{o}]\hat{\rho}$ in Equation (2.19) to incorporate the displacement ξ of the mode \hat{o} . The modified QME is

$$\frac{d}{dt}\hat{\rho} = -\frac{i}{\hbar} \left[\hat{H} - \frac{i\hbar}{2}(\xi^*\hat{o} - \xi\hat{o}^\dagger), \hat{\rho} \right] + \sum_j \mathcal{D}[\hat{u}_j]\hat{\rho} + \mathcal{D}[\hat{o} + \xi]\hat{\rho} . \quad (2.21)$$

Next, we derive an equation for the infinitesimal change $d\hat{\rho}$ of the system's state $\hat{\rho}$ in a time interval dt . The continuous measurement of the displaced mode \hat{o}_{\rightarrow} , given by Equation (2.20), can be described by a POVM with two results, namely, the detection of a photon in the time interval dt , or no detection event in dt . The corresponding measurement operators are $\hat{O}_1 = \hat{o}_{\rightarrow}\sqrt{dt}$ if a photon has been detected, and $\hat{O}_0 = \hat{1} - \hat{o}_{\rightarrow}^\dagger\hat{o}_{\rightarrow}dt/2$ otherwise. The form of \hat{O}_0 follows from the form of \hat{O}_1 and the fact that the condition (2.17) must be satisfied in each time step up to corrections of order dt^2 . Using Equation (2.18), the change of the state $\hat{\rho}$ in a time step dt due to the continuous measurement is

$$d\hat{\rho}|_{\text{meas}} = \left[\frac{\hat{O}_0\hat{\rho}\hat{O}_0^\dagger}{\text{Tr}[\hat{O}_0^\dagger\hat{O}_0\hat{\rho}]} - \hat{\rho} \right] (1 - dN) + \left[\frac{\hat{O}_1\hat{\rho}\hat{O}_1^\dagger}{\text{Tr}[\hat{O}_1^\dagger\hat{O}_1\hat{\rho}]} - \hat{\rho} \right] dN . \quad (2.22)$$

Here, dN is a random number that is unity if a photon has been emitted, and zero otherwise, *i.e.*,

$$dN^2 = dN . \quad (2.23)$$

According to the theory of POVMs, the probability to observe an emission event in the time step dt is given by $P(1) = \text{Tr}[\hat{O}_1^\dagger\hat{O}_1\hat{\rho}] = \text{Tr}[\hat{o}_{\rightarrow}^\dagger\hat{o}_{\rightarrow}\hat{\rho}]dt$. Since the emission of photons is a discrete process, dN is distributed according to a Poisson distribution with expectation value

$$\mathbb{E}[dN] = \text{Tr}[\hat{o}_{\rightarrow}^\dagger\hat{o}_{\rightarrow}\hat{\rho}]dt . \quad (2.24)$$

Inserting the explicit forms of \hat{O}_0 and \hat{O}_1 in Equation (2.22) and expanding to leading order in dt and dN , we find

$$\begin{aligned} d\hat{\rho}|_{\text{meas}} = & \left[-\frac{1}{2}\hat{\sigma}_{\rightarrow}^{\dagger}\hat{\sigma}_{\rightarrow}dt + \frac{1}{2}\text{Tr}(\hat{\sigma}_{\rightarrow}^{\dagger}\hat{\sigma}_{\rightarrow}\hat{\rho})dt \right] \hat{\rho} + \hat{\rho} \left[-\frac{1}{2}\hat{\sigma}_{\rightarrow}^{\dagger}\hat{\sigma}_{\rightarrow}dt + \frac{1}{2}\text{Tr}(\hat{\sigma}_{\rightarrow}^{\dagger}\hat{\sigma}_{\rightarrow}\hat{\rho})dt \right] \\ & + \left[\frac{\hat{\sigma}_{\rightarrow}\hat{\rho}\hat{\sigma}_{\rightarrow}^{\dagger}}{\text{Tr}(\hat{\sigma}_{\rightarrow}^{\dagger}\hat{\sigma}_{\rightarrow}\hat{\rho})} - \hat{\rho} \right] dN . \end{aligned}$$

On the other hand, the Hamiltonian term and the unmonitored dissipative interactions in Equation (2.21) change the state $\hat{\rho}$ in the time interval dt by

$$d\hat{\rho}|_{\text{rest}} = -\frac{i}{\hbar} \left[\hat{H} - \frac{i\hbar}{2}(\xi^*\hat{\sigma} - \xi\hat{\sigma}^{\dagger}), \hat{\rho} \right] dt + \sum_j \mathcal{D}[\hat{u}_j]\hat{\rho}dt .$$

Combining these results, we obtain the following SME:

$$d\hat{\rho} = [(\mathcal{L} + \mathcal{N})\hat{\rho} - \text{Tr}(\mathcal{N}\hat{\rho})\hat{\rho}] dt + \left[\frac{(\hat{\sigma} + \xi)\hat{\rho}(\hat{\sigma}^{\dagger} + \xi^*)}{\text{Tr}[(\hat{\sigma}^{\dagger} + \xi^*)(\hat{\sigma} + \xi)\hat{\rho}]} - \hat{\rho} \right] dN , \quad (2.25)$$

where the superoperators \mathcal{L} and \mathcal{N} are defined as follows:

$$\mathcal{L}\hat{\rho} = -\frac{i}{\hbar} \left[\hat{H} - \frac{i\hbar}{2}(\xi^*\hat{\sigma} - \xi\hat{\sigma}^{\dagger}), \hat{\rho} \right] + \sum_j \mathcal{D}[\hat{u}_j]\hat{\rho} , \quad (2.26)$$

$$\mathcal{N}\hat{\rho} = -\left\{ \frac{1}{2}(\hat{\sigma}^{\dagger} + \xi^*)(\hat{\sigma} + \xi), \hat{\rho} \right\} . \quad (2.27)$$

This stochastic differential equation describes two distinct contributions to the time evolution of the density matrix $\hat{\rho}$. The term proportional to the infinitesimal time step dt describes a continuous time evolution of the state $\hat{\rho}$ if no photon has been detected. The term proportional to the stochastic increment dN describes a so-called quantum jump event, *i.e.*, a sudden discontinuous change of the density matrix if a photon has been detected. The stochastic process defined by Equation (2.25) is a piecewise-deterministic process because $\hat{\rho}$ undergoes a continuous time evolution that is occasionally interrupted by discontinuous quantum jump events.

The term $\mathcal{N}\hat{\rho}$ stems from the fact that even the observation of no photon in the time interval dt contains information on the state $\hat{\rho}$ [Carmichael, 2008]: If no photons have been detected for several successive time steps, $\hat{\rho}$ describes most likely a state with a low photon number. The term $\mathcal{N}\hat{\rho}$ in Equation (2.25) modifies the state $\hat{\rho}$ accordingly. If we generalize the definition of the commutator to non-Hermitian arguments,

$$[\hat{H}, \hat{\rho}] = \hat{H}\hat{\rho} - \hat{\rho}\hat{H}^{\dagger} ,$$

the term $\mathcal{N}\hat{\rho}$ can be rewritten as a non-Hermitian correction $-i\hbar\hat{M}$ to the system Hamiltonian \hat{H} , where

$$\hat{M} = \frac{\hbar}{2}(\hat{\sigma}^{\dagger} + \xi^*)(\hat{\sigma} + \xi) . \quad (2.28)$$

Such a non-Hermitian term does not preserve the trace of the density matrix. However, Equation (2.25) is still trace preserving because of the nonlinear term $-\text{Tr}(\mathcal{N}\hat{\rho})\hat{\rho}$.

Using the fact that Equation (2.24) can be rewritten as

$$\mathbb{E}[dN] = -\text{Tr}(\mathcal{N}\hat{\rho})dt, \quad (2.29)$$

one can check that the ensemble average $\mathbb{E}[d\hat{\rho}]/dt$ of Equation (2.25) reproduces the unconditional QMEs (2.19) and (2.21). In this sense, the stochastic process defined in Equation (2.25) is equivalent to the corresponding QME [Carmichael, 2008].

Stochastic Schrödinger equation

If there are no unobserved dissipative channels, *i.e.*, $\hat{u}_j = 0$ for all j in Equation (2.19), the SME (2.25) will preserve the purity of a pure initial state $\hat{\rho}(t_0) = |\psi(t_0)\rangle\langle\psi(t_0)|$. Under these conditions, we can replace the SME by a stochastic Schrödinger equation (SSE) for a state vector $|\psi\rangle$,

$$\begin{aligned} d|\psi\rangle = & \left[-\frac{i}{\hbar} \left(\hat{H} - \frac{i\hbar}{2} (\xi^* \hat{o} - \xi \hat{o}^\dagger) - i\hbar \hat{M} \right) + \langle\psi| \hat{M} |\psi\rangle \right] |\psi\rangle dt \\ & + \left[\frac{(\hat{o} + \xi) |\psi\rangle}{\sqrt{\langle\psi| (\hat{o}^\dagger + \xi^*) (\hat{o} + \xi) |\psi\rangle}} - |\psi\rangle \right] dN, \end{aligned} \quad (2.30)$$

where \hat{M} has been defined in Equation (2.28). The stochastic increment dN is again a Poissonian increment fulfilling the relations $dN^2 = dN$ and

$$\mathbb{E}[dN] = \langle\psi| \left(\hat{M} + \hat{M}^\dagger \right) |\psi\rangle dt.$$

Using the relation

$$d\hat{\rho} = (d|\psi\rangle)\langle\psi| + |\psi\rangle(d\langle\psi|) + (d|\psi\rangle)(d\langle\psi|), \quad (2.31)$$

one can show that Equation (2.30) reproduces the SME (2.25) for $\hat{u}_j = 0$ to leading order in dt and dN . Note that the third term on the right-hand side of Equation (2.31) is actually relevant because of the relation $dN^2 = dN$.

2.2.3 Unbalanced homodyne detection

The SME and SSE obtained for photon counting describe a piecewise-deterministic stochastic processes, *i.e.*, the quantum state of the system evolves continuously between successive photon detection events but changes discontinuously if a photon is detected. This raises the question whether it is possible to find an unraveling of the QME (2.15) that corresponds to a continuous stochastic process, *e.g.*, a Wiener process. The free parameter ξ in the equations of motion hints that the answer will be affirmative since the unraveling of a QME is obviously not uniquely defined. In the following, we will show that the quantum trajectories become continuous for a large LO amplitude ξ . The corresponding experimental measurement is called homodyne detection.

In a first step, we derive the stochastic differential equations for unbalanced homodyne detection. The case of balanced homodyne detection will be discussed in Section 2.2.4.

Stochastic quantum master equation

To derive the stochastic differential equation for homodyne detection, we go back to Equation (2.25) and consider the case when the LO amplitude ξ is much larger than all energy scales of the system Hamiltonian \hat{H} and all dissipative decay rates contained in \hat{u}_j . In this limit, the LO signal will dominate the detected signal, $|\xi|^2 \gg \langle \hat{\sigma}^\dagger \hat{\sigma} \rangle$, and photons will be detected in each time step. The system is still only weakly perturbed by the measurement since most of the photons stem from the LO.

Following the discussion of Wiseman and Milburn [2009], we now derive the SME corresponding to the limit $|\xi|^2 \gg \langle \hat{\sigma}^\dagger \hat{\sigma} \rangle$ by focusing on a time interval $\delta t = \mathcal{O}(|\xi|^{-3/2})$. According to Equation (2.29), the average number of detected photons in the interval $[t, t + \delta t)$ is given by

$$\mathbb{E}(\delta N) = \left[|\xi|^2 + \text{Tr} \left[(\xi^* \hat{\sigma} + \xi \hat{\sigma}^\dagger) \hat{\rho}(t) \right] + \mathcal{O}(|\xi|^{1/2}) \right] \delta t, \quad (2.32)$$

where the last term stems from the change $\delta \hat{\rho}$ of the density matrix during the time interval δt . In the limit $|\xi| \rightarrow \infty$, the number of detected photons grows proportional to $|\xi|^2 \delta t = \mathcal{O}(|\xi|^{1/2})$, whereas the change of the system's state $\delta \hat{\rho}$ is of the order of $\mathcal{O}(\delta t) = \mathcal{O}(|\xi|^{-3/2})$ and tends to zero. This fact ensures that we can derive a differential equation for $\hat{\rho}$ by considering the time interval δt . Fluctuations in the number of detected photons δN are dominated by the Poissonian photon-number statistics of the local oscillator. Since the local-oscillator amplitude is very large, the Poissonian distribution can be approximated by a Gaussian distribution of mean $\mathbb{E}(\delta N)$ and variance $\sigma^2 = [|\xi|^2 + \mathcal{O}(|\xi|^{3/2})] \delta t$ [Wiseman and Milburn, 1993]. Therefore, we can approximate the stochastic evolution of δN by a continuous Wiener process [Breuer and Petruccione, 2002]

$$\delta N = |\xi|^2 \delta t \left[1 + \frac{\langle \xi^* \hat{\sigma} + \xi \hat{\sigma}^\dagger \rangle (t)}{|\xi|^2} \right] + |\xi| \delta W + \mathcal{O}(|\xi|^{-1/2}), \quad (2.33)$$

where the Wiener increment δW satisfies $\mathbb{E}(\delta W) = 0$ and $\delta W^2 = \delta t$ and is distributed according to a normal distribution of unit variance. In the limit $|\xi| \rightarrow \infty$, the detected photocurrent is given by

$$\frac{\mathbb{E}(\delta N)}{\delta t} = |\xi|^2 + |\xi| \left\langle e^{i\varphi} \hat{\sigma} + e^{-i\varphi} \hat{\sigma}^\dagger \right\rangle (t), \quad (2.34)$$

where we have decomposed the LO amplitude in polar coordinates,

$$\xi = |\xi| e^{-i\varphi}. \quad (2.35)$$

Therefore, the detected photocurrent measures a field quadrature $\langle e^{i\varphi} \hat{\sigma} + e^{-i\varphi} \hat{\sigma}^\dagger \rangle$ of the mode $\hat{\sigma}$ depending on the relative phase φ of the LO. Inserting Equation (2.33) in Equation (2.25) and taking the limit $|\xi| \rightarrow \infty$, we obtain the SME for homodyne detection,

$$\begin{aligned} d\hat{\rho} = & -\frac{i}{\hbar} \left[\hat{H}, \hat{\rho} \right] dt + \sum_j \mathcal{D}[\hat{u}_j] \hat{\rho} dt + \mathcal{D}[\hat{\sigma}] \hat{\rho} dt \\ & + \left[e^{i\varphi} \hat{\sigma} \hat{\rho} + e^{-i\varphi} \hat{\rho} \hat{\sigma}^\dagger - \left\langle e^{i\varphi} \hat{\sigma} + e^{-i\varphi} \hat{\sigma}^\dagger \right\rangle \hat{\rho} \right] dW, \end{aligned} \quad (2.36)$$

where we used the limits $\delta t \rightarrow dt$ and $\delta W \rightarrow dW$ for $|\xi| \rightarrow \infty$. The stochastic Wiener increment has the properties

$$dW^2 = dt \text{ and } \mathbb{E}(dW) = 0 , \quad (2.37)$$

and is distributed according to a normal distribution with unit variance. Using these properties, one can check that the ensemble average $\mathbb{E}(d\hat{\rho})/dt$ reproduces the unconditional QME (2.19).

Stochastic Schrödinger equation

Similar to the case of photon counting, it is possible to rewrite the homodyne-detection SME (2.36) as a SSE for a state vector $|\psi\rangle$ if there are no unobserved dissipative channels, *i.e.*, if $\hat{u}_j = 0$ for all j . The corresponding SSE is [Wiseman and Milburn, 2009]

$$\begin{aligned} d|\psi\rangle = & \left[-i\hat{H} - \frac{1}{2} \left(\hat{\sigma}^\dagger \hat{\sigma} - \langle e^{i\varphi} \hat{\sigma} + e^{-i\varphi} \hat{\sigma}^\dagger \rangle \hat{\sigma} e^{i\varphi} + \frac{1}{4} \langle e^{i\varphi} \hat{\sigma} + e^{-i\varphi} \hat{\sigma}^\dagger \rangle^2 \right) \right] |\psi\rangle dt \\ & + \left[\hat{\sigma} e^{i\varphi} - \frac{1}{2} \langle e^{i\varphi} \hat{\sigma} + e^{-i\varphi} \hat{\sigma}^\dagger \rangle \right] |\psi\rangle dW . \end{aligned} \quad (2.38)$$

Using $d\hat{\rho} = (d|\psi\rangle)\langle\psi| + |\psi\rangle(d\langle\psi|) + (d|\psi\rangle)(d\langle\psi|)$ and $dW^2 = dt$, one can verify that Equation (2.38) reproduces the SME (2.36) for $\hat{u}_j = 0$ to leading order in dt .

2.2.4 Balanced homodyne detection

Stochastic quantum master equation

Instead of mixing the LO signal with the output mode \hat{o} at a beam splitter with a transmittivity close to unity, one can also use a beam splitter with transmittivity 1/2. Then, the output modes are given by [Wiseman and Milburn, 1993]

$$\begin{aligned} \hat{o}_\rightarrow &= \frac{1}{\sqrt{2}} \hat{o} + \frac{i}{\sqrt{2}} \hat{o}_{\text{LO}} , \\ \hat{o}_\uparrow &= \frac{i}{\sqrt{2}} \hat{o} + \frac{1}{\sqrt{2}} \hat{o}_{\text{LO}} . \end{aligned}$$

Thus, for an incoming local-oscillator signal $\hat{o}_{\text{LO}} = i\xi + \hat{\nu}$, both outgoing modes will contain information on the system,

$$\begin{aligned} \hat{o}_\rightarrow &= \frac{1}{\sqrt{2}} (\hat{o} - \xi) + \frac{i}{\sqrt{2}} \hat{\nu} , \\ \hat{o}_\uparrow &= \frac{i}{\sqrt{2}} (\hat{o} + \xi) + \frac{1}{\sqrt{2}} \hat{\nu} , \end{aligned}$$

and, consequently, a photon detector must be placed at each outgoing arm. Using the relation

$$\mathcal{D}[\hat{o}]\hat{\rho} = \mathcal{D} \left[\frac{1}{\sqrt{2}} (\hat{o} - \xi) \right] \hat{\rho} + \mathcal{D} \left[\frac{1}{\sqrt{2}} (\hat{o} + \xi) \right] \hat{\rho} ,$$

one can rewrite Equation (2.19) as follows:

$$\frac{d}{dt}\hat{\rho} = -\frac{i}{\hbar} [\hat{H}, \hat{\rho}] + \sum_j \mathcal{D}[\hat{u}_j]\hat{\rho} + \mathcal{D}\left[\frac{1}{\sqrt{2}}(\hat{o} - \xi)\right]\hat{\rho} + \mathcal{D}\left[\frac{1}{\sqrt{2}}(\hat{o} + \xi)\right]\hat{\rho}.$$

Repeating the calculation outlined in Section 2.2.2, one obtains the SME

$$\begin{aligned} d\hat{\rho} = & [(\mathcal{L} + \mathcal{N})\hat{\rho} - \text{Tr}(\mathcal{N}\hat{\rho})\hat{\rho}]dt + \left[\frac{(\hat{o} + \xi)\hat{\rho}(\hat{o}^\dagger + \xi^*)}{\text{Tr}[(\hat{o}^\dagger + \xi^*)(\hat{o} + \xi)\hat{\rho}]} - \hat{\rho} \right] dN_{\hat{o}+\xi} \\ & + \left[\frac{(\hat{o} - \xi)\hat{\rho}(\hat{o}^\dagger - \xi^*)}{\text{Tr}[(\hat{o}^\dagger - \xi^*)(\hat{o} - \xi)\hat{\rho}]} - \hat{\rho} \right] dN_{\hat{o}-\xi} \end{aligned} \quad (2.39)$$

where the superoperators \mathcal{L} and \mathcal{N} are defined as follows:

$$\mathcal{L}\hat{\rho} = -\frac{i}{\hbar} [\hat{H}, \hat{\rho}] + \sum_j \mathcal{D}[\hat{u}_j]\hat{\rho}, \quad (2.40)$$

$$\mathcal{N}\hat{\rho} = -\left\{ \frac{1}{2} (\hat{o}^\dagger \hat{o} + |\xi|^2), \hat{\rho} \right\}. \quad (2.41)$$

The increments $dN_{\hat{o}\pm\xi} \in \{0, 1\}$ describe two independent stochastic Poisson processes and have the ensemble-averaged expectation values

$$\mathbb{E}[dN_{\hat{o}\pm\xi}] = \frac{1}{2} \text{Tr} \left[(\hat{o}^\dagger \pm \xi^*)(\hat{o} \pm \xi)\hat{\rho} \right] dt.$$

The homodyne signal is constructed by subtracting the signals of the two detectors, *i.e.*, the average detected photocurrent is

$$\frac{\mathbb{E}[dN_{\hat{o}+\xi}] - \mathbb{E}[dN_{\hat{o}-\xi}]}{dt} = \text{Tr} \left[(\xi^* \hat{o} + \xi \hat{o}^\dagger)\hat{\rho} \right].$$

Comparing this result to Equation (2.34), we find that the large constant offset $|\xi|^2$ has been canceled out. This is beneficial for an experimental implementation of homodyne detection, because the $|\xi|^2$ -term is an unwanted large background that may even fluctuate with the laser amplitude $|\xi|$. Note that while this background has been removed, the relevant information on the field quadrature of the quantum state $\hat{\rho}$ is identical both in the unbalanced and in the balanced homodyne detection scheme.

In the limit $|\xi| \rightarrow \infty$, the Poissonian processes $dN_{\hat{o}\pm\xi}$ can again be approximated by two continuous Wiener processes. The results of the calculation given in Section 2.2.3 can be taken over with the replacements $\xi \rightarrow \pm\xi/\sqrt{2}$ and $\hat{o} \rightarrow \hat{o}/\sqrt{2}$. In this way, one obtains the SME

$$\begin{aligned} d\hat{\rho} = & -\frac{i}{\hbar} [\hat{H}, \hat{\rho}] dt + \sum_j \mathcal{D}[\hat{u}_j]\hat{\rho}dt + \mathcal{D}[\hat{o}]\hat{\rho}dt \\ & + \left[e^{i\varphi}\hat{o}\hat{\rho} + e^{-i\varphi}\hat{\rho}\hat{o}^\dagger - \left\langle e^{i\varphi}\hat{o} + e^{-i\varphi}\hat{o}^\dagger \right\rangle \hat{\rho} \right] \frac{dW_{\hat{o}+\xi} - dW_{\hat{o}-\xi}}{\sqrt{2}}, \end{aligned}$$

where the independent Wiener increments fulfill $(dW_{\hat{o}\pm\xi})^2 = dt$, $dW_{\hat{o}\pm\xi}dW_{\hat{o}\mp\xi} = 0$, and $\mathbb{E}[dW_{\hat{o}\pm\xi}] = 0$. This result is identical to the SME (2.36) for unbalanced homodyne detection if one defines a new Wiener increment $dW = (dW_{\hat{o}+\xi} - dW_{\hat{o}-\xi})/\sqrt{2}$ which has the properties required in Section 2.2.3, *i.e.*, it satisfies the conditions $\mathbb{E}[dW] = 0$ and $dW^2 = dt$, and it is distributed according to a normal distribution with unit variance.

Stochastic Schrödinger equation

Consequently, the stochastic Schrödinger equation for balanced homodyne detection is given by Equation (2.38).

2.2.5 Stochastic master equation vs. stochastic Schrödinger equation

In the previous sections, we derived SSEs and SMEs for photon counting and homodyne detection. We argued that the SSE only applies to situations when there are no unobserved interactions with the environment. Otherwise, the SME approach must be taken. However, from the point of view of a theoretical physicist, one can always assume that all interactions with the environment were monitored. This trick is actually used in the so-called quantum Monte Carlo wave function method [Dalibard *et al.*, 1992; Dum *et al.*, 1992], which is a numerical approach to calculate the time evolution and correlation functions of dissipative quantum systems in a less memory-consuming way than by solving a QME of the form of Equation (2.15). To apply the quantum Monte Carlo wave function method, one rewrites a QME as a multidimensional SSE consisting of several independent stochastic Poisson processes by assuming that all dissipative processes in the QME were perfectly monitored. A potentially mixed initial state $\hat{\rho}(t_0)$ is decomposed into a statistical mixture of pure states $|\psi_j(t_0)\rangle$ and the time evolution of each of these pure states is calculated by averaging many quantum trajectories obtained from the SSE. In this way, only a N -dimensional state vector must be stored instead of a $N \times N$ -dimensional matrix, *i.e.*, the requirements on the computer's memory have been reduced. This comes at the cost that one has to calculate a large number of quantum trajectories to recover the dynamics of $\hat{\rho}(t)$ by an ensemble average.

With this in mind, it may seem unreasonable to construct a SME that describes some dissipative effects by Lindblad dissipators and others by a stochastic process. However, the SME and a quantum Monte Carlo wave function approach differ in the interpretation of the propagated states $\hat{\rho}$ and $|\psi\rangle$. The SME calculates a *strict quantum trajectory* in the sense of Wiseman and Milburn [1993], *i.e.*, each stochastic quantum jump event corresponds to an experimentally accessible detection event. Thus, the state $\hat{\rho}$ describes the quantum state of a dissipative quantum system in an experiment that has measured the corresponding series of detection events. In contrast, the quantum Monte Carlo wave function approach calculates a *lax trajectory* in the sense of Wiseman and Milburn [1993] because there are additional auxiliary stochastic processes that have no physical correspondence in an experimental setup but are merely added to convert the QME into a SSE. Therefore, the state $|\psi\rangle$ does not describe the quantum state of an actual experiment. Note, however, that a physical state could always be recovered by an ensemble average over all auxiliary dimensions of the stochastic process.

2.2.6 Conditional vs. unconditional dynamics

The detection record of a continuous measurement provides a label for quantum states that allows one to extract more information from a quantum system than in the corresponding unconditional experiment. As an example, Breuer and Petruccione [2002] consider a quantum system that is initialized in a certain state $\hat{\rho}(t_0)$ and whose dynamics is governed by an unconditional QME. At a certain time t_1 , the variance of

an observable \hat{A} with respect to the unconditional state $\hat{\rho}(t_1)$ is measured,

$$\langle(\Delta\hat{A})^2\rangle_{\hat{\rho}(t_1)} = \text{Tr}[\hat{A}^2\hat{\rho}(t_1)] - \left(\text{Tr}[\hat{A}\hat{\rho}(t_1)]\right)^2. \quad (2.42)$$

If a continuous measurement is performed such that the dynamics is described by a SSE for the state vector $|\psi\rangle$, the unconditional density matrix of the system at time t_1 can be decomposed into a set of pure states $|\psi_j\rangle$,

$$\hat{\rho}(t_1) = \sum_j p_j |\psi_j\rangle \langle\psi_j| ,$$

where each index j represents a certain photodetection record, $|\psi_j\rangle$ is the system state given this photodetection record, and p_j is the probability of observing the record j . By discarding all but one specific photodetection record j_0 , one can repeatedly prepare the corresponding state $|\psi_{j_0}\rangle$. Therefore, one can measure the variance of the observable \hat{A} with respect to the state $|\psi_{j_0}\rangle$,

$$\langle(\Delta\hat{A})^2\rangle_{|\psi_{j_0}\rangle} = \langle\psi_{j_0}|\hat{A}^2|\psi_{j_0}\rangle - \langle\psi_{j_0}|\hat{A}|\psi_{j_0}\rangle^2. \quad (2.43)$$

The variance (2.42) can now be decomposed into a sum of two variances,

$$\langle(\Delta\hat{A})^2\rangle_{\hat{\rho}(t_1)} = \sum_j p_j \langle(\Delta\hat{A})^2\rangle_{|\psi_j\rangle} + \left[\sum_j p_j \langle\psi_j|\hat{A}|\psi_j\rangle^2 - \left(\sum_j p_j \langle\psi_j|\hat{A}|\psi_j\rangle\right)^2 \right],$$

where the first term is the pure-state variance (2.43) ensemble-averaged over all possible records j , and the second term measures the classical statistical fluctuations of the expectation value $\langle\psi_j|\hat{A}|\psi_j\rangle$ over all possible records j . Both terms represent information that is inaccessible given only the unconditional state $\hat{\rho}(t_1)$.

2.3 Phase-space quasiprobability distributions

The concept of phase space is a convenient tool in classical physics to illustrate the state and the dynamics of a classical system [Nayfeh and Mook, 1995]. Wigner [1932] proposed a generalization of this concept to quantum systems by defining the Wigner function of a quantum state, which has the form of a joint probability density function of position and momentum. However, despite the fact that its marginal distributions are indeed proper probability distributions of position and momentum, the Wigner function itself may take negative values, therefore, it is only a quasiprobability distribution.

2.3.1 Harmonic oscillator

We now define continuous-variable phase-space quasiprobability distributions for a system that is defined on the infinite-dimensional Hilbert space of a harmonic oscillator. An overview of the definitions and conventions regarding the quantum harmonic oscillator is given in Appendix A. In addition to the Wigner function, a whole family of quasiprobability distributions exists, which can be defined by the s -parametrized characteristic function [Gerry and Knight, 2005]

$$C_{\hat{\rho}}(\lambda, s) = \text{Tr} \left[\hat{\rho} e^{\lambda\hat{a}^\dagger - \lambda^*\hat{a} + s|\lambda|^2/2} \right]. \quad (2.44)$$

For $s = 0$, the characteristic function reduces to the expectation value of the displacement operator $\hat{D}(\lambda)$, defined by

$$\hat{D}(\lambda) = e^{\lambda \hat{a}^\dagger - \lambda^* \hat{a}} . \quad (2.45)$$

The Glauber-Sudarshan \mathcal{P} -function, the Wigner function \mathcal{W} , and the Husimi \mathcal{Q} -function are defined via a Fourier transform of the characteristic function (2.44) for different values of the parameter λ ,

$$\mathcal{P}_{\hat{\rho}}(\alpha) = \frac{1}{\pi^2} \int d^2\lambda C_{\hat{\rho}}(\lambda, 1) e^{\lambda^* \alpha - \lambda \alpha^*} , \quad (2.46)$$

$$\mathcal{W}_{\hat{\rho}}(\alpha) = \frac{1}{\pi^2} \int d^2\lambda C_{\hat{\rho}}(\lambda, 0) e^{\lambda^* \alpha - \lambda \alpha^*} , \quad (2.47)$$

$$\mathcal{Q}_{\hat{\rho}}(\alpha) = \frac{1}{\pi^2} \int d^2\lambda C_{\hat{\rho}}(\lambda, -1) e^{\lambda^* \alpha - \lambda \alpha^*} , \quad (2.48)$$

where the integration range is the entire complex plane and $d^2z = d[\text{Re}(z)]d[\text{Im}(z)]$ [Bishop and Vourdas, 1994]. The variable $\alpha = \langle \alpha | \hat{a} | \alpha \rangle$ denotes the complex amplitude of a coherent state, cf. Appendix A. The \mathcal{P} , \mathcal{W} , and \mathcal{Q} function allow one to evaluate normal-ordered, symmetric, and antinormal-ordered operator averages, respectively, by integrating a corresponding polynomial in α and α^* over the entire complex plane. For instance, we have

$$\text{Tr}[\hat{a}^{\dagger p} \hat{a}^q \hat{\rho}] = \int d^2\alpha \mathcal{P}_{\hat{\rho}}(\alpha) \alpha^{*p} \alpha^q .$$

The three quasiprobability distributions can be mapped onto each other by folding them with Gaussian distributions [Carmichael, 2008],

$$\mathcal{Q}_{\hat{\rho}}(\alpha) = \frac{2}{\pi} \int d^2\lambda e^{-2|\lambda - \alpha|^2} \mathcal{W}_{\hat{\rho}}(\lambda) = \frac{1}{\pi} \int d^2\lambda e^{-|\lambda - \alpha|^2} \mathcal{P}_{\hat{\rho}}(\lambda) ,$$

$$\mathcal{W}_{\hat{\rho}}(\alpha) = \frac{2}{\pi} \int d^2\lambda e^{-2|\lambda - \alpha|^2} \mathcal{P}_{\hat{\rho}}(\lambda) .$$

Using the parity operator [Bishop and Vourdas, 1994]

$$\hat{\Pi} = e^{i\pi \hat{a}^\dagger \hat{a}} = \frac{1}{2\pi} \int d^2\xi \hat{D}(\xi) \quad (2.49)$$

and the property $\hat{D}(\alpha)\hat{D}(\beta) = e^{i\text{Im}(\alpha\beta^*)}\hat{D}(\alpha+\beta)$ of the displacement operator, one can rewrite the Wigner function as the expectation value of a displaced parity operator,

$$\mathcal{W}_{\hat{\rho}}(\alpha) = \frac{2}{\pi} \text{Tr} \left[\hat{\rho} \hat{D}(\alpha) \hat{\Pi} \hat{D}^\dagger(\alpha) \right] . \quad (2.50)$$

Similarly, the Husimi function can be rewritten as the expectation value of the corresponding quantum state $\hat{\rho}$ with respect to coherent states [Gerry and Knight, 2005],

$$\mathcal{Q}_{\hat{\rho}}(\alpha) = \frac{1}{\pi} \langle \alpha | \hat{\rho} | \alpha \rangle . \quad (2.51)$$

The \mathcal{P} , \mathcal{W} , and \mathcal{Q} functions are called quasiprobability distributions because they violate the requirements that probability distributions should be positive and not more singular than a Dirac delta distribution. For certain quantum states $\hat{\rho}$, the \mathcal{P} function can take negative values or it can even become a highly singular distribution [Mandel,

1986]. The Wigner function \mathcal{W} is always a proper function, but it can have negative values. Finally, Equation (2.51) shows that the Husimi \mathcal{Q}_ρ function is always positive for a positive semidefinite density matrix $\hat{\rho}$. However, the converse is not true, *i.e.*, not every positive \mathcal{Q} function actually corresponds to a positive semidefinite Hermitian state $\hat{\rho}$ [Gardiner, 1995].

The properties of the Wigner function turn it into a good witness for nonclassicality: If the Wigner function $\mathcal{W}_\rho(\alpha)$ has negative values, the corresponding state $\hat{\rho}$ is nonclassical [Gerry and Knight, 2005; Zurek, 2003]. For instance, it has been shown that negativity in the Wigner function of quantum states or quantum operations is a necessary condition to ensure that a quantum algorithm cannot efficiently be simulated by classical means [Mari and Eisert, 2012; Veitch *et al.*, 2013; Stahlke, 2014]. We will use this definition of nonclassicality in Chapter 4.

2.3.2 Spin

To visualize the quantum state of spin systems, we need to generalize the notion of phase-space quasiprobability distributions to finite-dimensional systems. In contrast to the case of an infinite-dimensional system, there are two alternative ways to accomplish this task.

The first option is to consider the spin eigenstates as discrete positions and to introduce the corresponding momenta by discrete Fourier transform [Buot, 1974; Wootters, 1987; Galetti and de Toledo Piza, 1988]. This gives rise to discrete phase-space quasiprobability distributions that are defined on a set of points on a torus. Analogously to the case of an infinite-dimensional system, integrating the Wigner function along a certain direction in phase space must yield a proper probability distribution, which is the marginal distribution along the perpendicular direction [Opatrný *et al.*, 1995; Gibbons *et al.*, 2004]. Similar discrete quasiprobability distributions arise if one defines joint probability distributions that describe simultaneous measurements of different spin components [Feynman, 2005; Cohen and Scully, 1986].

The second option is to define coherent states for finite-dimensional system, so-called spin-coherent states [Radcliffe, 1971; Arecchi *et al.*, 1972], see Appendix A.2. This gives rise to continuous phase-space quasiprobability distributions that are defined on a sphere [Agarwal, 1981; Brif and Mann, 1999]. We will choose this approach because it gives rise to continuous values of the amplitude and phase degree of freedom. Moreover, amplitude and phase can easily be identified by comparing spin-coherent states to the coherent states of an infinite-dimensional system.

We now generalize the Husimi \mathcal{Q} function (2.51) to spin systems. As derived in Appendix A.2, a spin-coherent state $|\theta, \varphi\rangle$ is given by the extremal spin state $|S, m_S = +S\rangle$ which has been rotated by the Euler angles $(\alpha, \beta, \gamma) = (\varphi, \theta, 0)$ [Radcliffe, 1971; Brink and Satchler, 1968],

$$|\theta, \varphi\rangle = e^{-i\varphi\hat{S}_z} e^{-i\theta\hat{S}_y} |S, S\rangle . \quad (2.52)$$

With this result in hand, we now define the Husimi \mathcal{Q} function for spins as

$$\mathcal{Q}_\rho(\theta, \varphi) = \frac{2S+1}{4\pi} \langle \theta, \varphi | \hat{\rho} | \theta, \varphi \rangle . \quad (2.53)$$

As shown in Appendix A.2, the spin-coherent state $|\theta, \varphi\rangle$ converges to the coherent state $|\alpha\rangle$ with $\alpha = \sqrt{2S} \tan(\theta/2) e^{i\varphi}$ in the limit $S \gg 1$ up to an irrelevant global phase factor. This result shows that the angles $\theta \in [0, \pi)$ and $\varphi \in [0, 2\pi)$ parametrize

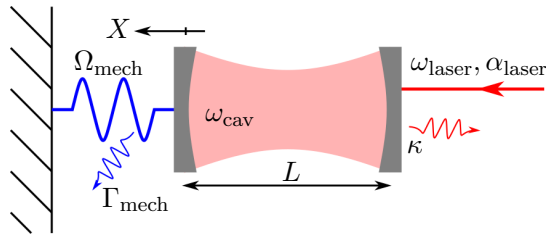


FIGURE 2.2: Sketch of an optomechanical system. A cavity is formed between a fixed mirror (right) and a movable mirror (left) that is mounted to a spring. The mechanical resonance frequency is denoted by Ω_{mech} . A displacement X of the movable mirror will change the cavity length L and, thus, the optical resonance frequency ω_{cav} . The cavity can be driven by a laser at frequency ω_{laser} , which has a complex amplitude α_{laser} . Both the cavity and the mechanics are subject to losses at the rates κ and Γ_{mech} , respectively.

the amplitude and phase of a spin-coherent state, respectively. We will use the Q function for spin systems in Chapters 5 and 6.

2.4 Optomechanical system

2.4.1 Optomechanical Hamiltonian

In the 17th century, the German astronomer Johannes Kepler noted that dust tails of comets always point away from the sun. He attributed this effect to radiation-pressure forces, which are due to the fact that photons carry momentum.¹ While radiation-pressure forces are usually negligible in our macroscopic world, they lead to an appreciable coupling between mechanical and optical degrees of freedom in setups at the micro- and nanoscale.

The optomechanical Hamiltonian is a generic model of the interaction between electromagnetic radiation and mechanical motion in the quantum regime, and it has become the key element to model a large number of different experiments in the field of cavity optomechanics [Aspelmeyer *et al.*, 2014]. In its simplest form, the optomechanical Hamiltonian describes the interaction between a mechanical mode \hat{b} at frequency Ω_{mech} and a single mode \hat{a} of the radiation field in a cavity at frequency ω_{cav} . The mechanical mode could be, for instance, a spring to which one of the end mirrors of the cavity is mounted, as shown in Figure 2.2. A displacement X of the cantilever changes the length L of the cavity and, thus, the resonance frequency ω_{cav} . To lowest order in the displacement, this gives rise to a parametric coupling between the cavity and the mechanical oscillator,

$$\omega_{\text{cav}}(L + X) \approx \omega_{\text{cav}} + X \frac{d\omega_{\text{cav}}}{dX} + \mathcal{O}(X^2). \quad (2.54)$$

Quantizing the radiation field and the mechanical motion, one obtains the following interaction Hamiltonian between the optical and the mechanical mode [Law, 1995].

$$\hat{H}_{\text{int}} = -\hbar g_0 \hat{a}^\dagger \hat{a} (\hat{b} + \hat{b}^\dagger), \quad (2.55)$$

¹In fact, both the radiation pressure and the solar wind exert forces on the particles emitted by the comet. Radiation pressure generates a comparatively small acceleration of solid dust particles whereas the larger acceleration of ionized particles is caused by the solar wind [Weigert *et al.*, 2005].

where $g_0 = Gx_{\text{zpf}}$ denotes the bare optomechanical coupling strength. The frequency pull parameter $G = -d\omega_{\text{cav}}/dX$ describes the frequency change per elongation. In our cantilever model, it has the form $G = \omega_{\text{cav}}/L$ [Aspelmeyer *et al.*, 2014]. The minus sign appears in the interaction Hamiltonian because an increase of the cavity length decreases the resonance frequency. Following the conventions introduced in Appendix A, the mechanical zero-point fluctuation is given by $x_{\text{zpf}} = \sqrt{\hbar/2m\Omega_{\text{mech}}}$, where m denotes the effective mechanical mass. The mechanical elongation expressed in terms of the creation and annihilation operator \hat{b}^\dagger and \hat{b} , respectively, is $\hat{X} = x_{\text{zpf}}(\hat{b}^\dagger + \hat{b})$.

Typically, the optical cavity is driven by a laser of strength α_{laser} at a frequency ω_{laser} . The total Hamiltonian of the setup in a frame rotating at the laser frequency, $|\psi_{\text{lab}}\rangle = \hat{U}|\psi_{\text{rot}}\rangle$ where $\hat{U}(t) = e^{-i\omega_{\text{laser}}\hat{a}^\dagger\hat{a}t}$, is

$$\hat{H}_{\text{OM}} = -\hbar\Delta\hat{a}^\dagger\hat{a} + \hbar\Omega_{\text{mech}}\hat{b}^\dagger\hat{b} - \hbar g_0\hat{a}^\dagger\hat{a}(\hat{b}^\dagger + \hat{b}) + \hbar\alpha_{\text{laser}}(\hat{a}^\dagger + \hat{a}) . \quad (2.56)$$

The detuning is defined as

$$\Delta = \omega_{\text{laser}} - \omega_{\text{cav}} . \quad (2.57)$$

One can account for mechanical and radiative losses by embedding the optomechanical Hamiltonian (2.56) in a QME of the form (2.15),

$$\frac{d}{dt}\hat{\rho} = -\frac{i}{\hbar}[\hat{H}_{\text{OM}}, \hat{\rho}] + \Gamma_{\text{mech}}(n_{\text{ph}} + 1)\mathcal{D}[\hat{b}]\hat{\rho} + \Gamma_{\text{mech}}n_{\text{ph}}\mathcal{D}[\hat{b}^\dagger]\hat{\rho} + \kappa\mathcal{D}[\hat{a}]\hat{\rho} , \quad (2.58)$$

where κ is the optical damping rate, Γ_{mech} is the mechanical damping rate, and n_{ph} is the thermal occupation number of the mechanical mode. Since typical mechanical frequencies are orders of magnitude smaller than the cavity frequency, one can assume that the photons are effectively coupled to a zero-temperature environment [Aspelmeyer *et al.*, 2014].

Optomechanical figures of merit

An important figure of merit of the optomechanical system defined by Equations (2.56) and (2.58) is the ratio between the bare optomechanical coupling strength and the mechanical frequency,

$$\frac{g_0}{\Omega_{\text{mech}}} .$$

Typically, optomechanical systems operate in the *weak-coupling regime* $g_0 \ll \Omega_{\text{mech}}$. This allows one to perform a semiclassical analysis of the optomechanical equations of motion, as discussed below in Section 2.4.2. Moreover, the optomechanical Hamiltonian can be linearized in the weak-coupling regime by reparametrizing the optical field as the sum of a coherent state $|\alpha\rangle$ and small quantum fluctuations $\delta\hat{a}$

$$\hat{a} = \alpha + \delta\hat{a} ,$$

where the condition $|\langle\delta\hat{a}\rangle| \ll |\alpha|$ holds. To leading order in $|\alpha|/|\langle\delta\hat{a}\rangle|$ and for $g_0 \ll \Omega_{\text{mech}}$, Equation (2.56), is approximated by the following linearized Hamiltonian:

$$\hat{H}_{\text{lin}} = -\hbar\Delta\delta\hat{a}^\dagger\delta\hat{a} + \hbar\Omega_{\text{mech}}\hat{b}^\dagger\hat{b} - \hbar g \left(e^{-i\phi}\delta\hat{a}^\dagger + e^{i\phi}\delta\hat{a} \right) (\hat{b}^\dagger + \hat{b}) , \quad (2.59)$$

where we decomposed the amplitude of the coherent state in polar coordinates, $\alpha = |\alpha| e^{-i\phi}$, and introduced the optomechanical coupling strength

$$g = g_0 |\alpha| . \quad (2.60)$$

Note that driving the optical cavity with a laser enhances the bare optomechanical coupling strength g_0 by the square root of the intracavity photon number $|\alpha|^2$. The QME in the linearized description is obtained by replacing $\hat{H}_{\text{OM}} \rightarrow \hat{H}_{\text{lin}}$ and $\hat{a} \rightarrow \delta\hat{a}$ in Equation (2.58). It provides a convenient description of many effects, for instance displacement sensing [Teufel *et al.*, 2009], coherent state transfer [Verhagen *et al.*, 2012], and optomechanical cooling [Wilson-Rae *et al.*, 2007; Marquardt *et al.*, 2007].

Another important quantity is the so-called sideband ratio

$$\frac{\kappa}{\Omega_{\text{mech}}} .$$

In the resolved-sideband regime $\kappa < \Omega_{\text{mech}}$, the optical resonance at ω_{cav} is sufficiently narrow to be able to detect mechanical sidebands at the frequencies $\omega_{\text{cav}} \pm \Omega_{\text{mech}}$. As we will discuss below, the steady state of the QME (2.58) can describe nonclassical mechanical limit-cycle oscillation in the resolved-sideband regime. The opposite regime $\kappa > \Omega_{\text{mech}}$ is called unresolved-sideband regime, Doppler regime, or bad-cavity limit [Aspelmeyer *et al.*, 2014].

Finally, the optomechanical cooperativity compares the optomechanical coupling strength g to the optical and mechanical decay rates,

$$\mathcal{C} = \frac{g^2}{\kappa\Gamma_{\text{mech}}} . \quad (2.61)$$

As we will discuss below in Section 2.4.2, the optomechanical cooperativity determines the onset of mechanical limit-cycle oscillations.

Experimental platforms

The optomechanical Hamiltonian (2.56) provides a theoretical model for a large variety of experimental setups. A straightforward realization of our sketch shown in Figure 2.2 is to suspend one of the end mirrors of a cavity [Arcizet *et al.*, 2006; Gigan *et al.*, 2006] or to insert a dielectric membrane into a cavity with fixed end mirrors [Thompson *et al.*, 2008]. In experiments with microdiscs [Jiang *et al.*, 2009], microtoroids [Rokhsari *et al.*, 2005], microspheres [Ma *et al.*, 2007], or droplets of liquid helium [Childress *et al.*, 2017], the optical whispering-gallery modes inside the rotationally symmetric structure are coupled to mechanical vibrations of the structure. Nanorods and nanobeams can be coupled to the evanescent radiation field of a cavity [Anetsberger *et al.*, 2009] such that the mechanical motion modulates the effective refractive index of the cavity or its loss rate. Optomechanical crystals [Eichenfield *et al.*, 2009] are a very promising platform to realize large arrays of coupled optomechanical systems [Peano *et al.*, 2015]. They are fabricated by patterning a planar substrate such that optical and mechanical modes localize at the same positions. In the microwave frequency range, optomechanical systems can be realized by coupling superconducting circuits to mechanical resonators using piezoelectric effects [O'Connell *et al.*, 2010] or capacitive coupling [Regal *et al.*, 2008].

2.4.2 Optomechanical instability

An interesting feature of the optomechanical system defined in Equations (2.56) and (2.58) is a dynamical multistability effect if the frequency of the laser drive exceeds the cavity frequency, *i.e.*, if the condition $\Delta > 0$ holds [Marquardt *et al.*, 2006]. For such a laser drive, the radiation-pressure force excites the mechanical resonator into periodic motion. If the mechanical damping rate Γ_{mech} is sufficiently small, the oscillation becomes multistable, *i.e.*, stable oscillations are possible at several different amplitudes for a given detuning Δ . In this section, we derive analytical formulas for this mechanical oscillation in the weak-coupling regime using a semiclassical approximation. We follow the discussion by Rodrigues and Armour [2010] and Armour and Rodrigues [2012].

From Equation (2.58), the following equations of motion of the expectation values $\langle \hat{a} \rangle$ and $\langle \hat{b} \rangle$ can be derived:

$$\begin{aligned} \frac{d}{dt} \langle \hat{a} \rangle &= i\Delta \langle \hat{a} \rangle + ig_0 \langle \hat{a}(\hat{b} + \hat{b}^\dagger) \rangle - i\alpha_{\text{laser}} - \frac{\kappa}{2} \langle \hat{a} \rangle , \\ \frac{d}{dt} \langle \hat{b} \rangle &= -i\Omega_{\text{mech}} \langle \hat{b} \rangle + ig_0 \langle \hat{a}^\dagger \hat{a} \rangle - \frac{\Gamma_{\text{mech}}}{2} \langle \hat{b} \rangle . \end{aligned}$$

These two differential equations do not form a closed system, therefore, we perform a semiclassical approximation that factorizes all expectation values of operators, *e.g.*, $\langle \hat{a}\hat{b} \rangle \approx \langle \hat{a} \rangle \langle \hat{b} \rangle$. This approximation neglects correlations between the optical and mechanical mode and is equivalent to a truncated-Wigner-function approximation [Walls and Milburn, 1994; Polkovnikov, 2010]. It describes the mechanical oscillation correctly in the weak-coupling limit $g_0 \ll \Omega_{\text{mech}}$ [Armour and Rodrigues, 2012]. Introducing the abbreviations $\alpha = \langle \hat{a} \rangle$ and $\beta = \langle \hat{b} \rangle$, we obtain the following closed set of nonlinear differential equations:

$$\frac{d}{dt} \alpha = i\Delta \alpha + ig_0 \alpha (\beta + \beta^*) - i\alpha_{\text{laser}} - \frac{\kappa}{2} \alpha , \quad (2.62a)$$

$$\frac{d}{dt} \beta = -i\Omega_{\text{mech}} \beta + ig_0 |\alpha|^2 - \frac{\Gamma_{\text{mech}}}{2} \beta . \quad (2.62b)$$

To proceed, we assume that the mechanical oscillation is the superposition of a time-dependent offset $\bar{\beta}$ and a harmonic oscillation at the mechanical frequency Ω_{mech} ,

$$\beta(t) = \bar{\beta}(t) + B(t)e^{-i[\Omega_{\text{mech}}t + \phi(t)]} . \quad (2.63)$$

For this ansatz, Equation (2.62a) takes the following form:

$$\frac{d}{dt} \alpha(t) = f(t)\alpha(t) + g(t) ,$$

where the time-dependent coefficients $f(t)$ and $g(t)$ are given by

$$\begin{aligned} f(t) &= -\frac{\kappa}{2} + i \left(\Delta + 2g_0 \text{Re}[\bar{\beta}(t)] + 2g_0 B(t) \cos[\Omega_{\text{mech}}t + \phi(t)] \right) , \\ g(t) &= -i\alpha_{\text{laser}} . \end{aligned}$$

The general solution of this differential equation is

$$\alpha(t) = \alpha(t_0) e^{\int_{t_0}^t dt' f(t')} + \int_{-\infty}^{\infty} dt' \Theta(t-t') e^{\int_{t'}^t dt'' f(t'')} g(t') . \quad (2.64)$$

To evaluate Equation (2.64), we assume adiabatic cavity dynamics, *i.e.*, the quantities $\bar{\beta}$, B , and ϕ vary on a timescale much larger than $1/\kappa$ and the cavity field α adjusts quasi-instantaneously to those values. Hence, we can consider them to be constant to solve the equation of motion (2.64) of $\alpha(t)$. Moreover, the damping term $-\kappa/2$ in the prefactor $f(t)$ ensures that the homogeneous solution, given by the first term of Equation (2.64), decays. Thus, in the long-time limit, the solution $\alpha(t)$ is only given by the second term of Equation (2.64), which we evaluate using the Fourier decomposition $e^{ia \sin(\Omega t + \phi)} = \sum_{k=-\infty}^{\infty} J_k(a) e^{ik(\Omega t + \phi)}$, where $J_k(x)$ denotes the k -th Bessel function of the first kind [Gradshteyn and Ryzhik, 1980]. We obtain the solution

$$\alpha(t) = e^{i\tilde{B} \sin(\Omega_{\text{mech}} t + \phi)} \sum_{k=-\infty}^{\infty} \frac{i\alpha_{\text{laser}} e^{ik\phi} J_k(-\tilde{B})}{g_k} e^{ik\Omega_{\text{mech}} t}, \quad (2.65)$$

where we introduced the abbreviations

$$\tilde{B} = \frac{2g_0 B}{\Omega_{\text{mech}}}, \quad (2.66)$$

$$g_k = i \left[\Delta + 2g_0 \text{Re}(\bar{\beta}) - k\Omega_{\text{mech}} \right] - \frac{\kappa}{2}. \quad (2.67)$$

Finally, we need to determine the values of $\bar{\beta}$, B , and ϕ self-consistently. To this end, we insert Equations (2.63) and (2.65) in Equation (2.62b) and sort by orders of $e^{-i\Omega_{\text{mech}} t}$. Since we are working in the weak-coupling limit $g_0 \ll \Omega_{\text{mech}}$, we can apply a rotating-wave approximation to drop fast-oscillating terms and obtain the following set of differential equations:

$$\frac{d}{dt} \bar{\beta}(t) = - \left[i\Omega_{\text{mech}} + \frac{\Gamma_{\text{mech}}}{2} \right] \bar{\beta}(t) + ig_0 N_{\text{opt}}(t), \quad (2.68a)$$

$$\frac{d}{dt} B(t) = - \left[\frac{\Gamma_{\text{mech}}}{2} + \frac{\Gamma_{\text{BA}}(t)}{2} \right] B(t), \quad (2.68b)$$

$$\frac{d}{dt} \phi(t) = \delta\Omega(t), \quad (2.68c)$$

where we introduced the abbreviations

$$N_{\text{opt}} = |\alpha_{\text{laser}}|^2 \sum_{k=-\infty}^{\infty} \frac{J_k^2(\tilde{B})}{|g_k|^2}, \quad (2.69)$$

$$\Gamma_{\text{BA}} = - \frac{2g_0^2 \kappa |\alpha_{\text{laser}}|^2}{\tilde{B}} \sum_{k=-\infty}^{\infty} \frac{J_k(\tilde{B}) J_{k+1}(\tilde{B})}{|g_k|^2 |g_{k+1}|^2}, \quad (2.70)$$

$$\delta\Omega = + \frac{2g_0^2 |\alpha_{\text{laser}}|^2}{\Omega_{\text{mech}} \tilde{B}} \sum_{k=-\infty}^{\infty} \frac{J_{k+1}(\tilde{B}) J_k(\tilde{B})}{|g_{k+1}|^2 |g_k|^2} \text{Re}(g_{k+1} g_k^*). \quad (2.71)$$

Here, N_{opt} is the number of photons in the cavity, Γ_{BA} is a modification of the mechanical damping due to retarded cavity backaction, and $\delta\Omega$ is the modification of the mechanical resonance frequency due to the optical spring effect [Aspelmeyer *et al.*, 2014]. Since the cavity field $\alpha(t)$ has been eliminated, B , $\bar{\beta}$, and ϕ are now again time-dependent quantities. Therefore, N_{opt} , Γ_{BA} , and $\delta\Omega$ also depend on time.

Equations (2.68a) and (2.68b) have a steady-state solution $d\bar{\beta}_{\text{ss}}/dt = dB_{\text{ss}}/dt = 0$, which is implicitly defined as the solution of the following set of coupled nonlinear

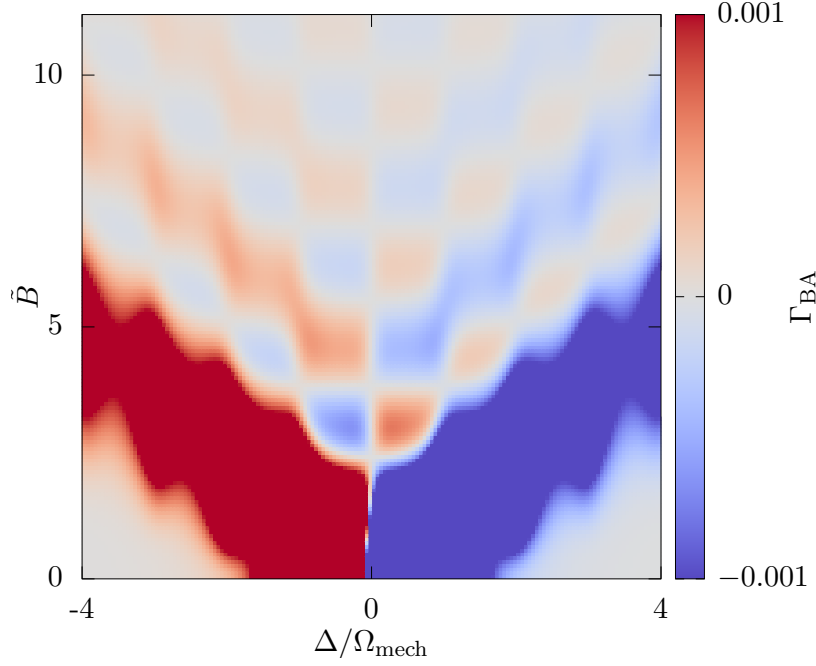


FIGURE 2.3: Optical backaction damping Γ_{BA} as a function of detuning Δ and the rescaled amplitude \tilde{B} . Parameters: $\Gamma_{\text{mech}}/\Omega_{\text{mech}} = 0$, $g_0/\Omega_{\text{mech}} = 0.16$, $\alpha_{\text{laser}}/\Omega_{\text{mech}} = 0.35$, and $\kappa/\Omega_{\text{mech}} = 0.5$.

equations:

$$\bar{\beta}_{\text{ss}} = \frac{g_0 |\alpha_{\text{laser}}|^2}{\Omega_{\text{mech}} - i\Gamma_{\text{mech}}/2} \sum_{k=-\infty}^{\infty} \frac{J_k^2(2g_0 B_{\text{ss}}/\Omega_{\text{mech}})}{\kappa^2/4 + [\Delta + 2g_0 \text{Re}(\bar{\beta}_{\text{ss}}) - k\Omega_{\text{mech}}]^2}, \quad (2.72a)$$

$$\Gamma_{\text{mech}} = \frac{g_0 \kappa \Omega_{\text{mech}} |\alpha_{\text{laser}}|^2}{B_{\text{ss}}} \sum_{k=-\infty}^{\infty} \frac{J_k(2g_0 B_{\text{ss}}/\Omega_{\text{mech}})}{\kappa^2/4 + [\Delta + 2g_0 \text{Re}(\bar{\beta}_{\text{ss}}) - k\Omega]^2} \times \frac{J_{k+1}(2g_0 B_{\text{ss}}/\Omega_{\text{mech}})}{\kappa^2/4 + [\Delta + 2g_0 \text{Re}(\bar{\beta}_{\text{ss}}) - (k+1)\Omega]^2}. \quad (2.72b)$$

The steady-state values of $\bar{\beta}_{\text{ss}}$ and B_{ss} define a constant frequency shift $\delta\Omega_{\text{ss}}$. Consequently, the phase $\phi(t)$ increases uniformly, $\phi(t) = \delta\Omega_{\text{ss}}t + \phi(0)$. Note that the initial phase $\phi(0)$ is a free parameter. Therefore, the mechanical oscillation of an optomechanical system driven above resonance, $\Delta > 0$, is an example of a limit-cycle oscillation, which will be discussed below in Section 2.6.

For fixed parameters Δ , Ω_{mech} , g_0 , α_{laser} , Γ_{mech} , and κ , Equation (2.72a) can be used to calculate the offset $\bar{\beta}$ as a function of the amplitude \tilde{B} . Given these values of $\bar{\beta}$, the optical backaction damping Γ_{BA} (2.70) can be evaluated as a function of \tilde{B} . This is shown in Figure 2.3. For low amplitudes and $\Delta \geq 0$, the optical backaction damping is negative, *i.e.*, it aims to excite mechanical oscillations. Stable oscillations will occur at amplitudes \tilde{B}_{ss} defined by the conditions

$$\begin{aligned} \Gamma_{\text{mech}} &< -\Gamma_{\text{BA}}(\tilde{B} < \tilde{B}_{\text{ss}}), \\ \Gamma_{\text{mech}} &= -\Gamma_{\text{BA}}(\tilde{B}_{\text{ss}}), \\ \Gamma_{\text{mech}} &> -\Gamma_{\text{BA}}(\tilde{B} > \tilde{B}_{\text{ss}}), \end{aligned}$$

i.e., at amplitudes \tilde{B}_{ss} for which the mechanical damping Γ_{mech} compensates the

optical backaction damping. For the case $\Gamma_{\text{mech}} = 0$ shown in Figure 2.3, these conditions are fulfilled at each transition from negative backaction damping (blue regions) to positive backaction damping (red regions) along the direction of the \tilde{B} axis. There are several solutions for each value of Δ , therefore, multistability can occur.

Obviously, the backaction damping must dominate over the mechanical damping at zero amplitude to start limit-cycle oscillations. Therefore, the condition

$$0 \leq \Gamma_{\text{mech}} < -\Gamma_{\text{BA}}(0) \quad (2.73)$$

must be satisfied to observe an onset of mechanical self-oscillations. Using the limits

$$\begin{aligned} \lim_{x \rightarrow 0} J_n(x) &= \delta_{n,0} , \\ \lim_{x \rightarrow 0} \frac{J_n(x)}{x} &= \begin{cases} \infty & n = 0 , \\ 1/2 & n = 1 , \\ 0 & n \geq 2 , \end{cases} \end{aligned}$$

we can express maximum backaction damping obtained at zero amplitude as follows:

$$\Gamma_{\text{BA}}(0) = g_0^2 \kappa |\alpha_{\text{laser}}|^2 \frac{|g_1|^2 - |g_{-1}|^2}{|g_1|^2 |g_0|^2 |g_{-1}|^2} = -\frac{g_0^2}{\kappa} N_{\text{opt}}(0) \times \mathcal{O}(1) .$$

Therefore, condition (2.73) can be rephrased in terms of the cooperativity (2.61),

$$C = \frac{g_0^2 N_{\text{opt}}(0)}{\kappa \Gamma_{\text{mech}}} = \frac{|\Gamma_{\text{BA}}(0)|}{\Gamma_{\text{mech}}} \gtrsim 1 ,$$

which means that a cooperativity larger than unity is required to start mechanical limit-cycle oscillations.

The mechanical limit-cycle oscillation is also called *phonon lasing* [Khurgin *et al.*, 2012a,b]. Similar to an optical (photon) laser, there is a threshold pump power above which mechanical limit-cycle oscillations and a narrowing of the mechanical linewidth are observed [Grudinin *et al.*, 2010; Anetsberger *et al.*, 2009; Cohen *et al.*, 2015]. Numerical [Qian *et al.*, 2012; Nation, 2013] and analytical studies [Rodrigues and Armour, 2010] predicted that phonon lasing is accompanied by reduced fluctuations of the mechanical amplitude of oscillation in the resolved-sideband regime $\kappa < \Omega_{\text{mech}}$. This effect can be quantified by the mechanical Fano factor

$$F = \frac{\langle (\hat{b}^\dagger \hat{b})^2 \rangle - \langle \hat{b}^\dagger \hat{b} \rangle^2}{\langle \hat{b}^\dagger \hat{b} \rangle} , \quad (2.74)$$

which measures the variance $\langle (\Delta \hat{b}^\dagger \hat{b})^2 \rangle$ of amplitude fluctuations normalized to the phonon-number expectation value $\langle \hat{b}^\dagger \hat{b} \rangle$. A coherent (*i.e.*, classical) state has a Poissonian phonon-number distribution and a Fano factor of unity. Thermal states have a Fano factor larger than unity. A Fano factor smaller than unity indicates a squeezed state with a sub-Poissonian phonon-number distribution, which is a nonclassical state [Mandel, 1986; Gerry and Knight, 2005]. The Fano factor has a one-to-one relation to the Mandel Q parameter [Mandel, 1986],

$$F = Q + 1 ,$$

and can be experimentally determined by measuring the second-order correlation function [Gerry and Knight, 2005]

$$g^{(2)}(\tau) = \frac{\langle \hat{b}^\dagger \hat{b}^\dagger(\tau) \hat{b}(\tau) \hat{b} \rangle}{\langle \hat{b}^\dagger \hat{b} \rangle \langle \hat{b}^\dagger(\tau) \hat{b}(\tau) \rangle},$$

whose zero-lag value $g^{(2)}(0)$ is related to the Fano factor as follows:

$$g^{(2)}(0) = \frac{F - 1}{\langle \hat{b}^\dagger \hat{b} \rangle} + 1.$$

2.5 Kerr oscillator

From the large-angle oscillation of a pendulum to the restoring force of a mechanical spring at large elongations, nonlinearity is omnipresent in Nature [Nayfeh and Mook, 1995]. A famous example of a weakly nonlinear system is the Duffing oscillator, which is described by the equation of motion

$$m\ddot{x} + m\omega_0^2 x + m\epsilon x^3 = 0,$$

where m is the effective mass of the system, ω_0 is the harmonic resonance frequency and ϵ denotes the strength of the nonlinearity. The nonlinearity is weak in the sense that the time-averaged potential energy is dominated by the harmonic term, $|\overline{m\epsilon x^4}| \ll |\overline{m\omega_0^2 x^2}|$. The classical Hamiltonian of the Duffing oscillator is

$$H_{\text{Duffing}} = \frac{1}{2m} p^2 + \frac{1}{2} m\omega_0^2 x^2 + \frac{1}{4} m\epsilon x^4. \quad (2.75)$$

Since the harmonic part of the potential dominates, H_{Duffing} can be quantized using the eigenstates of a quantum harmonic oscillator. Promoting x and p to operators \hat{X} and \hat{P} , respectively, rewriting the Hamiltonian (2.75) in terms of the ladder operators \hat{a} and \hat{a}^\dagger introduced in Appendix A, and using a rotating-wave approximation, one can show that the quantized Duffing Hamiltonian \hat{H}_{Duffing} is equivalent to the so-called Kerr Hamiltonian,

$$\begin{aligned} \hat{H}_{\text{Kerr}} &= \hbar\omega_0 \hat{a}^\dagger \hat{a} + \hbar K \hat{a}^\dagger \hat{a} (\hat{a}^\dagger \hat{a} + 1) + \text{const} \\ &= \hbar(\omega_0 + 2K) \hat{a}^\dagger \hat{a} + \hbar K \hat{a}^\dagger \hat{a}^\dagger \hat{a} \hat{a} + \text{const}, \end{aligned}$$

with $K = 3\epsilon x_{\text{zpf}}^2 / 4\omega_0$. The first line of \hat{H}_{Kerr} shows that the Kerr Hamiltonian describes an oscillator with a nonequidistant level spacing. In the following, we will absorb the small frequency shift $2K \propto \epsilon/\omega_0$ into the harmonic resonance frequency ω_0 .

The classical Duffing oscillator can be driven by external time-dependent forces, *e.g.*, a harmonic external force at frequency ω_{har} and amplitude F_{har} , which is described by the Hamiltonian

$$H_{\text{har}} = -x F_{\text{har}} \cos(\omega_{\text{har}} t + \phi_{\text{har}}), \quad (2.76)$$

or a parametric modulation of the resonance frequency ω_0 , which corresponds to the Hamiltonian

$$H_{\text{par}} = \frac{1}{2} m \delta\omega_{\text{par}}^2 x^2 \cos(\omega_{\text{par}} t + \phi_{\text{par}}). \quad (2.77)$$

To obtain a quantum description of these external forces, we replace x and p by the corresponding operators and switch to a rotating frame defined by $\hat{U}(t) = e^{-i\omega_{\text{har}}\hat{a}^\dagger\hat{a}t}$. Setting $\omega_{\text{par}} = 2\omega_{\text{har}}$ and dropping rapidly rotating terms in a rotating wave approximation, we arrive at the following Hamiltonian of a driven Kerr oscillator:

$$\hat{H}_0 = -\hbar\Delta\hat{a}^\dagger\hat{a} + \hbar K\hat{a}^\dagger\hat{a}^\dagger\hat{a}\hat{a} + \hbar\left(\alpha_1\hat{a}^\dagger + \text{H.c.}\right) + \hbar\left(\alpha_2\hat{a}^\dagger\hat{a}^\dagger + \text{H.c.}\right), \quad (2.78)$$

where we introduced the detuning

$$\Delta = \omega_{\text{har}} - \omega_0 = \frac{\omega_{\text{par}}}{2} - \omega_0 \quad (2.79)$$

between the drive frequency $\omega_{\text{har}} = \omega_{\text{par}}/2$ and the natural frequency ω_0 of the oscillator. The amplitudes of the harmonic (single-photon) and parametric (two-photon) drives are denoted by $\alpha_1 = -e^{-i\phi_{\text{ext}}}F_{\text{ext}}/\sqrt{8m\hbar\omega_0}$ and $\alpha_2 = e^{-i\phi_{\text{par}}}\delta\omega_{\text{par}}^2/8\omega_0$, respectively. By embedding Equation (2.78) into a QME describing single-photon losses, we obtain the following model of a driven dissipative Kerr oscillator, which will we use as a generic model of a nonlinear quantum system in Chapter 4:

$$\frac{d}{dt}\hat{\rho} = -\frac{i}{\hbar}\left[\hat{H}_0, \hat{\rho}\right] + \kappa(n_{\text{th}} + 1)\mathcal{D}[\hat{a}]\hat{\rho} + \kappa n_{\text{th}}\mathcal{D}[\hat{a}^\dagger]\hat{\rho}, \quad (2.80)$$

Here, κ denotes the energy decay rate and n_{th} is the thermal photon occupation number of the oscillator due to an interaction with a finite-temperature bath. In the next sections, we will review the steady-state solution of the Kerr oscillator for the harmonic and the parametric drive separately.

2.5.1 Harmonic drive

We now consider Equation (2.80) for the case $\alpha_2 = 0$. Without loss of generality, we assume α_1 to be real and nonnegative. Similar to the treatment of the optomechanical system in Section 2.4.2, we derive an equation of motion for the expectation value $\alpha = \langle\hat{a}\rangle$ and perform a semiclassical approximation by factorizing expectation values of multiple operators. In this way, we obtain the following equation of motion [Drummond and Walls, 1980]:

$$\frac{d}{dt}\alpha = \left(i\Delta - \frac{\kappa}{2}\right)\alpha - 2iK|\alpha|^2\alpha - i\alpha_1.$$

This equation has a steady-state solution $d\alpha_{\text{ss}}/dt = 0$. Decomposing $\alpha_{\text{ss}} = |\alpha_{\text{ss}}|e^{i\varphi_{\text{ss}}}$ in polar coordinates, we find the following set of conditions for the steady-state amplitude and phase:

$$\begin{aligned} 0 &= -\frac{\kappa}{2}|\alpha_{\text{ss}}| - \alpha_1 \sin(\varphi_{\text{ss}}), \\ 0 &= \Delta - 2K|\alpha_{\text{ss}}|^2 - \frac{\alpha_1}{|\alpha_{\text{ss}}|} \cos(\varphi_{\text{ss}}). \end{aligned}$$

Elimination of φ_{ss} yields a polynomial whose roots define $|\alpha_{\text{ss}}|$,

$$4K^2|\alpha_{\text{ss}}|^6 - 4K\Delta|\alpha_{\text{ss}}|^4 + \left(\Delta^2 + \frac{\kappa^2}{4}\right)|\alpha_{\text{ss}}|^2 - \alpha_1^2 = 0. \quad (2.81)$$

Given a steady-state amplitude $|\alpha_{\text{ss}}|$, the corresponding phase φ_{ss} up to integer multiples of 2π is

$$\varphi_{\text{ss}} = \begin{cases} -\arcsin(\kappa |\alpha_{\text{ss}}|/2\alpha_1) & \text{if } \Delta - 2K |\alpha_{\text{ss}}|^2 \geq 0, \\ -\pi + \arcsin(\kappa |\alpha_{\text{ss}}|/2\alpha_1) & \text{if } \Delta - 2K |\alpha_{\text{ss}}|^2 < 0. \end{cases} \quad (2.82)$$

Despite the fact that, in general, the roots of Equation (2.81) need to be found numerically, we can still analytically determine the number of stable solutions. To simplify the notation, it is beneficial to introduce the dimensionless quantities [Meaney *et al.*, 2014]

$$\delta = \frac{\Delta}{\kappa}, \quad (2.83)$$

$$P = \frac{\alpha_1^2 K}{\kappa^3}, \quad (2.84)$$

$$\alpha_0 = \sqrt{\frac{K}{\kappa}} \alpha_{\text{ss}}, \quad (2.85)$$

which represent a dimensionless detuning, a dimensionless rescaled drive power, and a rescaled amplitude. In terms of these quantities, Equation (2.81) reads as

$$4|\alpha_0|^6 - 4\delta |\alpha_0|^4 + \left(\delta^2 + \frac{1}{4}\right) |\alpha_0|^2 - P = 0. \quad (2.86)$$

This equation has a unique solution $|\alpha_0|^2$ if the condition $\delta < \sqrt{3}/2$ holds. In the case $\delta > \sqrt{3}/2$, there are three solutions if the drive power P is in the interval $(P_-(\delta), P_+(\delta))$ defined by the two boundaries

$$P_{\pm}(\delta) = \frac{\delta}{9} \left(\frac{\delta^2}{3} + \frac{3}{4} \right) \pm \frac{1}{3\sqrt{3}} \sqrt{\frac{\delta^2}{3} - \frac{1}{4}}^3. \quad (2.87)$$

On the boundaries $P = P_-(\delta)$ or $P = P_+(\delta)$, there are two solutions for $|\alpha_0|^2$. The two boundaries $P_{\pm}(\delta)$ coalesce at the critical point $(\delta_{\text{crit}}, P_{\text{crit}}) = (\sqrt{3}/2, \sqrt{3}/18)$, as shown in Figure 2.4(a).

All properties of the rescaled semiclassical solution $|\alpha_0|$ are defined by Equation (2.86), which is independent of the ratio K/κ . Classically, this ratio merely rescales the amplitude of oscillation as shown in Equation (2.85). However, in the quantum case, it also determines the distribution of the quantum fluctuations in phase space, *i.e.*, the shape of the steady-state Wigner function. The deformation of the Wigner function as a function of K/κ is illustrated in Figure 2.4(b) and can be analyzed by transforming the QME (2.80) to a frame where the semiclassical solution α_{ss} has been subtracted,

$$\frac{d}{dt} \hat{\rho}' = -\frac{i}{\hbar} \left[\hat{H}'_0, \hat{\rho}' \right] + \kappa (n_{\text{th}} + 1) \mathcal{D}[\hat{b}] \hat{\rho}' + \kappa n_{\text{th}} \mathcal{D}[\hat{b}^\dagger] \hat{\rho}', \quad (2.88)$$

$$\begin{aligned} \hat{H}'_0(-\alpha_{\text{ss}}) &= -\hbar\kappa \left(\delta - 4|\alpha_0|^2 \right) \hat{a}^\dagger \hat{a} + \hbar\kappa \left(\alpha_0^2 \hat{a}^\dagger \hat{a}^\dagger + \text{H.c.} \right) \\ &+ 2\hbar\kappa \sqrt{\frac{K}{\kappa}} \left(\alpha_0 \hat{a}^\dagger \hat{a}^\dagger \hat{a} + \text{H.c.} \right) + \hbar\kappa \frac{K}{\kappa} \hat{a}^\dagger \hat{a}^\dagger \hat{a} \hat{a}, \end{aligned} \quad (2.89)$$

where $\hat{\rho}' = \hat{D}(-\alpha_{\text{ss}}) \hat{\rho} \hat{D}^\dagger(-\alpha_{\text{ss}})$ and $\alpha_{\text{ss}} = \sqrt{\kappa/K} \alpha_0$. In the limit $K \ll \kappa$, the steady-state amplitude $|\alpha_{\text{ss}}|$ is very large and the terms in the second line of the Hamiltonian (2.89) can be neglected. Therefore, the steady state is a squeezed state at a large

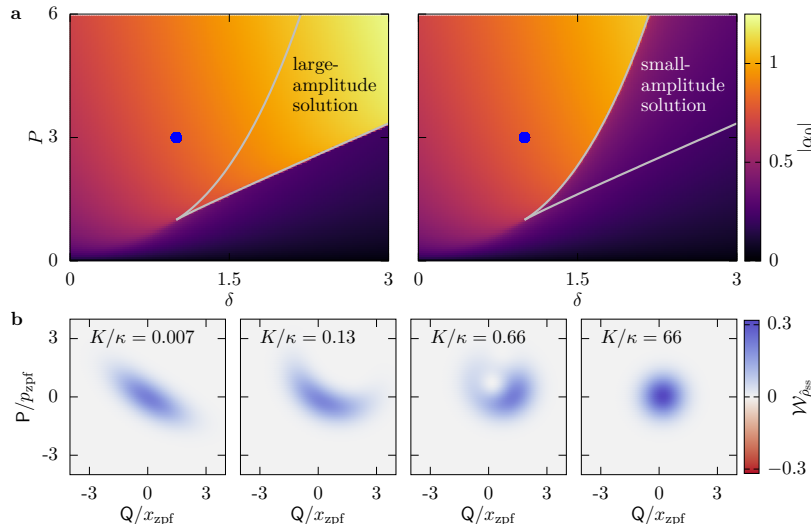


FIGURE 2.4: **(a)** Amplitude of the rescaled semiclassical solution α_0 of the driven and damped Kerr oscillator, defined by Equations (2.78) and (2.80), subject to a harmonic drive, *i.e.*, $\alpha_2 = 0$. The gray lines indicate the boundaries $P_{\pm}(\delta)$ defined in Equation (2.87). Inside the gray lines, there are three solutions for α_0 . The stable solutions at large and small amplitude are shown in the left and right subplot, respectively. Outside this region, there is only one stable solution. **(b)** Wigner function of the steady-state solution $\hat{\rho}_{ss}$ for the parameters $(P, \delta) = (3.0, 1.0)$, indicated in (a) by the blue circle, and different ratios of K/κ . The plot area is centered around the semiclassical steady-state amplitude $\alpha_{ss} = \sqrt{\kappa/K}\alpha_0$. The shape of the Wigner function depends on the ratio K/κ .

amplitude and its Wigner function has the shape of an ellipse. If the ratio K/κ is increased, $|\alpha_{ss}|$ decreases and the term proportional to $\sqrt{K/\kappa}$ in Equation (2.89) becomes relevant. This leads to a deformation of the Wigner function to a banana shape. In the limit $K \gg \kappa$, the steady-state amplitude converges to zero, Equation (2.88) reduces to an undriven but damped Kerr oscillator, whose steady-state solution is the vacuum state.

2.5.2 Parametric drive

We now consider a purely parametric drive, *i.e.*, we set $\alpha_1 = 0$. In this case, the Hamiltonian (2.78) can be rewritten as follows:

$$\hat{H}_0 = -\hbar\Delta\hat{a}^\dagger\hat{a} + \hbar K \left(\hat{a}^\dagger\hat{a}^\dagger + \frac{\alpha_2^*}{K} \right) \left(\hat{a}\hat{a} + \frac{\alpha_2}{K} \right) - \hbar|\alpha_2|^2. \quad (2.90)$$

In the following, we will ignore the irrelevant constant term $\hbar|\alpha_2|^2$. For a resonant parametric drive, *i.e.*, $\Delta = 0$, the ground-state subspace of this Hamiltonian is spanned by the two coherent states $|\pm i\sqrt{\alpha_2/K}\rangle$ defined in Appendix A.1. Moreover, the parity operator $\hat{\Pi}$, defined in Equation (2.49), commutes with \hat{H} at zero detuning, *i.e.*, parity is a conserved quantity. Thus, a good basis to describe the ground-state subspace are the even- and odd-parity cat state

$$|\mathcal{C}_{\pm}(\alpha)\rangle = \frac{|\alpha\rangle \pm |-\alpha\rangle}{\sqrt{2 \pm 2e^{-2|\alpha|^2}}}, \quad (2.91)$$

where $\alpha = i\sqrt{\alpha_2/K}$.

For nonzero detuning, the term $-\hbar\Delta\hat{a}^\dagger\hat{a}$ breaks parity conservation and lifts the degeneracy between the two cat states. Their expectation values with respect to the photon-number operator are

$$\langle \mathcal{C}_\pm(\alpha) | \hat{a}^\dagger\hat{a} | \mathcal{C}_\pm(\alpha) \rangle = |\alpha|^2 \frac{1 \mp e^{-2|\alpha|^2}}{1 \pm e^{-2|\alpha|^2}}. \quad (2.92)$$

Note that both expectation values converge to the value $|\alpha|^2$ in the limit $|\alpha|^2 \gg 1/2$, because the overlap between the coherent states decreases exponentially as a function of the amplitude α . In this limit, the two cat states $|\mathcal{C}_\pm(\alpha)\rangle$ become again indistinguishable with respect to their photon-number expectation value.

Having understood the closed-system dynamics defined by the Hamiltonian (2.90), we can now consider the dissipative case defined by Equation (2.80). The single-photon dissipators break parity conservation, too, such that each loss of a photon to the environment changes the parity of the cat state. In the limit $\kappa \ll K$, the amplitude α of the cat state, which has been derived by rewriting the Kerr Hamiltonian in the form (2.90), will be unchanged up to corrections of $\mathcal{O}(\kappa/K)$ in the presence of single-photon loss, but the system will evolve to an incoherent mixture of the two coherent states $|\alpha\rangle$ and $|\alpha\rangle$ that constitute the cat states $|\mathcal{C}_\pm(\alpha)\rangle$. We will use these results in Section 4.5.

2.6 Synchronization

In Section 2.4.2, we found that a blue-detuned laser drive applied to an optomechanical system excites mechanical oscillations at a constant amplitude without determining the phase of the oscillation. This is the defining feature of a limit-cycle oscillator and allows one to study synchronization phenomena. In this thesis, we will discuss synchronization in the quantum regime in Chapters 5 and 6. As a preparation, we will introduce classical synchronization in this section. Moreover, we will review important quantum limit-cycle oscillators and quantum synchronization measures that have been proposed in the literature.

2.6.1 Classical limit-cycle oscillator

Synchronization is the adjustment of rhythms of self-sustained oscillations due to a weak perturbation [Pikovsky *et al.*, 2003].

A *self-sustained oscillator* is an autonomous active system [Pikovsky *et al.*, 2003]. *Active* means that the system contains an internal source of energy that sets it into periodic motion. *Autonomous* means that the system's equations of motion are time independent. Thus, after some transient dynamics depending on the initial conditions, the periodic motion will be characterized only by internal parameters of the system. For a classical noiseless system, this motion can be represented by a closed curve in phase-space, which is called the *limit cycle* and is sketched in Figure 2.5(a). One can define a *phase* φ that parametrizes the state of oscillation along the limit cycle and that increases uniformly at the natural angular frequency ω_0 of oscillation,

$$\frac{d\varphi}{dt} = \omega_0. \quad (2.93)$$

The limit cycle is stable, *i.e.*, trajectories of systems with initial conditions in the vicinity of the limit cycle will eventually converge to the limit cycle [Strogatz, 2015;

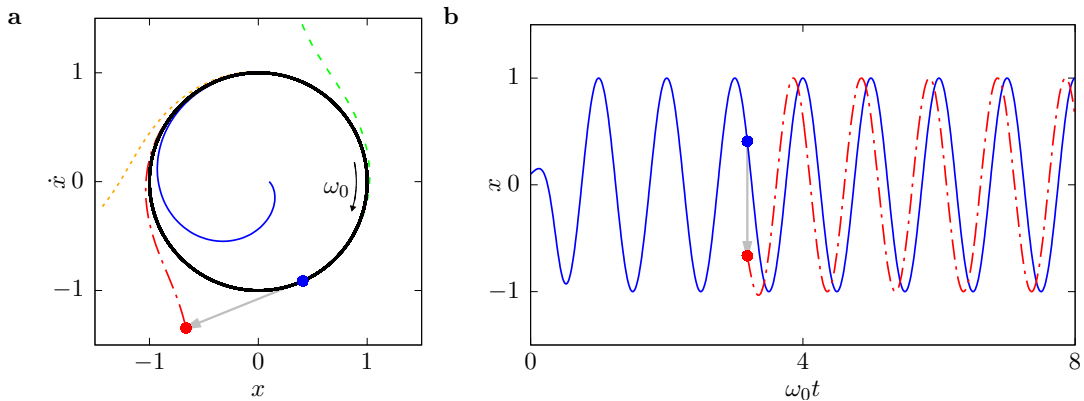


FIGURE 2.5: **(a)** Phase-space portrait of the dynamics of a limit-cycle oscillator. The trajectories of different initial conditions (thin lines) converge in the long-time limit to the same closed curve in phase space, which is called the limit cycle (thick black line). **(b)** Amplitude $x(t)$ as a function of time for the blue trajectory shown in (a). After transient dynamics, the system oscillates harmonically at frequency ω_0 and at a constant amplitude. The phase of oscillation is free, therefore, after a perturbation of the system by a kick (gray arrow from the blue to the red dot), the amplitude relaxes back to its constant value, but the perturbation of the phase persists.

Pikovsky *et al.*, 2003]. More specifically, the limit-cycle amplitude is asymptotically stable and the phase along the limit cycle is neutrally stable: If the amplitude of oscillation is perturbed, the system will relax back to the limit-cycle amplitude of oscillation and the difference between the instantaneous amplitude and the limit cycle remains bounded for all times. However, if the phase of oscillation is perturbed, the system will not relax back to the original phase but it will oscillate along the limit cycle with the new perturbed phase as shown in Figure 2.5(b). In the following, we will also use the name *limit-cycle oscillator* to denote a self-sustained oscillator.

A classic example of a self-sustained oscillator is the van der Pol (vdP) oscillator [van der Pol, 1926]. Its dynamics is given by the second-order differential equation [Pikovsky *et al.*, 2003]

$$\ddot{x} + \omega_0^2 x - 2\epsilon \dot{x}(1 - \beta x^2) = 0, \quad (2.94)$$

where x denotes the position of the oscillator and ω_0 is the natural frequency of oscillation. The parameters ϵ and β determine the shape of the limit cycle and the amplitude of oscillation, respectively. In the limit of a weak nonlinearity, $\epsilon \ll \omega_0$, the solution of the vdP differential equation (2.94) describes a harmonic oscillation at frequency ω_0 whose amplitude and phase vary slowly compared to the period $2\pi/\omega_0$. To separate this fast oscillation from the much slower amplitude and phase dynamics, we switch to a rotating frame,

$$x(t) = \frac{1}{2} [A(t)e^{i\omega_0 t} + A^*(t)e^{-i\omega_0 t}] . \quad (2.95a)$$

$$\dot{x}(t) = \frac{1}{2} i\omega_0 [A(t)e^{i\omega_0 t} - A^*(t)e^{-i\omega_0 t}] , \quad (2.95b)$$

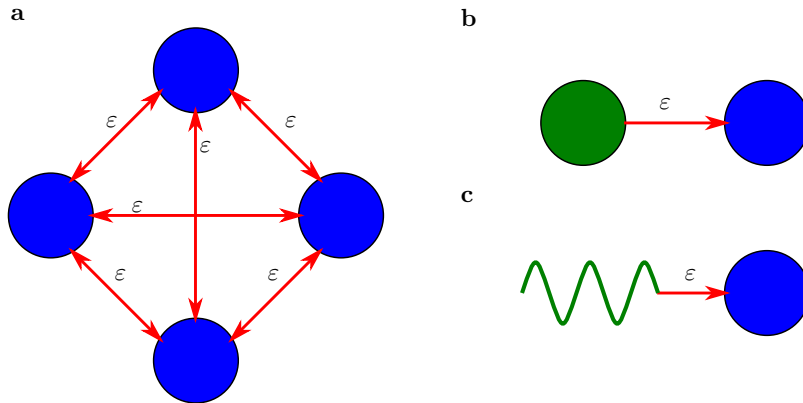


FIGURE 2.6: Different synchronization scenarios. **(a)** For mutual synchronization, limit-cycle oscillators (blue circles) form a network and influence each other reciprocally. **(b)** For master-slave synchronization, one limit-cycle oscillator (green circle) influences the other limit-cycle oscillator(s) unidirectionally (blue circle). **(c)** Synchronization of a limit-cycle oscillator (blue circle) to an external signal (green wave). This is an effective model for master-slave synchronization and for synchronization in a network if a mean-field approach is used.

where the complex variable $A(t)$ captures the slow amplitude and phase dynamics. Its equation of motion is

$$\frac{d}{dt}A = \epsilon \left(1 - \frac{\beta}{4} |A|^2 \right) A . \quad (2.96)$$

This result reveals that the amplitude of a vdP oscillator is stabilized by the balance between a gain of energy that grows linearly with the amplitude and a nonlinear damping term.

2.6.2 Classical synchronization phenomena

To study synchronization phenomena, a weak perturbation is applied to the limit-cycle oscillator. In the following, we will call this perturbation the *signal*. A method to generate such a perturbation is to couple limit-cycle oscillators with a coupling strength ϵ , such that each oscillator is influenced by the motion of other oscillators in the network. This case is called *mutual synchronization* and is illustrated in Figure 2.6(a). An example of mutual synchronization is the synchronization of clapping in applauding crowds [Néda *et al.*, 2000].

Individual limit-cycle oscillators in the network may differ in their susceptibility to perturbations. As an extreme limit, one can imagine a network of only two oscillators where the susceptibility of one oscillator is zero, such that this oscillator is not influenced by the motion of the other one at all. This scenario describes *unidirectional synchronization* and is illustrated in Figure 2.6(b). An example of unidirectional synchronization is the adjustment of our biological clocks to the natural day-night rhythm dictated by Earth's rotation [Aschoff, 1965].

As an effective model of unidirectional synchronization, one can consider only one limit-cycle oscillator that is subjected to an external signal of strength ϵ , as shown in Figure 2.6(c). The same picture is obtained if one applies mean-field approximations to a network of coupled limit-cycle oscillators. In this case, the effect of all other oscillators on a certain limit-cycle oscillator is treated as an external signal that must be

determined self-consistently. For simplicity, we will focus on the case of unidirectional synchronization in the following discussion, which is based on the standard textbook by Pikovsky *et al.* [2003].

The perturbation introduced by the external signal is considered to be “weak” in the sense that the force exerted on the limit-cycle oscillator influences its phase but not its amplitude dynamics. In this limit, one can ignore the amplitude dynamics and derive an effective equation of motion for the phase φ , which has the general form

$$\frac{d\varphi}{dt} = \omega_0 + \varepsilon q(m\varphi - n\omega t) . \quad (2.97)$$

Here, m and n are integers that are relatively prime and ω is the frequency of the external signal. The 2π -periodic function q describes the effective response of the limit-cycle oscillator to a periodic external signal and is called *phase sensitivity function* or *phase response curve* [Pikovsky, 2015]. It can be calculated by averaging the equation of motion of the slowly varying complex amplitude A in a frame rotating at the signal frequency ω over a period $2\pi/\omega$. This eliminates all rotating terms except for the resonant ones which fulfill $n\omega \approx m\omega_0$. Defining the *relative phase*

$$\phi_{m:n} = m\varphi - n\omega t \quad (2.98)$$

and the detuning

$$\Delta_{m:n} = m\omega_0 - n\omega , \quad (2.99)$$

we can rewrite Equation (2.97) as follows:

$$\frac{d\phi_{m:n}}{dt} = \Delta_{m:n} + \varepsilon m q(\phi) . \quad (2.100)$$

The same equation can be obtained for the case of mutually coupled oscillators. In the simplest case, the signal frequency is close to the natural frequency of oscillation, *i.e.*, $m = n = 1$, and $-q$ is a sine function. This yields the Adler equation describing 1 : 1 synchronization [Adler, 1946]

$$\frac{d\phi}{dt} = \Delta - \varepsilon \sin(\phi) ,$$

where $\phi = \phi_{1:1}$ and $\Delta = \Delta_{1:1}$.

Depending on the detuning $\Delta_{m:n}$ the signal strength ε , and the phase sensitivity function $q(\phi)$, Equation (2.100) gives rise to different time evolutions of the relative phase $\phi_{m:n}$ [Pikovsky *et al.*, 2003; Strogatz, 2000], which are summarized in Figure 2.7. In the following, we will denote the extremal values of the phase sensitivity function by q_{\max} and q_{\min} .

Phase locking If the condition $\varepsilon m q_{\min} \leq \Delta_{m:n} \leq \varepsilon m q_{\max}$ holds, Equation (2.100) has at least one stable fixed point and the relative phase $\phi_{m:n}$ takes a constant value ϕ_0 , as shown by the blue curve in Figure 2.7. This implies that the phase of the limit-cycle oscillator is determined by the phase of the signal according to the relation

$$\varphi(t) = \frac{1}{m}(\phi_0 + n\omega t) .$$

The value of the phase lag ϕ_0 depends on ε and Δ .

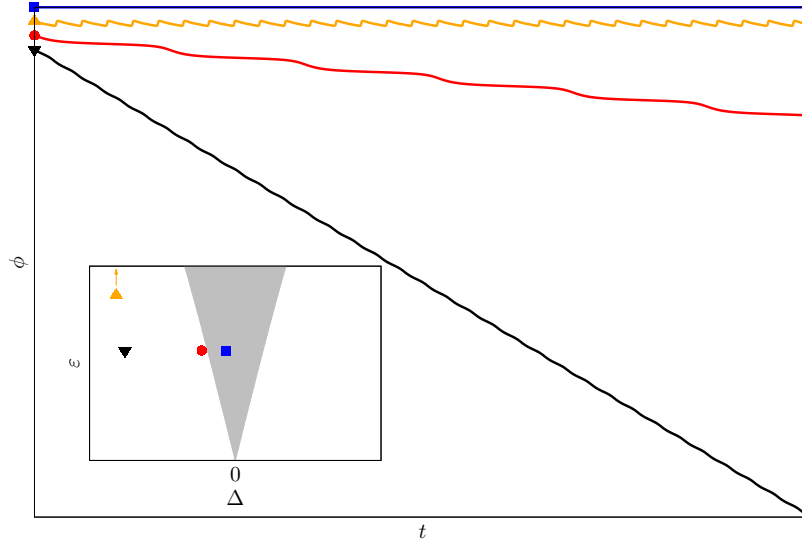


FIGURE 2.7: **Main plot:** Sketch of the evolution of the relative phase $\phi(t) = \phi_{1:1}(t) = \varphi(t) - \omega t$ between limit-cycle oscillator and signal for different parameters of the detuning $\Delta = \Delta_{1:1} = \omega_0 - \omega$ and the signal strength ε . In the phase-locked regime, $\phi(t)$ is either constant (curve starting with a blue square) or it oscillates around a constant mean value (orange, triangle pointing upwards). In the regime of frequency entrainment, the relative phase increases by 2π during phase slips which are separated by plateaus of almost constant phase (red, circle). On average, the relative phase increases, *i.e.*, the system is not synchronized. For very large detuning, the relative phase increases linearly in time (black, triangle pointing downwards). **Inset:** Region of synchronization, called Arnold tongue, for 1 : 1 phase locking (gray area). The markers indicate the parameters of the corresponding curves in the main sketch.

More generally, there may be situations where there is no constant solution ϕ_0 , but the time-dependent relative phase $\phi_{m:n}(t)$ oscillates around a fixed mean value ϕ_0 such that the difference $|\phi_{m:n}(t) - \phi_0|$ is bounded, *i.e.*, the condition

$$(|\phi_{m:n}(t) - \phi_0| \bmod 2\pi) < 2\pi$$

holds. This is shown by the orange curve in Figure 2.7. In this case, the phase $\varphi(t)$ of the limit-cycle oscillator is still locked to the phase of the signal on average.

Note that in the case of $n : m$ phase locking with $n \neq 1$ or $m \neq 1$, the *oscillation frequencies* of the signal and the limit-cycle oscillator, ω and $\dot{\varphi}$, respectively, are different.

Frequency locking In the case of 1 : 1 synchronization, *i.e.*, $n = m = 1$, phase locking implies that the frequencies of signal and limit-cycle oscillator are the same, $\dot{\varphi} = \omega$. This phenomenon is called frequency locking.

Again, even if there is no constant solution for the phase lag ϕ_0 , frequency locking can still be present on average.

Frequency entrainment Outside the range of phase locking, *i.e.*, if the conditions $\Delta_{m:n} \gtrsim \varepsilon m q_{\max}$ or $\Delta_{m:n} \lesssim \varepsilon m q_{\max}$ hold, the relative phase $\phi_{m:n}$ is no longer constant. However, sufficiently close to the regime of phase locking, the signal

still influences the limit-cycle oscillator and its average frequency deviates from the natural frequency of oscillation. In this regime, the relative phase increases by 2π in rapid *phase slips* that are interchanged with intervals of almost constant relative phase, as shown by the red curve in Figure 2.7.

Incoherence For very large detuning, $\Delta_{m:n} \gg \varepsilon m q_{\max}$ or $\Delta_{m:n} \ll \varepsilon m q_{\min}$, the limit-cycle oscillator is not affected by the external signal at all. Therefore, it oscillates at its natural frequency of oscillation ω_0 and the relative phase between $\phi_{m:n}(t) = m\omega_0 t - n\omega t$ increases linearly, as shown by the black curve in Figure 2.7.

With increasing detuning $|\Delta|$, there is a crossover from frequency entrainment to incoherence. During this crossover, the frequency of phase slips grows until $\phi(t)$ increases uniformly.

In the limit of a weak signal strength ε , the regions of $n : m$ phase locking in the $\Delta - \varepsilon$ phase diagram have a triangular shape as shown in the inset of Figure 2.7. Because of this characteristic shape, the regions of synchronization are called *Arnold tongues*. If the signal strength ε increases, a crossover from synchronization to various types of forced oscillations happens. During this crossover, the physical picture of a limit-cycle oscillator as an individual entity, which is separate from the signal or other limit-cycle oscillators in the network, breaks down. Instead, one should analyze the combined system consisting of the limit-cycle oscillator and the signal, or the entire network of limit-cycle oscillators, as a single dynamical system [Pikovsky *et al.*, 2003]. Consequently, the Arnold tongue loses its meaning as the region in the $\Delta - \varepsilon$ phase diagram where synchronization occurs. So far, no definition of the “upper end” of the Arnold tongue for classical synchronization has been given [Pikovsky, 2015].

The different phenomena described so far apply both to mutually and unidirectional coupled limit-cycle oscillators. However, there are some effects that occur only in networks of mutually coupled limit-cycle oscillators. The mutual coupling may cause a suppression of oscillation, called *oscillation quenching*, which arises if the coupling introduces additional dissipation that cannot be compensated by the internal source of energy of the self-sustained oscillators [Pikovsky *et al.*, 2003]. As a consequence, the oscillation breaks down and the oscillators evolve towards a time-independent state. One distinguishes two different types of oscillation quenching, depending on the type of the final state [Koseska *et al.*, 2013]:

Amplitude death All oscillators approach the same fixed point of their equation of motion, *i.e.*, the resulting steady-state of the network is homogeneous.

Oscillation death The oscillators approach different fixed points, *i.e.*, the resulting steady-state of the network is inhomogeneous.

Moreover, oscillators in a subpart of a network could be phase locked whereas other oscillators remain incoherent. This phenomenon is called *partial synchronization* [Strogatz, 2000] and happens, *e.g.*, in the Kuramoto model at the transition from an incoherent to a fully synchronized state [Kuramoto, 1984] and in disordered networks of oscillators [Ko and Ermentrout, 2008]. A particularly interesting case are so-called *chimera states* where synchronized and incoherent subpopulations coexist in networks of identical oscillators [Kuramoto and Battogtokh, 2002; Abrams and Strogatz, 2004].

Finally, synchronization can also be studied in chaotic systems if the oscillation resembles a periodic oscillation with a randomly varying amplitude and period time [Pikovsky *et al.*, 2003]. A famous example of such a chaotic oscillator is the Lorenz

system [Lorenz, 1963]. A mean frequency of oscillation can be defined by counting the number of periods $N_{\Delta T}$ in a time interval ΔT ,

$$\bar{f} = \frac{N_{\Delta T}}{\Delta T}$$

When two or more chaotic oscillators are coupled, the following phenomena may happen [Pikovsky *et al.*, 2003; Boccaletti *et al.*, 2002]:

Phase synchronization The oscillators adjust their mean frequencies of oscillation such that there is phase locking, but the amplitude dynamics remains chaotic, *i.e.*, there is no correlation between the amplitudes of the oscillators.

Complete synchronization The coupling influences both the mean frequencies and the amplitudes of the oscillators, such that their trajectories in phase space almost coincide or even become identical.

Variations of these scenarios can be observed, *e.g.*, complete synchronization with a time delay between the two trajectories, so-called *lag synchronization*, or *intermittent synchronization*, where periods of synchronized motion are interrupted by local incoherent dynamics [Boccaletti *et al.*, 2002].

2.6.3 Quantum limit-cycle oscillators

Classical synchronization has been observed in a broad range of experiments [Pikovsky *et al.*, 2003], among them electrical circuits [Pecora and Carroll, 1990], laser arrays [Winful and Rahman, 1990; Roy and Thornburg, 1994], arrays of Josephson junctions [Benz and Burroughs, 1991], and micromechanical oscillators [Agrawal *et al.*, 2013; Matheny *et al.*, 2014]. By miniaturizing a classical self-sustained oscillator, one ultimately obtains a quantum-mechanical limit-cycle oscillator. With our increasing abilities to fabricate and control micro- and nanomechanical objects, quantum limit-cycle oscillators come within experimental reach.

Consequently, several proposals have been made to study quantum synchronization: Zhirov and Shepelyansky [2006] proposed a dissipative quantum system that can be implemented in current-driven Josephson junctions or in cold-atom experiments. Heinrich *et al.* [2011] suggested to couple optomechanical systems that are driven into mechanical limit-cycle motion. Holmes *et al.* [2012] considered an array of nanomechanical resonators that are coupled by a microwave cavity. Lee and Cross [2013] proposed to use nonlinear optical cavities to implement a limit-cycle oscillator. Finally, Lee and Sadeghpour [2013] and Walter *et al.* [2014] introduced a quantum counterpart of the vdP limit-cycle oscillator which can be implemented with trapped ions or optomechanical systems. The quantum vdP oscillator is modeled by the QME

$$\frac{d}{dt}\hat{\rho} = -\frac{i}{\hbar} \left[\hbar\omega_0\hat{a}^\dagger\hat{a}, \hat{\rho} \right] + \gamma_g\mathcal{D}[\hat{a}^\dagger]\hat{\rho} + \gamma_d\mathcal{D}[\hat{a}^2]\hat{\rho},$$

which describes a harmonic oscillator subject to dissipative single-photon gain and two-photon loss processes. This QME implements the circular limit-cycle oscillation of a classical vdP oscillator in the weakly nonlinear regime $\epsilon \ll \omega_0$, which can be verified by calculating the semiclassical equation of motion of $\langle \hat{a} \rangle = A(t)e^{-i\omega_0 t}$. The amplitude $A(t)$ evolves according to the equation of motion

$$\frac{d}{dt}A = \frac{\gamma_g}{2} \left(1 - \frac{2\gamma_d}{\gamma_g} |A|^2 \right) A, \quad (2.101)$$

which is identical to Equation (2.96), if one defines $\epsilon = \gamma_g/2$ and $\beta/4 = 2\gamma_d/\gamma_g$.

If the QME (2.101) is solved for a coherent initial state, a periodic oscillation at the natural frequency ω_0 is found as expected from the classical equation of motion. However, quantum fluctuations make an important difference to the classical case in the long-time limit: Since the phase of oscillation along the limit cycle is free, the quantum system will dephase and explore all possible phases of oscillation. Therefore, an initial coherent state will spread along the phase direction and the system will ultimately reach a completely dephased, rotationally symmetric steady state.

The proposals mentioned above have been justified and motivated by their semi-classical equations of motion, which reproduce a classical limit-cycle oscillator. A framework that defines quantum synchronization independently of any classical limit has been missing so far and is the subject of Chapter 5.

2.6.4 Quantum synchronization measures

To quantify the degree of quantum synchronization, various measures have been proposed that generalize the concepts of classical synchronization reviewed in Section 2.6.2 to the quantum regime. They can be grouped into several categories:

Measures of phase localization Classically, phase locking is defined as a fixed or at least bounded relative phase ϕ between two coupled limit-cycle oscillators or between a limit-cycle oscillator and an external signal. In quantum systems, mutual coupling or external signals aim to establish a fixed relative phase, too. However, this process competes with the dephasing due to quantum fluctuations. As a consequence, the relative phase will in general not reach a fixed value, but the uniform distribution of the relative phase ϕ in the limit-cycle state will localize at a certain relative phase. This localization can be used to quantify phase locking.

The phase distribution $P(\phi|\hat{\rho})$ of a state $\hat{\rho}$ can be obtained by calculating its Wigner function $\mathcal{W}_{\hat{\rho}}(\alpha)$, introduced in Section 2.3, and integrating out the amplitude [Lee and Sadeghpour, 2013],

$$P(\phi|\hat{\rho}) = \int_0^\infty dr r \mathcal{W}_{\hat{\rho}}(re^{i\phi}) .$$

Alternatively, one can use the phase states $|\phi\rangle$ introduced by Barnett and Pegg [1986] to calculate a phase distribution [Hush *et al.*, 2015],

$$P(\phi|\hat{\rho}) = \langle \phi | \hat{\rho} | \phi \rangle .$$

The relative phase distribution $P(\phi|\hat{\rho})$ can be condensed into a single-number measure of quantum synchronization by taking the maximum difference between the phase distribution in the presence of a signal and the uniform phase distribution of the limit-cycle state [Hush *et al.*, 2015],

$$\mathcal{S}(\hat{\rho}) = \max_{\phi \in [0, 2\pi)} \left[P(\phi|\hat{\rho}) - \frac{1}{2\pi} \right] .$$

An alternative approach to obtain a single-number measure of quantum synchronization is inspired by the order parameter of the Kuramoto model [Kuramoto, 1984]. Here, one calculates the complex quantity [Ludwig and Marquardt, 2013;

Weiss *et al.*, 2016]

$$S'(\hat{\rho}) = \frac{\langle \hat{a} \rangle}{\sqrt{\langle \hat{a}^\dagger \hat{a} \rangle}},$$

where the expectation values are taken with respect to the state $\hat{\rho}$. For a phase-symmetric state, *i.e.*, the limit-cycle state, the numerator $\langle \hat{a} \rangle$ is zero. If an external signal localizes the state at a mean relative phase ϕ_0 , this phase invariance is broken and the numerator acquires a finite value $\langle \hat{a} \rangle \approx \sqrt{\langle \hat{a}^\dagger \hat{a} \rangle} e^{i\phi_0}$. The denominator normalizes S' such that its absolute value for a coherent state is unity. A drawback of this measure is that it is sensitive to a shift of the center of the limit cycle by the signal.

Measures of the oscillation frequency Instead of characterizing the relative phase ϕ , Walter *et al.* [2014] proposed to quantify frequency entrainment and frequency locking by calculating the average frequency of oscillation of the limit-cycle oscillator. Classically, this frequency can be extracted from the power spectrum of an oscillating variable. The corresponding quantum-mechanical steady-state power spectrum is defined as follows:

$$S_{\hat{a}^\dagger \hat{a}}(\omega) = \int_{-\infty}^{\infty} d\tau \left\langle \hat{a}^\dagger(\tau) \hat{a}(0) \right\rangle_{\text{ss}} e^{i\omega\tau}.$$

The power spectrum has a dominating peak at the average frequency of oscillation, which allows one to track the transition from frequency locking via entrainment to incoherence.

Distance measures between trajectories Mari *et al.* [2013] proposed to quantify synchronization in networks of coupled oscillators based on the distance between the trajectories of individual limit-cycle oscillators in phase space. This approach generalizes the notion of complete synchronization in chaotic systems to the quantum case. In continuous-variable systems, such as optomechanical systems or the quantum vdP oscillator, the state of each limit-cycle oscillator j in the network can be characterized by the position and momentum operators \hat{q}_j and \hat{p}_j , respectively. Using the operators for the relative position and momentum between the oscillators j and k ,

$$\hat{q}_-(t) = \frac{1}{\sqrt{2}}[\hat{q}_j(t) - \hat{q}_k(t)] \quad \text{and} \quad \hat{p}_-(t) = \frac{1}{\sqrt{2}}[\hat{p}_j(t) - \hat{p}_k(t)],$$

the following measure for complete quantum synchronization can be constructed

$$S_c = \frac{1}{\langle \hat{q}_-^2(t) + \hat{p}_-^2(t) \rangle}.$$

Whereas this measure would diverge for completely synchronized classical systems, it can be shown that the Heisenberg uncertainty principle imposes the bound $S_c(t) \leq 1/\hbar$ in quantum systems. Importantly, this quantum synchronization measure allows one to isolate the impact of quantum fluctuations on synchronization by subtracting the semiclassical dynamics.

A measure that generalizes the notion of phase synchronization of chaotic systems to the quantum regime can be constructed in a similar way [Mari *et al.*, 2013]: Using the position and momentum operators, one calculates the ladder

operator $\hat{a}_j(t) = [\hat{q}_j(t) + i\hat{p}_j(t)]/\sqrt{2}$, which can be decomposed as follows:

$$\hat{a}_j(t) = [r_j(t) + \hat{a}'_j(t)] e^{i\varphi_j(t)} ,$$

where $r_j(t)$ and $\varphi_j(t)$ denote the amplitude and phase of the expectation value $\langle \hat{a}_j(t) \rangle$, respectively. The quadratures $\hat{q}'_j(t)$ and $\hat{p}'_j(t)$ of the new operator

$$\hat{a}'_j(t) = \frac{1}{\sqrt{2}}[\hat{q}'_j(t) + i\hat{p}'_j(t)]$$

describe fluctuations of the amplitude and phase, respectively. Consequently, the phase difference between the oscillators j and k is given by

$$\hat{p}'_-(t) = \frac{1}{\sqrt{2}}[\hat{p}'_j(t) - \hat{p}'_k(t)] .$$

Phase synchronization can now be quantized by the measure

$$S_p = \frac{1}{2\langle \hat{p}'_-(t)^2 \rangle} ,$$

which fulfills $S_p \leq 1/\hbar$ for states with a positive \mathcal{P}_ρ function.

Measures of correlations or entanglement Classical synchronization can be quantified by studying correlations in the motion of coupled oscillators [Boccaletti *et al.*, 2002]. This approach can be generalized to the quantum regime by calculating correlations between expectation values [Galve *et al.*, 2017; Zhu *et al.*, 2015] or by studying the mutual information between two oscillators [Ameri *et al.*, 2015]. Mutual information captures both classical correlations and quantum effects, the so-called quantum discord [Modi *et al.*, 2012], which allows one to distinguish between classical and quantum effects in synchronization. In a similar line of reasoning, entanglement has been proposed as a measure of quantum synchronization [Lee *et al.*, 2014].

However, these methods to quantify synchronization are subject of an ongoing scientific controversy since inconsistent results have been reported: Roulet and Bruder [2018b] gave an example of a system of two coupled limit-cycle oscillators where mutual information and a synchronization measure based on the relative phase distribution give contradictory results. Moreover, in this system, it was found that the presence of synchronization implies entanglement between the oscillators, but the converse statement is not necessarily true. Lee *et al.* [2014] reported an entanglement tongue similar to the Arnold tongue of synchronization, but the entanglement tongue appeared only above a critical coupling strength. This effect could be related to the different structure of the considered limit cycles and the use of different entanglement measures. Finally, synchronization without any entanglement has been reported by Mari *et al.* [2013] and Ameri *et al.* [2015] for large limit-cycle amplitudes. These results can be understood as the consequence of a transition from quantum synchronization to classical synchronization if the limit-cycle amplitude increases.

2.7 Quantum computing

Simulating quantum systems on classical hardware is inefficient because the number of degrees of freedom of a quantum system grows exponentially with the system size.

Therefore, already a moderate-size quantum system composed of about 60 two-level systems exceeds the capabilities of current classical supercomputers. Already in the early days of quantum computing, Feynman [1982] pointed out that the same task can be performed efficiently on a computer that obeys the laws of quantum mechanics. Since then, it has been predicted that quantum computers will outperform their classical counterparts on specific tasks [Deutsch and Jozsa, 1992; Shor, 1997] not only because of their ability to efficiently store quantum states in an exponentially large Hilbert space, but also because of their ability to use interference and entanglement as additional resources for information processing [Veitch *et al.*, 2012; Stahlke, 2014; Rahimi-Keshari *et al.*, 2016]. Recently, the first experimental demonstration of this so-called *quantum supremacy* has been reported [Arute *et al.*, 2019; Pednault *et al.*, 2019].

In Chapter 6, we will use quantum simulation techniques to implement and study quantum synchronization on a state-of-the-art quantum computer. As a preparation, we will review the basics of quantum information processing and we will introduce the concept of quantum simulation in this section. This review is based on the standard textbook by Nielsen and Chuang [2011].

2.7.1 Elements of quantum computing

A classical computer stores information in a register of bits, where each bit represents a discrete value of either 0 or 1. A quantum computer stores information in a register of quantum bits (qubits). Each qubit is a quantum two-level system and its state is a superposition of the basis states $|0\rangle$ and $|1\rangle$,

$$|\psi\rangle = \alpha |0\rangle + \beta |1\rangle ,$$

where α and β are complex numbers fulfilling the normalization condition $|\alpha|^2 + |\beta|^2 = 1$. Since quantum states are defined only up to an irrelevant global phase factor, the state $|\psi\rangle$ has two independent degrees of freedom, which are, *e.g.*, the absolute value of α and the relative phase between α and β . The basis states $|0\rangle$ and $|1\rangle$ are the eigenstates of the Pauli operator $\hat{Z} \equiv \hat{\sigma}_z$,

$$\begin{aligned} \hat{Z} |0\rangle &= + |0\rangle , \\ \hat{Z} |1\rangle &= - |1\rangle . \end{aligned} \tag{2.102}$$

Multiple qubits can be combined to a quantum register. In this thesis, we will follow the convention to represent the most-significant bit by the left-most qubit in the quantum register, *i.e.*, a N -qubit register in the state

$$|q_{N-1}q_{N-2}\dots q_0\rangle = |q_{N-1}\rangle_{N-1} \otimes |q_{N-2}\rangle_{N-2} \otimes \dots \otimes |q_0\rangle_0 ,$$

represents the number $\sum_{j=0}^{N-1} q_j 2^j$ in binary notation where $q_j \in \{0, 1\}$. The Hilbert space $\mathcal{H}^{(N)}$ of this N -qubit register is the product of N single-qubit Hilbert spaces $\mathcal{H}^{(1)}$,

$$\mathcal{H}^{(N)} = \mathcal{H}_{N-1}^{(1)} \otimes \mathcal{H}_{N-2}^{(1)} \otimes \dots \otimes \mathcal{H}_0^{(1)} , \tag{2.103}$$

and has the dimension 2^N . Therefore, the number of degrees of freedom of the quantum state of this register is

$$2(2^N - 1) , \tag{2.104}$$

i.e., the number of parameters that can be stored scales exponentially with the length N of the register.

On a classical computer, computations are performed by applying logical operations, *e.g.*, AND, OR, NOT, *etc.*, which manipulate the state of the classical register. These operations are called gates. Similarly, on a quantum computer, calculations are performed by applying *quantum gates* that change the state of the quantum register. For instance, the quantum-mechanical equivalent of a NOT gate is the Pauli operator $\hat{X} \equiv \hat{\sigma}_x$,

$$\begin{aligned}\hat{X} |0\rangle &= |1\rangle , \\ \hat{X} |1\rangle &= |0\rangle .\end{aligned}\tag{2.105}$$

To preserve the normalization condition $\langle\psi|\psi\rangle = 1$ of quantum states, quantum gates must be unitary operations.

To enable arbitrary calculations, a classical computer must be able to perform any logical operation on its register. Therefore, it must at least provide a set of basic logical operations that can be combined to construct any other logical gate. This set is called a universal set of logical gates. The smallest universal set of logical gates is given by the NAND gate, which is a logical AND gate followed by a NOT gate. Similarly, a quantum computer must be able to perform any unitary transformation of the state of its quantum register. Therefore, it must provide a *universal set of quantum gates* which allows one to construct any unitary operation by a suitable combination of the basic quantum gates. A possible universal set of quantum gates is given by the Hadamard gate \hat{H} ,

$$\begin{aligned}\hat{H} |0\rangle &= \frac{1}{\sqrt{2}} (|0\rangle + |1\rangle) , \\ \hat{H} |1\rangle &= \frac{1}{\sqrt{2}} (|0\rangle - |1\rangle) ,\end{aligned}\tag{2.106}$$

the so-called $\pi/8$ -gate \hat{T} ,

$$\begin{aligned}\hat{T} |0\rangle &= |0\rangle , \\ \hat{T} |1\rangle &= e^{i\pi/4} |1\rangle ,\end{aligned}\tag{2.107}$$

and the two-qubit CNOT gate, which applies a NOT gate to its target qubit if the control qubit is in the state $|1\rangle$, but does not change the target qubit if the control qubit is in the state $|0\rangle$.

A convenient way to represent quantum calculations graphically are quantum circuit diagrams. An example of a quantum circuit diagram is

$$\begin{array}{c} q_0 : |0\rangle \text{ --- } \boxed{\text{X}} \text{ --- } \bullet \text{ --- } \bullet \text{ --- } \boxed{\text{T}} \text{ --- } \boxed{\text{Z}} \text{ --- } \boxed{\text{---}} \\ | \\ q_1 : |1\rangle \text{ --- } \boxed{\text{H}} \text{ --- } \boxed{\text{X}} \text{ --- } \oplus \text{ --- } \circ \text{ --- } \boxed{\text{---}} |0\rangle \text{ ---} \end{array}\tag{2.108}$$

In a circuit diagram, a quantum register is represented by a set of horizontal lines, each of them representing one qubit. Single-qubit operations are depicted by boxes that are placed on the line of the corresponding qubit. Controlled two-qubit operations are indicated by vertical lines connecting control and target qubit. A box specifying the type of the controlled operation is placed on the line of the target qubit and a dot is placed on the line of the control qubit. A solid (empty) dot indicates that the

operation is applied to the target qubit if the control qubit is in the state $|1\rangle$ ($|0\rangle$). Circuit diagrams are read from left to right and single-qubit gates placed vertically below each other can be executed simultaneously.

The sample circuit shown in Equation (2.108) represents the following quantum algorithm: The initial state of the quantum register is $|q_1q_0\rangle = |10\rangle$. In a first step, a NOT gate \hat{X} is applied to q_0 and a Hadamard gate \hat{H} is applied to q_1 . The next two steps are two equivalent notations of a CNOT gate, where the control qubit is q_0 and the target qubit is q_1 . The solid dot indicates that the NOT gate is only applied if q_0 is in the state $|1\rangle$. Then, a \hat{T} gate is applied to q_0 , followed by a controlled \hat{Z} gate where the target qubit is now q_0 and the control qubit is q_1 . The empty dot indicates that the \hat{Z} gate is applied only if q_1 is in the state $|0\rangle$. Finally, both qubits are measured in the eigenbasis of the \hat{Z} operator. This measurement collapses quantum superpositions, *i.e.*, the outputs are classical bits 0 or 1 for each measured quantum bit. After the measurement, qubit q_1 is reset to the state $|0\rangle$.

2.7.2 Quantum simulation

The term quantum simulation describes the task to calculate the time evolution of a given quantum system Q by means of another quantum system S – the quantum simulator [Feynman, 1982].

To calculate the time evolution of a large quantum system Q, one has to keep track of an exponential number of degrees of freedom. This is inefficient on classical hardware. However, if a quantum system S is used, its Hilbert space scales exponentially with the size of S, too. Therefore, with a suitable mapping between the Hilbert spaces \mathcal{H}_Q and \mathcal{H}_S of Q and S, respectively, the size of the simulator S grows only polynomially with the size of Q, and the problem of exponentially increasing memory resources is solved. Once the mapping between Q and S is fixed, one has to implement the time evolution of Q on the quantum simulator. The following two options exist to accomplish this task:

In *analog quantum simulation*, one chooses a quantum simulator whose Hamiltonian \hat{H}_S and dissipative dynamics have the same form as the Hamiltonian \hat{H}_Q and the dissipative dynamics of Q, respectively. An example of this approach is the quantum simulation of a Bose-Hubbard Hamiltonian using a lattice of cold atoms [Jaksch *et al.*, 1998; Greiner *et al.*, 2002]: Overlapping laser beams create an optical lattice that can be used to trap cold atoms. Atoms can tunnel through the potential wells separating the different lattice sites, which corresponds to a hopping process from one site of the Bose-Hubbard Hamiltonian to another one. The shape of the optical lattice can be modified by tuning the lasers, such that different parameters of the Hamiltonian \hat{H}_Q can be simulated. By initializing a certain distribution of atoms in the lattice and measuring their dynamics as a function of time, one can study the time evolution of Q. Analog quantum simulators are typically restricted to a certain class of Hamiltonians \hat{H}_Q and a certain range of experimentally feasible parameters.

In *digital quantum simulation*, the quantum simulator S is a universal quantum computer. At first sight, a problem may arise because the quantum computer usually does not provide gates that directly implement the desired time evolution of Q. However, this problem can be solved by discretizing the time axis such that the state of the quantum simulator encodes the state of Q at integer multiples of a small time step dt . These states are linked by a time evolution operator $\hat{U}(dt)$, which can be approximated by a quantum circuit to arbitrary precision since the quantum computer provides a universal set of quantum gates. Repeating the quantum circuit of a single time step n times, the time evolution of Q can be simulated up to a desired final

time $T = ndt$. Lloyd [1996] pointed out that the following two conditions must be satisfied to ensure that a digital quantum simulation of the time evolution of Q over the simulated time T is efficient:

1. The sequence of gates that implement the time evolution operator $\hat{U}(dt)$ must grow only polynomially with the system size M and
2. the total run time of the quantum simulation must grow only polynomially with the simulated time T .

Both requirements can be satisfied if the Hamiltonian of the physical system has a local structure *i.e.*, if it can be decomposed in the form

$$\hat{H} = \sum_{j=1}^{L(M)} \hat{H}_j, \quad (2.109)$$

where $L(M)$ is a polynomial of M and each term \hat{H}_j acts only on an m_j -dimensional subspace of \mathcal{H}_Q [Lloyd, 1996]. Luckily, the Hamiltonians of many physically relevant systems have such a local form.

If the time step $dt = T/n$ is sufficiently small, the exact time evolution generated by the Hamiltonian \hat{H}_Q can be approximated by a series of short time evolutions generated by the Hamiltonians \hat{H}_j ,

$$e^{-i\hat{H}T/\hbar} = \left(e^{-i\hat{H}_1 dt/\hbar} e^{-i\hat{H}_2 dt/\hbar} \dots e^{-i\hat{H}_L dt/\hbar} \right)^n + \mathcal{O}\left(\frac{T^2}{n}\right). \quad (2.110)$$

The number n of times steps required to simulate $e^{-i\hat{H}T/\hbar}$ to accuracy ϵ is

$$n = \mathcal{O}\left(\frac{T^2}{\epsilon}\right). \quad (2.111)$$

Each term $e^{-i\hat{H}_j dt/\hbar}$ is a unitary transformation, represented by a $m_j \times m_j$ matrix, that can be specified by $\mathcal{O}(m_j^2)$ operations. Consequently, the total number of operations to generate the time evolution $e^{-i\hat{H}T/\hbar}$ is

$$N_{\text{op}} = \mathcal{O}\left(n \sum_{j=1}^{L(M)} m_j^2\right) \leq \mathcal{O}[nL(M)m^2], \quad (2.112)$$

where we introduced $m = \max_j\{m_j\}$ [Lloyd, 1996]. The number of operations scales polynomially in the system size M since we required that $L(M)$ is a polynomial of M . Generating a single unitary transformation $e^{-i\hat{H}_j dt/\hbar}$ on a quantum computer takes a time

$$T_{\text{op}} \propto \frac{T}{n} = \mathcal{O}\left(\frac{\epsilon}{T}\right). \quad (2.113)$$

Combining Equations (2.111)–(2.113), we find that the total run time of the quantum simulation scales linearly in T . Consequently, the time evolution under a local Hamiltonian of the form (2.109) can be efficiently simulated on a quantum computer.

Equation (2.110) is an example of a so-called Suzuki-Trotter decomposition of the unitary transformation $e^{-i\hat{H}T/\hbar}$ [Trotter, 1959; Suzuki, 1976]. These decompositions provide a formal way to break a complicated unitary transformation down to more

simple transformations that can be approximated by the quantum gates of a quantum computer. Several Suzuki-Trotter decomposition formulas exist, which yield different approximation errors in terms of the time step dt . Equation (2.110) corresponds to the most simple decomposition scheme

$$e^{i(\hat{A}+\hat{B})dt} = e^{i\hat{A}dt}e^{i\hat{B}dt} + \mathcal{O}(dt^2) .$$

To implement a digital quantum simulation of quantum synchronization in Chapter 6, we will use a higher-order approximation that is obtained by symmetrizing the expression on the right-hand side [Nielsen and Chuang, 2011],

$$e^{i(\hat{A}+\hat{B})dt} = e^{i\hat{A}dt/2}e^{i\hat{B}dt}e^{i\hat{A}dt/2} + \mathcal{O}(dt^3) .$$

This decomposition is equivalent to a higher-order numerical integration algorithm for an ordinary differential equation. It reduces the approximation error per time step at the cost of increasing the number of quantum gates per time step.

Chapter 3

Nonclassical States of Motion in an Optomechanical Limit Cycle

The results presented in this chapter have been published in:

M. Koppenhöfer, C. Bruder, and N. Lörch,
Unraveling nonclassicality in the optomechanical instability,
 Physical Review A **97**, 063812 (2018).

3.1 Motivation

In recent years, optomechanical experiments have started to enter the quantum regime. Sideband cooling of mechanical oscillations to the quantum ground state [Teufel *et al.*, 2011; Chan *et al.*, 2011], sensing of mechanical motion at the standard quantum limit [Teufel *et al.*, 2009; Purdy *et al.*, 2013; Schreppler *et al.*, 2014], quantum state transfer between the optical and mechanical subsystems [Verhagen *et al.*, 2012; Palomaki *et al.*, 2013], and phonon lasing [Grudinin *et al.*, 2010; Anetsberger *et al.*, 2009; Cohen *et al.*, 2015] have been demonstrated. These experiments triggered an increased interest in quantum effects in phonon lasing beyond the scope of the semiclassical theory summarized in Section 2.4.2. Theoretical studies [Rodrigues and Armour, 2010; Qian *et al.*, 2012; Nation, 2013; Machado and Blanter, 2016] have led to the prediction [Lörch *et al.*, 2014] that the phonon distribution of such an optomechanical phonon laser can be nonclassical if the system is operated in the resolved-sideband regime. In this context, nonclassicality means a sub-Poissonian phonon-number statistics, quantified by a Fano factor below unity. However, an experimental observation of this nonclassicality is still missing.

Continuous measurements, such as homodyne detection or photon counting, can provide information on the state of a quantum system [Wiseman and Milburn, 2009]. As discussed in Section 2.2, these measurements give rise to a conditional time evolution since the state $\hat{\rho}(t)$ of the system at a given time t depends on the previous measurement results. The measurement record can be used for real-time state reconstruction, which has been experimentally demonstrated both in the regime of negligible optical backaction and in the quantum regime [Briant *et al.*, 2003; Iwasawa *et al.*, 2013; Wieczorek *et al.*, 2015]. In a second step, the knowledge of the system's state can be used to implement feedback mechanisms, *e.g.*, to cool the motion of the system [Mancini *et al.*, 1998; Doherty and Jacobs, 1999; Hopkins *et al.*, 2003; Wilson *et al.*, 2015], or to generate squeezed mechanical states of motion of a levitated nanosphere by combining sideband cooling and Markovian feedback [Genoni *et al.*, 2015].

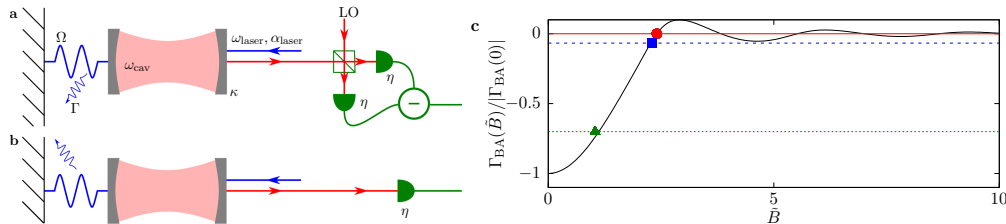


FIGURE 3.1: Sketch of the considered setup. An optomechanical system is monitored by a continuous measurement, either homodyne detection (a) or photon counting (b). A blue-detuned laser drive is applied to the optomechanical system to induce mechanical limit cycles. (c) Optically induced damping Γ_{BA} as a function of the rescaled amplitude $\tilde{B} = 2g_0 B / \Omega_{\text{mech}}$ in the regime $|\Delta| < \Omega_{\text{mech}}$. This corresponds to a vertical cut through Figure 2.3 at a fixed value of the detuning Δ . Limit-cycle amplitudes for the different parameter sets of the mechanical damping considered in this project (cf. Table 3.1) are indicated by solid markers. The colors and marker symbols correspond to the ones of the data sets in Figure 3.2.

Whereas sideband cooling requires a laser drive below the resonance frequency of the optical cavity, we now consider the opposite limit of a laser drive above resonance, which induces mechanical limit-cycle motion. We investigate the impact of a continuous measurement on phonon lasing, with a focus on the nonclassicality of the mechanical state, quantified by its Fano factor. Our results show that a continuous measurement of the output field of the optical cavity can be used to induce nonclassical states of mechanical motion by reducing the mechanical amplitude fluctuations. In contrast to existing proposals based on unconditional dynamics [Rodrigues and Armour, 2010; Lörch *et al.*, 2014], which require operation in the resolved-sideband regime to observe nonclassical mechanical states, our approach opens the possibility to generate nonclassical self-oscillations in the unresolved-sideband regime. This comes at the cost of obtaining a time-dependent, stochastically fluctuating Fano factor because of the conditional dynamics of the optomechanical system. We characterize the magnitude of these fluctuations and show that the conditional Fano factor can become smaller than unity, notably even in the unresolved-sideband regime, where it has been proven that the Fano factor in the case of unconditional dynamics is always larger than unity [Lörch *et al.*, 2014].

This chapter is structured as follows. The optomechanical system is introduced in Section 3.2 and important properties are briefly reviewed. The methods and parameter regimes used to study the influence of continuous measurements on mechanical limit-cycle motion are introduced in Section 3.3. Numerical results are presented in Section 3.4 and subsequently discussed in Section 3.5. Finally, we conclude in Section 3.6.

3.2 Optomechanical system

We consider an optomechanical system described by the standard optomechanical Hamiltonian (2.56) and the quantum master equation (2.58),

$$\frac{d}{dt}\hat{\rho} = -\frac{i}{\hbar} [\hat{H}_{\text{OM}}, \hat{\rho}] + \Gamma_{\text{mech}}(n_{\text{ph}} + 1)\mathcal{D}[\hat{b}]\hat{\rho} + \Gamma_{\text{mech}}n_{\text{ph}}\mathcal{D}[\hat{b}^\dagger]\hat{\rho} + \kappa\mathcal{D}[\hat{a}]\hat{\rho}, \quad (3.1)$$

$$\hat{H}_{\text{OM}} = -\hbar\Delta\hat{a}^\dagger\hat{a} + \hbar\Omega_{\text{mech}}\hat{b}^\dagger\hat{b} - \hbar g_0\hat{a}^\dagger\hat{a}(\hat{b}^\dagger + \hat{b}) + \hbar\alpha_{\text{laser}}(\hat{a}^\dagger + \hat{a}), \quad (3.2)$$

where \hat{a} and \hat{b} are the bosonic annihilation operators of an optical photon and a mechanical phonon, respectively, and

$$\Delta = \omega_{\text{laser}} - \omega_{\text{cav}} \quad (3.3)$$

is the detuning between the laser and the cavity as introduced in Equation (2.57). The mechanical frequency is denoted by Ω_{mech} , g_0 is the bare optomechanical coupling strength, and α_{laser} is the complex amplitude of the laser driving the cavity. The Lindblad dissipators \mathcal{D} are defined in Equation (2.12). The mechanical and optical damping rates and the thermal phonon number are denoted by Γ_{mech} , κ , and n_{ph} , respectively. A continuous measurement, *i.e.*, photon counting or homodyne detection of the optical quadrature

$$\hat{a}e^{i\varphi} + \hat{a}^\dagger e^{-i\varphi} , \quad (3.4)$$

is performed on the output port of the optical cavity, as shown in Figures 3.1(a) and (b), respectively. The measured optical quadrature can be selected by adjusting the relative phase φ between the local oscillator (LO) and the laser driving the optical cavity. In an experiment, some photons will not be detected because of absorption or scattering on their way to the detector and because of imperfections of the photon detection process. Therefore, we assume that the continuous measurement has an overall detection efficiency $0 \leq \eta \leq 1$. We will discuss in Section 3.3 how to simulate imperfect photon detection.

To drive the optomechanical system into mechanical limit-cycle motion, we assume that a laser drive above resonance is applied to the optical cavity, $\alpha_{\text{laser}} > 0$ and $\Delta > 0$. As derived in Section 2.4.2, the mechanical motion can be described in a semiclassical approximation by [Rodrigues and Armour, 2010; Marquardt *et al.*, 2006]

$$\langle b \rangle = \bar{\beta}_{\text{ss}} + B_{\text{ss}} e^{-i[(\Omega_{\text{mech}} + \delta\Omega_{\text{ss}})t + \phi]} , \quad (3.5)$$

where B_{ss} is the steady-state amplitude of the limit-cycle motion and the complex quantity $\bar{\beta}_{\text{ss}}$ describes a constant offset. Both quantities are implicitly defined by Equations (2.72a) and (2.72b): At the mechanical steady-state amplitude B_{ss} , the negative optical backaction damping at the rate Γ_{BA} defined in Equation (2.70) is compensated by the intrinsic mechanical damping at the rate Γ_{mech} , as sketched in Figure 3.1(c). The coupling to the optical cavity also introduces a renormalization $\delta\Omega_{\text{ss}}$ of the mechanical resonance frequency, which has been defined in Equation (2.71).

The optical backaction damping introduces a characteristic relaxation rate Γ_{rel} at which an initial mechanical amplitude $B(0)$ decays towards the steady-state amplitude B_{ss} . To derive this rate, we consider a small amplitude fluctuation $B(t) = B_{\text{ss}} + \delta B(t)$, where $|\delta B(t)| \ll B_{\text{ss}}$. Equation (2.72a) implies that an amplitude fluctuation δB introduces a change of the mechanical offset $\bar{\beta}$ of the order of g_0/Ω_{mech} . Since we are working in the weak-coupling limit $g_0 \ll \Omega_{\text{mech}}$, we ignore this correction in the derivation of the amplitude relaxation rate. A Taylor expansion of Equation (2.68b) in in terms of δB yields

$$\frac{d}{dt} \delta B(t) = -\frac{\Gamma_{\text{rel}}}{2} \delta B(t) .$$

Thus, after a small perturbation $\delta B(0)$, the mechanical amplitude relaxes exponentially towards its steady-state value,

$$\delta B(t) = \delta B(0) e^{-\Gamma_{\text{rel}} t/2} .$$

The amplitude relaxation rate is given by

$$\begin{aligned} \Gamma_{\text{rel}} &= B \left. \frac{\partial \Gamma_{\text{BA}}}{\partial B} \right|_{B_{\text{ss}}} \\ &= \Gamma_{\text{mech}} - 2g_0^2 \kappa |\alpha_{\text{laser}}|^2 \sum_{k=-\infty}^{\infty} \frac{J'_{k+1}(\tilde{B}_{\text{ss}}) J_k(\tilde{B}_{\text{ss}}) + J_{k+1}(\tilde{B}_{\text{ss}}) J'_k(\tilde{B}_{\text{ss}})}{|g_{k+1}|^2 |g_k|^2}, \end{aligned} \quad (3.6)$$

where $\tilde{B}_{\text{ss}} = 2g_0 B_{\text{ss}} / \Omega_{\text{mech}}$. The terms g_k in the denominator are defined in Equation (2.67) and $J_k(x)$ denotes the k -th Bessel function of the first kind.

3.3 Methods and parameters

Motivated by previous theoretical investigations [Rodrigues and Armour, 2010; Qian *et al.*, 2012; Nation, 2013; Lörch *et al.*, 2014], we will use the mechanical Fano factor (2.74) to quantify the nonclassicality of the mechanical limit-cycle oscillation,

$$F = \frac{\langle (\hat{b}^\dagger \hat{b})^2 \rangle - \langle \hat{b}^\dagger \hat{b} \rangle^2}{\langle \hat{b}^\dagger \hat{b} \rangle}.$$

As discussed in Section 2.4.2, a Fano factor below unity indicates nonclassical mechanical states. In the following, we will compare the Fano factor of three different quantities:

1. The instantaneous Fano factor $F(t)$ of the stochastic quantum state $\hat{\rho}(t)$ along a quantum trajectory,
2. its ensemble average

$$F_{\text{cond}} = \mathbb{E}[F(t)], \quad (3.7)$$

which is time-independent after some initial transient dynamics and can be interpreted as the Fano factor of a time-averaged mechanical state along a quantum trajectory (cf. Section 3.5), and

3. the steady-state Fano factor F_{ss} associated with the unconditional steady-state solution $\hat{\rho}_{\text{ss}}$ of the QME (3.1).

The parameters of our numerical study are determined as follows. We will concentrate most of the time on the experimentally relevant weak-coupling limit $g_0 \ll \Omega_{\text{mech}}$. As for the mechanical damping rate Γ_{mech} , we will consider three different parameter regimes which are schematically represented in Figure 3.1(c) by horizontal lines:

- (i) Negligible mechanical damping (solid red line). In this case, the theory developed by Lörch *et al.* [2014] is directly applicable. Furthermore, a measurement at perfect detection efficiency, $\eta = 1$, evolves the system into a pure state. Since the backaction damping Γ_{BA} oscillates around zero, mechanical limit-cycle motion is possible at each positively-sloped root of Γ_{BA} .

The potential amplitudes of limit-cycle motion are separated by regions of positive backaction damping, whose maximum value decreases if the cavity decay rate κ is increased. Quantum fluctuations may drive the system across these regions of positive backaction damping. Therefore, for increasing κ , the mechanical amplitude can show multistability between several limit cycles or it

may even become unstable such that there is no limit cycle at all. As a consequence, all parameters considered in this work are in the resolved-sideband regime if the mechanical damping rate is set to zero.

- (ii) A nonzero mechanical damping that is small compared to the value of the backaction damping $|\Gamma_{\text{BA}}(0)|$ at zero mechanical amplitude, but large enough such that there is a unique limit cycle (dashed blue line). Here, we will investigate cavity decay rates κ beyond the resolved-sideband regime.

The two parameter regimes introduced so far are advantageous for numerical simulations, since, for an appropriate choice of g_0 , we can avoid multistability by widely separating the limit cycle amplitudes in Fock space, whereas the fluctuations in the phonon number $\hat{b}^\dagger\hat{b}$ are still sufficiently small to allow us to restrict the Hilbert space dimension to a numerically feasible value. However, current optomechanical limit-cycle experiments operate at very small values of g_0/κ , the ratio $\kappa/\Omega_{\text{mech}}$ can be smaller than one, but the cooperativity (2.61) is not much larger than unity. Therefore, the limit-cycle amplitude is situated in the parabolic region of the curve of $\Gamma_{\text{BA}}(\tilde{B})$ in experiments [Cohen *et al.*, 2015].

- (iii) To provide a result in a parameter regime corresponding to typical experiments, we also investigate a mechanical damping of the order of $|\Gamma_{\text{BA}}(0)|$ [dotted green line in Figure 3.1(c)]. Since the limit-cycle amplitude and the required Hilbert-space dimension scale inversely proportional to the bare optomechanical coupling strength g_0 , choosing too small values for the coupling strength g_0 is numerically not feasible. Therefore, we will increase the value of g_0 compared to typical experimental values to be able to restrict the Hilbert-space dimension to a numerically tractable value, but we keep the limit-cycle amplitude in the parabolic regime of $\Gamma_{\text{BA}}(\tilde{B})$.

The strength of amplitude fluctuations around the limit-cycle amplitude depends on the mechanical damping rate Γ_{mech} , the thermal phonon number n_{ph} , and the drive power $|\alpha_{\text{laser}}|^2$ [Lörch *et al.*, 2014]. Therefore, we choose to keep these three parameters fixed while changing the cavity decay rate κ . Since the backaction damping Γ_{BA} depends on the cavity decay rate κ , too, the optomechanical limit-cycle may become unstable for too large values of κ . We choose the constant laser drive α_{laser} such that the limit cycle is stable over the entire range of considered cavity decay rates. To determine the value of the detuning Δ , we exploit the fact that the steady-state mechanical Fano factor F_{ss} has several local minima as a function of the detuning [Lörch *et al.*, 2014]. For fixed values of Γ_{mech} , n_{ph} , g_0 , α_{laser} , and κ , we choose the smallest positive detuning Δ such that the mechanical motion is stable and the steady-state Fano factor F_{ss} is locally minimal. An overview of the numerical parameters obtained by this procedure is given in Table 3.1. For specific parameter sets, we also investigate the impact of inefficient detection, $\eta < 1$, of finite mechanical temperature $n_{\text{ph}} > 0$, and of the bare optomechanical coupling strength g_0 .

Under the assumption of a perfect photodetection process, stochastic differential equations for photon counting and homodyne detection have been derived in Sections 2.2.2 and 2.2.3, respectively. The resulting SMEs (2.25) and (2.36) turn out to be useful to study the more realistic case of an imperfect photon detection process, too, since the case of imperfect photodetection can actually be mapped onto a modified continuous measurement with perfect photodetection. To model imperfect

TABLE 3.1: Numerical parameters used to investigate the three different parameter regimes introduced in Section 3.3. A minus sign in the regime (i) indicates that there is no stable limit cycle for the given value of the cavity decay rate κ .

		$\kappa/\Omega_{\text{mech}}$	0.1	0.5	1.0	1.5	2.0	2.5	3.0
parameter regime (i), ●									
g_0/Ω_{mech}	0.16	$\Delta/\Omega_{\text{mech}}$	0.05	0.21	0.37	–	–	–	–
$\Gamma_{\text{mech}}/\Omega_{\text{mech}}$	0	φ_{opt}/π	0.0	0.0	0.9	–	–	–	–
$\alpha_{\text{laser}}/\Omega_{\text{mech}}$	0.35	B_{ss}	7.5	7.6	8.0	–	–	–	–
n_{ph}	0	$\langle n \rangle_{\text{ss}}$	55.5	57.7	64.7	–	–	–	–
parameter regime (ii), ■									
g_0/Ω_{mech}	0.36	$\Delta/\Omega_{\text{mech}}$	0.00	0.15	0.27	0.36	1.44	1.22	0.74
$\Gamma_{\text{mech}}/\Omega_{\text{mech}}$	0.00125	φ_{opt}/π	0.0	0.9	0.8	0.6	0.4	0.3	0.3
$\alpha_{\text{laser}}/\Omega_{\text{mech}}$	0.3	B_{ss}	3.2	3.2	3.2	3.2	4.6	3.8	2.6
n_{ph}	0	$\langle n \rangle_{\text{ss}}$	9.4	10.3	11.3	11.8	22.2	15.3	8.0
parameter regime (iii), ▲									
g_0/Ω_{mech}	0.16	$\Delta/\Omega_{\text{mech}}$	0.05						
$\Gamma_{\text{mech}}/\Omega_{\text{mech}}$	0.0006	φ_{opt}/π	0.15						
$\alpha_{\text{laser}}/\Omega_{\text{mech}}$	0.1	B_{ss}	3.2						
n_{ph}	0	$\langle n \rangle_{\text{ss}}$	10.8						

photodetection, we split the cavity damping term into two Lindblad dissipators,

$$\begin{aligned} \mathcal{D}[\hat{a}]\hat{\rho} &= \eta\mathcal{D}[\hat{a}]\hat{\rho} + (1-\eta)\mathcal{D}[\hat{a}]\hat{\rho} \\ &= \mathcal{D}[\sqrt{\eta}\hat{a}]\hat{\rho} + \mathcal{D}[\sqrt{1-\eta}\hat{a}]\hat{\rho}, \end{aligned} \quad (3.8)$$

where the first dissipative operator $\sqrt{\eta}\hat{a}$ is now considered to describe a perfectly monitored dissipative channel whereas the second operator $\sqrt{1-\eta}\hat{a}$ is treated as an unmonitored dissipative process. Combining Equations (3.1) and (3.8), we obtain a QME of the form (2.19) if we define the Lindblad operators \hat{o} and \hat{u}_j as follows:

$$\begin{aligned} \hat{o} &= \sqrt{\kappa\eta}\hat{a}, & \hat{u}_2 &= \sqrt{\Gamma_{\text{mech}}(n_{\text{ph}}+1)}\hat{b}, \\ \hat{u}_1 &= \sqrt{\kappa(1-\eta)}\hat{a}, & \hat{u}_3 &= \sqrt{\Gamma_{\text{mech}}n_{\text{ph}}}\hat{b}^\dagger. \end{aligned} \quad (3.9)$$

With these definitions, we can use the SMEs (2.25) and (2.36) to simulate photon counting and homodyne detection, respectively, for any value $0 \leq \eta \leq 1$ of the overall detection efficiency.

The eigenvalues of the deterministic part of the stochastic differential equations have a large imaginary component, such that explicit integration algorithms are unstable even for relatively small time steps. Therefore, we use a semi-implicit Milstein algorithm, which is implicit with respect to the deterministic part of the time evolution [Kloeden and Platen, 1995], to integrate the stochastic differential equation in the case of homodyne detection. This algorithm has already been implemented in the QUTIP package [Johansson *et al.*, 2012], which is used for all numerical calculations in this project. To solve the stochastic differential equation for photon counting, we implemented a fourth-order implicit Runge-Kutta algorithm [Rannacher, 2014].

As discussed in Section 2.2, the unconditional dynamics of the optomechanical system can be recovered from the stochastic unraveling by an ensemble-average

over many quantum trajectories. Hence, observables of the system do not change their average value in the presence of continuous measurements. For instance, the ensemble-averaged phonon-number expectation value $\mathbb{E}[\langle \hat{b}^\dagger \hat{b} \rangle]$ reproduces the unconditional steady-state phonon-number expectation value $\langle \hat{b}^\dagger \hat{b} \rangle_{\text{ss}}$ after some initial transient time. However, the continuous measurement leads to a purification of the state [Wiseman and Milburn, 2009], *i.e.*, if the system is initialized in a non-pure initial state $\hat{\rho}(0)$, a continuous measurement will increase its purity and the von Neumann entropy

$$S_{\text{vN}}(t) = -k_{\text{B}} \text{Tr} [\hat{\rho}(t) \ln \hat{\rho}(t)] \quad (3.10)$$

will decrease. Here, k_{B} denotes the Boltzmann constant. Likewise, the ensemble-average of functions of observables, such as the conditional mechanical Fano factor F_{cond} , may have different values than the corresponding steady-state result F_{ss} .

3.4 Nonclassical mechanical limit-cycle motion

Figures 3.2(a)–(c) show the phonon-number expectation value $\langle \hat{b}^\dagger \hat{b} \rangle(t)$, the von Neumann entropy $S_{\text{vN}}(t)$, and the Fano factor $F(t)$ for a single quantum trajectory obtained by homodyne detection, as well as their ensemble-averaged mean values $\mathbb{E}[\langle \hat{b}^\dagger \hat{b} \rangle(t)]$, $\mathbb{E}[S_{\text{vN}}(t)]$, and $\mathbb{E}[F(t)]$. The system is initialized in the steady-state solution $\hat{\rho}_{\text{ss}}$ of the QME (3.1) at times $t < 0$. At time $t = 0$, homodyne detection is switched on and $\langle \hat{b}^\dagger \hat{b} \rangle$, S_{vN} , and F evolve stochastically. As expected, homodyne detection does not change the mean phonon-number expectation value $\mathbb{E}[\langle \hat{b}^\dagger \hat{b} \rangle(t)]$, but our increasing knowledge of the system state causes the mean von Neumann entropy $\mathbb{E}[S_{\text{vN}}(t)]$ and the mean Fano factor $\mathbb{E}[F(t)]$ to decrease. Empirically, an exponential decay towards new conditional mean values is found, with a decay rate that is approximately twice the amplitude relaxation rate (3.6),

$$\mathbb{E}[S_{\text{vN}}(t)] \approx (S_{\text{ss}} - S_{\text{cond}})e^{-2\Gamma_{\text{rel}}t} + S_{\text{cond}} , \quad (3.11)$$

$$\mathbb{E}[F(t)] \approx (F_{\text{ss}} - F_{\text{cond}})e^{-2\Gamma_{\text{rel}}t} + F_{\text{cond}} . \quad (3.12)$$

The residual value S_{cond} for times $t \gg 1/\Gamma_{\text{rel}}$ depends on the strength of the remaining dissipative channels of the system. For zero mechanical damping and perfect detection, there is no unmonitored dissipative interaction and the system evolves into a pure entangled state, having zero von Neumann entropy. In the case of nonzero mechanical damping, shown here, or for imperfect detection efficiency, there is an additional unmonitored decay channel such that the system evolves into a mixed state, having nonzero von Neumann entropy, $S_{\text{cond}} \gtrsim 0$.

In the case of homodyne detection, the ensemble-averaged Fano factor F_{cond} depends on the measured optical quadrature, *i.e.*, it is a function of the homodyne angle φ . Note that φ and $\varphi + \pi$ effectively measure the same quadrature. In the following, all homodyne detection data is given at the optimal angle φ_{opt} that minimizes F_{cond} . The numerical values of φ_{opt} are given in Table 3.1.

The instantaneous Fano factor $F(t)$ fluctuates around its ensemble average F_{cond} . To quantify these fluctuations for long times $t \gg 1/\Gamma_{\text{rel}}$, we calculate a histogram $p(F)$ of the instantaneous Fano factor $F(t)$ over many trajectories, which is shown in Figure 3.2(e). In the following, we will quantify the properties of this histogram by three numbers, namely,

- (i) its mean value, the Fano factor F_{cond} ,

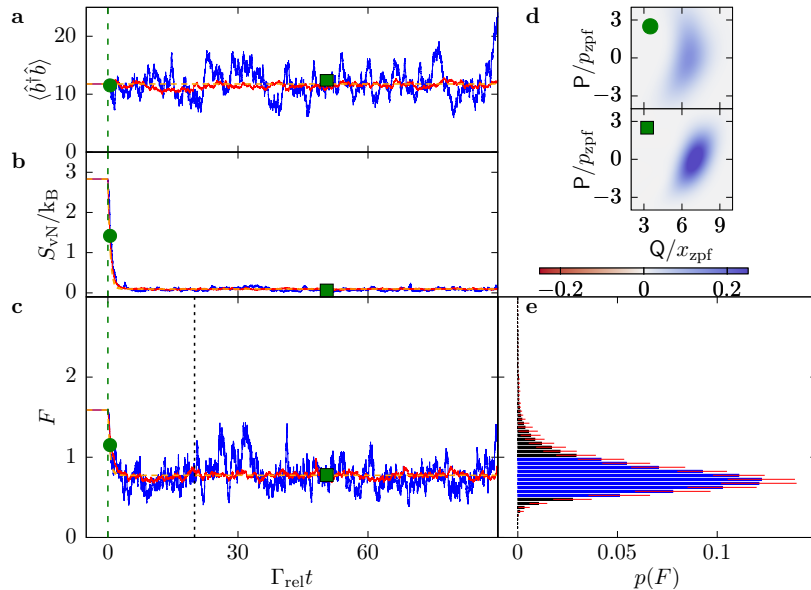


FIGURE 3.2: Evolution of (a) the phonon-number expectation value $\langle \hat{b}^\dagger \hat{b} \rangle$, (b) the von Neumann entropy S_{vN} , and (c) the Fano factor F under homodyne detection for a single trajectory (solid blue curves). The corresponding ensemble averages over 30 trajectories are shown as solid red curves, and the theoretical expectations in the limit of an average over infinitely many trajectories, Equations (3.11) and (3.12), respectively, are shown as dashed orange curves. At times $t < 0$ the system is assumed to be in its steady state, homodyne detection is switched on at $t = 0$. (d) Wigner function of the mechanical state in a frame rotating at Ω_{mech} at two different times indicated by green markers on the trajectories. The zero-point fluctuations are defined by $x_{\text{zpf}} = \sqrt{\hbar/2m\Omega_{\text{mech}}}$ and $p_{\text{zpf}} = \sqrt{\hbar m\Omega_{\text{mech}}/2}$, where m denotes the effective mechanical mass, cf. Appendix A.1. (e) Distribution of the Fano factor for times larger than the data-acquisition start time indicated by the dotted black line in (c). The data includes all 30 trajectories. The blue bars of the histogram comprise at least 70% of the total probability. Parameters are the values in Table 3.1 that are highlighted in boldface type and $\eta = 1$.

- (ii) the probability $p(F < F_{\text{ss}})$ to obtain a Fano factor smaller than the steady-state value F_{ss} , and
- (iii) the range of values of the Fano factor that contains at least 70% of the total probability. This range is indicated by blue bars in the histogram and can be asymmetrically distributed around the mean value F_{cond} in the resolved-sideband regime. To determine this range, we calculate the cumulative distribution function of the histogram and exclude all bins that have a value smaller than 15% or larger than 85%.

For the parameters used in Figure 3.2, the conditional Fano factor is found to be smaller than the steady-state value, $F_{\text{cond}} < F_{\text{ss}}$. Using the three figures of merit of the histogram introduced above, we now investigate this reduction of the Fano factor F_{cond} for different optical damping rates κ , for different types of continuous measurements, and for mechanical damping rates Γ_{mech} in the three different regimes introduced in Section 3.3.

Our results are summarized in Figure 3.3. As predicted by Rodrigues and Armour [2010] and Lörch *et al.* [2014], the steady-state Fano factor F_{ss} is smaller than unity

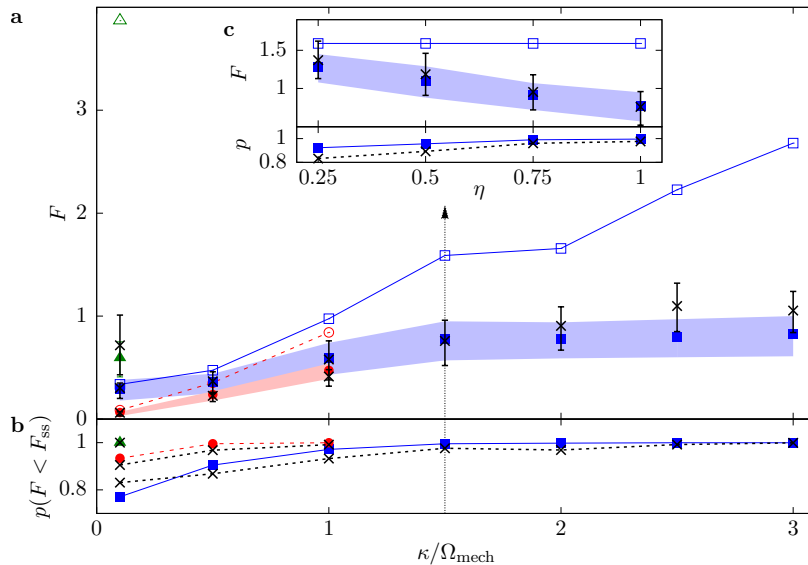


FIGURE 3.3: **(a)** Mean conditional Fano factor F_{cond} (solid markers), steady-state Fano factor F_{ss} (open markers) and **(b)** probability $p(F < F_{\text{ss}})$ to observe a Fano factor smaller than F_{ss} . Red circles and dashed lines correspond to homodyne detection and zero mechanical damping [regime (i)]. Blue squares and solid lines correspond to homodyne detection and a mechanical damping small compared to $|\Gamma_{\text{BA}}(0)|$ [regime (ii)]. Green triangles represent the case of homodyne detection and a mechanical damping rate large compared to $|\Gamma_{\text{BA}}(0)|$ [regime (iii)]. The black crosses adjacent to the results for homodyne detection indicate the corresponding results for photon counting. The shaded regions and error bars represent the ranges of Fano factors that contain at least 70 % of all counts. All curves are calculated at perfect detection efficiency, $\eta = 1$, with the parameters given in Table 3.1. **(c)** Influence of imperfect detection, $\eta < 1$, for the parameters highlighted in boldface type in Table 3.1.

in the resolved-sideband regime $\kappa \ll \Omega_{\text{mech}}$ at zero mechanical damping. This prediction still holds for small mechanical damping, but is not applicable for a mechanical damping of the order of $|\Gamma_{\text{BA}}(0)|$. If κ is increased towards the unresolved-sideband regime $\kappa > \Omega_{\text{mech}}$, the steady-state Fano factor grows and takes values much larger than unity.

Whereas the conditional mechanical Fano factor F_{cond} increases with κ in the resolved-sideband regime, too, it saturates to a value of the order of unity in the unresolved-sideband regime. In the resolved-sideband regime, F_{cond} depends only weakly on the homodyne angle φ and homodyne detection and photon counting yield the same results within the statistical errors. Towards the unresolved-sideband regime or for large mechanical damping, however, the choice of an optimal homodyne angle φ_{opt} allows one to reach smaller values of F_{cond} than for photon counting. The optimal homodyne angle is the one for which the measured optical quadrature, whose semiclassical dynamics is given by Equation (2.65), has the shortest period time and is closest to a harmonic oscillation.

Figure 3.3(a) shows that homodyne detection and photon counting measurements decrease the conditional Fano factor F_{cond} with respect to F_{ss} for all considered values of Γ_{mech} and κ . Since F_{cond} is bounded in the unresolved-sideband regime but F_{ss} increases with κ , the probability $p(F < F_{\text{ss}})$ to observe a Fano factor smaller than the steady-state Fano factor in a continuous measurement increases towards the

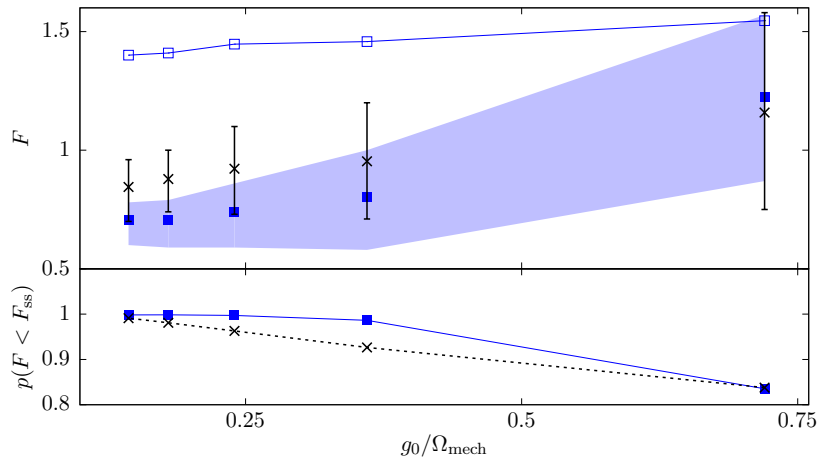


FIGURE 3.4: Influence of the optomechanical single-photon coupling strength g_0 on F_{ss} , F_{cond} , and $p(F < F_{ss})$. Filled blue squares indicate the results for homodyne detection, black crosses the ones for photon counting. The steady-state Fano factor F_{ss} is shown in open blue squares. The product $g_0 |\alpha_{laser}| = 0.108 \Omega_{mech}^2$ is kept constant. Parameters are $\kappa/\Omega_{mech} = 1.5$, $\Gamma/\Omega_{mech} = 0.005$, $g_0/\Omega_{mech} = (0.144, 0.18, 0.24, 0.36, 0.72)$, $\alpha_{laser}/\Omega_{mech} = (0.75, 0.60, 0.45, 0.30, 0.15)$, $\Delta/\Omega_{mech} = (0.61, 0.58, 0.55, 0.44, 0.07)$, $n_{ph} = 0$, and $\varphi_{opt}/\pi = (0.4, 0.3, 0.3, 0.2, 0.6)$. The corresponding values of $\langle n \rangle_{ss}$ and B_{ss} are $\langle n \rangle_{ss} = (43.8, 28.8, 15.6, 7.0, 2.0)$ and $B_{ss} = (6.8, 5.4, 4.0, 2.5, 0.3)$.

unresolved-sideband regime and approaches unity, as shown in Figure 3.3(b).

Figure 3.3(c) shows the influence of the detection efficiency η on F_{ss} , F_{cond} , and $p(F < F_{ss})$ for a fixed ratio $\kappa/\Omega_{mech} = 1.5$. The smaller the detection efficiency the less information can be gained out of the continuous measurement. Therefore, F_{cond} tends towards the steady-state value F_{ss} for low detection efficiency.

In Figure 3.4, we investigate the influence of the optomechanical single-photon coupling strength g_0 on the reduction of the Fano factor. In the weak-coupling limit $g_0 \ll \Omega$, the steady-state Fano factor is expected to be only a function of $g_0 |\alpha_{laser}|$ [Lörch *et al.*, 2014]. Therefore, to obtain comparable results, we rescale both $|\alpha_{laser}|$ and g_0 at a time such that their product $g_0 |\alpha_{laser}|$ is kept constant. The graph of F_{ss} in Figure 3.4 confirms this prediction. The mean Fano factor F_{cond} increases with the optomechanical coupling strength and approaches the steady-state value F_{ss} . Likewise, the probability $p(F < F_{ss})$ decreases.

Finally, Figure 3.5 shows the influence of the mechanical temperature, expressed in terms of the thermal phonon number n_{ph} , on the reduction of the Fano factor. A reduction of F_{cond} compared to F_{ss} is observed for all considered temperatures. However, in order to observe a nonclassical Fano factor $F_{cond} < 1$, a small effective thermal occupation number $n_{ph} \lesssim 1$ is required.

3.5 Discussion and experimental implementation

The numerical results shown in Figure 3.3 indicate that a continuous measurement of the cavity output of an optomechanical system decreases the mean mechanical Fano factor F_{cond} compared to the steady-state value F_{ss} obtained in the absence of a continuous measurement. The difference $F_{ss} - F_{cond}$ is particularly large in the unresolved-sideband regime and for a mechanical damping close to $|\Gamma_{BA}(0)|$. For parameters

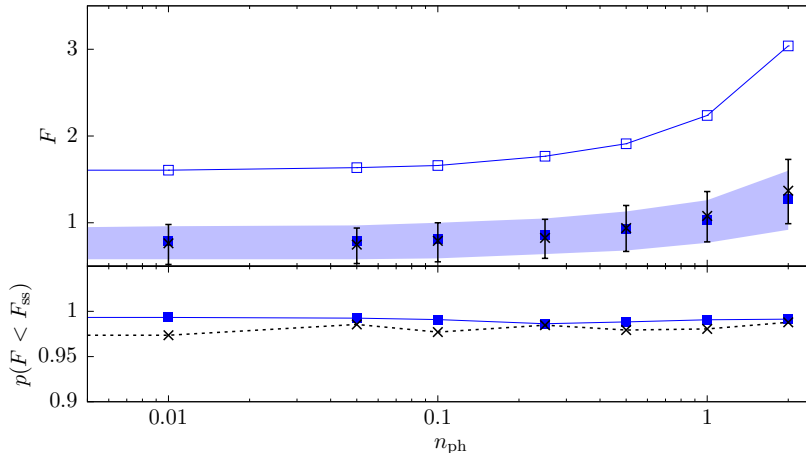


FIGURE 3.5: Influence of the mechanical temperature, expressed in terms of the thermal phonon number n_{ph} , on F_{ss} , F_{cond} , and $p(F < F_{\text{ss}})$. Filled blue squares indicate the results for homodyne detection, black crosses the ones for photon counting. The steady-state Fano factor F_{ss} is shown in open blue squares. Parameters are $\kappa/\Omega_{\text{mech}} = 1.5$, $\Gamma/\Omega_{\text{mech}} = 0.00125$, $g_0/\Omega_{\text{mech}} = 0.36$, $\alpha_{\text{laser}}/\Omega_{\text{mech}} = 0.3$, $\Delta/\Omega_{\text{mech}} = (0.36, 0.36, 0.36, 0.35, 0.34, 0.34, 0.33)$, and $\varphi_{\text{opt}}/\pi = 0.6$. The corresponding values of $\langle n \rangle_{\text{ss}}$ and B_{ss} are $\langle n \rangle_{\text{ss}} = (11.8, 11.8, 11.8, 11.8, 11.8, 11.9, 12.1)$ and $B_{\text{ss}} = 3.2$.

similar to the ones realized in current experiments (cf. green triangles in Figure 3.3), a large steady-state Fano factor $F_{\text{ss}} > 3$ is strongly reduced to $F_{\text{cond}} < 1$ and a nonclassical state is observed with probability one. A similar but less pronounced reduction effect is observed in the resolved-sideband regime. In the unresolved-sideband regime, photon-counting reduces the Fano factor from a steady-state value much larger than unity to a mean value F_{cond} close to unity. Homodyne detection allows one to decrease F_{cond} even further by optimizing the homodyne angle φ . By this means, a nonclassical mean Fano factor $F_{\text{cond}} < 1$ can be achieved even in the unresolved-sideband regime.

These numerical results can be qualitatively understood as follows. The measurement record allows one to distinguish mechanical states obtained in different quantum trajectories, which are indistinguishable in the case of unconditional dynamics, as discussed in Section 2.2.6. The instantaneous mechanical state has a lower uncertainty in amplitude and phase than the mechanical steady state because the steady state represents an ensemble average over many quantum trajectories. To discuss the impact of a continuous measurement on the Fano factor, it is sufficient to focus on the amplitude dynamics, *i.e.*, the phonon-number distribution of the mechanical states. The phonon-number distribution $p_{\text{ss}}(n)$ of the steady state is given by an ensemble average over mechanical states $j = 1, 2, \dots$ at different amplitudes $n_j = \langle \hat{b}^\dagger \hat{b} \rangle_j$. Each of those mechanical states has a photon-number distribution $p_{\text{bare}}^{(j)}(n)$ that is narrower than $p_{\text{ss}}(n)$, as sketched in Figure 3.6. The steady-state Fano factor F_{ss} is determined by p_{ss} , the fluctuating Fano factor $F(t)$ along the quantum trajectory j is determined by $p_{\text{bare}}^{(j)}$, and the average conditional Fano factor F_{cond} is determined by the ensemble-averaged properties of the set of distributions $\{p_{\text{bare}}^{(j)}\}$.

To derive a minimal model for the properties of F_{cond} , we define the ensemble-averaged phonon-number distribution

$$p_{\text{bare}}(n) = \mathbb{E} \left[p_{\text{bare}}^{(j)}(n + n_j) \right],$$

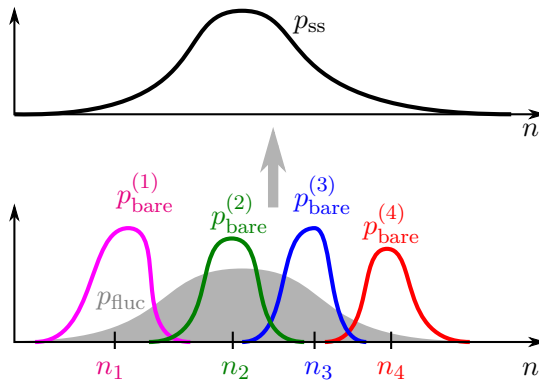


FIGURE 3.6: A physical argument why a continuous measurement causes a reduction of the Fano factor. The steady-state phonon distribution $p_{\text{ss}}(n)$ (top) is an ensemble average over many different mechanical states j , each described by a phonon distribution $p_{\text{bare}}^{(j)}(n)$ centered around a mean phonon number n_j (bottom). The phonon number n_j fluctuates around the steady-state value according to the distribution $p_{\text{fluc}}(n)$ (gray area in the lower plot). A continuous measurement tracks the diffusive evolution of n_j and gives access to the phonon distributions $p_{\text{bare}}^{(j)}(n)$, which have a smaller Fano factor than the steady-state phonon distribution.

which is a zero-mean distribution. The continuous measurement of the optical cavity allows us to infer the state of the mechanical subsystem and to track the amplitude $\langle \hat{b}^\dagger \hat{b} \rangle(t)$ of the mechanical state, which is distributed according to the distribution $p_{\text{fluc}}(n)$. In line with our numerical parameters shown in Table 3.1, we assume that both p_{bare} and p_{fluc} are narrow distributions in the following sense:

$$\sqrt{\langle n^2 \rangle_{\text{bare}}} \ll \langle n \rangle_{\text{ss}} , \quad (3.13)$$

$$\sqrt{\langle n^2 \rangle_{\text{fluc}} - \langle n \rangle_{\text{fluc}}^2} < \langle n \rangle_{\text{fluc}} . \quad (3.14)$$

These conditions imply that p_{bare} and p_{fluc} are peaked at $n \approx 0$ and $n \approx \langle n \rangle_{\text{fluc}}$, respectively, and decay to zero elsewhere. Therefore, we can extend their range of definition to the entire real line, $n \in (-\infty, \infty)$. Moreover, these conditions implicitly contain the assumption that the shape of the individual distributions $p_{\text{bare}}^{(j)}(n)$ for large steady-state amplitudes $\langle n \rangle_{\text{ss}}$ is almost independent of the instantaneous amplitude n_j and can be approximated by a generic distribution $p_{\text{bare}}(n)$. The steady-state phonon distribution is then given by a convolution of the two distributions,

$$p_{\text{ss}}(n) = \int_0^\infty dn' p_{\text{fluc}}(n') p_{\text{bare}}(n - n') . \quad (3.15)$$

Using the fact that p_{bare} has zero mean, we find $\langle n \rangle_{\text{ss}} = \langle n \rangle_{\text{fluc}}$ and

$$F_{\text{ss}} = \frac{\langle n^2 \rangle_{\text{fluc}} - \langle n \rangle_{\text{fluc}}^2}{\langle n \rangle_{\text{fluc}}} + \frac{\langle n^2 \rangle_{\text{bare}}}{\langle n \rangle_{\text{fluc}}} . \quad (3.16)$$

If the continuous measurement indicates that the mechanical amplitude of the instantaneous state $\hat{\rho}(t)$ is n' , the conditional phonon-number distribution of this state is

on average given by

$$p_{\text{bare}|n'}(n) = p_{\text{bare}}(n - n')$$

and the corresponding instantaneous Fano factor is $F(t|n') = \langle n^2 \rangle_{\text{bare}}/n'$. Taking the average over the fluctuating amplitude, we find

$$F_{\text{cond}} = \left\langle \frac{1}{n} \right\rangle_{\text{fluc}} \langle n^2 \rangle_{\text{bare}}. \quad (3.17)$$

Comparing Equations (3.16) and (3.17), we find the relation

$$\begin{aligned} F_{\text{ss}} &= F_{\text{fluc}} + F_{\text{cond}} + \langle n^2 \rangle_{\text{bare}} \left[\frac{1}{\langle n \rangle_{\text{fluc}}} - \left\langle \frac{1}{n} \right\rangle_{\text{fluc}} \right] \\ &= F_{\text{fluc}} + F_{\text{cond}} + \mathcal{O} \left[\frac{\langle n^2 \rangle_{\text{bare}}}{\langle n \rangle_{\text{ss}}} \right], \end{aligned} \quad (3.18)$$

where F_{fluc} denotes the Fano factor of the distribution p_{fluc} of the mechanical amplitude. The correction term on the right-hand side is negligible in the limit of a large phonon-number expectation value $\langle n_{\text{ss}} \rangle$. Thus, the steady-state Fano factor is the sum of the conditional Fano factor of the mechanical states, which is resolved by a continuous measurement, and the Fano factor of the fluctuations of the phonon number $\langle \hat{b}^\dagger \hat{b} \rangle$, which smear out the phonon-number distribution to the broad steady-state distribution obtained in the case of unconditional dynamics. This analytical result is well confirmed by our numerics and is the generalization of the decomposition of observables discussed in Section 2.2.6 to the mechanical Fano factor.

It is reasonable that imperfect photon detection reduces the impact of the continuous measurement such that F_{cond} tends towards F_{ss} in the limit $\eta \rightarrow 0$, as shown in Figure 3.3(c). If all knowledge of the measurement is discarded, $\eta \rightarrow 0$, the continuous measurement is effectively absent, *i.e.*, $\hat{\sigma} \rightarrow 0$ and $\hat{u}_1 \rightarrow \sqrt{\kappa} \hat{a}$. In this limit, the SME reproduces the unconditional QME (3.1) and the mechanical state $\hat{\rho}(t)$ along each quantum trajectory is identical to $\hat{\rho}_{\text{ss}}$. However, note that even for a moderate detection efficiency of 50%, a continuous measurement still reduces the Fano factor by about 25%.

Figure 3.4 shows that the conditional Fano factor F_{cond} tends towards the steady-state value F_{ss} if the weak-coupling regime $g_0 \ll \Omega_{\text{mech}}$ is left. Since we keep the product $g_0 |\alpha_{\text{laser}}|$ fixed, the drive strength $|\alpha_{\text{laser}}|$ decreases if the bare optomechanical coupling strength g_0 grows. Thus, the mean value $\langle n \rangle_{\text{fluc}}$ of the distribution p_{fluc} is shifted to smaller phonon numbers and the variance of p_{fluc} decreases. Consequently, the broadening effect of the convolution (3.15) on p_{ss} is reduced such that F_{fluc} decreases and F_{cond} approaches F_{ss} . Interestingly, despite the fact that the conditions (3.13) and (3.14) are violated, numerically the decomposition (3.18) of the steady-state Fano factor F_{ss} is still found to be correct.

Finally, Figure 3.5 indicates that the reduction of F_{cond} with respect to F_{ss} is present at all considered temperatures of the mechanical environment. However, to observe a *nonclassical* Fano factor $F_{\text{cond}} < 1$ for the parameters considered here, a small thermal phonon occupation $n_{\text{ph}} \lesssim 1$ is required. Therefore, cryogenic temperatures or a precooling of the mechanics, *e.g.*, using optomechanical cooling [Teufel *et al.*, 2011; Chan *et al.*, 2011], are necessary. We stress that n_{ph} refers to an effective bath occupation number of such a combined mechanical and optical bath.

Continuous measurements of optomechanical limit cycles are experimentally feasible with current technology. Optical homodyne detection on optomechanical systems

is routinely done in experiments [Briant *et al.*, 2003; Iwasawa *et al.*, 2013; Wiczorek *et al.*, 2015]. The same holds for the realization of optomechanical limit cycles [Anetsberger *et al.*, 2009; Grudinin *et al.*, 2010; Zhang *et al.*, 2012; Bagheri *et al.*, 2013; Cohen *et al.*, 2015]. To detect a sub-Poissonian mechanical state, optomechanical state-reconstruction techniques applicable to both the resolved-sideband and the unresolved-sideband regime are required. A proposal for state-reconstruction in the unresolved-sideband regime has been published recently [Shahandeh and Ringbauer, 2019]. In the resolved-sideband regime, several schemes are established and could be adapted to this setup [Vanner *et al.*, 2015]. For state-reconstruction schemes based on an optomechanical state transfer of the mechanical state to the optical cavity followed by an optical tomography [Verhagen *et al.*, 2012], it could be beneficial to add an auxiliary readout cavity to the system. The properties of the mechanical amplitude fluctuations could potentially even be characterized by the photon-counting measurement itself using the measurement scheme demonstrated by Cohen *et al.* [2015]. Hence, the effect discussed here could already be verified in the resolved-sideband regime with state-of-the-art experimental techniques and there is a theoretical proposal on how to proceed in the case of the unresolved-sideband regime.

3.6 Summary

In this project, we numerically analyzed how homodyne and photon counting measurements of the optical cavity output decrease the mean mechanical Fano factor F_{cond} of an optomechanical system below its steady-state value F_{ss} . In the resolved-sideband regime at small mechanical damping, the steady-state limit cycle is already nonclassical, $F_{\text{ss}} < 1$, such that the gain of nonclassicality due to a continuous measurement is small. However, in the unresolved-sideband regime, the mean Fano factor F_{cond} is drastically reduced compared to F_{ss} and the system is found in a nonclassical mechanical state for a macroscopic fraction of the observation time. In particular for the parameter regime inspired by typical experimental setups, we observe a large decrease of the mechanical Fano factor. The reduction of the Fano factor is robust against imperfect photon detection and finite temperature of the mechanical environment. However, to observe nonclassical mechanical states, a low effective thermal phonon number n_{ph} is necessary.

In conclusion, optical continuous measurements are a promising way to reduce amplitude fluctuations of the mechanical subsystem not only in the limit of cooling [Mancini *et al.*, 1998; Doherty and Jacobs, 1999; Hopkins *et al.*, 2003; Wilson *et al.*, 2015], but also for optomechanical limit cycles. This opens a route to the creation of nonclassical mechanical states in a new parameter range, namely, outside the resolved-sideband regime.

The results and figures presented in this chapter have been published in parts in [Koppenhöfer *et al.*, 2018].

Chapter 4

Heralded Dissipative Generation of Nonclassical States in Nonlinear Systems

The results presented in this chapter have been published in:

M. Koppenhöfer, C. Bruder, and N. Lörch,
Heralded dissipative preparation of nonclassical states in a Kerr oscillator,
 Physical Review Research **2**, 013071 (2020).

4.1 Motivation

Nonlinearity is a crucial prerequisite for quantum algorithms to outperform their classical counterparts in quantum information processing because it gives rise to states or operations that cannot be efficiently described in a classical framework [Nielsen and Chuang, 2011]. An important property to evaluate the usefulness of a quantum state in this context is the occurrence of negative values in its Wigner phase-space quasiprobability distribution [Veitch *et al.*, 2012; Stahlke, 2014; Rahimi-Keshari *et al.*, 2016]. However, such nonclassical states are challenging to prepare and stabilize because of unavoidable decoherence due to interaction with an unmonitored environment. For example, the perhaps simplest nonlinear quantum system, a driven and damped quantum oscillator with a Kerr nonlinearity, has a steady-state Wigner function that is strictly positive [Kheruntsyan *et al.*, 1996; Kheruntsyan, 1999; Bartolo *et al.*, 2016].

Here, we circumvent this restriction and quantify the potential of such a system to stabilize nonclassical states with negative Wigner density. We consider setups where a detector continuously monitors the emitted photons. Such information leaking out of the system has already been useful in the context of entanglement generation [Cabrillo *et al.*, 1999; Plenio *et al.*, 1999; Nha and Carmichael, 2004; Carvalho *et al.*, 2007; Viviescas *et al.*, 2010], teleportation [Bose *et al.*, 1999], cooling [Mancini *et al.*, 1998; Doherty and Jacobs, 1999; Hopkins *et al.*, 2003; Wilson *et al.*, 2015], and nonclassical optomechanical limit cycles [Koppenhöfer *et al.*, 2018], since the continuous observation modifies the system's dynamics. In general, the states of the system during a continuous monitoring can have negative Wigner densities, but they fluctuate stochastically and feedback protocols are necessary to stabilize a particular state [Minganti *et al.*, 2016]. Here, we demonstrate that quantum trajectories can continuously relax to deterministic states whose presence is revealed by the detection signal. This mechanism opens a new alternative path in heralded quantum state preparation and allows

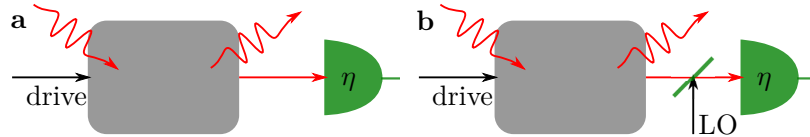


FIGURE 4.1: **(a)** A driven nonlinear dissipative quantum system (gray box) is monitored by a photon-counting measurement with detection efficiency η . The detection signal provides a herald for the creation of a pseudosteady state in the system. **(b)** In a homodyne detection setup, a local oscillator (LO) signal is added before the detection, which allows one to modify the pseudosteady state.

one to stabilize certain nonclassical states without feedback, including Schrödinger kitten states.

In contrast to most heralded state preparation protocols relying on a photon detection event that heralds the *projection* to a (potentially maintained) target state [Clausen *et al.*, 1999; Lund *et al.*, 2004; Lance *et al.*, 2006; Bimbard *et al.*, 2010; Takeda *et al.*, 2013; Galland *et al.*, 2014; Hong *et al.*, 2017; Zhang and Baranger, 2019], we explore the opposite approach and use the photon-counting measurement to identify a time evolution which continuously *relaxes* the system into the target state, similar to Sörgel and Hornberger [2015]. Because the system will stay in this state conditioned on no further photon detection events, we will refer to it as a *pseudosteady state*, to distinguish our mechanism from dissipative steady-state stabilization [Poyatos *et al.*, 1996; Krauter *et al.*, 2011; Mamaev *et al.*, 2018; Brunelli *et al.*, 2018].

On one hand, our results shed light on the actual dynamics of a dissipative quantum system when the information leaking out to the environment is not discarded. On the other hand, they can be seen as a practical protocol for heralded state preparation in dissipative quantum systems that is feasible with current technology.

This chapter is structured as follows. In Section 4.2, we introduce a general model of a continuously monitored driven dissipative quantum system, which is based on a QME. We also introduce the driven and damped Kerr oscillator, which will serve as an example to illustrate the protocol. Then, an overview of the protocol is given in Section 4.3. The mathematical derivation of the pseudosteady state and its associated relaxation rate is summarized in Section 4.4 for the case of a SME and of a SSE. Subsequently, numerical results on the generation of nonclassical states, characterized by a negative Wigner function, are presented and discussed in Section 4.5. In particular, Section 4.5.2 is devoted to the question how to increase the nonclassicality of a state by changing the continuous detection method. The impact of imperfect detection and finite temperature on the state generation protocol is discussed in Section 4.6. Finally, we comment on the experimental implementation of the protocol in Section 4.7 and conclude in Section 4.8.

4.2 Continuously monitored dissipative quantum system

We consider a dissipative quantum system that exchanges photons with a finite-temperature environment. Its QME is

$$\frac{d}{dt}\hat{\rho} = \mathcal{L}_0\hat{\rho} + \kappa(n_{\text{th}} + 1)\mathcal{D}[\hat{a}]\hat{\rho} + \kappa n_{\text{th}}\mathcal{D}[\hat{a}^\dagger]\hat{\rho}, \quad (4.1)$$

where \hat{a} is the photon annihilation operator, κ denotes the energy decay rate, n_{th} is the thermal photon number due to interaction with the environment, and the Lindblad dissipators \mathcal{D} are defined in Equation (2.12). In general, \mathcal{L}_0 can be any completely positive and trace-preserving linear superoperator such that Equation (4.1) has a steady-state solution $\hat{\rho}_{\text{ss}}$. A photon detector constantly monitors the emission of photons by the system into the environment, as shown in Figure 4.1(a). The photon detection process is assumed to have an overall detection efficiency $0 \leq \eta \leq 1$. Imperfect detection, $\eta < 1$, may be caused by losses of photons on the way to the detector, *i.e.*, absorption or scattering, or by imperfections of the photon detectors. As discussed in Section 3.3, imperfect detection can be modeled by splitting the Lindblad dissipator in two terms, cf. Equation (3.8),

$$\mathcal{D}[\hat{a}]\hat{\rho} = \mathcal{D}[\sqrt{\eta}\hat{a}]\hat{\rho} + \mathcal{D}[\sqrt{1-\eta}\hat{a}]\hat{\rho}.$$

The first term describes photon emission at a rescaled emission rate and will be treated as a perfectly monitored dissipative interaction. The second term represents an unmonitored dissipative interaction. In addition, we assume that the beam of emitted photons may be displaced by a local oscillator (LO) signal $\sqrt{\kappa(n_{\text{th}}+1)}\eta\xi$ before detection, as shown in Figure 4.1(b). As derived in Section 2.2.2, this displacement gives rise to a modified QME of the form of Equation (2.15),

$$\begin{aligned} \frac{d}{dt}\hat{\rho} &= \mathcal{L}_0\hat{\rho} - \frac{i}{\hbar} \left[i\hbar\frac{\kappa}{2}(n_{\text{th}}+1)\eta \left(\xi\hat{a}^\dagger - \xi^*\hat{a} \right), \hat{\rho} \right] + \kappa n_{\text{th}}\mathcal{D}[\hat{a}^\dagger]\hat{\rho} \\ &\quad + \kappa(n_{\text{th}}+1)\eta\mathcal{D}[\hat{a}+\xi]\hat{\rho} + \kappa(n_{\text{th}}+1)(1-\eta)\mathcal{D}[\hat{a}]\hat{\rho}. \end{aligned}$$

As derived in Section 2.2.2, a continuous detection of the photons emitted via the Lindblad operator $\hat{a} + \xi$ is modeled by the SME

$$d\hat{\rho} = \bar{\mathcal{L}}\hat{\rho}dt + \left[\frac{(\hat{a} + \xi)\hat{\rho}(\hat{a}^\dagger + \xi^*)}{\text{Tr}[(\hat{a}^\dagger + \xi^*)(\hat{a} + \xi)\hat{\rho}]} - \hat{\rho} \right] dN, \quad (4.2)$$

$$\bar{\mathcal{L}}\hat{\rho} = (\mathcal{L} + \mathcal{N})\hat{\rho} - \text{Tr}(\mathcal{N}\hat{\rho})\hat{\rho}. \quad (4.3)$$

The continuous part of the time evolution is given by the nonlinear superoperator $\bar{\mathcal{L}}$. We introduced the abbreviations

$$\begin{aligned} \mathcal{L}\hat{\rho} &= \mathcal{L}_0\hat{\rho} - \frac{i}{\hbar} \left[i\hbar\frac{\kappa}{2}(n_{\text{th}}+1)\eta \left(\xi\hat{a}^\dagger - \xi^*\hat{a} \right), \hat{\rho} \right] \\ &\quad + \kappa n_{\text{th}}\mathcal{D}[\hat{a}^\dagger]\hat{\rho} + \kappa(n_{\text{th}}+1)(1-\eta)\mathcal{D}[\hat{a}]\hat{\rho}, \end{aligned} \quad (4.4)$$

$$\mathcal{N}\hat{\rho} = -\frac{\kappa}{2}(n_{\text{th}}+1)\eta \left\{ (\hat{a}^\dagger + \xi^*)(\hat{a} + \xi), \hat{\rho} \right\}. \quad (4.5)$$

The stochastic increment dN is either zero or unity and is distributed according to a Poissonian distribution with expectation value

$$\mathbb{E}[dN] = \kappa(n_{\text{th}}+1)\eta\text{Tr} \left[(\hat{a}^\dagger + \xi^*)(\hat{a} + \xi)\hat{\rho} \right] dt. \quad (4.6)$$

As discussed in Section 2.2, the limit $\xi \rightarrow 0$ corresponds to conventional photon detection, shown in Figure 4.1(a), whereas the limit $\xi \rightarrow \infty$ corresponds to homodyne detection.

As a model system to illustrate our state generation protocol, we use a Kerr nonlinear oscillator. In this case, the superoperator \mathcal{L}_0 is given by

$$\mathcal{L}_0 \hat{\rho} = -\frac{i}{\hbar} \left[\hat{H}_0, \hat{\rho} \right], \quad (4.7)$$

where \hat{H}_0 is the Hamiltonian (2.78) of a Kerr nonlinear oscillator,

$$\hat{H}_0 = -\hbar\Delta\hat{a}^\dagger\hat{a} + \hbar K\hat{a}^\dagger\hat{a}^\dagger\hat{a}\hat{a} + \hbar\left(\alpha_1\hat{a}^\dagger + \alpha_2\hat{a}^\dagger\hat{a}^\dagger + \text{H.c.}\right). \quad (4.8)$$

Here, K denotes the strength of the Kerr nonlinearity and α_1 and α_2 denote the strength of the harmonic and parametric drives, respectively, as introduced in Section 2.5. We work in a frame rotating at the harmonic drive frequency ω_{har} , and Δ is the detuning of the drives with respect to the natural frequency ω_0 defined in Equation (2.79). Note that for this choice of \mathcal{L}_0 and \hat{H}_0 , Equation (4.1) has a strictly positive steady-state Wigner function for any choice of the parameters [Kheruntsyan *et al.*, 1996; Kheruntsyan, 1999; Bartolo *et al.*, 2016].

4.3 Heralded state preparation protocol

The SME (4.2) describes a continuous time evolution of the state $\hat{\rho}$ that is interrupted by discontinuous quantum jump events. This will lead to an interplay of two timescales: After initial transient dynamics, the quantum trajectories fluctuate on average around the steady state $\hat{\rho}_{\text{ss}}$ of Equation (4.1), as shown in Figure 4.2(a). This steady state determines the average rate of quantum jumps,

$$\Gamma_{\text{jump}} = \frac{\mathbb{E}[\text{d}N]}{\text{d}t} = -\text{Tr}(\mathcal{N}\hat{\rho}_{\text{ss}}). \quad (4.9)$$

Between two adjacent quantum jumps, the state $\hat{\rho}$ evolves continuously according to the nonlinear superoperator $\bar{\mathcal{L}}$, which has a steady-state solution fulfilling

$$\bar{\mathcal{L}}\hat{\rho}_{\text{ps}} = 0 \quad (4.10)$$

and an associated relaxation rate Γ_{rel} towards $\hat{\rho}_{\text{ps}}$. In the following, we will call $\hat{\rho}_{\text{ps}}$ the *pseudosteady state* of the stochastic quantum master equation (4.2) because it is a steady state conditioned on the absence of photon detection events.

If the condition $\Gamma_{\text{rel}} \gtrsim \Gamma_{\text{jump}}$ holds, the waiting time between two adjacent quantum jumps can be much larger than the relaxation time and $\hat{\rho}$ relaxes exponentially to $\hat{\rho}_{\text{ps}}$, as shown in Figure 4.2(b). Hence, a photon detection event followed by no further click of the detector for several relaxation times $1/\Gamma_{\text{rel}}$ heralds the preparation of the state $\hat{\rho}_{\text{ps}}$ and the waiting time since the last detection event determines the state preparation fidelity.

This state preparation mechanism differs from other state preparation protocols studied in the literature in the following way. Previous state preparation protocols [Clausen *et al.*, 1999; Lund *et al.*, 2004; Lance *et al.*, 2006; Bimbard *et al.*, 2010; Takeda *et al.*, 2013; Galland *et al.*, 2014; Hong *et al.*, 2017; Zhang and Baranger, 2019] considered a composite closed quantum system consisting of the subsystem S hosting the target state and an ancillary system A that is measured during the protocol. The combined system is initialized in a state that is easily accessible, usually the joint ground state of S and A . Next, a time evolution is applied that generates a superposition of quantum states which includes the target state in S entangled with a

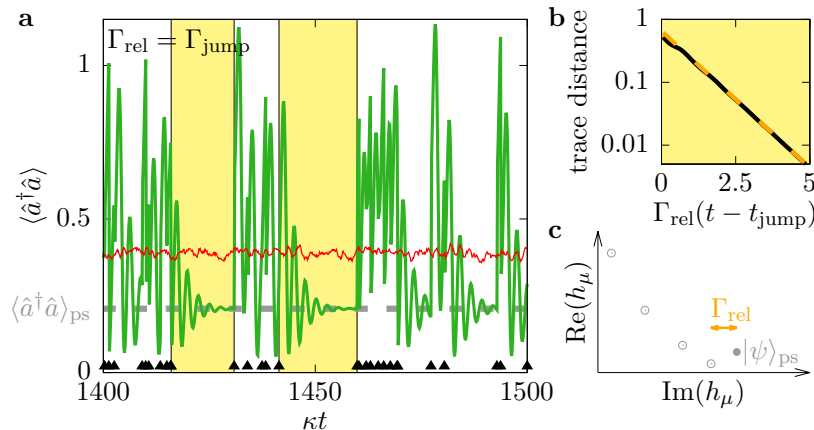


FIGURE 4.2: **(a)** Photon number $\langle \hat{a}^\dagger \hat{a} \rangle$ of a Kerr oscillator subjected to a harmonic drive and photon counting (solid green line). The quantum trajectory consists of a continuous time evolution towards a pseudosteady state $\hat{\rho}_{\text{ss}}$ whose photon number is indicated by the thick dashed gray line. This time evolution is interrupted by quantum jump events at random times indicated by black triangles. An ensemble averaged over 500 quantum trajectories (thin solid red line) reproduces the constant steady-state result $\langle \hat{a}^\dagger \hat{a} \rangle_{\text{ss}}$. In the intervals highlighted in light yellow, the waiting time between two adjacent quantum jumps is longer than 5 times the relaxation time. **(b)** After a quantum jump event, the trace distance between the instantaneous state and the pseudosteady state (solid black line) decays exponentially at a rate Γ_{rel} (dashed orange line). **(c)** Spectrum of the non-Hermitian Hamiltonian that defines the relaxation dynamics for $\eta = 1$ and $n_{\text{th}} = 0$. The relaxation rate Γ_{rel} is the imaginary part of the smallest gap between the stable eigenstate $|\psi\rangle_{\text{ps}}$ (solid circle) and the unstable eigenstates (open circles). Parameters are $\Delta/\kappa = 1.5$, $K/\kappa = 2.2$, $|\alpha_1|^2 K/\kappa^3 = 1.5$, $\alpha_2/\kappa = 0$, and $\xi = 0$.

unique herald state in A . If the measurement of the ancillary subsystem A yields the outcome corresponding to this herald state, the joint state of S and A has collapsed such that the desired target state is realized in S . Our approach differs from these heralding protocols in the following two points. First, it does not require an ancillary system but instead it directly observes the leaky cavity that is going to host the target state $\hat{\rho}_{\text{ps}}$. Second, it does not generate the target state by a collapse of the wave function, since the absence of a detection event is used as a herald. Instead, the target state $\hat{\rho}_{\text{ps}}$ is generated by an intrinsic relaxation process that is induced by the continuous measurement.

Conditions on the competing rates Γ_{rel} and Γ_{jump} to generate nonclassical states in a Kerr nonlinear oscillator will be discussed in more detail in Section 4.5. Before, we express the state $\hat{\rho}_{\text{ps}}$ and its associated relaxation rate Γ_{rel} in terms of the properties of the superoperators \mathcal{L} and \mathcal{N} .

4.4 Pseudosteady state and relaxation rate

4.4.1 Stochastic quantum master equation

In the following we require that the QME (4.1) has a steady-state solution $\hat{\rho}_{\text{ss}}$ and that the superoperator $\mathcal{L} + \mathcal{N}$ has a set of left and right eigenstates $\check{\rho}_\mu$ and $\hat{\rho}_\mu$, respectively,

which are defined by

$$(\mathcal{L} + \mathcal{N})\hat{\rho}_\mu = \lambda_\mu \hat{\rho}_\mu , \quad (4.11)$$

$$(\mathcal{L} + \mathcal{N})^\dagger \check{\rho}_\mu = \lambda_\mu^* \check{\rho}_\mu . \quad (4.12)$$

We assume that these eigenstates can be normalized to form a complete orthonormal basis with respect to the Hilbert-Schmidt scalar product,

$$(\check{\rho}_\nu, \hat{\rho}_\mu) = \text{Tr}(\check{\rho}_\nu^\dagger \hat{\rho}_\mu) = \delta_{\nu, \mu} , \quad (4.13)$$

which is a valid assumption for all systems that do not have exceptional points [Moiseyev, 2011]. A pseudosteady state of Equation (4.2) is a density matrix $\hat{\rho}$ that is Hermitian, positive semidefinite, normalized to unit trace, and that is a stable solution of the nonlinear equation

$$\bar{\mathcal{L}}\hat{\rho} = 0 . \quad (4.14)$$

In a first step, we now determine the solutions of Equation (4.14). Their stability will be discussed below. We decompose $\hat{\rho}$ with respect to the basis of eigenstates of $\mathcal{L} + \mathcal{N}$,

$$\hat{\rho} = \sum_{\mu} c_{\mu} \hat{\rho}_{\mu} , \quad (4.15)$$

where the expansion coefficients c_{μ} need to be determined. By construction, \mathcal{L} is a trace-preserving superoperator, *i.e.*, the condition $\text{Tr}(\mathcal{L}\hat{\rho}) = 0$ holds for any state $\hat{\rho}$. Taking the trace of Equation (4.11), we find the relation

$$\text{Tr}(\mathcal{N}\hat{\rho}_{\mu}) = \lambda_{\mu} \text{Tr}(\hat{\rho}_{\mu}) . \quad (4.16)$$

Calculating the Hilbert-Schmidt product of $\bar{\mathcal{L}}\hat{\rho} = 0$ with respect to all left eigenstates $\check{\rho}_{\nu}$ and using Equation (4.16), we obtain the following set of conditions for the expansion coefficients c_{μ} :

$$\forall \mu : \quad c_{\mu} \left[\lambda_{\mu} - \sum_{\beta} c_{\beta} \lambda_{\beta} \text{Tr}(\hat{\rho}_{\beta}) \right] = 0 . \quad (4.17)$$

For a nondegenerate eigenvalue λ_{μ} , all expansion coefficients must be zero except for the coefficient c_{μ} of the corresponding eigenstate $\hat{\rho}_{\mu}$. Consequently, each eigenstate $\hat{\rho}_{\mu}$ to a nondegenerate eigenvalue λ_{μ} is a solution of Equation (4.14) provided that it is Hermitian, positive semidefinite, and has nonzero trace such that it can be normalized by choosing $c_{\mu} = 1/\text{Tr}(\hat{\rho}_{\mu})$,

$$\hat{\rho} = c_{\mu} \hat{\rho}_{\mu} = \frac{\hat{\rho}_{\mu}}{\text{Tr}(\hat{\rho}_{\mu})} .$$

For a N -fold degenerate eigenvalue $\lambda = \lambda_{\mu_1} = \lambda_{\mu_2} = \dots = \lambda_{\mu_N}$, all but the coefficients c_{μ_i} belonging to the degenerate subspace $\{\lambda_{\mu_1}, \dots, \lambda_{\mu_N}\}$ are zero. Any statistical mixture of the eigenstates in the degenerate subspace,

$$\hat{\rho} = \sum_{j=1}^N c_{\mu_j} \hat{\rho}_{\mu_j} ,$$

is a solution of Equation (4.14) provided that it describes a Hermitian and positive semidefinite density matrix that is normalized to unit trace, $\sum_{j=1}^N c_{\mu_j} \text{Tr}(\hat{\rho}_{\mu_j}) = 1$.

Since $\bar{\mathcal{L}}$ is a nonlinear superoperator, some of the solutions to $\bar{\mathcal{L}}\hat{\rho} = 0$ may be unstable against perturbations. To analyze the stability of a solution $\hat{\rho}$ to eigenvalue λ , we perform a linear stability analysis [Strogatz, 2015] and make the ansatz

$$\hat{\chi} = (\hat{\rho} + \varepsilon\hat{\sigma})[1 - \varepsilon\text{Tr}(\hat{\sigma})] , \quad (4.18)$$

where $\varepsilon \ll 1$ is a small parameter and $\hat{\sigma}$ is a Hermitian and positive-semidefinite density matrix that is orthogonal to $\hat{\rho}$. Note that $\hat{\chi}$ is normalized to leading order in ε . The projectors on the state $\hat{\rho}$ and the subspace orthogonal to $\hat{\rho}$ are given by

$$\mathcal{P}_{\hat{\rho}} = \hat{\rho}\text{Tr}(\hat{\rho}^\dagger \cdot) , \quad (4.19)$$

$$\mathcal{P}_{\perp\hat{\rho}} = \mathbb{1} - \mathcal{P}_{\hat{\rho}} , \quad (4.20)$$

respectively. The suitably normalized left state $\check{\rho}$ associated with the state $\hat{\rho}$ given in Equation (4.15) is

$$\check{\rho} = \frac{\sum_{\mu} c_{\mu} \check{\rho}_{\mu}}{\sum_{\beta} |c_{\beta}|^2} .$$

We now expand $\hat{\chi} = \bar{\mathcal{L}}\hat{\chi}$ in powers of ε . The first-order terms give rise to the condition

$$\frac{d}{dt}\hat{\sigma} - \hat{\rho}\text{Tr}\left(\frac{d}{dt}\hat{\sigma}\right) = (\mathcal{L} + \mathcal{N})\hat{\sigma} - \text{Tr}(\mathcal{N}\hat{\sigma})\hat{\rho} - \lambda\hat{\sigma} + \lambda\text{Tr}(\hat{\sigma})\hat{\rho} . \quad (4.21)$$

Since $\hat{\sigma}$ must be orthogonal to $\hat{\rho}$, we project Equation (4.21) on the subspace perpendicular to $\hat{\rho}$ using the projector $\mathcal{P}_{\perp\hat{\rho}}$ and we decompose the perturbation $\hat{\sigma}$ with respect to the basis of eigenstates of $\mathcal{L} + \mathcal{N}$ as follows:

$$\hat{\sigma} = \mathcal{P}_{\perp\hat{\rho}} \sum_{\mu} d_{\mu} \hat{\rho}_{\mu} . \quad (4.22)$$

In this way, we obtain the following condition for the expansion coefficients d_{μ} ,

$$\sum_{\mu} \dot{d}_{\mu} \mathcal{P}_{\perp\hat{\rho}} \hat{\rho}_{\mu} = \sum_{\mu} d_{\mu} (\lambda_{\mu} - \lambda) \mathcal{P}_{\perp\hat{\rho}} \hat{\rho}_{\mu} . \quad (4.23)$$

The state $\hat{\rho}$ is stable if all expansion coefficients d_{μ} of perturbations orthogonal to $\hat{\rho}$ decay to zero. The overall relaxation rate is dominated by the contribution $\mathcal{P}_{\perp\hat{\rho}} \hat{\rho}_{\mu}$ with the slowest decay rate.

For a nondegenerate spectrum $\{\lambda_{\mu}\}$, we can simplify Equation (4.23) further. In this case, each solution $\hat{\rho}$ of Equation (4.14) is an eigenstate $\hat{\rho}_{\alpha}$ of $\mathcal{L} + \mathcal{N}$ to eigenvalue $\lambda = \lambda_{\alpha}$ and we can rewrite Equation (4.23) to

$$\forall \mu \neq \alpha : \quad \frac{d}{dt} d_{\mu} = (\lambda_{\mu} - \lambda) d_{\mu} .$$

Hence, the state $\hat{\rho} = \hat{\rho}_{\alpha}$ is stable if $\text{Re}(\lambda_{\mu} - \lambda) \leq 0$ holds for all $\mu \neq \alpha$, *i.e.*, if $\lambda = \lambda_{\alpha}$ is the eigenvalue of the spectrum with the largest real part. The decay rate of a state $\hat{\rho}_{\mu}$ towards $\hat{\rho}$ is given by $\Gamma_{\text{rel}\mu \rightarrow \alpha} = -\text{Re}(\lambda_{\mu} - \lambda_{\alpha})$, which is the real part of the spectral gap between the two eigenstates. The relaxation rate is dominated by smallest decay

rate, *i.e.*,

$$\Gamma_{\text{rel}} = \min_{\mu \neq \alpha} \text{Re}(\lambda_\alpha - \lambda_\mu) .$$

4.4.2 Stochastic Schrödinger equation

In the limit of perfect detection efficiency, $\eta = 1$, and zero temperature, $n_{\text{th}} = 0$, and if the superoperator \mathcal{L}_0 in Equation (4.1) describes only unitary dynamics, as given in Equation (4.7), the photon counting measurement can be modeled by the SSE

$$d|\psi\rangle = \mathcal{H}|\psi\rangle dt + \left[\frac{(\hat{a} + \xi)|\psi\rangle}{\sqrt{\langle\psi|(\hat{a}^\dagger + \xi^*)(\hat{a} + \xi)|\psi\rangle}} - |\psi\rangle \right] dN , \quad (4.24)$$

$$\mathcal{H}|\psi\rangle = \left[-\frac{i}{\hbar} \left(\hat{H} - i\hbar\hat{M} \right) + \langle\psi|\hat{M}|\psi\rangle \right] |\psi\rangle , \quad (4.25)$$

where the continuous time evolution is given by the nonlinear operator \mathcal{H} . It is characterized by the non-Hermitian Hamiltonian $\hat{H} - i\hbar\hat{M}$ composed of the Hermitian operators

$$\begin{aligned} \hat{H} &= \hat{H}_0 - i\hbar\frac{\kappa}{2} \left(\xi^*\hat{a} - \xi\hat{a}^\dagger \right) , \\ \hat{M} &= \frac{\kappa}{2} (\hat{a}^\dagger + \xi^*)(\hat{a} + \xi) . \end{aligned}$$

As derived in Section 2.2.2, $dN \in \{0, 1\}$ is a Poissonian increment with an ensemble-averaged expectation value

$$\mathbb{E}[dN] = \langle\psi| \left(\hat{M} + \hat{M}^\dagger \right) |\psi\rangle dt .$$

We now derive the pseudosteady states of the SSE (4.24). These are normalized quantum states $|\psi\rangle$ that are stable stationary solutions of the nonlinear equation

$$\frac{d}{dt} |\psi\rangle = \mathcal{H} |\psi\rangle . \quad (4.26)$$

A stationary solution $|\psi(t)\rangle = e^{-iE_\psi t/\hbar} |\psi(0)\rangle$ characterized by a real energy E_ψ can actually exist because the decay of the norm of $|\psi\rangle$ due to the non-Hermitian term $-i\hbar\hat{M}$ in Equation (4.25) is compensated by the nonlinear term $\langle\psi|\hat{M}|\psi\rangle$. Inserting the ansatz for a stationary solution into Equation (4.26), we find the following nonlinear equation for $|\psi\rangle = |\psi(0)\rangle$.

$$-\frac{i}{\hbar} E_\psi |\psi\rangle = \mathcal{H} |\psi\rangle . \quad (4.27)$$

As for the case of a SME discussed in Section 4.4.1, we assume that the QME (4.1) has a steady-state solution $\hat{\rho}_{\text{ss}}$ and that the non-Hermitian Hamiltonian $\hat{H} - i\hbar\hat{M}$ has a set of left and right eigenstates

$$(\hat{H} - i\hbar\hat{M}) |\psi_\mu\rangle = h_\mu |\psi_\mu\rangle , \quad (4.28)$$

$$(\hat{H} - i\hbar\hat{M})^\dagger |\bar{\psi}_\mu\rangle = h_\mu^* |\bar{\psi}_\mu\rangle , \quad (4.29)$$

that form a complete orthonormal basis with respect to the scalar product

$$\langle \bar{\psi}_\mu | \psi_\nu \rangle = \delta_{\mu,\nu} .$$

We now decompose $|\psi\rangle$ with respect to this basis,

$$|\psi\rangle = \sum_{\mu} c_{\mu} |\psi_{\mu}\rangle . \quad (4.30)$$

Inserting this decomposition into Equation (4.27) and taking the scalar product with respect to all states $|\psi^{\nu}\rangle$, we obtain the following set of conditions for the expansion coefficients c_{μ} :

$$\forall \mu : \quad c_{\mu} \left[-\frac{i}{\hbar} (E_{\psi} - h_{\mu}) - \sum_{\beta,\gamma} c_{\beta}^* c_{\gamma} \langle \psi_{\beta} | \hat{M} | \psi_{\gamma} \rangle \right] = 0 . \quad (4.31)$$

For a nondegenerate eigenvalue h_{μ} , all expansion coefficients must be zero except for the coefficient c_{μ} of the corresponding eigenstate $|\psi_{\mu}\rangle$. Inserting this into Equation (4.31), we find that each normalized eigenstate $|\psi_{\mu}\rangle$ to a nondegenerate eigenvalue h_{μ} is a stationary solution of Equation (4.26) with real energy $E_{\psi_{\mu}} = \langle \psi_{\mu} | \hat{H} | \psi_{\mu} \rangle$,

$$|\psi\rangle = \frac{|\psi_{\mu}\rangle}{\sqrt{\langle \psi_{\mu} | \psi_{\mu} \rangle}} .$$

For a degenerate eigenvalue $h = h_{\nu_1} = \dots = h_{\nu_N}$, any normalized superposition $|\psi\rangle = \sum_{i=1}^N c_{\nu_i} |\psi_{\nu_i}\rangle$ of the eigenstates belonging to this degenerate subspace is a pseudosteady state with $E_{\psi} = \langle \psi | \hat{H} | \psi \rangle$.

Since \mathcal{H} is a nonlinear operator, some of the stationary solutions of Equation (4.27) may be unstable. To analyze the stability of a stationary state $|\psi\rangle$ with associated eigenvalue h , we make the ansatz

$$|\chi\rangle = e^{-iE_{\psi}t} (|\psi\rangle + \varepsilon |\sigma\rangle) [1 - \varepsilon \text{Re}(\langle \psi | \sigma \rangle)] , \quad (4.32)$$

where $\varepsilon \ll 1$ is a small parameter and $|\sigma\rangle$ is a state orthogonal to $|\psi\rangle$. Note that $|\chi\rangle$ is normalized to leading order in ε . We now expand $d|\chi\rangle/dt = \mathcal{H}|\chi\rangle$ in powers of ε . Projecting the first-order terms on the subspace perpendicular to $|\psi\rangle$ gives rise to the condition

$$\frac{d}{dt} \hat{P}_{\perp|\psi} |\sigma\rangle = -\frac{i}{\hbar} \left[\hat{P}_{\perp|\psi} (\hat{H} - i\hbar\hat{M}) \hat{P}_{\perp|\psi} - h \right] \hat{P}_{\perp|\psi} |\sigma\rangle ,$$

where the projectors $\hat{P}_{|\psi}\rangle$ and $\hat{P}_{\perp|\psi}\rangle$ on the subspace spanned by $|\psi\rangle$ and the orthogonal subspace, respectively, are defined by

$$\hat{P}_{|\psi}\rangle = |\psi\rangle \langle \bar{\psi}| , \quad (4.33)$$

$$\hat{P}_{\perp|\psi}\rangle = \hat{\mathbf{1}} - \hat{P}_{|\psi}\rangle . \quad (4.34)$$

The suitably normalized left state $|\bar{\psi}\rangle$ associated with the state $|\psi\rangle = \sum_{\mu} c_{\mu} |\psi_{\mu}\rangle$ is

$$|\bar{\psi}\rangle = \frac{\sum_{\mu} c_{\mu} |\bar{\psi}_{\mu}\rangle}{\sum_{\nu} |c_{\nu}|^2} .$$

Again, we decompose with respect to the basis of eigenstates $|\psi_\mu\rangle$ of $\hat{H} - i\hbar\hat{M}$,

$$|\sigma\rangle = \sum_{\mu} d_{\mu} |\psi_{\mu}\rangle , \quad (4.35)$$

and we obtain the condition

$$\sum_{\mu} \dot{d}_{\mu} \hat{P}_{\perp} |\psi_{\mu}\rangle = -\frac{i}{\hbar} \sum_{\mu} d_{\mu} (h_{\mu} - h) \hat{P}_{\perp} |\psi_{\mu}\rangle . \quad (4.36)$$

The state $|\psi\rangle$ is stable if all expansion coefficients c_{μ} associated with perturbations orthogonal to $|\psi\rangle$ decay to zero.

Recall that for a non-degenerate spectrum $\{h_{\mu}\}$, the pseudosteady state $|\psi\rangle = |\psi_{\alpha}\rangle$ is an eigenstate of $\hat{H} - i\hat{M}$ to eigenvalue $h = h_{\alpha}$. Therefore, we can rewrite Equation (4.36) to

$$\forall \mu \neq \alpha : \quad \frac{d}{dt} d_{\mu} = -\frac{i}{\hbar} (h_{\mu} - h) d_{\mu} . \quad (4.37)$$

Hence, the state $|\psi\rangle = |\psi_{\alpha}\rangle$ is stable if $\text{Im}(h_{\mu} - h) \leq 0$ holds for all $\mu \neq \alpha$, *i.e.*, if $h = h_{\alpha}$ is the eigenvalue of the spectrum with the largest imaginary part. The decay rate of any state $|\psi_{\mu}\rangle$ towards $|\psi\rangle$ is given by $\Gamma_{\text{rel}\mu \rightarrow \alpha} = -\text{Im}(h_{\mu} - h_{\alpha})/\hbar = \langle \psi_{\mu} | \hat{M} | \psi_{\mu} \rangle - \langle \psi_{\alpha} | \hat{M} | \psi_{\alpha} \rangle$, which is the imaginary part of the spectral gap between the two eigenstates $|\psi_{\mu}\rangle$ and $|\psi_{\alpha}\rangle$. The overall relaxation rate is dominated by the smallest decay rate,

$$\Gamma_{\text{rel}} = \min_{\mu \neq \alpha} \frac{\text{Im}(h_{\alpha} - h_{\mu})}{\hbar} .$$

Thus, for a non-degenerate spectrum $\{h_{\mu}\}$ there is only one stable pseudosteady state $|\psi\rangle_{\text{ps}}$ and the relaxation rate is determined by the smallest imaginary gap between this stable pseudosteady state and the unstable eigenstates of $\hat{H} - i\hbar\hat{M}$. This is shown in Figure 4.2(c) for a Kerr oscillator subjected to a harmonic drive.

4.5 Nonclassical states in a Kerr oscillator

In this section, we illustrate the state preparation protocol introduced in Section 4.3 by applying it to a driven and damped Kerr oscillator, introduced in Section 2.5. In a first step, we will concentrate on the limit of perfect detection efficiency, $\eta = 1$, and zero temperature, $n_{\text{th}} = 0$. Therefore, we will use the description of the photon-counting process in terms of a SSE, introduced in Section 4.4.2. The more general case will be discussed in Section 4.6.

Our goal is to generate nonclassical pseudosteady states. The state $\hat{\rho}$ of a quantum system can be represented by its Wigner function

$$\mathcal{W}_{\hat{\rho}}(\alpha) = \frac{2}{\pi} \text{Tr} \left[\hat{\rho} \hat{D}(\alpha) \hat{\Pi} \hat{D}^{\dagger}(\alpha) \right] ,$$

which has been introduced in Section 2.3. The Wigner function is a quasi-probability distribution in phase space and negative values of $\mathcal{W}_{\hat{\rho}}(\alpha)$ indicate a nonclassical state [Gerry and Knight, 2005; Zurek, 2003]. In the following, we will show that the pseudosteady state $\hat{\rho}_{\text{ps}}$ of a Kerr oscillator can have a negative Wigner function $\mathcal{W}_{\hat{\rho}}(\alpha)$,

whereas the steady-state Wigner function $\mathcal{W}_{\hat{\rho}_{\text{ss}}}(\alpha)$ has been proven to be strictly positive [Kheruntsyan *et al.*, 1996; Kheruntsyan, 1999; Bartolo *et al.*, 2016]. As a single-number measure of negativity, we use the modulus of the minimum of the Wigner function,

$$N(\hat{\rho}) = \left| \min_{\alpha} [\mathcal{W}_{\hat{\rho}}(\alpha)] \right|, \quad (4.38)$$

which is non-zero if $\mathcal{W}_{\hat{\rho}}(\alpha)$ has negative values and zero otherwise.

Adding a nonlinearity to the system, for instance via the Kerr term in \hat{H}_0 , is a necessary condition to create nonclassical states. Without nonlinearity, all terms in Equation (4.3) are at most quadratic in $\hat{a}^{(\dagger)}$ and can only give rise to states with strictly positive Wigner functions if the initial state is Gaussian [Gardiner and Zoller, 2000]. Note that having a nonlinearity is not a sufficient condition for nonclassicality since the steady state of a Kerr oscillator subjected to harmonic and parametric drives always has a strictly positive Wigner function despite its intrinsic nonlinearity.

4.5.1 Harmonic drive

In this section, we assume that only a harmonic drive is applied to the Kerr oscillator, $\alpha_1 \geq 0$ and $\alpha_2 = 0$. In this case, the steady-state solution is characterized by the dimensionless detuning Δ/κ , the rescaled drive power $|\alpha_1|^2 K/\kappa^3$, and the ratio K/κ [Meaney *et al.*, 2014], as discussed in Section 2.5.1. In Figure 4.3(a), we plot the scaling of the jump rate Γ_{jump} , the relaxation rate Γ_{rel} , and the negativity $N(|\psi\rangle_{\text{ps}})$ as a function of the ratio K/κ for fixed values of the dimensionless detuning and the rescaled drive power, and for $\xi = 0$.

In the limit $K \gg \kappa$, we find that the relaxation rate converges to a constant value, the jump rate decreases inversely proportional to K/κ , and the negativity decays to zero. These results can be understood as follows. If the relaxation towards $|\psi\rangle_{\text{ps}}$ is much faster than the typical interval between quantum jump events kicking the system out of the pseudosteady state, $\Gamma_{\text{rel}} \gg \Gamma_{\text{jump}}$, the system will be in the pseudosteady state almost all the time along every quantum trajectory. Since an ensemble average over many quantum trajectories must reproduce the unconditional steady state, the pseudosteady state must converge to the unconditional steady state in the limit $K \gg \kappa$. Consequently, the negativity converges to zero since the unconditional steady state of a Kerr oscillator has a classical Wigner function, $N(\hat{\rho}_{\text{ss}}) = 0$.

The relaxation rate Γ_{rel} is determined by the imaginary part of the spectrum, $-\hbar\langle\hat{M}\rangle = -\kappa\langle\hat{a}^\dagger\hat{a}\rangle/2$, which represents the photon-number expectation values of the eigenstates of the non-Hermitian Hamiltonian $\hat{H}_0 - i\hbar M$. In the limit $K \gg \kappa$, the non-Hermitian Hamiltonian is dominated by the Kerr term and its eigenstates converge to Fock states. The smallest spectral gap is determined by the difference of the Fock states $|0\rangle$ and $|1\rangle$, *i.e.*, it is constant,

$$\frac{\Gamma_{\text{rel}}}{\kappa} \rightarrow \frac{1}{2}.$$

In particular, we find $|\psi\rangle_{\text{ps}} \rightarrow |0\rangle$ and $\hat{\rho}_{\text{ss}} \rightarrow |0\rangle\langle 0|$ in the limit $K \gg \kappa$, as motivated above by the argument based on the ensemble-average over quantum trajectories.

The scaling of Γ_{jump} with κ/K reflects the properties of the semiclassical solution of the driven and damped Kerr oscillator, discussed in Section 2.5: The semiclassical steady-state photon number $|\alpha_{\text{ss}}|^2$ scales proportional to κ/K , see Equation (2.85). Up to corrections due to the shape and spread of the Wigner function in phase space, the same scaling must apply to the quantum-mechanical photon-number expectation

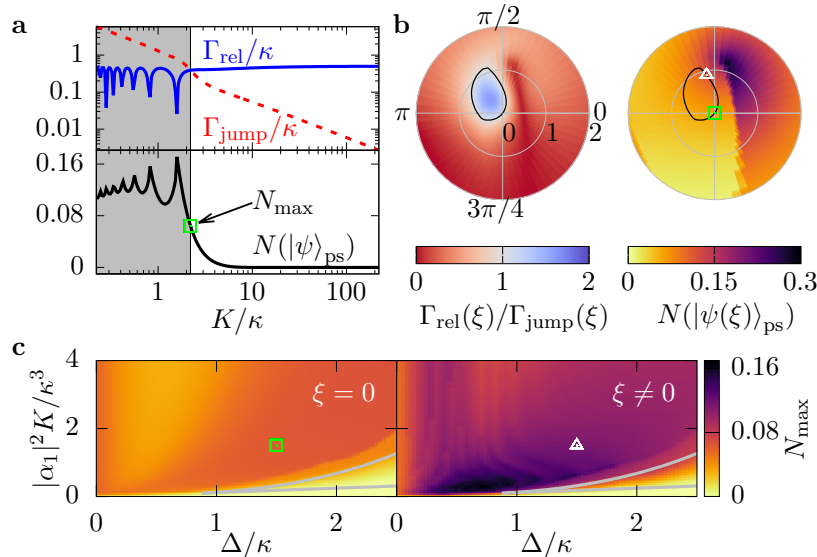


FIGURE 4.3: **(a)** Relaxation rate Γ_{rel} towards the pseudosteady state $|\psi\rangle_{\text{ps}}$ (solid blue), jump rate Γ_{jump} (dotted red), and negativity of the Wigner function (solid black) for a Kerr oscillator subject to a harmonic drive, a dimensionless detuning $\Delta/\kappa = 1.5$, and a rescaled drive power $|\alpha_1|^2 K/\kappa^3 = 1.5$. In the area highlighted in gray, the quantum trajectory is dominated by stochastic quantum jump events, $\Gamma_{\text{jump}} \geq \Gamma_{\text{rel}}$, and $|\psi\rangle_{\text{ps}}$ cannot be prepared. The open green rectangle indicates the maximum observable negativity N_{max} and the parameters of Figure 4.2. **(b)** Adding a LO signal $\sqrt{\kappa}\xi$ allows one to unravel different pseudosteady states. The ratio $\Gamma_{\text{rel}}(\xi)/\Gamma_{\text{jump}}(\xi)$ (left plot) and the negativity $N(|\psi(\xi)\rangle_{\text{ps}})$ (right plot) now depend on the complex LO signal ξ . All states within the black curve indicating $\Gamma_{\text{rel}}(\xi)/\Gamma_{\text{jump}}(\xi) = 1$ can be prepared in a heralded way. The value of ξ indicated by an open white triangle maximizes $N(|\psi(\xi)\rangle_{\text{ps}})$ under this constraint. **(c)** Maximum observable negativity N_{max} as a function of dimensionless detuning and rescaled drive power without (left) and with (right) an optimization of the LO signal ξ . In the triangle enclosed by the gray lines, two semiclassical steady-state solutions α_{ss} exist as discussed in Section 2.5.1.

value, $\langle \hat{a}^\dagger \hat{a} \rangle \approx |\alpha_{\text{ss}}|^2 \propto \kappa/K$. Therefore, the jump rate scales inversely proportional to the Kerr nonlinearity,

$$\frac{\Gamma_{\text{jump}}}{\kappa} \propto \frac{\kappa}{K}.$$

This result shows that for $K \gtrsim \kappa$, relaxation rate and jump rate will become comparable, $\Gamma_{\text{rel}} \gtrsim \Gamma_{\text{jump}}$. In this regime, the pseudosteady state differs from $\hat{\rho}_{\text{ss}}$ and can be nonclassical, as shown in Figure 4.3(a). Quantum jumps let each quantum trajectory explore many different states $|\psi\rangle(t)$ which compensate negative values of $\mathcal{W}_{|\psi\rangle_{\text{ps}}}(\alpha)$ and ensure that an ensemble average still reproduces a strictly positive steady-state Wigner function $\mathcal{W}_{\hat{\rho}_{\text{ss}}}(\alpha)$. Since Γ_{rel} is comparable to or larger than the jump rate Γ_{jump} , relaxation processes towards $|\psi_{\text{ps}}\rangle$ are possible between successive quantum jumps.

This is no longer the case in the limit $K \ll \kappa$, when the quantum trajectory is dominated by stochastic quantum jump events. The intervals between two quantum jumps are much shorter than the relaxation time, $\Gamma_{\text{jump}} \gg \Gamma_{\text{rel}}$, and the state $|\psi(t)\rangle$

can no longer relax to $|\psi\rangle_{\text{ps}}$. Considering this, we define the *maximum observable negativity* N_{max} as the maximum of $N(|\psi\rangle_{\text{ps}})$ in the regime $\Gamma_{\text{rel}} \geq \Gamma_{\text{jump}}$. The left subplot of Figure 4.3(c) displays N_{max} as a function of the dimensionless detuning and the rescaled drive power. Usually, the negativity $N(|\psi\rangle_{\text{ps}})$ decreases monotonically as a function of K/κ , such that the maximum observable negativity N_{max} is achieved for $\Gamma_{\text{rel}} = \Gamma_{\text{jump}}$. However, in the regime where two stable semiclassical solutions exist, which is enclosed by the gray lines in Figure 4.3(c), the largest negativity is observed for $\Gamma_{\text{rel}} > \Gamma_{\text{jump}}$.

4.5.2 Unraveling different pseudosteady states

As discussed in Section 2.2.3, the procedure of unraveling a quantum master equation is not unique [Wiseman and Milburn, 2009]. Consequently, the operator \mathcal{H} is not uniquely defined and many different pseudosteady states $|\psi\rangle_{\text{ps}}$ can be stabilized to a given steady-state solution $\hat{\rho}_{\text{ss}}$. This gives us a turning knob to tune the pseudosteady state and its negativity by modifying the way how the system is continuously monitored. To illustrate this point, we now consider the homodyne detection setup shown in Figure 4.1(b). A beam splitter is placed between the system and the photon detector, such that a LO signal $\sqrt{\kappa(n_{\text{th}} + 1)}\eta\xi$ is added to the system's output. Combining Equations (4.6) and (4.9), we find that the jump rate depends on ξ ,

$$\Gamma_{\text{jump}}(\xi) = \kappa(n_{\text{th}} + 1)\eta \left\langle (\hat{a}^\dagger + \xi^*)(\hat{a} + \xi) \right\rangle_{\text{ss}} .$$

The SME (4.2) in the case $\xi \neq 0$ can be rewritten as a SME of a pure photon-counting measurement ($\xi' = 0$) in a displaced frame

$$|\psi'\rangle = \hat{D}(\xi) |\psi\rangle \quad (4.39)$$

with a modified Hamiltonian

$$\hat{H}'_0(\xi) = \hat{D}(\xi)\hat{H}_0\hat{D}^\dagger(\xi) - i\hbar\frac{\kappa}{2}(\xi^*\hat{a} - \xi\hat{a}^\dagger) .$$

Thus, displacing the output mode \hat{a} also modifies the Hamiltonian and, therefore, the relaxation rate $\Gamma_{\text{rel}}(\xi)$. The ratio $\Gamma_{\text{rel}}(\xi)/\Gamma_{\text{jump}}(\xi)$ as a function of the LO signal in the limit $n_{\text{th}} \rightarrow 0$ and $\eta \rightarrow 1$ is shown in Figure 4.3(b).

In contrast to the standard homodyne detection limit $|\xi| \gg \langle \hat{a} \rangle$, where the LO signal dominates and the quantum trajectory is a continuous Wiener process [Wiseman and Milburn, 2009], we consider the opposite limit $|\xi| \lesssim \langle \hat{a} \rangle$, such that the detection of photons is still a Poissonian quantum jump process. Moreover, a state $|\psi(\xi)\rangle_{\text{ps}}$ can only be prepared if $\Gamma_{\text{rel}} \leq \Gamma_{\text{jump}}$ holds, which restricts ξ to the area inside the black curve in Figure 4.3(b). Nevertheless, an optimization of the LO signal ξ under these constraints significantly increases the maximum observable negativity N_{max} over the case of $\xi = 0$, as shown in the right subplot of Figure 4.3(c).

Note that our protocol reveals that the unbalanced and balanced homodyne detection schemes introduced in Sections 2.2.3 and 2.2.4, respectively, differ if the LO signal ξ is small. Only in the limit of a strong LO signal, $|\xi|^2 \gg \langle \hat{a}^\dagger \hat{a} \rangle$, both detection schemes give rise to the same SME (2.36) describing a continuous Wiener process. While the overall detection signal is proportional to a field quadrature of $\hat{\rho}$ independent of the value of $|\xi|$, the SMEs (2.25) and (2.39) approximating homodyne detection as a photon-counting process are actually different. In particular, except for an irrelevant constant factor $|\xi|^2$ in the superoperator \mathcal{N} , the nonlinear continuous time evolution $\bar{\mathcal{L}}\hat{\rho} = (\mathcal{L} + \mathcal{N})\hat{\rho} - \text{Tr}(\mathcal{N}\hat{\rho})\hat{\rho}$ for balanced homodyne detection, defined

by Equations (2.40) and (2.41), is identical to the corresponding result obtained for photon counting without any displacement of the mode, defined by Equations (2.26) and (2.27) for $\xi = 0$. This implies, that displacing the mode \hat{a} before detection is only useful if an asymmetric beam splitter with a transmittivity larger than 50 % is used.

4.5.3 Parametric drive

Our protocol can be used to stabilize small Schrödinger cat states in a Kerr oscillator without the need for feedback [Minganti *et al.*, 2016]. To demonstrate this, we consider a resonant parametric drive, *i.e.*, $\Delta = 0$, $\alpha_1 = 0$, and $\alpha_2 \geq 0$. Again, we focus on the case $\eta = 1$ and $n_{\text{th}} = 0$, and we set $\xi = 0$. For these parameters, the non-Hermitian Hamiltonian $\hat{H}_0 - i\hbar\hat{M}$ commutes with the parity operator $\hat{\Pi}$, defined in Equation (2.49). Thus, the spectrum consists of two subspaces of eigenstates having different parity, $\{h_\mu^\pm\}$. The operator \mathcal{H} preserves parity and does not mix these subspaces, therefore, both the even and the odd-parity eigenstate $|\psi_{\mu_0}^\pm\rangle$ with largest imaginary part of the eigenvalue $h_{\mu_0}^\pm$ are stable, as shown in Figure 4.4(a), and their relaxation rates are determined by the imaginary parts of the spectral gaps to the unstable eigenstates of the corresponding parity.

While we redefined here the relaxation rate Γ_{rel} to take into account parity conservation, the relevant quantity to be compared to Γ_{jump} in the heralding protocol is still the *first* spectral gap,

$$\Gamma_{\text{asy}} = \text{Im}(h_{\mu_0}^+ - h_{\mu_0}^-). \quad (4.40)$$

Photon detection events change the parity of the state $|\psi\rangle$ and approximately map the stable states $|\psi_{\mu_0}^\pm\rangle$ onto one another, such that the quantum trajectories jump between the two states, as shown in Figure 4.4(b). The rate Γ_{asy} measures the asymmetry in the jump rates of $|\psi_{\mu_0}^\pm\rangle$, which stems from their different photon-number expectation values. If $\Gamma_{\text{asy}} \geq \Gamma_{\text{jump}}$ holds, the states can be discriminated in the photon detection signal and the longer-lived state $|\psi_{\mu_0}^+\rangle$ can be prepared in a heralded way, *i.e.*, $|\psi\rangle_{\text{ps}} = |\psi_{\mu_0}^+\rangle$. The relaxation rate Γ_{rel} towards $|\psi\rangle_{\text{ps}}$ is given by the *second* spectral gap and determines the relaxation $\hat{a}|\psi_{\mu_0}^-\rangle \rightarrow |\psi_{\mu_0}^+\rangle$, as shown in Figure 4.4(c). Since $\Gamma_{\text{rel}} > \Gamma_{\text{asy}}$ holds, the relaxation to the target state within the heralding interval is guaranteed.

Similar to the case of a harmonic drive, Figure 4.4(d) shows that there is a trade-off between a large ratio $\Gamma_{\text{asy}}/\Gamma_{\text{jump}}$ and a large negativity $N(|\psi\rangle_{\text{ps}})$. Again, this is because the steady-state Wigner function $\mathcal{W}_{\hat{\rho}_{\text{ss}}}$ is strictly positive and the pseudosteady state converges to the unconditional steady state in the limit $\Gamma_{\text{asy}} \gg \Gamma_{\text{rel}}$. The negativity $N(|\psi\rangle_{\text{ps}})$ vanishes also in the limit $K/\kappa \rightarrow 0$, as shown in Figure 4.4, because in the absence of a Kerr nonlinearity the parametric drive will only create squeezed states with a strictly positive Wigner function.

Importantly, in the limit $K \gg \kappa$ the states $|\psi_{\mu_0}^\pm\rangle$ converge to the even and odd Schrödinger cat states $|\mathcal{C}_\pm\rangle$, introduced in Section 2.5.2,

$$|\mathcal{C}_\pm\rangle = \frac{|\alpha\rangle \pm |-\alpha\rangle}{\sqrt{2 \pm 2e^{-2|\alpha|^2}}},$$

where $\alpha = i\sqrt{\alpha_2/K}$. In this regime, the steady-state solution $\hat{\rho}_{\text{ss}}$ is a statistical mixture of the two indistinguishable cat states $|\mathcal{C}_\pm\rangle$ and has a strictly positive Wigner function. For $\alpha_2/K \lesssim 1/2$, the two cat states differ in their photon-number expectation values (2.92), such that the small correction $-i\hbar\hat{M} \propto \kappa\hat{a}^\dagger\hat{a}$ due to the

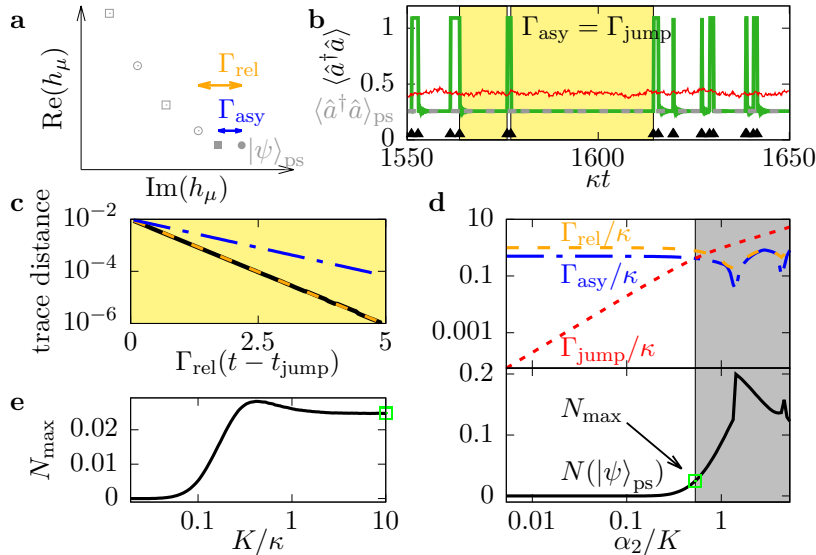


FIGURE 4.4: **(a)** Spectrum of even-parity (circles) and odd-parity (squares) stable (solid markers) and unstable (open markers) eigenstates of the non-Hermitian Hamiltonian that defines the relaxation dynamics for a Kerr oscillator subject to a resonant parametric drive. The imaginary part of the gap between the two stable states determines their jump-rate asymmetry Γ_{asy} . **(b)** Photon-number $\langle \hat{a}^\dagger \hat{a} \rangle$ in the steady-state regime. An average over 500 trajectories reproduces the steady-state result (thin red), which determines the jump rate Γ_{jump} . Each quantum trajectory (solid green line) jumps between the stable states of opposite parity (jump times indicated by black triangles). If $\Gamma_{\text{asy}} \gtrsim \Gamma_{\text{jump}}$ holds, one can prepare the stable even-parity eigenstate $|\psi\rangle_{\text{ps}}$ in a heralded way. **(c)** After a quantum jump event, the trace distance between $|\psi(t)\rangle$ and $|\psi\rangle_{\text{ps}}$ (solid black) decays exponentially. Since parity is conserved, the relaxation happens at a rate Γ_{rel} (dashed orange), which is the imaginary part of the second spectral gap. For comparison, the dash-dotted blue line indicates a decay at the rate Γ_{asy} corresponding to the first spectral gap. **(d)** Relaxation rate Γ_{rel} (dashed orange), jump-rate asymmetry Γ_{asy} (dash-dotted blue), total jump rate Γ_{jump} (dashed red), and Wigner-function negativity (solid black) as a function of the drive strength. In the gray area, the time evolution is dominated by stochastic quantum jumps, $\Gamma_{\text{jump}} \geq \Gamma_{\text{asy}}$, and $|\psi\rangle_{\text{ps}}$ cannot be prepared. **(e)** Maximum observable negativity as a function of the dimensionless Kerr nonlinearity K/κ . Parameters: $\Delta/\kappa = 0$, $K/\kappa = 10$, $\alpha_1/\kappa = 0$, $\alpha_2/\kappa = 5.3$, $\xi = 0$, $n_{\text{th}} = 0$, and $\eta = 1$.

photon detection breaks this symmetry and allows us to stabilize a small even-parity Schrödinger cat state $|\mathcal{C}_+\rangle = |\psi\rangle_{\text{ps}}$ without feedback. Since these states have a small size $|\alpha|^2 \leq 1$, they are called Schrödinger kitten states [Ourjoumtsev *et al.*, 2006].

4.6 Finite temperature and imperfect photon detection

In an experiment, the environment of the Kerr nonlinear oscillator has a finite temperature and it may emit photons into the dissipative quantum system. Moreover, current photon detectors have detection efficiencies of less than 100 % such that photons emitted by the Kerr oscillator may escape undetected. Both effects give rise to unmonitored dissipative processes that require us to go beyond the stochastic Schrödinger equation (4.24) that has been used so far in our numerical investigations. Instead, we must directly use the SME (4.2) for the density matrix $\hat{\rho}$.

In the limit $\mathcal{L}_0\hat{\rho} \rightarrow -i[\hat{H}_0, \hat{\rho}]/\hbar$, $n_{\text{th}} \rightarrow 0$, and $\eta \rightarrow 1$, the stochastic Schrödinger equation (4.24) and the stochastic quantum master equation (4.2) can be mapped onto one another. The right eigenstates $|\psi_j\rangle$ of $\hat{H} - i\hbar\hat{M}$, defined in Equation (4.28), can be used to construct the right eigenstates $\hat{\rho}_\mu = \hat{\rho}_{i,j} = |\psi_i\rangle\langle\psi_j|$ of $\mathcal{L} + \mathcal{N}$, defined in Equation (4.11). The associated eigenvalues fulfill $\lambda_\mu = \lambda_{i,j} = -i(h_i - h_j^*)$. Brody and Graefe [2012] have shown that mixed stationary states can be constructed by convex combination of eigenstates $\hat{\rho}_{j,j}$ associated with real eigenvalues $\lambda_{j,j}$.

For finite temperature $n_{\text{th}} > 0$, imperfect detection efficiency $0 \leq \eta < 1$, or additional dissipation channels in \mathcal{L}_0 , this one-to-one relation between the SSE and the SME breaks down because the Lindblad dissipators contained in \mathcal{L} in Equation (4.4) mix different basis states $\hat{\rho}_{i,j}$. Note that non-Hermitian states $\hat{\rho}_{i,j \neq i}$ are never mixed with Hermitian states $\hat{\rho}_{i,i}$ since, by construction of the superoperators \mathcal{L} and \mathcal{N} , the condition

$$[(\mathcal{L} + \mathcal{N})\hat{\rho}]^\dagger = (\mathcal{L} + \mathcal{N})\hat{\rho}^\dagger$$

holds. Therefore, $\overline{\mathcal{L}}\hat{\rho}$ preserves the Hermiticity of an initial Hermitian state $\hat{\rho}$. Moreover, the eigenvalues $\lambda_{i,j}$ are either real if $\hat{\rho}_{i,i}$ is a Hermitian eigenstate, or they form pairs of complex conjugate eigenvalues $\lambda_{i,j \neq i} = \lambda_{j \neq i,i}^*$ if they are associated with non-Hermitian eigenstates $\hat{\rho}_{i,j}$ and $\hat{\rho}_{j,i}$. The Wigner function $\mathcal{W}_{\hat{\rho}}$ of a statistical mixture ρ of states $\hat{\rho}_{i,i}$ is an average over the Wigner functions $\mathcal{W}_{\hat{\rho}_{i,i}}$ of the individual states contained in the mixture. Therefore, negativities that may be present in the individual Wigner functions $\mathcal{W}_{\hat{\rho}_{i,i}}$ are ultimately averaged out to a non-negative pseudosteady-state Wigner function in the limits $\eta \rightarrow 0$ or $n_{\text{th}} \rightarrow \infty$.

A numerical evaluation of the minimum of the pseudosteady-state Wigner function, $\min_\alpha[\mathcal{W}_{\hat{\rho}_{\text{ps}}}(\alpha)] = -N(\hat{\rho}_{\text{ps}})$ for finite temperature or imperfect photon detection is shown in Figure 4.5. Note that imperfect photon detection both includes a loss of photons on the way to the detector and a detection efficiency less than unity at the detector itself. Thermal effects average out the negativity at a thermal photon number of about $n_{\text{th}} \approx 0.1$. Hence, negative Wigner functions can be observed in the optical frequency range, but pre-cooling or cryogenic environments are necessary for microwave-frequency setups.

Importantly, Figure 4.5 demonstrates that imperfect photon detection is not a major challenge. Even for a relatively low detection efficiency of $\eta \approx 0.25$ for a harmonic drive and $\eta \approx 0.5$ for a parametric drive, negativities in the Wigner function are still present. Thus, current photon detection efficiencies in the optical and infrared range of above 88% are promising to resolve nonclassical states [Takeuchi *et al.*, 1999; Fukuda *et al.*, 2011]. The single-photon detection efficiency in the microwave regime

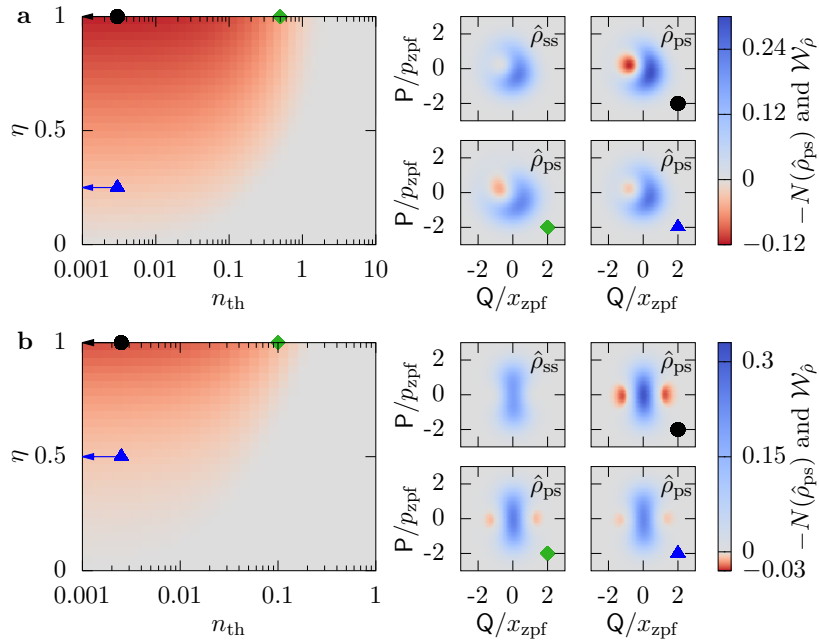


FIGURE 4.5: **(a)** Impact of finite temperature or imperfect detection on the pseudosteady state of a Kerr oscillator subject to a harmonic drive. The main plot shows the minimum of the Wigner function as a function of the thermal photon number n_{th} and the detection efficiency η . The smaller plots show the Wigner function $W_{\hat{\rho}}(\alpha)$ of selected states. The origin has been shifted to the respective steady-state expectation value $\langle \hat{a} \rangle_{\text{ss}}$. Top row: Wigner function of steady-state $\hat{\rho}_{\text{ss}}$ and pseudosteady state $\hat{\rho}_{\text{ps}}$ for $n_{\text{th}} = 0$ and $\eta = 1$. Bottom row: Wigner function of pseudosteady state $\hat{\rho}_{\text{ps}}$ for $n_{\text{th}} = 0.5$ and $\eta = 1$ (left) and $n_{\text{th}} = 0$ and $\eta = 0.25$ (right). Parameters are $\Delta/\kappa = 1.5$, $|\alpha_1|^2 K/\kappa^3 = 1.5$, $\alpha_2/\kappa = 0$, $K/\kappa = 2.2$, $\xi/\sqrt{\kappa} = 0.9 \times \exp(1.8i)$. **(b)** Same plots for a Kerr oscillator subject to a parametric drive. Top row: Wigner function of steady-state $\hat{\rho}_{\text{ss}}$ and pseudosteady state $\hat{\rho}_{\text{ps}}$ for $n_{\text{th}} = 0$ and $\eta = 1$. Bottom row: Wigner function of pseudosteady state for $n_{\text{th}} = 0.1$ and $\eta = 1$ (left) and $n_{\text{th}} = 0$ and $\eta = 0.5$ (right). Parameters are $\Delta/\kappa = 0$, $\alpha_1/\kappa = 0$, $\alpha_2/\kappa = 5.3$, $K/\kappa = 10$, $\xi = 0$.

is still lower [Munro *et al.*, 2005], but recently values exceeding 70% have been reached [Besse *et al.*, 2018; Kono *et al.*, 2018].

4.7 Experimental implementation

Our results demonstrate that quantum oscillators with Kerr nonlinearities of the order of the decay rate κ are sufficient to observe negative pseudosteady state Wigner functions. Such nonlinear resonators can be realized in a variety of platforms, *e.g.*, superconducting circuits [Rimberg *et al.*, 2014; Heikkilä *et al.*, 2014] and trapped ions [Zhao and Babikov, 2008; Home *et al.*, 2011]. Potentially, even hybrid optomechanical systems could reach the required nonlinearities [Jacobs and Landahl, 2009; Zhang *et al.*, 2015a; Rimberg *et al.*, 2014; Chu *et al.*, 2018]. To ensure $\Gamma_{\text{jump}} \lesssim \Gamma_{\text{rel}}$, the steady-state photon number needs to be small, $\langle \hat{a}^\dagger \hat{a} \rangle_{\text{ss}} \lesssim 1$.

A first step towards an experimental realization of our proposal is to demonstrate the nonclassicality of the pseudosteady state in a Wigner function tomography. Walentowitz and Vogel [1996] and Banaszek and Wódkiewicz [1996] described techniques how this measurement can be performed with minimal complexity using the existing

setup shown in Figure 4.1(b). Their protocols are based on the fact that the value of the Wigner function $\mathcal{W}(0)$ at the origin of phase space can be obtained by simple photon detection. A displacement of the mode prior to detection allows one to measure the Wigner function at different positions in phase space. A possible experiment will consist of repeated runs of data collection, each one measuring one pixel $\mathcal{W}(\alpha)$ of the Wigner function. Each run starts with a state preparation step as described in Section 4.3. When the generation of a nonclassical state is heralded, the tomography step begins and the LO signal is suddenly changed to displace the state and measure the Wigner function at the coordinate α .

Other ways to perform a Wigner function tomography have been demonstrated in experiments with superconducting circuits or trapped ions. There, one measures the interaction of an (artificial) atom with the nonclassical quantum state to reconstruct the Wigner function [Lougovski *et al.*, 2003; Hofheinz *et al.*, 2009; Shalibo *et al.*, 2013].

Having verified the nonclassicality of the pseudosteady state, the next experimental step is to extract and use it. Optomechanical systems are promising candidates for this task, because they allow one to perform on-demand state-swap operations between their modes [Aspelmeyer *et al.*, 2014]. An experimental protocol could consist of a state preparation step in an optical mode of the system, followed by a state swap to another mode if the presence of a nonclassical state is heralded. The properties of the target mode of the state swap can be tailored to the task one wishes to perform with the nonclassical state.

4.8 Summary

We have shown that continuous photon detection can stabilize nonclassical pseudosteady states in a driven and damped Kerr nonlinear oscillator, whose steady-state Wigner function is known to be strictly positive. The required nonlinearities and photon detection efficiencies are feasible with current technology. We have applied this effect to prepare Schrödinger kitten states in a Kerr parametric oscillator. Making use of the jump-rate asymmetry between the states of different parity, we demonstrated that observation is sufficient to stabilize such nonclassical states, even in the absence of feedback.

Viewed from a different angle, we have proposed a scheme of a heralding protocol to stabilize quantum states driven-dissipative nonlinear quantum systems. The main working principle is that the photon-counting measurement induces a continuous nonlinear time evolution between quantum jumps that relaxes the system towards a pseudosteady state.

The results and figures presented in this chapter have been published in parts in [Koppenhöfer *et al.*, 2020a].

Chapter 5

Quantum Synchronization

The results presented in this chapter have been published in:

M. Koppenhöfer and A. Roulet,
Optimal synchronization deep in the quantum regime: Resource and fundamental limit,
 Physical Review A **99**, 043804 (2019).

5.1 Motivation

Since the first observation reported by Huygens [1673] four centuries ago, synchronization [Pikovsky *et al.*, 2003] has provided a universal framework to capture features shared by very different complex systems, such as chaotic electronic circuits and biological neuron networks [Pecora and Carroll, 1990; Chagnac-Amitai and Connors, 1989; Ferrari *et al.*, 2015; Rodrigues *et al.*, 2016]. As introduced in Section 2.6, the essence of synchronization is the ability of a self-sustained oscillator to adjust its rhythm when subjected to a weak perturbation.

Recently, significant progress has been made in understanding whether quantum systems could synchronize as well. In particular, the van der Pol (vdP) oscillator, a classic self-sustained oscillator extensively used in biology [van der Pol and van der Mark, 1928; Rowat and Selverston, 1993; Jewett and Kronauer, 1998; Rompala *et al.*, 2007], has been investigated in the quantum regime of a few excitations. Lee and Sadeghpour [2013] as well as Walter *et al.* [2014] demonstrated that synchronization to a harmonic signal survives in this limit despite the inevitable presence of quantum noise. Since then, the quantum vdP oscillator has been used to probe various features of quantum synchronization [Weiss *et al.*, 2017], such as the role of the number-phase uncertainty [Davis-Tilley *et al.*, 2018] or the exciting possibility to enhance synchronization by applying a squeezing signal [Sonar *et al.*, 2018]. Yet, the infinite-dimensional Hilbert space combined with the intrinsic nonlinear and dissipative dynamics have limited studies to numerical explorations of parameter space, usually guided by an analytical description of the classical limit.

Addressing the challenge of understanding quantum synchronization beyond numerics, Roulet and Bruder [2018a] have recently identified a single spin 1 as the smallest quantum system that can host a limit-cycle oscillator. Its finite Hilbert space of dimension 3 has already proved useful to discuss analytically the relation between entanglement and quantum synchronization [Roulet and Bruder, 2018b]. Here, we develop an analytical framework to describe quantum synchronization, with the aim to understand the resources on which quantum synchronization relies, the role of quantum effects, and by which means synchronization can reach the fundamental limit imposed by the laws of quantum mechanics. We identify the coherences between

energy levels as the resource of quantum synchronization. As a consequence, we will be able to define an upper boundary of the synchronization region as a function of the signal strength, which extends the well-known Arnold tongue to a snake-like split tongue. Moreover, we will introduce a novel type of synchronization blockade due to quantum interference effects.

To put the spin-1 platform on solid grounds, the first question we address is whether this minimal system with no classical analogue is actually complex enough to capture all the features of quantum synchronization that appear in classically-inspired systems like the vdP oscillator. We answer this question by bridging the gap between the two architectures, demonstrating that a vdP oscillator operating deep in the quantum regime can be represented in the spin-1 platform, even though the spin phase space lives on a sphere and does not correspond to a position-momentum representation. This result allows us to connect with previous numerical findings obtained on the harmonic-oscillator platform, and to further improve on them thanks to the analytical accessibility of the spin-1 system. In particular, we find that, while squeezing indeed does improve the phase locking of a vdP limit cycle, an even better performance can be achieved by additionally modifying the semiclassical component of the signal, which is the equivalent of a harmonic drive for a spin system. We prove that this signal yields the optimal synchronization that is achievable for a vdP limit cycle.

We then move on to the equatorial limit cycle which was originally used to demonstrate phase locking to a semiclassical signal [Roulet and Bruder, 2018a]. Despite being insensitive to a squeezing signal, this pure-state limit cycle is shown to outperform the optimally-driven vdP oscillator, highlighting the complex interplay between the different quantum resources.

Finally, we take full advantage of the spin-1 Hilbert space and identify the maximum synchronization that can be achieved without imposing any limit cycle nor a specific form of the signal. This fundamental limit is shown to be an asymptotically strict bound that requires (i) a statistical mixture of energy eigenstates in the limit cycle, *i.e.*, a larger amplitude uncertainty than that of a pure state, and (ii) a breaking of the symmetry between the extremal spin eigenstates. Note that the related question of optimizing the signal to maximize the synchronization of a noisy classical limit cycle is also a subject of research in classical nonlinear dynamics [Pikovsky, 2015].

This chapter is structured as follows. In Section 5.2, we develop the framework to describe quantum synchronization, which will provide a consistent method to formalize how large the signal strength can be without becoming comparable to the stabilization of the limit cycle. We discuss in Section 5.3 how this result allows us to extend the notion of the Arnold tongue. Our framework prepares the ground to quantitatively compare the synchronization behavior of different limit-cycle oscillators. In Sections 5.4 and 5.5, we investigate the spin-1 implementations of the quantum vdP oscillator and of the equatorial limit cycle, respectively. This discussion will lead to a bound on the maximum synchronization that can be achieved in a spin-1 system, which is derived in Section 5.6. The effect of interference-based quantum synchronization blockade is discussed in Section 5.7. Finally, we discuss the prospects of an experimental observation of quantum synchronization in Section 5.8 and conclude in Section 5.9.

5.2 Framework

As introduced in Section 2.6.2, a limit-cycle oscillator is an autonomous active system, characterized by a free Hamiltonian \hat{H}_{sys} , that undergoes a stable periodic motion represented by a closed curve in phase space. The stability of this natural rhythm is ensured by the presence of amplitude-dependent gain and damping via a dissipative coupling to an environment. In contrast to a coherent drive, such a source of energy does not imprint any preferred phase on the oscillation. As a consequence, an external perturbation – the signal – can freely adjust the phase of the periodic motion without affecting the amplitude. This phenomenon is called synchronization. A discussion of classical synchronization including an overview of different synchronization phenomena has been given in Section 2.6.2.

We now develop a framework that generalizes the notion of synchronization to the quantum regime. We consider the synchronization of a limit-cycle oscillator to a coherent external signal of strength ε that is described by a Hamiltonian \hat{H}_{ext} . This scenario can be modeled by a QME of the form

$$\frac{d}{dt}\hat{\rho} = \mathcal{L}_0\hat{\rho} - \frac{i}{\hbar}\varepsilon \left[\hat{H}_{\text{ext}}, \hat{\rho} \right] , \quad (5.1)$$

where $\hat{\rho}$ is the density matrix of the system. The superoperator \mathcal{L}_0 defines the limit cycle of the system. We require that Equation (5.1) has a unique steady-state solution. This generic equation is the starting point for any study of synchronization of a single limit-cycle oscillator in the quantum regime. Actually, it also describes the synchronization of multiple oscillators under a mean-field approximation [Ludwig and Marquardt, 2013; Lee and Sadeghpour, 2013; Lee *et al.*, 2014]. Typically, Equation (5.1) is simulated numerically for a specific limit cycle and a specific signal, for instance, a quantum vdP limit cycle subject to a squeezing signal [Sonar *et al.*, 2018]. We will however leave \mathcal{L}_0 and \hat{H}_{ext} unspecified for now and instead derive some general properties that must be fulfilled by the QME (5.1) in order to describe a limit-cycle oscillator. In our examples, we will focus for simplicity on a spin-1 system. However, we stress that the methods we introduce in the rest of this section are not tied to this particular platform, but can be readily applied to limit-cycle oscillators living in a different phase space, *e.g.*, oscillator-based systems. An overview of the corresponding results for an oscillator-based system is given in Appendix B.

5.2.1 Phase space and phase variable

As a first step, we have to introduce the notion of a phase that parametrizes the dynamics of the limit-cycle oscillator. Following Roulet and Bruder [2018a], we employ the Husimi \mathcal{Q} -function, introduced in Section 2.3, as a phase portrait of the limit-cycle oscillator. The Husimi function exists both for oscillator-based systems, such as the quantum vdP oscillator, and for spin-based systems, see Section 2.3. In the case of a spin-1 system, it is defined as follows:

$$\mathcal{Q}_{\hat{\rho}}(\theta, \phi) = \frac{3}{4\pi} \langle \theta, \phi | \hat{\rho} | \theta, \phi \rangle ,$$

where the angles $\theta \in [0, \pi)$ and $\phi \in [0, 2\pi)$ define coordinates on the surface of a sphere. The states $|\theta, \phi\rangle$ are the spin-coherent states introduced in Appendix A.2 [Radcliffe, 1971; Arecchi *et al.*, 1972], which precess over time at the natural frequency

ω_0 set by the free Hamiltonian

$$\hat{H}_{\text{sys}} = \omega_0 \hat{S}_z , \quad (5.2)$$

i.e., $|\theta, \phi\rangle \rightarrow |\theta, \phi + \omega_0 t\rangle$. Here, the z -axis has been chosen as the spin quantization axis and \hat{S}_z is the corresponding spin-component operator. This oscillation is illustrated in Figure 5.1(a). The longitude angle ϕ thus plays the role of the phase variable at the core of the synchronization formalism, which parametrizes the oscillation along the closed curve in phase space.

From the phase-space representation, we can derive the phase distribution $P_{\hat{\rho}}$ of a state $\hat{\rho}$ by integrating out the amplitude degree of freedom, *i.e.*, the angle θ in the case of a spin-1 system,

$$P_{\hat{\rho}}(\phi) = \int_0^\pi d\theta \sin(\theta) \mathcal{Q}_{\hat{\rho}}(\theta, \phi) . \quad (5.3)$$

Equipped with the phase distribution $P_{\hat{\rho}}(\phi)$, we define a phase rotation by an angle α as the transformation $\hat{R}(\alpha)$ that changes the state $\hat{\rho}$ to $\hat{\rho}' = \hat{R}(\alpha)\hat{\rho}\hat{R}^\dagger(\alpha)$ such that

$$P_{\hat{\rho}'}(\phi) = P_{\hat{\rho}}(\phi - \alpha) .$$

For a spin-1 system, this transformation is achieved by the operator describing rotations around the quantization axis set by the free Hamiltonian \hat{H}_{sys} ,

$$\hat{R}(\alpha) = e^{-i\alpha\hat{S}_z/\hbar} . \quad (5.4)$$

A detailed summary of the corresponding results for oscillator-based systems, such as the quantum vdp oscillator [Lee and Sadeghpour, 2013; Walter *et al.*, 2014], is given in Appendix B. For these systems, the free Hamiltonian is $\hat{H}_{\text{sys}} = \hbar\omega_0\hat{a}^\dagger\hat{a}$ and the notion of a phase can be defined by decomposing the argument of the Husimi function $\mathcal{Q}_{\hat{\rho}}(\alpha)$ in polar coordinates, $\alpha = re^{i\phi}$.

5.2.2 Limit-cycle stabilization

Having defined the notion of a phase, we can now derive conditions on the form of the QME (5.1) that must be fulfilled to describe a limit-cycle oscillator. These conditions will also define the set of possible limit-cycle states.

The limit cycle is specified by the superoperator \mathcal{L}_0 in Equation (5.1), which contains all terms that are present even if no signal is applied, $\varepsilon = 0$, and has the form

$$\mathcal{L}_0\hat{\rho} = -\frac{i}{\hbar} \left[\hat{H}_{\text{sys}}, \hat{\rho} \right] + \sum_{j=1}^N \gamma_j \mathcal{D}[\hat{O}_j]\hat{\rho} , \quad (5.5)$$

This dynamics is composed of the oscillation at the natural frequency ω_0 , generated by the free Hamiltonian \hat{H}_{sys} , and of a set of N Lindblad dissipators \mathcal{D} of the form (2.12), which represent gain and loss induced by the environment. The limit-cycle state is the steady state of the dissipative map \mathcal{L}_0 . Different choices of coupling operators \hat{O}_j and their corresponding rates γ_j define where and how the limit cycle is stabilized in phase space. At this point, the fact that a limit cycle can be stabilized in infinitely many ways seems to seriously hinder any attempt to proceed further without focusing on a particular limit cycle. However, we now show that the properties of a limit cycle impose strong constraints on the coupling to the environment, which allows us to

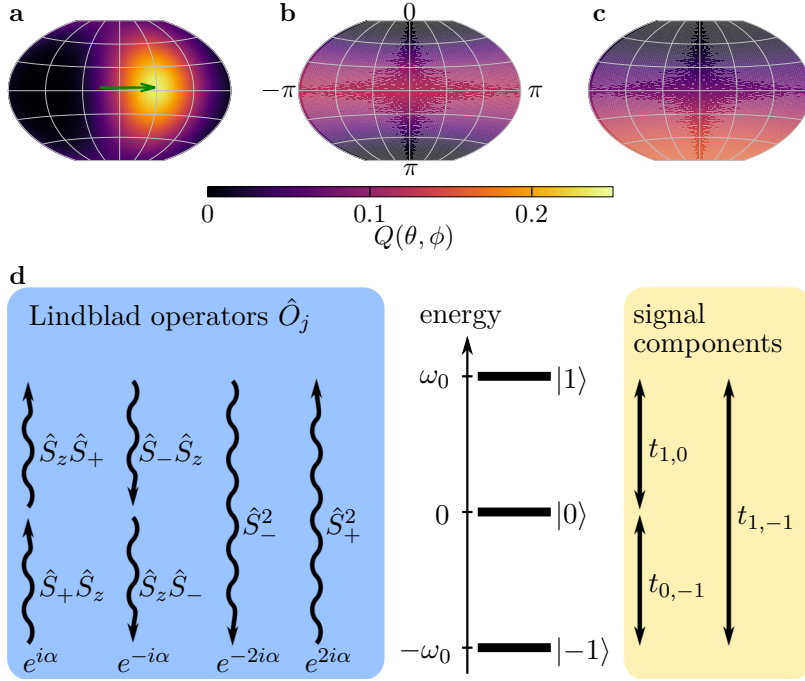


FIGURE 5.1: Illustration of the spherical phase space of a spin-1 system. **(a)** Spin-coherent state $|\theta, \phi\rangle = |1.5, 1\rangle$. The green arrow indicates its direction of oscillation in phase space. **(b)** Equatorial limit cycle $|0\rangle$ considered in Sections 5.3 and 5.5. **(c)** Limit cycle of the van der Pol oscillator deep in the quantum regime, considered in Section 5.4. **(d)** Energy-level structure of a spin-1 system (center), signal components and corresponding coefficients $t_{i,j}$ of the signal Hamiltonian \hat{H}_{ext} (right), and dissipative Lindblad operators \hat{O}_j that describe unidirectional transitions between two levels (left). The coupling operators are invariant under rotations $\hat{R}_z(\alpha) = e^{-i\alpha\hat{S}_z/\hbar}$ up to a phase factor indicated in the bottom row. Any linear combination of operators within the same column yields again a valid dissipative coupling operator.

narrow down the class of allowed operators and leads to a common structure for valid limit-cycle states.

The defining feature of a limit cycle is the ability to stabilize the amplitude of oscillation while leaving the phase completely free. The phase is then linearly increasing in time at the natural frequency ω_0 and can be readily adjusted by a weak external signal \hat{H}_{ext} , possibly to a different frequency. We postpone the open question of how strong the signal can be without affecting the amplitude of oscillation to Section 5.2.6, and focus here instead on the necessary requirement for the phase to be free before applying any signal.

The absence of any phase preference in the limit-cycle state implies that the dynamics generated by \mathcal{L}_0 must be invariant under phase rotations $\hat{R}(\alpha)$ defined in Equation (5.4). This is achieved by requiring that the Hamiltonian is invariant under phase rotations,

$$\hat{R}(\alpha)\hat{H}_{\text{sys}}\hat{R}^\dagger(\alpha) = \hat{H}_{\text{sys}} ,$$

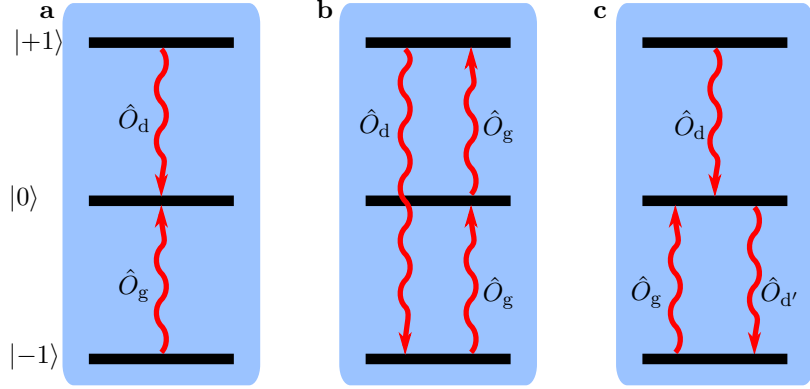


FIGURE 5.2: Overview of the dissipative stabilization mechanisms of spin-1 limit cycles considered in this chapter. **(a)** Stabilization of the equatorial limit cycle $|0\rangle$, discussed in Section 5.5, by the operators $\hat{O}_g = \hat{S}_+ \hat{S}_z$ and $\hat{O}_d = \hat{S}_- \hat{S}_z$. **(b)** Stabilization of the van der Pol limit cycle, discussed in Section 5.4, by the operators $\hat{O}_g = \hat{S}_z \hat{S}_+ - \hat{S}_+ \hat{S}_z / \sqrt{2}$ and $\hat{O}_d = \hat{S}_-^2 / \sqrt{2}$. **(c)** Asymmetric limit-cycle stabilization discussed in Section 5.6. The dissipative transition $\hat{O}_{d'} = \hat{S}_z \hat{S}_-$ has been added to the stabilization of the equatorial limit cycle shown in (a). The gain and relaxation rates associated with the operators \hat{O}_g , \hat{O}_d , and $\hat{O}_{d'}$ are γ_g , γ_d , and $\gamma_{d'}$, respectively.

and that the coupling operators \hat{O}_j are invariant up to a phase factor,

$$\hat{R}(\alpha) \hat{O}_j \hat{R}^\dagger(\alpha) = e^{i\nu_j(\alpha)} \hat{O}_j,$$

which does not play any role because of the incoherent nature of the coupling to the environment. Hence, the set of allowed coupling operators, shown in Figure 5.1(d), is given by all operators that satisfy $\langle m | \hat{O}_j | n \rangle \neq 0$ only for a fixed nonzero difference $d = m - n$,

$$\langle m | \hat{O}_j | n \rangle \propto \delta_{m-n,d}, \quad (5.6)$$

where $|n\rangle \equiv |S, n\rangle$ denotes an eigenstate of \hat{S}_z as defined in Appendix A.2. Physically, the operators \hat{O}_j correspond to incoherent population transfers between the eigenstates of \hat{H}_{sys} , which can be combined to stabilize the limit-cycle state of choice without imposing any phase during the relaxation. Note that we are intentionally omitting diagonal operators \hat{O}_j spanned by \hat{S}_z and \hat{S}_z^2 in Figure 5.1(d), which would in principle be allowed, because their effect is to generate dephasing without contributing to the amplitude stabilization. Thus, admitting those operators will only degrade synchronization. An overview of the specific spin-1 limit-cycle stabilization mechanisms considered in this chapter is given in Figure 5.2.

An important consequence of the form of the coupling operators is that the dynamics of the limit cycle leads to decoherence in the energy eigenbasis, yielding a diagonal limit-cycle state that is invariant under phase rotations,

$$\begin{pmatrix} \rho_{+1,+1} & 0 & 0 \\ 0 & \rho_{0,0} & 0 \\ 0 & 0 & \rho_{-1,-1} \end{pmatrix},$$

where $1 \geq \rho_{k,k} \geq 0$ and $\sum_k \rho_{k,k} = 1$. In the following, this feature will be key to understand the quantum-mechanical resources on which synchronization relies.

5.2.3 External signal

Now that we have identified the general form of a limit cycle, the remaining ingredient of Equation (5.1) is the external signal which is applied to synchronize the oscillator. In general, the signal Hamiltonian \hat{H}_{ext} is a combination of all coherent transitions between the energy eigenstates. In a spin-1 system, there are three such transitions and the corresponding Hamiltonian reads as follows in a frame rotating at the signal frequency ω_{ext} and under a rotating-wave approximation:

$$\hat{H}_{\text{ext}} = \hbar \left(t_{0,1} \hat{S}_z \hat{S}_+ - t_{-1,0} \hat{S}_+ \hat{S}_z + t_{-1,1} \hat{S}_+^2 + \text{H.c.} \right) . \quad (5.7)$$

As illustrated in Figure 5.1(d), \hat{H}_{ext} consists of two individual signal components applied to the transitions $|-1\rangle \leftrightarrow |0\rangle$ and $|0\rangle \leftrightarrow |1\rangle$, and a squeezing component addressing directly the transition $|1\rangle \leftrightarrow |-1\rangle$. The complex parameters $t_{n,m}$ describe the relative phases and amplitudes of these components. For instance, a semiclassical signal of the form $2\varepsilon[\cos(\varphi)\hat{S}_x + \sin(\varphi)\hat{S}_y]$ corresponds to the first two transitions being equally driven, $t_{0,1} = t_{-1,0} = e^{i\varphi}/2$, and no squeezing component, $t_{-1,1} = 0$. Note that the signal Hamiltonian is completely off-diagonal in the spin basis,

$$\langle m | \hat{H}_{\text{ext}} | m' \rangle \propto 1 - \delta_{m,m'} . \quad (5.8)$$

Working in a rotating frame implies that \hat{H}_{sys} now takes the form

$$\hat{H}_{\text{sys}} = \Delta \hat{S}_z ,$$

where Δ denotes the detuning between the natural frequency of oscillation and the signal frequency,

$$\Delta = \omega_0 - \omega_{\text{ext}} . \quad (5.9)$$

5.2.4 Perturbation theory

Having fully characterized the spin-1 system in terms of the available limit cycles and signals, we now connect the two components. By definition, synchronization can only be achieved for a signal strength ε small enough such that the original limit cycle is only weakly perturbed [Pikovsky *et al.*, 2003]. Going beyond this regime would affect not only the phase of the oscillation but also its amplitude, and thus the limit cycle would be deformed. In the following, we refer to this undesired regime as forcing.

Inspired by the fact that the signal should be a small perturbation, we perform an expansion of the density matrix in terms of the signal strength ε ,

$$\hat{\rho} = \sum_{k=0}^{\infty} \varepsilon^k \hat{\rho}^{(k)} . \quad (5.10)$$

The precise definition of a “small” signal is derived in Section 5.2.6. For now, it is sufficient to note that by counting powers of ε we can formally split the state $\hat{\rho}$ into the limit-cycle state, characterized by $\hat{\rho}^{(0)}$, and higher-order corrections $\hat{\rho}^{(k)}$, $k \geq 1$, stemming from the signal. As we will show below, all features of quantum synchronization are captured by the first-order term $\hat{\rho}^{(1)}$. Inserting the expansion (5.10) into the quantum master equation (5.1) and collecting orders of ε , we obtain a set of

recursive differential equations [Li *et al.*, 2014],

$$\frac{d}{dt}\hat{\rho}^{(k)} = \mathcal{L}_0\hat{\rho}^{(k)} + (1 - \delta_{k,0})\mathcal{L}_{\text{ext}}\hat{\rho}^{(k-1)}, \quad (5.11)$$

where each term of the density-matrix expansion is normalized according to

$$\text{Tr} [\hat{\rho}^{(k)}] = \delta_{k,0}.$$

The superoperator \mathcal{L}_{ext} contains the signal Hamiltonian,

$$\mathcal{L}_{\text{ext}}\hat{\rho} = -\frac{i}{\hbar} [\hat{H}_{\text{ext}}, \hat{\rho}]. \quad (5.12)$$

To understand Equation (5.11) further, we note that the QME (5.1) is a linear first-order differential equation for the density matrix $\hat{\rho}$. Therefore, the superoperator \mathcal{L}_0 can be represented as a matrix acting on a vector

$$\boldsymbol{\rho} = \begin{pmatrix} \boldsymbol{\rho}_{\text{pop}} \\ \boldsymbol{\rho}_{\text{coh}} \end{pmatrix}.$$

of density matrix elements, where $\boldsymbol{\rho}_{\text{pop}}$ and $\boldsymbol{\rho}_{\text{coh}}$ are vectors containing the populations and coherences of the density matrix $\hat{\rho}$, respectively. The property (5.6) of the Lindblad operators gives rise to a block-diagonal structure of the matrix representing \mathcal{L}_0 ,

$$\left(\begin{array}{c|c} \mathcal{L}_0^{\text{pop}} & 0 \\ \hline 0 & \mathcal{L}_0^{\text{coh}} \end{array} \right),$$

where the subblocks $\mathcal{L}_0^{\text{pop}}$ and $\mathcal{L}_0^{\text{coh}}$ act only on the populations $\boldsymbol{\rho}_{\text{pop}}$ and the coherences $\boldsymbol{\rho}_{\text{coh}}$ of the density matrix, respectively. The subblock $\mathcal{L}_0^{\text{pop}}$ is negative semidefinite and its zero eigenvalue is associated with the limit-cycle state $\hat{\rho}^{(0)}$. The subblock $\mathcal{L}_0^{\text{coh}}$ has complex eigenvalues with negative real parts that lead to a decay of the coherences to zero. The signal term $\mathcal{L}_{\text{ext}}\hat{\rho}^{(k-1)}$ constitutes an inhomogeneity of the differential equation and is represented by the vector

$$\boldsymbol{\rho}_{\text{ext}}^{(k-1)} = \begin{pmatrix} \boldsymbol{\rho}_{\text{ext}}^{\text{pop},(k-1)} \\ \boldsymbol{\rho}_{\text{ext}}^{\text{coh},(k-1)} \\ \boldsymbol{\rho}_{\text{ext}} \end{pmatrix}.$$

Its entries depend on the density-matrix expansion coefficient $\hat{\rho}^{(k-1)}$ and read as

$$\langle m | \mathcal{L}_{\text{ext}}\hat{\rho}^{(k-1)} | n \rangle = -i \sum_j \left[\langle m | \hat{H}_{\text{ext}} | j \rangle \rho_{j,n}^{(k-1)} - \rho_{m,j}^{(k-1)} \langle j | \hat{H}_{\text{ext}} | n \rangle \right]. \quad (5.13)$$

To leading order $k = 0$, Equation (5.11) describes the situation without any signal being applied, *i.e.*, the limit-cycle state. As discussed in Section 5.2.2, the superoperator \mathcal{L}_0 relaxes the system to a diagonal steady state

$$\hat{\rho}^{(0)} = \begin{pmatrix} * & 0 & 0 \\ 0 & * & 0 \\ 0 & 0 & * \end{pmatrix}, \quad \text{Tr} [\hat{\rho}^{(0)}] = 1, \quad (5.14)$$

where the stars represent non-negative entries that depend on the specific form of the limit cycle.

The next order $k = 1$ accounts for the fact that a weak external signal is applied to synchronize the limit-cycle oscillator. Using the condition (5.8) on the form of the external signal and the diagonal structure (5.14) of $\hat{\rho}^{(0)}$, we find that $\mathcal{L}_{\text{ext}}\hat{\rho}^{(0)}$ constitutes an inhomogeneity only for the equation of motion of the coherences, but it vanishes for the populations,

$$\frac{d}{dt} \begin{pmatrix} \rho_{\text{pop}}^{(1)} \\ \rho_{\text{coh}}^{(1)} \end{pmatrix} = \begin{pmatrix} \mathcal{L}_0^{\text{pop}} & 0 \\ 0 & \mathcal{L}_0^{\text{coh}} \end{pmatrix} \cdot \begin{pmatrix} \rho_{\text{pop}}^{(1)} \\ \rho_{\text{coh}}^{(1)} \end{pmatrix} + \begin{pmatrix} \mathbf{0} \\ \rho_{\text{ext}}^{\text{coh},(0)} \end{pmatrix} .$$

Thus, the first-order expansion coefficient $\hat{\rho}^{(1)}$ is the result of a trade-off between the signal part $\mathcal{L}_{\text{ext}}\hat{\rho}^{(0)}$, which aims to build up coherences in $\hat{\rho}^{(1)}$, and the limit-cycle stabilization $\mathcal{L}_0\hat{\rho}^{(1)}$, which tries to decrease them towards a completely dephased limit-cycle state. Thus, the coherences of $\hat{\rho}^{(1)}$ are given by

$$\rho_{n,m \neq n}^{(1)} = - \sum_{j,k} \left(\mathcal{L}_0^{\text{coh}} \right)_{n,m;j,k}^{-1} \langle j | \mathcal{L}_{\text{ext}}\hat{\rho}^{(0)} | k \rangle . \quad (5.15)$$

The populations of $\hat{\rho}^{(1)}$ are zero because the equation of motion of the populations the same as for the populations $\rho_{n,n}^{(0)}$ of the limit-cycle state, but the normalization condition now reads $\text{Tr}[\hat{\rho}^{(1)}] = 0$. Hence, we find a purely off-diagonal first-order correction term

$$\hat{\rho}^{(1)} = \begin{pmatrix} 0 & * & * \\ * & 0 & * \\ * & * & 0 \end{pmatrix} , \quad (5.16)$$

where the stars represent complex entries compatible with the condition $\hat{\rho}^{(1)\dagger} = \hat{\rho}^{(1)}$. This analytical result demonstrates that quantum synchronization achieves phase localization by building up coherences and leaving populations untouched. The latter is equivalent to preserving the closed curve of the limit cycle in phase space.

As the signal strength ε is increased, higher-order corrections become relevant and all matrix elements are nonzero in general,

$$\hat{\rho}^{(k \geq 2)} = \begin{pmatrix} * & * & * \\ * & * & * \\ * & * & * \end{pmatrix} , \quad \text{Tr} \left[\hat{\rho}^{(k \geq 2)} \right] = 0 . \quad (5.17)$$

Now, the coherences driven to first order in ε give rise to a second-order correction of populations due to the signal Hamiltonian \hat{H}_{ext} , *i.e.*, the signal is moving the limit cycle away from its original position in phase space. This corresponds to the oscillator being forced. In the following, we will restrict the study to the synchronization regime, where higher-order corrections can be neglected,

$$\hat{\rho} \approx \hat{\rho}^{(0)} + \varepsilon \hat{\rho}^{(1)} . \quad (5.18)$$

A condition on the signal strength ε that ensures the validity of this approximation is derived below in Section 5.2.6.

5.2.5 Synchronization measure

Before continuing our discussion of the quantum synchronization framework, we introduce the specific measure of quantum synchronization that we will use to compare

the synchronization of different limit-cycle oscillators and signals. An overview of various quantum synchronization measures proposed in the literature has been given in Section 2.6.4. Note that, although we will focus on a specific quantum synchronization measure in the following, the general framework does actually not rely on our particular choice.

We will quantify synchronization using the marginal distribution of the phase of the oscillator, $P_{\hat{\rho}}(\phi)$, which has already been defined in Equation (5.3). Since the dissipative source of energy does not favor any phase ϕ of the oscillator, the intrinsic quantum noise inevitably leads to phase diffusion such that the limit-cycle state $\hat{\rho}^{(0)}$ has a uniform phase distribution $P_{\hat{\rho}^{(0)}} = 1/2\pi$, similar to a noisy classical limit-cycle oscillator. Therefore, to measure phase locking of the limit-cycle oscillator to an external signal, we define the shifted phase distribution

$$S_{\hat{\rho}}(\phi) = P_{\hat{\rho}}(\phi) - \frac{1}{2\pi} , \quad (5.19)$$

which is identically zero if and only if the distribution $P_{\hat{\rho}}(\phi)$ is uniform, *i.e.*, if no phase preference is developed.

Expressed in terms of a spin-1 density matrix, the shifted phase distribution has the form

$$S_{\hat{\rho}}(\phi) = \frac{3}{8\sqrt{2}} |\rho_{1,0} + \rho_{0,-1}| \cos[\phi + \arg(\rho_{1,0} + \rho_{0,-1})] + \frac{1}{2\pi} |\rho_{1,-1}| \cos[2\phi + \arg(\rho_{1,-1})] , \quad (5.20)$$

where $\rho_{n,m} = \langle n | \hat{\rho} | m \rangle$ are the matrix elements of the state $\hat{\rho}$. A similar formula containing only the $\cos(\phi)$ term has been derived in the specific case of a limit-cycle defined in a Kerr nonlinear oscillator by Lörch *et al.* [2016]. Following Lee and Sadeghpour [2013], Roulet and Bruder [2018a], and Lörch *et al.* [2017], we use the maximum of the shifted phase distribution to obtain a single-number measure of synchronization,

$$\mathcal{S}(\hat{\rho}) = \max_{\phi \in [0, 2\pi)} S_{\hat{\rho}}(\phi) . \quad (5.21)$$

Note that $S_{\hat{\rho}}(\phi)$ depends only on the coherences of $\hat{\rho}$ and thus, since we are restricting ourselves to the synchronization regime (5.18), on the first-order correction $\hat{\rho}^{(1)}$. Also note that the prefactor of the $\cos(\phi)$ term shows that building up coherences is not a sufficient condition to break the rotational invariance of the limit-cycle state. Interference effects between the coherences $\rho_{1,0}$ and $\rho_{0,-1}$ are expected to either enhance or hinder the synchronization behavior. We address this point in Section 5.7 where we discuss the possibility of synchronization blockade, despite the energy levels of the spin-1 system being equally spaced.

Combining Equations (5.18) and (5.20), we find that the phase localization increases linearly proportional to the signal strength, $S_{\hat{\rho}}(\phi) = \varepsilon S_{\hat{\rho}^{(1)}}(\phi)$. On the other hand, we have shown that ε cannot be increased indefinitely as the system will eventually leave the perturbative regime of synchronization. When comparing the ability of different limit cycles to synchronize to different signals, we thus need a general rule how to set the value of ε while ensuring that the signal remains a weak perturbation. In the spirit of all past studies, which fixed both the signal and the limit cycle, a natural guess would be that normalizing every expression with respect to ε is sufficient to compare different situations. However, this approach cannot be reliable for two the following reasons.

First, it neglects the dissipative stabilization of the limit-cycle. The relation

$$\mathcal{D}[c\hat{O}_j]\hat{\rho} = |c|^2 \mathcal{D}[\hat{O}_j]\hat{\rho} ,$$

where c is a complex prefactor, allows us to rescale the dissipative transition rates by absorbing prefactors into the dissipative transition operators. Even though $\mathcal{D}[\hat{O}_j]\hat{\rho}$ and $\mathcal{D}[c\hat{O}_j]\hat{\rho}$ describe the same transitions between energy levels, the corresponding limit-cycle oscillators will in general differ in their susceptibility to external signals. This has to be taken into account when determining the signal strength ε .

Second, the signal Hamiltonian (5.7) contains the parameters $t_{i,j}$, which determine the relative strength of the signal on each individual transition as shown in Figure 5.1(d). An increase in ε can be compensated by a corresponding decrease of the parameters $t_{i,j}$ without changing the effective signal Hamiltonian $\varepsilon\hat{H}_{\text{ext}}$ at all. Thus, we are required to derive a dimensionless parameter η that defines the drive strength ε and ensures the validity of the first-order approximation (5.18) in full generality. This is the subject of the next section.

5.2.6 Determining the signal strength

By direct analogy with a classical system, one way to quantify the deformation of a limit cycle is to monitor its change in energy. If the signal becomes more than a perturbation, one expects energy to be pumped into the system such that the amplitude of the oscillation is modified and the limit cycle is shifted in phase space. Following this reasoning, the small parameter η would then be proportional to the change in the average occupation of the energy levels, which reads for the spin system

$$p_{\text{avg}}(\varepsilon) = \text{Tr} \left[\hat{S}_z \left(\hat{\rho}(\varepsilon) - \hat{\rho}^{(0)} \right) \right] . \quad (5.22)$$

A bound on $\eta \propto p_{\text{avg}}(\varepsilon)$ will then implicitly define the maximum admissible signal strength.

As a first sanity check, this deformation measure indeed vanishes in the perturbative regime, where it amounts to evaluate the average occupation of the purely off-diagonal correction $\hat{\rho}^{(1)}$ given in Equation (5.16). To test it further and check whether it properly detects all types of deformations that can be induced by the signal, we consider a subclass of dissipative stabilization mechanisms, shown in Figure 5.2(a), which relax the system to the equatorial state $\hat{\rho}^{(0)} = |0\rangle\langle 0|$. The stabilization can be obtained by the two Lindblad operators $\hat{O}_g = \hat{S}_+\hat{S}_z$ and $\hat{O}_d = \hat{S}_-\hat{S}_z$, where the ratio γ_g/γ_d of the associated transition rates can be freely adjusted to modify the response of the limit cycle to perturbations. The equatorial limit cycle will be discussed in more detail in Section 5.5. For the rest of this section, it is sufficient to restrict ourselves to a semiclassical signal, *i.e.*, $t_{0,1} = t_{-1,0}$ and $t_{-1,1} = 0$.

For the balanced case $\gamma_g = \gamma_d$, Figure 5.3(a) shows that the signal attracts the phase ϕ towards 0 and π without leaving the equator, which appears to be a synchronized state. To confirm this visual impression, we track the deformation measure $p_{\text{avg}}(\varepsilon)$, which stays at zero for the considered range of signal strengths. It thus appears that the phase localization is indeed achieved by synchronizing the oscillator to the applied signal. Yet, the following two intriguing features do not agree with this interpretation.

First, we have derived in Equation (5.20) that a synchronized distribution with two stable phases can only emerge by building up coherence between the extremal states, *i.e.*, $\rho_{-1,1} \neq 0$, which in turn requires some initial population in the states $|\pm 1\rangle$.

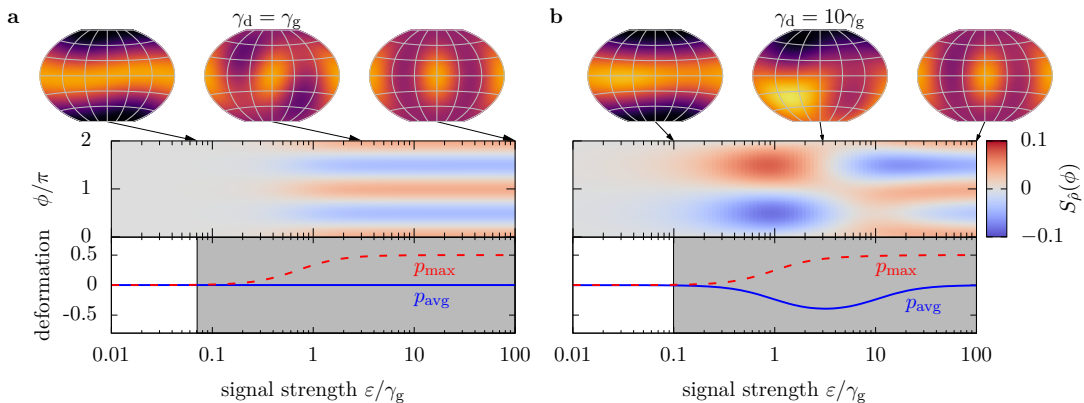


FIGURE 5.3: Shifted phase distribution $S_{\hat{\rho}}(\phi)$ and deformation measures $p_{\text{avg}}(\varepsilon)$ and $p_{\text{max}}(\varepsilon)$ as a function of the signal strength ε for the equatorial limit cycle discussed in Section 5.2.6 with (a) balanced rates $\gamma_d/\gamma_g = 1$ and (b) imbalanced rates $\gamma_d/\gamma_g = 10$. In both cases, a resonant semiclassical signal is applied, *i.e.*, $t_{0,1} = t_{-1,0}$, $t_{-1,1} = 0$, and $\Delta = 0$. The gray background in the lower plots indicates the regime of forcing according to Equation (5.25), $\varepsilon(\eta) = \eta\gamma_g\gamma_d/\sqrt{\gamma_g^2 + \gamma_d^2}$, evaluated for $\eta = 0.1$. The plots of the \mathcal{Q} -function show the state of the system for different values of the signal strength.

However, this is not possible for the present limit cycle, where only the equatorial state is populated. To be specific, for a semiclassical signal and the equatorial limit-cycle state $\hat{\rho}^{(0)} = |0\rangle\langle 0|$, Equation (5.13) predicts that the coherences $\rho_{1,0}$ and $\rho_{0,-1}$ will be built up by the signal, but the coherence $\rho_{1,-1}$ will decay to zero,

$$\begin{aligned} \langle 1 | \mathcal{L}_{\text{ext}} \hat{\rho}^{(0)} | 0 \rangle &= -i\sqrt{2}t_{0,1} , \\ \langle 0 | \mathcal{L}_{\text{ext}} \hat{\rho}^{(0)} | -1 \rangle &= +i\sqrt{2}t_{-1,0} , \\ \langle 1 | \mathcal{L}_{\text{ext}} \hat{\rho}^{(0)} | -1 \rangle &= 0 . \end{aligned}$$

Thus, any synchronized phase distribution of this limit cycle must have only a single peak.

Second, if one were to extend the plot range to even larger signal strength, the deformation measure would actually be found to vanish for any value of ε . This triggers the suspicion that the measure $p_{\text{avg}}(\varepsilon)$ may not play its role of signaling the transition from the perturbative to the forcing regime for the limit cycle under consideration. Its failure is based in the fact that the expectation value adds up the changes $\rho_{k,k}(\varepsilon) - \rho_{k,k}^{(0)}$ of different populations. This opens the door for cancellation effects, which make the measure $p_{\text{avg}}(\varepsilon)$ insensitive to certain deformations of the limit cycle.

To address this issue, we consider the more fine-grained measure

$$p_{\text{max}}(\varepsilon) = \max_{n \in \{-1,0,1\}} \left| \rho_{n,n}(\varepsilon) - \rho_{n,n}^{(0)} \right| , \quad (5.23)$$

which tracks the maximum change of the individual populations instead of the averaged value $p_{\text{avg}}(\varepsilon)$. Taking the absolute value of the change of each population rules out cancellation effect, and focusing only on the maximum change avoids double-counting. As shown in Figure 5.3(a), this measure is able to detect that the emergence of the two peaks in the phase distribution belongs to the forcing regime. Indeed, the

onset of the peaks is found to be accompanied by a transfer of population from the equatorial state to the extremal states, which can only be achieved by higher-order contributions (5.17) in the perturbation expansion of $\hat{\rho}$. However, because of the symmetry of both the limit cycle $\gamma_d = \gamma_g$ and the semiclassical signal $t_{0,1} = t_{-1,0}$, this transfer is evenly distributed between the extremal states, which explains why the average occupation $p_{\text{avg}}(\varepsilon)$ remained blind to this deformation.

These results imply that the balanced limit cycle $\gamma_g = \gamma_d$ is unable to synchronize to a semiclassical signal. Physically, this follows from the fact that, to first order, the coherences $\rho_{1,0}$ and $\rho_{0,-1}$ are generated with equal amplitudes but opposite sign, and therefore counteract each other in attempting to localize the phase distribution (5.20). This effect is discussed in more detail in Section 5.7. On the other hand, in the unbalanced case, one of the coherences is able to take the lead and a single-peak phase distribution emerges as illustrated in Figure 5.3(b). This is in agreement with the results reported by Roulet and Bruder [2018a]. Moreover, when the signal strength is further increased, the limit cycle is now clearly deformed towards one of the poles when it enters the forcing regime, before it comes back to the equator for very large signal strength and forms the same double-peaked distribution that has already been found in the balanced case.

These results demonstrate the difficulty of measuring the deformation of a quantum limit cycle based on variations of the populations, which are captured by the second-order term $\hat{\rho}^{(2)}$. In fact, there remain some combinations of limit cycle and signal for which even the refined measure $p_{\text{max}}(\varepsilon)$ is unable to identify the transition to the forcing regime. To this end, we consider a quantum vdP limit-cycle oscillator, which is defined by the dissipative coupling operators $\hat{O}_g = \hat{S}_z \hat{S}_+ - \hat{S}_+ \hat{S}_z / \sqrt{2}$ and $\hat{O}_d = \hat{S}_-^2 / \sqrt{2}$ with the respective rates γ_g and γ_d , as shown in Figure 5.2. The vdP system will be discussed in more detail in Section 5.4. We consider a signal where the ratio between the semiclassical signal components can be adjusted, $t_{0,1} = r$ and $t_{-1,0} = 1/\sqrt{2}$, but there is no squeezing signal, $t_{-1,1} = 0$.

As shown in Figure 5.4, there is a range of values $1/\sqrt{2} \lesssim r \lesssim 5.5$ for which the deformation measure $p_{\text{max}}(\varepsilon)$ is nonmonotonous and has a local maximum, then decreases towards zero, before it increases strongly and converges to a constant value in the limit $\varepsilon \rightarrow \infty$. This implies that for a threshold value η smaller than the local maximum, there are up to three solutions ε_i that satisfy $\eta = p_{\text{max}}(\varepsilon_i)$. For a very pronounced local maximum, *e.g.*, the dashed green line in Figure 5.4, the measure provides a clear indicator that the limit cycle is deformed to an intermediate state for $\varepsilon \gtrsim \min\{\varepsilon_i\}$, before it converges to another deformed state in the strongly forced regime $\varepsilon \gg \max\{\varepsilon_i\}$. In this situation, $\varepsilon_{\text{max}} = \min\{\varepsilon_i\}$ is straightforwardly identified as the maximum signal strength allowed for synchronization. However, the value of the local maximum decreases with r , and in particular for $r \approx 5$ the peak almost vanishes, as shown by the dotted red line in Figure 5.4. This means that for any fixed value of the threshold η there is a value of r such that the first deviation of $p_{\text{max}}(\varepsilon)$ is not detected, without having a physical argument that it does not belong to the forcing regime. Consequently, the measure $p_{\text{max}}(\varepsilon)$ fails to give a definite answer for the transition to the forcing regime.

The physical reason for this behavior is that the energy in the finite-dimensional Hilbert space of a spin system is bounded, *i.e.*, the amplitude cannot simply grow indefinitely in phase space when the signal strength is increased. With increasing

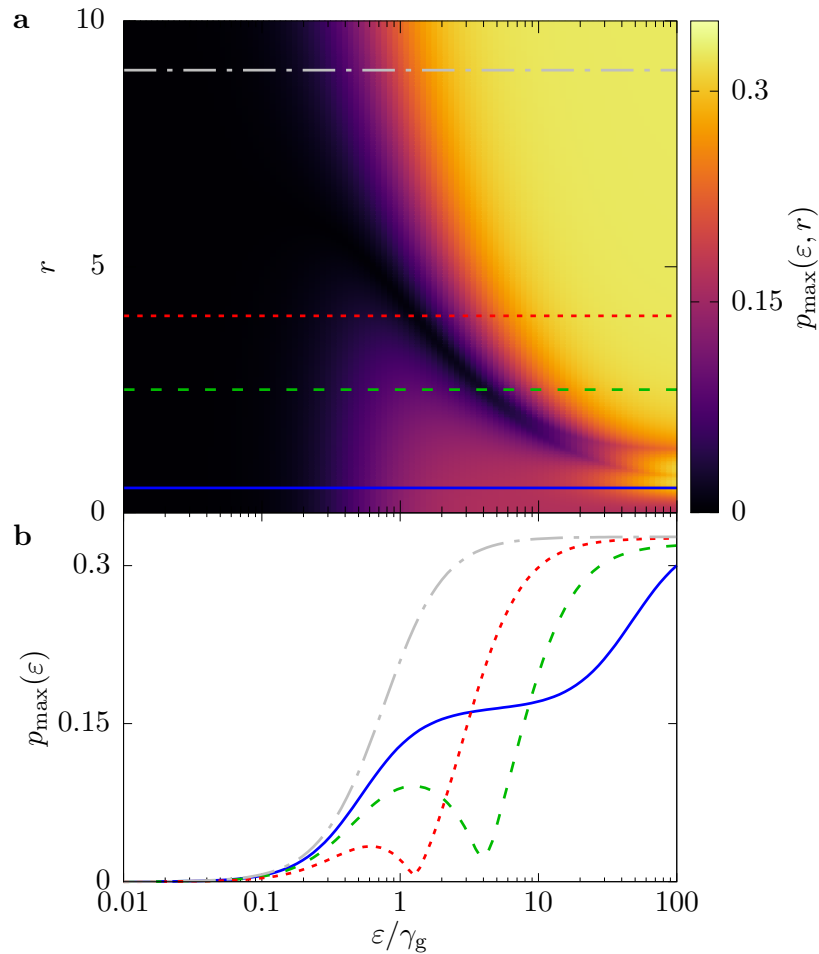


FIGURE 5.4: **(a)** Deformation measure $p_{\max}(\varepsilon, r)$ for a van der Pol limit cycle as a function of the signal strength ε and the ratio $r = t_{0,1}/\sqrt{2}t_{-1,0}$ of the amplitudes of the semiclassical signal components. Squeezing is switched off, $t_{-1,1} = 0$. **(b)** Cuts $p_{\max}(\varepsilon)$ for fixed values $r = 0.5, 2.5, 4$, and 9 , indicated by the corresponding horizontal lines in (a). Parameters are $\gamma_d/\gamma_g = 100$ and $\Delta = 0$.

signal strength ε , the vdP limit cycle deep in the quantum regime,

$$\frac{1}{3} \begin{pmatrix} 0 & \\ & 1 \\ & & 2 \end{pmatrix},$$

is deformed to the signal-dependent state

$$\frac{1}{2 + 4r^4} \begin{pmatrix} 2r^2 & \sqrt{2}r(1 - 2r^2) \\ \sqrt{2}r(1 - 2r^2) & 1 \\ & & 1 - 2r^2 + 4r^4 \end{pmatrix}, \quad (5.24)$$

which is obtained in the limit $\varepsilon \gg \gamma_d \gg \gamma_g$.

For $r \leq 1/\sqrt{2}$ and a small signal strength $\varepsilon \lesssim \gamma_g$, the $t_{-1,0}$ signal component dominates and transfers population from the state $|-1\rangle$ to the state $|0\rangle$, until a balance $\rho_{-1,-1} \approx \rho_{0,0} \approx 1/2$ is reached for $\gamma_g < \varepsilon < \gamma_d$. This is the reason for the first plateau of the solid blue line in Figure 5.4(b). Since the dissipation rate γ_d is still the largest rate, the state $|+1\rangle$ is almost unpopulated. For an even larger signal strength $\varepsilon \approx \gamma_d$,

the signal overcomes dissipation and population is transferred from the states $|-1\rangle$ and $|0\rangle$ to the state $|+1\rangle$, until the state (5.24) is reached in the limit $\varepsilon \gg \gamma_d$, with a distribution $\rho_{0,0} \geq \rho_{-1,-1} \geq \rho_{1,1}$ that is determined by the signal.

In the opposite limit $r \gg 1/\sqrt{2}$, the $t_{0,1}$ signal component dominates. If the signal strength overcomes the gain rate, $\varepsilon \gg \gamma_g$, the signal creates a balance $\rho_{0,0} \approx \rho_{1,1}$, which leads to an effective depletion of both levels because of the dissipative transition $|1\rangle \rightarrow |-1\rangle$, *i.e.*, we find $\rho_{-1,-1} \rightarrow 1$ and $\rho_{1,1} = \rho_{0,0} \rightarrow 0$. This is shown by the dash-dotted gray line in Figure 5.4(b).

For intermediate values, $r \gtrsim 1/\sqrt{2}$, a crossover between these two scenarios occurs. A weak signal $\varepsilon \ll \gamma_g$ attempts to equalize the populations $\rho_{0,0}$ and $\rho_{-1,-1}$ such that population is dominantly transferred from $|-1\rangle$ to $|0\rangle$. For an intermediate signal strength $\gamma_g < \varepsilon < \gamma_d$, the signal aims to equalize $\rho_{0,0}$ and $\rho_{1,1}$, thus, population is now dominantly transferred from the states $|-1\rangle$ and $|0\rangle$ to the state $|1\rangle$. This causes the dip in the dotted red and dashed green curve in Figure 5.4(b). Because of the dissipative transition $|+1\rangle \rightarrow |-1\rangle$, the levels $|0\rangle$ and $|1\rangle$ are depleted and the population of the state $|-1\rangle$ increases, such that the system approaches the state (5.24) with a distribution $\rho_{-1,-1} \geq \rho_{1,1} \geq \rho_{0,0}$ in the limit $\varepsilon \gg \gamma_d, \gamma_g$. In conclusion, for $r > 1/\sqrt{2}$, the limit cycle is deformed twice, but the first redistribution process $|-1\rangle \rightarrow |0\rangle$ becomes less pronounced if r increases. Therefore, this redistribution of population in the forcing regime can be very hard to distinguish from the initial limit-cycle state.

To circumvent this problem, we propose to avoid any coarse-grained deformation measure based on the change of populations contained in $\hat{\rho}^{(2)}$. Instead, we derive the dimensionless parameter η of the perturbation expansion (5.18) explicitly using only the first-order correction term $\hat{\rho}^{(1)}$. To this end, we require that the first-order correction in Equation (5.18) remains small with respect to the leading order term,

$$\|\varepsilon \hat{\rho}^{(1)}\| \ll \|\hat{\rho}^{(0)}\| .$$

Here $\|\hat{O}\| = \sqrt{\text{Tr}(\hat{O}^\dagger \hat{O})}$ stands for the Hilbert-Schmidt norm in the operator space, also known as the Liouville space [Fano, 1957]. In practice, we impose a fixed threshold value $0 \leq \eta \ll 1$ on the inequality and set

$$\varepsilon = \eta \frac{\|\hat{\rho}^{(0)}\|}{\|\hat{\rho}^{(1)}\|} . \quad (5.25)$$

The parameter η is precisely the expansion parameter that needs to be small to ensure the validity of Equation (5.18). It is also the key ingredient that will allow us to compare all sorts of signals and limit cycles, and we end this section by discussing the physical interpretation of Equation (5.25).

The numerator

$$\|\hat{\rho}^{(0)}\| = \sqrt{\sum_m |\rho_{m,m}^{(0)}|^2} \quad (5.26)$$

is similar to the inverse participation ratio used to characterize Anderson localization [Wegner, 1980; Evers and Mirlin, 2000], or to the effective dimension that determines the equilibration of a closed quantum system undergoing unitary dynamics [Linden *et al.*, 2009; Gogolin and Eisert, 2016]. In the three-dimensional Hilbert space of a spin 1, the norm $\|\hat{\rho}^{(0)}\|$ takes values between $\sqrt{1/(2S+1)} = \sqrt{1/3}$, for a limit cycle that is a uniform incoherent mixture of all energy eigenstates, and 1, for a

limit cycle that consists of a single state. It captures the fact that a limit cycle with a wider spread of amplitude in phase space is more susceptible to deformations than a narrow limit cycle formed by a single pure state.

The denominator is most easily interpreted by assuming that the subblock $\mathcal{L}_0^{\text{coh}}$ is diagonalizable, *i.e.*, that its left and right eigenstates associated with the eigenvalue Γ_l , $\check{\mu}_l$ and $\hat{\mu}_l$, respectively, form an orthonormal basis spanning the space of coherences. More details of this basis have been given in Section 4.4.1. In the following, we will call the eigenstates $\hat{\mu}_l$ the ‘‘eigencoherences’’ of the system. We now expand the term $\mathcal{L}_{\text{ext}}\hat{\rho}^{(0)}$ in this basis,

$$\mathcal{L}_{\text{ext}}\hat{\rho}^{(0)} = \sum_l g_l \hat{\mu}_l, \quad (5.27)$$

$$g_l = \text{Tr}[\check{\mu}_l^\dagger (\mathcal{L}_{\text{ext}}\hat{\rho}^{(0)})]. \quad (5.28)$$

It is possible to restrict the sum to the basis states of the coherences, since the populations of $\mathcal{L}_{\text{ext}}\hat{\rho}^{(0)}$ are zero. Inserting this result into Equation (5.15), we find

$$\hat{\rho}^{(1)} = - \sum_l \hat{\mu}_l \frac{g_l}{\Gamma_l},$$

which allows us to rewrite the norm as follows:

$$\|\hat{\rho}^{(1)}\| = \sqrt{\sum_{l,k} \frac{g_l}{\Gamma_l} \frac{g_k^*}{\Gamma_k^*} \text{Tr}(\hat{\mu}_k^\dagger \hat{\mu}_l)}. \quad (5.29)$$

For the examples discussed at the beginning of this section, *i.e.*, the dissipative mechanisms stabilizing the equatorial state $|0\rangle$ and the van der Pol limit cycle deep in the quantum regime $\gamma_d \gg \gamma_g$, the superoperator \mathcal{L}^{coh} becomes diagonal such that the left and right eigenvectors are identical, $\check{\mu}_l \rightarrow \hat{\mu}_l$. Using the orthonormality of the left and right eigenstates of \mathcal{L}^{coh} , we can simplify Equation (5.29) as follows:

$$\|\hat{\rho}^{(1)}\| = \sqrt{\sum_l \left| \frac{g_l}{\Gamma_l} \right|^2}. \quad (5.30)$$

The coefficients g_l describe how strongly a certain eigencoherence is driven away from zero by the signal \mathcal{L}_{ext} . They are compared to the corresponding relaxation rates Γ_l that try to decrease them to zero. Hence, the denominator $\|\hat{\rho}^{(1)}\|$ of Equation (5.25) ensures that the overall effect of the signal on each eigencoherence remains small compared to the dissipative stabilization of the limit cycle. Note that the assumptions that $\mathcal{L}_0^{\text{coh}}$ is diagonalizable and that the eigencoherences form a complete orthonormal basis have only been used to discuss the physical meaning of the threshold η . In particular, the definition (5.25) remains well-defined even if these simplifying assumptions do not hold.

5.3 Extended Arnold tongue

As a first application of the formalism developed in Section 5.2, we address the open question of delimiting the synchronization region as a function of the detuning Δ and the signal strength ε . It is known from classical physics that the range of detunings for which synchronization exists increases with the signal strength [Pikovsky *et al.*, 2003].

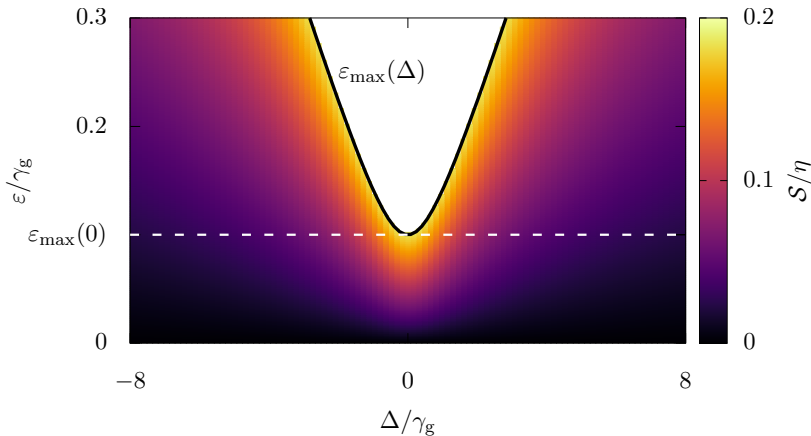


FIGURE 5.5: Extended Arnold tongue for the equatorial limit-cycle oscillator introduced in Section 5.2.6 with imbalanced dissipation rates, $\gamma_d/\gamma_g = 100$, subject to a semiclassical signal, $t_{0,1} = t_{-1,0} = 0.5$, $t_{-1,1} = 0$. Usually, the Arnold tongue is plotted for any detuning Δ up to a maximum cutoff value $\varepsilon_{\max}(0)$, indicated here by a dashed white line. Our framework allows us to derive the boundary between the synchronization regime (colored) and the forcing regime (white) as a function of the detuning, $\varepsilon(\Delta) = \eta/\sqrt{(\gamma_d^2 + \Delta^2)^{-1} + (\gamma_g^2 + \Delta^2)^{-1}}$, which is represented by the solid black line. The Arnold tongue is extended for nonzero detuning and becomes a snake-like split tongue. The numerical value of the threshold parameter is $\eta = 0.1$.

This yields the classic triangular region of synchronization called “Arnold tongue” shown in Figure 2.7. Moreover, there is a crossover from synchronization to forced oscillation if the signal strength becomes too large. Therefore, the Arnold tongue is typically plotted up to an arbitrary signal strength ε_{\max} that is qualitatively chosen to ensure that the signal is only weakly perturbing the limit cycle for any value of the detuning [Lee *et al.*, 2014; Sonar *et al.*, 2018; Roulet and Bruder, 2018a,b].

Our method allows us to go beyond this qualitative approach and to formally derive an analytical upper boundary of the Arnold tongue by explicitly tracking the validity of the perturbation theory for a fixed threshold η . Figure 5.5 illustrates this result for the equatorial limit cycle introduced in Section 5.2.6 and stabilized by the transitions shown in Figure 5.2(a). We can obtain the maximum signal that is permitted on resonance, $\varepsilon_{\max}(0)$, which determines the maximal signal strength ε_{\max} for a simple horizontal cut of the Arnold tongue, shown by the dashed white line in Figure 5.5. However, our results reveal that the boundary of the synchronization region is actually a function of the detuning, $\varepsilon_{\max}(\Delta)$, *i.e.*, the standard horizontal cut discards an entire part of the Arnold tongue. The physical origin of this uncharted region is that the ability of the signal to synchronize the limit-cycle oscillator (*i.e.*, to build up coherences) is reduced if the detuning is increased. To compensate this decrease, the signal strength can be increased beyond the resonant bound,

$$\varepsilon_{\max}(\Delta) \geq \varepsilon_{\max}(0) .$$

Therefore, the Arnold tongue must be extended to larger off-resonant drive strengths and becomes a snake-like split tongue.

In the following sections, we will apply our framework to specific well-known limit cycles to determine the maximum synchronization that is possible in each system. First, we will discuss the quantum vdP model.

5.4 Van der Pol limit cycle

The vdP oscillator has been proposed a century ago [van der Pol, 1926] and has become an important model to gain theoretical insight into the phenomenon of synchronization. After the success of the model in the classical world, it has been quantized and studied in the regime of a few excitations to probe features of quantum synchronization [Lee and Sadeghpour, 2013; Walter *et al.*, 2014]. At first sight, it may not be clear whether any link can be drawn between a mathematical model formulated within the position-momentum phase space of an oscillator and a spin-1 system, which is a purely quantum system with no classical analogue. However, we will show that, when operated deep in quantum regime, the vdP limit cycle can be faithfully represented in the spin-1 platform, which grants access to tractable analytics and demonstrates the versatility of the most elementary quantum unit to study quantum synchronization.

5.4.1 Harmonic oscillator vs. spin 1

The defining characteristic of the vdP model is its stabilization of self-sustained oscillations, which is balancing a linear gain of energy against a nonlinear damping. This is the key feature used to construct the quantum model of the vdP limit-cycle oscillator proposed by Lee and Sadeghpour [2013] and Walter *et al.* [2014]. As derived in Section 2.6, a quantum-mechanical system that converges to the dynamics of a classical weakly nonlinear vdP oscillator is given by a harmonic oscillator, $\hat{H}_{\text{sys}} = \hbar\omega_0\hat{a}^\dagger\hat{a}$ with single-photon gain and two-photon loss processes, $\hat{O}_g = \hat{a}^\dagger$ and $\hat{O}_d = \hat{a}^2$, respectively, [Lee and Sadeghpour, 2013; Walter *et al.*, 2014]

$$\frac{d}{dt}\hat{\rho} = -\frac{i}{\hbar} \left[\hbar\omega_0\hat{a}^\dagger\hat{a}, \hat{\rho} \right] + \gamma_g\mathcal{D}[\hat{a}^\dagger]\hat{\rho} + \gamma_d\mathcal{D}[\hat{a}^2]\hat{\rho}.$$

We will now discuss how the quantum vdP model defined for a harmonic oscillator can be mapped onto a spin-1 system. The vdP oscillator can be brought to the quantum regime by increasing the damping rate, $\gamma_d \gg \gamma_g$, such that occupied Fock states are strongly relaxed towards the bottom of the energy ladder except for the first excited state, which is unaffected by the two-photon loss. The oscillator is then confined in the vicinity of the first excited state and mostly couples to the vacuum and the two-photon Fock state when submitted to a weak signal. Hence, deep in the quantum regime $\gamma_d \gg \gamma_g$, the van der Pol oscillator can effectively be restricted to the three lowest Fock states [Lee and Sadeghpour, 2013; Walter *et al.*, 2014]. Therefore, the three levels of a spin-1 system provide a valid support for the vdP limit cycle. To implement the dissipative dynamics in the spin platform, we consider a single-excitation gain process and a two-excitation loss process of the form

$$\begin{aligned} \hat{O}_g &= \hat{S}_z\hat{S}_+ - \hat{S}_+\hat{S}_z/\sqrt{2}, \\ \hat{O}_d &= \hat{S}_-^2/\sqrt{2}, \end{aligned}$$

with the transition rates γ_g and γ_d , respectively, as shown in Figure 5.2(b). The numerical prefactors are chosen such that the matrix representations of \hat{O}_g and \hat{O}_d are identical to the matrix representations of the creation \hat{a}^\dagger and two-photon annihilation \hat{a}^2 operators of a harmonic oscillator restricted to the three lowest Fock states.

Similarly, we renormalize the signal coefficients for the rest of the section as follows:

$$\begin{aligned} t_{0,1} &= \tau_{0,1} , \\ t_{-1,0} &= \tau_{-1,0}/\sqrt{2} , \\ t_{-1,1} &= \tau_{-1,1}/\sqrt{2} . \end{aligned} \tag{5.31}$$

Having specified the stabilization of the limit cycle, we obtain the steady-state populations by solving Equation (5.11) for the leading order $k = 0$, *i.e.*, $\mathcal{L}_0 \hat{\rho}^{(0)} = 0$. This yields the limit-cycle populations

$$\begin{aligned} \rho_{1,1}^{(0)} &= \frac{\gamma_g}{3\gamma_d + \gamma_g} , \\ \rho_{0,0}^{(0)} &= \frac{\gamma_d}{3\gamma_d + \gamma_g} , \\ \rho_{-1,-1}^{(0)} &= \frac{2\gamma_d}{3\gamma_d + \gamma_g} . \end{aligned} \tag{5.32}$$

In the quantum regime $\gamma_d \gg \gamma_g$, the populations converge to the values $(0, 1/3, 2/3)$, which are precisely those of a van der Pol limit cycle implemented in a harmonic oscillator [Lee and Sadeghpour, 2013; Walter *et al.*, 2014]. Hence, as long as the oscillator is confined deep in the quantum regime, its effective density matrix truncated to the first three levels of the harmonic ladder is identical to that of a spin-based vdP oscillator. Since the perturbation expansion (5.11) is valid for both oscillator-based and spin-based systems, the equivalence remains true once a signal \mathcal{L}_{ext} is applied. Conversely, any difference between the states of the two platforms indicates that the oscillator is transitioning towards the classical regime, populating higher Fock states, and thus losing the possibility to be represented in a spin-1 system.

To conclude the comparison, we note that there remains a fundamental difference between the two platforms, namely the phase space representation which is at the core of the synchronization phenomenon. For a spin-based oscillator, the infinite position-momentum plane of a harmonic oscillator is replaced by a sphere, *i.e.*, a space of different topology. Nevertheless, as discussed in Appendix B, a phase distribution $P_{\hat{\rho}}(\phi)$ for oscillator-based systems and a corresponding shifted phase distribution $S_{\hat{\rho}}(\phi)$ can be defined in several ways. For the approach based on phase eigenstates introduced by Susskind and Glogower [1964], which has been used by Hush *et al.* [2015] and Lörch *et al.* [2016] to quantify quantum synchronization, one finds

$$\begin{aligned} S_{\hat{\rho}}^{\text{osc}}(\phi) &= \frac{1}{2\pi} |\rho_{1,0} + \rho_{2,1}| \cos[\phi + \arg(\rho_{1,0} + \rho_{2,1})] \\ &\quad + \frac{1}{2\pi} |\rho_{2,0}| \cos[2\phi + \arg(\rho_{2,0})] . \end{aligned} \tag{5.33}$$

This result has the same form as the expression (5.20) for spin-based systems up to a different numerical prefactor of the $\cos(\phi)$ term. Therefore, the qualitative synchronization behavior of the vdP model will be identical in both platforms and we can exploit the spin system to characterize its deep quantum limit analytically. For the rest of this section, formulas are given in the deep quantum limit $\gamma_d \gg \gamma_g$ and in the limit $\gamma_d \gg \Delta$ unless stated differently.

5.4.2 Semiclassical and squeezing signal

We start by considering a situation explored in a recent numerical study, which showed that the synchronization of a vdP oscillator can be significantly enhanced by exploiting the quantumness of the system, specifically by adding a squeezing component to a semiclassical signal [Sonar *et al.*, 2018]. Our analytical study will reveal that there is actually an optimal amplitude of the squeezing component beyond which synchronization decreases again.

Using Equation (5.15), we compute the first-order correction $\hat{\rho}^{(1)}$, which is valid for arbitrary dissipative rates,

$$\rho_{1,0}^{(1)} = \frac{2\sqrt{2}i\gamma_g\tau_{-1,0}}{(\gamma_d + \gamma_g + i\Delta)(3\gamma_g + 2i\Delta)} \left[\rho_{0,0}^{(0)} - \rho_{-1,-1}^{(0)} \right] + \frac{\sqrt{2}i\tau_{0,1}}{\gamma_d + \gamma_g + i\Delta} \left[\rho_{1,1}^{(0)} - \rho_{0,0}^{(0)} \right], \quad (5.34a)$$

$$\rho_{0,-1}^{(1)} = \frac{2i\tau_{-1,0}}{3\gamma_g + 2i\Delta} \left[\rho_{0,0}^{(0)} - \rho_{-1,-1}^{(0)} \right], \quad (5.34b)$$

$$\rho_{1,-1}^{(1)} = \frac{2\sqrt{2}i\tau_{-1,1}}{\gamma_g + 2\gamma_d + 4i\Delta} \left[\rho_{1,1}^{(0)} - \rho_{-1,-1}^{(0)} \right]. \quad (5.34c)$$

Combining this result with Equation (5.20), we obtain the synchronization measure

$$\begin{aligned} \mathcal{S}_{\varepsilon\hat{\rho}^{(1)}}(\phi) &= \varepsilon \frac{3}{8\sqrt{2}} |\rho_{1,0}^{(1)} + \rho_{0,-1}^{(1)}| \cos \left[\phi + \arg(\rho_{1,0}^{(1)} + \rho_{0,-1}^{(1)}) \right] \\ &\quad + \varepsilon \frac{1}{2\pi} |\rho_{1,-1}^{(1)}| \cos \left[2\phi + \arg(\rho_{1,-1}^{(1)}) \right]. \end{aligned}$$

Inspection of Equation (5.34) reveals that, by changing the phase of the signal component $\tau_{-1,1}$, we can shift the maxima of the $\cos(2\phi)$ term relative to the maximum of the $\cos(\phi)$ term. If the condition

$$2 \arg \left[\rho_{1,0}^{(1)} + \rho_{0,-1}^{(1)} \right] = \arg \left[\rho_{1,-1}^{(1)} \right] \quad (5.35)$$

holds, both terms share a common maximum at $\phi = -\arg[\rho_{1,-1}^{(1)}]/2$. In the following, we assume that the phase of $\tau_{-1,1}$ has been adjusted in this way such that Equation (5.21) takes the form

$$\mathcal{S}(\varepsilon\hat{\rho}^{(1)}) = \varepsilon \left[\frac{3}{8\sqrt{2}} |\rho_{1,0}^{(1)} + \rho_{0,-1}^{(1)}| + \frac{1}{2\pi} |\rho_{1,-1}^{(1)}| \right]. \quad (5.36)$$

This result indicates that adding a squeezing signal will increase the synchronization measure \mathcal{S} but this effect may be compensated by a decrease of the overall signal strength ε , which is determined according to Equation (5.25).

Following Sonar *et al.* [2018], we now focus on a semiclassical signal. In the spin system considered here, this corresponds to fixing the coefficients as $\tau_{0,1} = \tau_{-1,0}$ and $\tau_{-1,1} \neq 0$. The resulting synchronization measure \mathcal{S} is plotted in Figure 5.6. Near resonance, $\Delta \approx 0$, \mathcal{S} corroborates the numerical results of Sonar *et al.* [2018], namely, the vdP oscillator synchronizes better to signals dominated by a squeezing harmonic where

$$\tau_{\text{ratio}} = \frac{|\tau_{-1,1}|}{|\tau_{0,1}|} \gg 1. \quad (5.37)$$

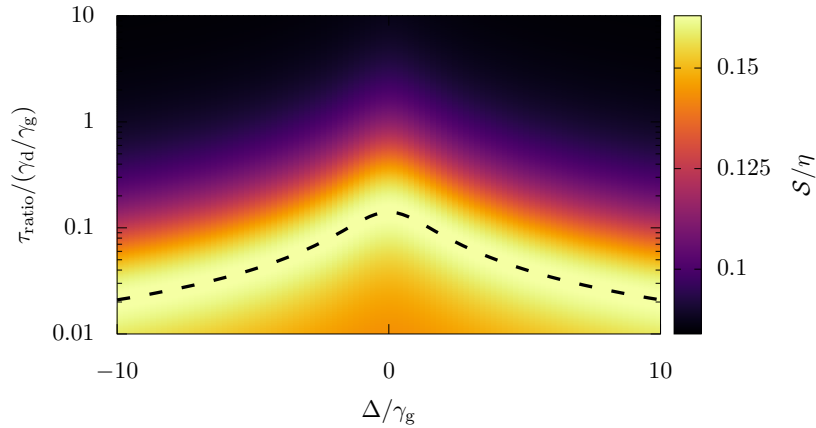


FIGURE 5.6: Synchronization of the van der Pol oscillator deep in the quantum regime to a combination of semiclassical and squeezing components at relative strength $\tau_{\text{ratio}} = |\tau_{-1,1}|/|\tau_{0,1}|$. The color bar ranges from the minimum synchronization $\sqrt{5}/2/6\pi$ achieved for $\tau_{\text{ratio}} \rightarrow \infty$ to the maximum synchronization $\mathcal{S}/\eta = \sqrt{5(32 + 9\pi^2)}/48\pi$ at the optimal ratio $\tau_{\text{ratio}}^{\text{opt}}$, which is indicated by the dashed black line. Parameters are $\gamma_d/\gamma_g = 1000$ and $\eta = 0.1$.

However, it seems that this advantage is substantially reduced, if not suppressed, when trying to lock to an off-resonant signal $|\Delta| \gg \gamma_g$. There, the semiclassical component should be favored in order to maximize phase localization.

To investigate this trade-off and establish whether squeezing is only beneficial within a narrow bandwidth around resonance, we turn to analytics and investigate the synchronization measure \mathcal{S} more closely. In the quantum regime $\gamma_d \gg \gamma_g$, it takes the compact form

$$\mathcal{S} = \eta \frac{\sqrt{5}}{48\pi} \frac{3\pi\gamma_d + 8\tau_{\text{ratio}}\sqrt{9\gamma_g^2 + 4\Delta^2}}{\sqrt{\gamma_d^2 + 2\tau_{\text{ratio}}^2(9\gamma_g^2 + 4\Delta^2)}}. \quad (5.38)$$

Indeed, the maximum synchronization

$$\max_{\tau_{\text{ratio}}} \frac{\mathcal{S}}{\eta} = \frac{\sqrt{5(32 + 9\pi^2)}}{48\pi} \approx 0.163$$

is achieved by the optimal squeezing ratio

$$\tau_{\text{ratio}}^{\text{opt}} = \frac{4}{3\pi} \frac{\gamma_d}{\sqrt{9\gamma_g^2 + 4\Delta^2}},$$

which is maximum on resonance and tends to zero for large detuning. On the other hand, synchronization to a purely semiclassical signal without the squeezing component, $\tau_{\text{ratio}} = 0$, is limited to

$$\lim_{\tau_{\text{ratio}} \rightarrow 0} \frac{\mathcal{S}}{\eta} = \frac{\sqrt{5}}{16} \approx 0.140.$$

Thus, having a squeezing component in addition to a semiclassical one is always beneficial to synchronize the vdP limit-cycle oscillator. However, note that synchronization

decreases again in the limit of a very strong squeezing signal, where we find

$$\lim_{\tau_{\text{ratio}} \rightarrow \infty} \frac{\mathcal{S}}{\eta} = \frac{1}{6\pi} \sqrt{\frac{5}{2}} \approx 0.084 .$$

The existence of an optimal squeezing amplitude has not been observed in the numerical study by Sonar *et al.* [2018] since the semiclassical and squeezing signals could not be compared to each other. In our approach, different signals can be compared since the signal strength ε is adjusted such that each signal has the same impact on the deformation of the limit cycle according to Equation (5.25). An increase of the coherence $\rho_{1,-1}^{(1)}$ due to a squeezing signal must be compensated by a decrease of the semiclassical signal components, which decreases the coherences $\rho_{1,0}^{(1)}$ and $\rho_{0,-1}^{(1)}$. Consequently, there must be an optimal combination of semiclassical and squeezing that delivers the largest value of the synchronization measure \mathcal{S}/η .

The different numerical values of maximum synchronization for a pure semiclassical or a pure squeezing signal stem from the different weights that the phase-space representation attributes to the spin-1 states. These weights are reflected in the numerical prefactors of the synchronization measure (5.20). The same amplitude of the terms $|\rho_{1,0}^{(1)} + \rho_{0,-1}^{(1)}|$ and $|\rho_{1,-1}^{(1)}|$, determined by the maximum signal strength (5.25), will lead to different amplitudes of $\mathcal{S}_{\hat{\rho}}(\phi)$, as illustrated by the relation

$$\left(\frac{3}{8\sqrt{2}}\right)^{-1} \lim_{\tau_{\text{ratio}} \rightarrow 0} \frac{\mathcal{S}}{\eta} = \left(\frac{1}{2\pi}\right)^{-1} \lim_{\tau_{\text{ratio}} \rightarrow \infty} \frac{\mathcal{S}}{\eta} .$$

5.4.3 Optimized signal

In the previous section, we discussed results that had previously been obtained in a harmonic-oscillator based system, and we demonstrated the power of the spin-1 platform to go beyond a numerical analysis using our framework for quantum synchronization. We now conclude our study of the vdP limit-cycle oscillator by answering the fundamental question of what is the maximum synchronization that can be achieved for a vdP oscillator deep in the quantum regime.

To this end, we relax the semiclassical restriction $\tau_{0,1} = \tau_{-1,0}$ and employ the following parametrization of the signal:

$$\tau_{0,1} = \cos(\zeta) e^{i\chi} , \quad (5.39a)$$

$$\tau_{-1,0} = \sin(\zeta) , \quad (5.39b)$$

$$|\tau_{-1,1}| = \tau_{\text{ratio}} . \quad (5.39c)$$

The angle $0 \leq \zeta \leq \pi/2$ parametrizes the strength of the two semiclassical signal components and the angle $0 \leq \chi \leq 2\pi$ determines their relative phase. The phase of the squeezing drive is still fixed by the condition (5.35) and τ_{ratio} again parametrizes the strength of the squeezing component. For this parametrization, the synchronization measure has the general form

$$\mathcal{S} = \frac{p_1}{\sqrt{p_2 + p_3 \tau_{\text{ratio}}^2}} (p_4 + p_5 \tau_{\text{ratio}}) ,$$

where the fraction stems from the definition of ε in Equation (5.25), and the term in brackets stems from the square brackets in Equation (5.36). Deep in the quantum

regime, the coefficients p_k have the following form to leading order in γ_g/γ_d :

$$\begin{aligned} p_1 &= \frac{\sqrt{5}}{3}\eta + \mathcal{O}\left[\frac{\gamma_g}{\gamma_d}\right], \\ p_2 &= \frac{8\sin^2(\zeta)}{9(9\gamma_g^2 + 4\Delta^2)} + \mathcal{O}\left[\frac{\gamma_g}{\gamma_d}\right], \\ p_3 &= \frac{16}{9\gamma_g^2}\frac{\gamma_g^2}{\gamma_d^2} + \mathcal{O}\left[\left(\frac{\gamma_g}{\gamma_d}\right)^3\right], \\ p_4 &= \frac{1}{4\sqrt{2}}\frac{\sin(\zeta)}{\sqrt{9\gamma_g^2 + 4\Delta^2}} + \mathcal{O}\left[\frac{\gamma_g}{\gamma_d}\right], \\ p_5 &= \frac{\sqrt{2}}{3\pi\gamma_g}\frac{\gamma_g}{\gamma_d} + \mathcal{O}\left[\left(\frac{\gamma_g}{\gamma_d}\right)^2\right]. \end{aligned}$$

We have $p_3/p_2 = \mathcal{O}[(\gamma_g/\gamma_d)^2]$ and $p_5/p_4 = \mathcal{O}(\gamma_g/\gamma_d)$, *i.e.*, the terms p_3 and p_5 stemming from the squeezing signal are suppressed compared to the corresponding terms originating from the semiclassical signal. Synchronization is maximal if both signal components contribute equally to \mathcal{S} , therefore, the optimal ratio between the semiclassical and the squeezing components is of the order of γ_d/γ_g ,

$$\tau_{\text{ratio}}^{\text{opt}} = \frac{p_2 p_5}{p_3 p_4} = \frac{4\sin(\zeta)\gamma_g}{3\pi\sqrt{9\gamma_g^2 + 4\Delta^2}}\frac{\gamma_d}{\gamma_g} + \mathcal{O}(1),$$

which compensates the asymmetry between the semiclassical and squeezing contributions and maximizes \mathcal{S} with respect to the parameter τ_{ratio} . Focusing on the resonant case $\Delta = 0$ for simplicity, we find that the optimal relative phase of the semiclassical signal components is

$$\chi^{\text{opt}}|_{\Delta=0} = 0$$

and that the optimal relative strength of the two components is given by the angle

$$\zeta^{\text{opt}}|_{\Delta=0} = \text{arccot}\left(\frac{\sqrt{2}\gamma_d}{3\gamma_g}\right) + \mathcal{O}\left[\left(\frac{\gamma_g}{\gamma_d}\right)^2\right].$$

This result is illustrated in Figure 5.7. As displayed in the inset, the maximum synchronization that is possible for a vdP limit-cycle oscillator in the quantum regime takes the value

$$\left.\frac{\mathcal{S}}{\eta}\right|_{\Delta=0, \chi^{\text{opt}}, \zeta^{\text{opt}}, \tau_{\text{ratio}}^{\text{opt}}} = \frac{\sqrt{40 + \frac{45}{2}\pi^2}}{24\pi} \approx 0.215. \quad (5.40)$$

This results will allow us to compare the vdP model with other limit cycles available in the spin-1 system. Note that, despite the convergence $\zeta^{\text{opt}} \rightarrow 0$ deep in the quantum regime, the semiclassical signal component $\tau_{-1,0}$ cannot be simply switched off by setting $\zeta = 0$ because synchronization will then be limited to

$$\lim_{\zeta \rightarrow 0} \left.\frac{\mathcal{S}}{\eta}\right|_{\Delta=0, \chi^{\text{opt}}, \tau_{\text{ratio}}^{\text{opt}}} = \frac{\sqrt{5(32 + 9\pi^2)}}{48\pi} \approx 0.163.$$

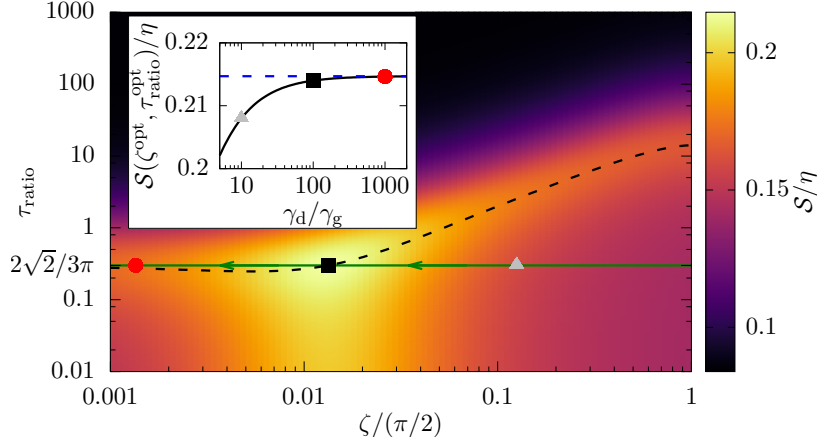


FIGURE 5.7: **Main plot:** Synchronization of the van der Pol oscillator deep in the quantum regime, $\gamma_d/\gamma_g = 100$, to a resonant signal of the general form (5.39) with $\chi = 0$. For reference, the dashed black line indicates the optimal ratio of squeezing for a given ζ . The solid markers indicate from right to left the optimal signal parameters for $\gamma_d/\gamma_g = 10, 100$, and 1000 . In the quantum regime, the optimal value of τ_{ratio} converges to $\tau_{\text{ratio}}^{\text{opt}} = 2\sqrt{2}/3\pi$ and ζ^{opt} decreases with γ_d/γ_g , as indicated by the solid green arrows. **Inset:** S/η evaluated at the optimal values $\tau_{\text{ratio}}^{\text{opt}}$ and ζ^{opt} as a function of γ_d/γ_g . Maximum synchronization is obtained in the limit $\gamma_d/\gamma_g \rightarrow \infty$ where S/η converges to $\sqrt{40 + 45\pi^2/2}/24\pi \approx 0.215$, indicated by the dashed blue line. The threshold parameter is $\eta = 0.1$.

5.5 Equatorial limit cycle

5.5.1 Limit-cycle stabilization

We now move away from classically-inspired limit cycles and consider the equatorial limit cycle used in Section 5.2.6. It is stabilized by the dissipative coupling operators

$$\begin{aligned}\hat{O}_g &= \hat{S}_+ \hat{S}_z, \\ \hat{O}_d &= \hat{S}_- \hat{S}_z,\end{aligned}$$

with rates γ_g and γ_d , respectively. The key feature of the resulting stabilization is its simplicity, because the extremal states $|\pm 1\rangle$ are independently relaxed to the equatorial state $|0\rangle$ and the limit cycle is

$$\hat{\rho}^{(0)} = |0\rangle\langle 0|. \quad (5.41)$$

Incidentally, the absence of initial population in the extremal states $\rho_{\pm 1, \pm 1}^{(0)} = 0$ renders the limit cycle insensitive to a squeezing signal, such that $\rho_{1, -1}^{(1)}$ is bound to stay zero,

$$\begin{aligned}\rho_{1,0}^{(1)} &= -\frac{i\sqrt{2}}{\gamma_d + i\Delta} t_{0,1}, \\ \rho_{0,-1}^{(1)} &= +\frac{i\sqrt{2}}{\gamma_g + i\Delta} t_{-1,0}, \\ \rho_{1,-1}^{(1)} &= 0.\end{aligned} \quad (5.42)$$

However, the two remaining coherences can be built up independently by the signal components of the corresponding transitions. Therefore, we can optimize them independently to maximize the synchronization measure \mathcal{S} given by Equation (5.20), and we will find that a straightforward combination of the semiclassical signal components outperforms the maximal synchronization achieved by a vdP limit cycle.

To proceed further, we choose the following parametrization of the signal:

$$t_{0,1} = \cos(\zeta)e^{i\chi}, \quad (5.43a)$$

$$t_{-1,0} = \sin(\zeta), \quad (5.43b)$$

$$t_{-1,1} = 0. \quad (5.43c)$$

Remarkably, this time the synchronization measure can be expressed in a compact form without imposing any constraint on the signal,

$$\frac{\mathcal{S}}{\eta} = \frac{3}{16} \sqrt{1 - 2 \frac{\sin(\zeta) \cos(\zeta) \cos(\chi + \alpha)}{r \cos^2(\zeta) + \frac{1}{r} \sin^2(\zeta)}}, \quad (5.44)$$

where we defined the abbreviations

$$r = \sqrt{\frac{\gamma_g^2 + \Delta^2}{\gamma_d^2 + \Delta^2}},$$

$$\alpha = \arg\left(\frac{1}{\gamma_g - i\Delta} \frac{1}{\gamma_d + i\Delta}\right).$$

5.5.2 Semiclassical signal

First, we analyze synchronization to a semiclassical signal, $t_{0,1} = t_{-1,0}$, which corresponds to $\chi = 0$ and $\zeta = \pi/4$ in the parametrization (5.43). This reproduces the scenario studied by Roulet and Bruder [2018a], where synchronization was found to vanish for balanced dissipation rates $\gamma_d = \gamma_g$. Within the present framework, we can go a step further and identify the physical origin of this singularity. For balanced rates, the semiclassical signal builds up both coherences at the same strength against the same relaxation rate, such that the coherences have identical absolute values but opposite phases, $\rho_{0,1} = -\rho_{-1,0}$. Since the synchronization measure (5.20) is a function of their sum, $|\rho_{0,1} + \rho_{-1,0}|$, this will lead to destructive interference, captured by the factor $\cos(\chi + \alpha) = 1$ in Equation (5.44), and no synchronization is observed,

$$\left. \frac{\mathcal{S}}{\eta} \right|_{\gamma_g = \gamma_d, \chi = 0, \zeta = \frac{\pi}{4}} = 0.$$

Building on this understanding, we find that for any finite asymmetry between the rates, one of the coherences dominates such that the impact of the destructive interference is reduced,

$$\left. \frac{\mathcal{S}}{\eta} \right|_{\chi = 0, \zeta = \frac{\pi}{4}} = \frac{3}{16} \sqrt{1 - 2 \frac{\gamma_g \gamma_d + \Delta^2}{\gamma_d^2 + \gamma_g^2 + 2\Delta^2}}. \quad (5.45)$$

For imbalanced rates, synchronization is largest on resonance, $\Delta = 0$. Maximum synchronization to a semiclassical signal is obtained for highly asymmetric relaxation

rates,

$$\lim_{\gamma_d/\gamma_g \rightarrow \infty} \frac{\mathcal{S}}{\eta} \Big|_{\chi=0, \zeta=\frac{\pi}{4}, \Delta=0} = \frac{3}{16} \approx 0.188 ,$$

where only one of the coherences contributes without being suppressed by the other. Comparing to the vdP limit cycle, this value is larger than the one obtained for the same semiclassical signal, $\mathcal{S}/\eta \approx 0.140$, but it is lower than the one obtained for the optimized signal, $\mathcal{S}/\eta \approx 0.215$, which combined all three coherences.

5.5.3 Optimized signal

Equation (5.42) shows that in the case of an equatorial limit cycle, the coherences $\rho_{1,0}^{(1)}$ and $\rho_{0,-1}^{(1)}$ can be built up individually by modifying the two corresponding semiclassical signal components. To improve on the vdP model, we thus aim for a signal where the coherences are built in phase and therefore interfere constructively. At the level of the synchronization measure (5.44), this amounts to require $\cos(\chi + \alpha) = -1$. We are then left with the task of maximizing the term $2 \sin(\zeta) \cos(\zeta) / [\cos^2(\zeta)r + \sin^2(\zeta)/r]$. This yields the optimal angles

$$\chi^{\text{opt}} = \pi - \alpha , \quad (5.46a)$$

$$\zeta^{\text{opt}} = \arctan(r) , \quad (5.46b)$$

where the second condition implies that both coherences have the same amplitude. The resulting constructive interference yields

$$\frac{\mathcal{S}}{\eta} \Big|_{\chi^{\text{opt}}, \zeta^{\text{opt}}} = \frac{3}{16} \sqrt{2} \approx 0.265 , \quad (5.47)$$

which is the maximum synchronization that is possible for the equatorial limit cycle and which is larger than the corresponding result for a quantum vdP limit cycle. This result is illustrated in Figure 5.8 for the case of balanced dissipation rates, where synchronization to a semiclassical signal is not possible.

5.6 Maximum synchronization in the quantum regime

So far, we used the framework for quantum synchronization developed in Section 5.2 to compare specific limit-cycle oscillators and to optimize the applied signals in the quantum regime. However, we can go beyond this and derive a fundamental limit to synchronization deep in the quantum regime. In contrast to the previous sections, we will not focus on any specific limit cycle. Instead, we will only rely on the paradigm of synchronization and on the properties of the spin-1 system supporting the limit cycle, which follow from the laws of quantum mechanics. With these quite general assumptions, we will perform an optimization over all signals and all possible limit cycles of a spin-1 system.

5.6.1 Upper bound on quantum synchronization

In a first step, we derive an upper bound on the synchronization measure $\mathcal{S}(\hat{\rho})$ based on the analytical insights gathered in the previous sections. As discussed in Section 5.2.2,

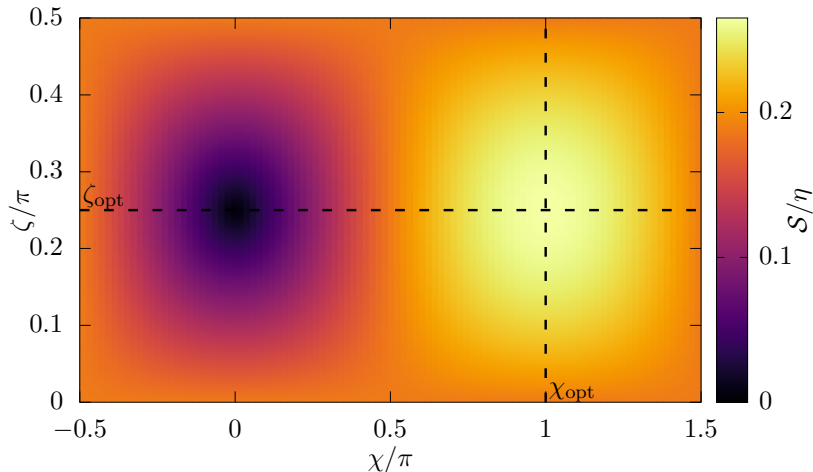


FIGURE 5.8: Equatorial limit cycle with balanced dissipation rates $\gamma_g = \gamma_d$ subject to a resonant signal parametrized by the convention of Equation (5.43). The relative phase χ between the semiclassical signal components determines the relative phase of the coherences $\rho_{0,1}$ and $\rho_{-1,0}$. They interfere constructively for $\chi^{\text{opt}} = \pi$ and destructively for $\chi = 0$. The parameter ζ determines if the amplitudes of the two signal components are equal ($\zeta^{\text{opt}} = \pi/4$) or different. The maximum synchronization for the equatorial limit cycle, $\mathcal{S}/\eta = 3\sqrt{2}/16 \approx 0.265$, is obtained at the intersection of the dashed black lines where both coherences have the same amplitude and interfere constructively. A semiclassical signal corresponds to $\chi = 0$. The threshold parameter is $\eta = 0.1$.

the rotational invariance of the limit-cycle state requires a diagonal steady-state density matrix, which we parametrize by

$$\hat{\rho}^{(0)} = \frac{1}{2} \begin{pmatrix} 1 - a - \delta & & \\ & 2a & \\ & & 1 - a + \delta \end{pmatrix}. \quad (5.48)$$

Here $0 \leq a \leq 1$ is the population of the equatorial state $|0\rangle$, and δ is a real parameter that satisfies the conditions $|a \pm \delta| \leq 1$ and characterizes the asymmetry in the populations of the extremal states $|\pm 1\rangle$. In Equation (5.20) we have identified the coherences between energy eigenstates as the resource of quantum synchronization. The first-order correction of the expansion (5.18) can be parametrized as follows:

$$\hat{\rho}^{(1)} = \begin{pmatrix} 0 & b & c \\ b^* & 0 & d \\ c^* & d^* & 0 \end{pmatrix}, \quad (5.49)$$

where b , c , and d are arbitrary complex parameters. As usual, we further set the phase of c such that the maxima of the $\cos(\phi)$ and $\cos(2\phi)$ terms in $S_{\hat{\rho}}(\phi)$ coincide.

Substituting Equation (5.25) into Equation (5.21), we find that the synchronization measure $\mathcal{S}(\hat{\rho})$ is a product of the term

$$\eta \|\hat{\rho}^{(0)}\| = \frac{\eta}{\sqrt{2}} \sqrt{1 - 2a + 3a^2 + \delta^2},$$

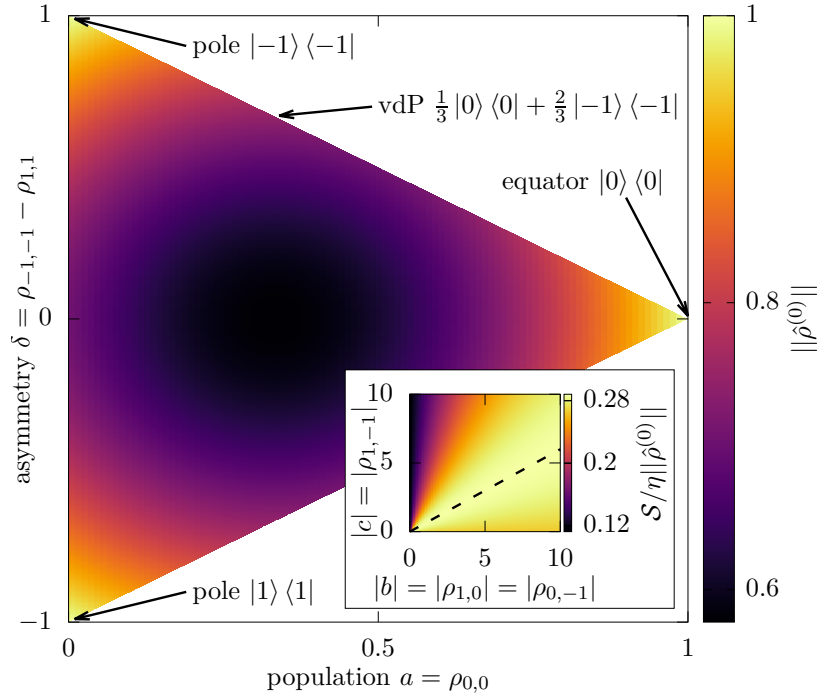


FIGURE 5.9: **Main plot:** Value of $\|\hat{\rho}^{(0)}\|$ for the triangular set of physical limit-cycle states $\hat{\rho}^{(0)}$ parametrized by Equation (5.48). The minimum value of the norm, $1/\sqrt{3}$, is obtained for $(a, \delta) = (1/3, 0)$. The maximum value, 1, is obtained for the extremal points of the triangle, which represent pure states. The van der Pol limit cycle corresponds to the point $(a, \delta) = (1/3, 2/3)$. **Inset:** Factor $(3|2b|/8\sqrt{2} + |c|/2\pi)/\|\hat{\rho}^{(1)}\|$ as a function of the coherences b and c introduced in Equation (5.49). The maximum value $\sqrt{8 + 9\pi^2/2}/8\pi$ is achieved along the dashed black line $|b|/|c| = 3\pi/4\sqrt{2}$. If the coherence $\rho_{-1,1}$ cannot be built up, $|c| = 0$, a value of $3/8\sqrt{2}$ is obtained.

which depends only on the structure (5.48) of the limit cycle and is shown in the main plot of Figure 5.9, and of the term

$$\frac{q_1 |b + d| + q_2 |c|}{\sqrt{2(|b|^2 + |c|^2 + |d|^2)}},$$

which depends only on the coherences introduced in Equation (5.49) and is shown in the inset. The prefactors q_1 and q_2 depend on the phase-space representation and take the values $q_1 = 3/8\sqrt{2}$ and $q_2 = 1/2\pi$ for a spin-based system.

An upper bound to the synchronization achievable in the spin-1 system can be derived by maximizing both terms individually. The norm $\|\hat{\rho}^{(0)}\|$ takes its maximal value of unity for pure energy eigenstates, which are represented by the extremal points of the set of physical limit-cycle states shown in Figure 5.9. On the other hand, the second term of $\mathcal{S}(\hat{\rho})$ is maximized if $b = d$ holds and if the ratio of the coherences satisfies

$$\frac{|b|}{|c|} = \frac{q_1}{q_2} = \frac{3\pi}{4\sqrt{2}},$$

which is indicated by the dashed black line in the inset of Figure 5.9. Taking the product of the two maxima, we find that the synchronization measure is bounded

TABLE 5.1: Synchronization performance $\mathcal{S}(\hat{\rho})/\eta$ of the quantum van der Pol and the equatorial limit cycle for different signals. The results are bounded by the maximum synchronization that can be achieved in a spin-1 system, $\mathcal{S}_{\max} = 0.288\eta$.

limit cycle	signal		
	semiclassical	semiclassical & squeezing	optimal
van der Pol	0.140	0.163	0.215
equatorial	0.188	0.188	0.265

from above by

$$\mathcal{S} \leq \mathcal{S}_{\max} = \eta q_2 \sqrt{\frac{1}{2} + \frac{q_1^2}{q_2^2}}. \quad (5.50)$$

This bound takes the numerical value

$$\frac{\mathcal{S}_{\max}}{\eta} = \frac{\sqrt{2(16 + 9\pi^2)}}{16\pi} \approx 0.288$$

for a spin-based system and

$$\frac{\mathcal{S}_{\max}}{\eta} = \frac{\sqrt{3}}{2\sqrt{2}\pi} \approx 0.195$$

for the phase-space of a harmonic oscillator introduced in Equation (5.33).

5.6.2 Tightness of the bound

As summarized in Table 5.1, all the combinations of limit cycles and signals considered so far stay below the bound (5.50). Therefore, it remains to determine whether any physical limit-cycle oscillator can actually reach the bound \mathcal{S}_{\max} .

This search is complicated by the trade-off that exists between maximizing $\|\hat{\rho}^{(0)}\|$ and reaching the optimal ratio $|b|/|c|$. To illustrate this point, we classify the limit cycles studied in the previous sections with respect to these two quantities. The vdP limit cycle with the optimized signal discussed in Section 5.4.3 successfully implements the optimal ratio of the coherences, but, since its limit cycle is a statistical mixture of different spin states, it does not maximize $\|\hat{\rho}^{(0)}\|$. On the other hand, the equatorial limit cycle discussed in Section 5.5.3 implements the optimal value $\|\hat{\rho}^{(0)}\| = 1$ by stabilizing the pure equatorial state $|0\rangle$, but the symmetry $\rho_{1,1} = \rho_{-1,-1} = 0$ then enforces $|c| = 0$, putting the optimal ratio of the coherences out of reach.

To design a combination of limit cycle and signal that reaches \mathcal{S}_{\max} , we thus need to break the symmetry between the states $|\pm 1\rangle$, while ensuring that the limit cycle remains close to a pure state. To this end, we supplement the equatorial limit cycle by a third decay channel,

$$\begin{aligned} \hat{O}_g &= \hat{S}_+ \hat{S}_z, \\ \hat{O}_d &= \hat{S}_- \hat{S}_z, \\ \hat{O}_{d'} &= \hat{S}_z \hat{S}_-, \end{aligned}$$

as shown in Figure 5.2(c). The additional dissipative channel $\hat{O}_{d'}$ with a corresponding rate $\gamma_{d'}$ induces an asymmetry in the limit cycle,

$$\hat{\rho}^{(0)} = \begin{pmatrix} 0 & \\ \frac{\gamma_g}{\gamma_g + \gamma_{d'}} & \\ & \frac{\gamma_{d'}}{\gamma_g + \gamma_{d'}} \end{pmatrix}. \quad (5.51)$$

We focus on the regime $\gamma_{d'} \ll \gamma_g$ where the limit cycle remains close to the state $|0\rangle$. However, in contrast to the purely equatorial case, the present limit cycle is sensitive to a squeezing signal, *i.e.*, we can exploit the small but finite asymmetry in the populations of the extremal states $|\pm 1\rangle$ to engineer a non-vanishing coherence $|c|$. In the limit $\gamma_{d'} \ll \gamma_g$, the optimal ratio $|b|/|c| = 3\pi/4\sqrt{2}$ is obtained by choosing the amplitude

$$|t_{-1,1}| = \frac{4}{3\pi} \sqrt{\frac{(\gamma_g + \gamma_d)^2 + 4\Delta^2}{\gamma_d^2 + \gamma_g^2 + 2\Delta^2}} \frac{\gamma_g}{\gamma_{d'}} \quad (5.52)$$

of the squeezing component, whereas the angles χ^{opt} and ζ^{opt} are the same as in Equation (5.46). The divergence of the squeezing amplitude in the limit $\gamma_{d'} \rightarrow 0$, $|t_{-1,1}| \propto \gamma_g/\gamma_{d'}$, reflects the fact that the squeezing signal requires an asymmetry between the $|\pm 1\rangle$ states to build up the coherence $\rho_{1,-1}^{(1)}$. The synchronization measure reads

$$\mathcal{S} = \eta \frac{\sqrt{2(16 + 9\pi^2)}}{16\pi} \sqrt{\frac{\gamma_g^2 + \gamma_{d'}^2}{(\gamma_g + \gamma_{d'})^2}} \xrightarrow{\gamma_{d'} \ll \gamma_g} \mathcal{S}_{\text{max}}. \quad (5.53)$$

Hence, in the regime of interest $\gamma_{d'} \ll \gamma_g$, we find that the synchronization converges to the upper bound \mathcal{S}_{max} by approaching the equatorial limit-cycle state with $\|\hat{\rho}^{(0)}\| \approx 1$ while keeping the ratio of the coherences set to $|b|/|c| = 3\pi/4\sqrt{2}$. This result demonstrates that the upper bound (5.50) is tight and indeed corresponds to the maximum synchronization achievable in a spin-1 system. Importantly, this bound applies to all quantum limit-cycle oscillators that can be restricted to the three lowest states in the quantum regime, such as the quantum vdP oscillator.

5.6.3 Discussion

The bound (5.50) optimizes the synchronization measure \mathcal{S} , introduced in Section 5.2.5, over all limit-cycle states and all signals that can be applied in a spin-1 system. These very different systems are made comparable by the universal definition (5.25) of a weak signal strength, which compares the limit-cycle stabilization to the transitions induced by the signal. The question of maximizing the synchronization of a limit-cycle oscillator to an external signal is also subject of current research in classical physics.

Hasegawa and Arita [2014] focus on the limit cycle of circadian clocks, which regulate the periodic daily activity of animals. In this case, the external signal, *i.e.*, the daylight cycle, is given and the task is to find a limit cycle that provides an optimal trade-off between frequency stability of the circadian clock and its ability to synchronize to the daylight cycle. In the quantum case, it is usually easier to modify the external signal than the dissipative limit-cycle stabilization. Nevertheless, our framework allows one to address similar questions in the quantum case.

Harada *et al.* [2010], Zlotnik and Li [2012], and Tanaka [2014] consider the reverse problem of finding an optimal external signal that maximizes the range of detuning

$[\Delta_{\min}, \Delta_{\max}]$ over which synchronization is observed, *i.e.*, the width of the Arnold tongue. The signal $f(\theta)$ is restricted to have (i) a fixed time-averaged power over one period, $\int_0^{2\pi} f^2(\theta) d\theta/2\pi$, (ii) a fixed time-averaged area, $\int_0^{2\pi} |f(\theta)| d\theta/2\pi$, or (iii) a bounded magnitude $|f(\theta)| \leq \text{const}$. The limit-cycle oscillator is characterized by its phase-response function governing the phase equation. In this approach, there is no connection between the signal and the dissipative stabilization of the limit cycle, but the constraints (i) to (iii) allow the authors to compare different signals applied to the same limit-cycle oscillator among each other. The optimal signal is found to be a combination of rescaled and shifted phase-response functions. The same approach has been used by Zlotnik *et al.* [2013] to find a signal that minimizes the transient time to synchronize a limit-cycle oscillator to a signal – a question that is reminiscent of optimal quantum control theory.

Finally, Pikovsky [2015] has considered the case of a noisy classical limit-cycle oscillator subjected to an external signal with fixed time-averaged power. In the limit of very large noise, a purely harmonic signal $f(t) \propto \cos(t)$ is found to be optimal. For the vdP limit cycle, the harmonic drive is also optimal in the limit of very weak noise. However, other limit-cycle oscillators may be optimally synchronized to a biharmonic drive composed of oscillations at $\cos(t)$ and $\cos(2t)$.

5.7 Interference-based quantum synchronization blockade

Discussing the vdP and the equatorial limit cycle, we have already found hints on interference effects between the coherences $\rho_{1,0}$ and $\rho_{0,-1}$. Now, we will discuss this effect in more detail and we will show that such interference effects lead to a novel type of synchronization blockade. For clarity of the formulas, we focus here on the equatorial limit cycle but the same quantum effect is present in other systems, including the quantum vdP limit cycle.

Quantum synchronization blockade was first reported in a study of two coupled nonlinear Kerr oscillators by Lörch *et al.* [2017], where conservation of energy was found to favor the synchronization of detuned oscillators that are approximately stabilized to different Fock states. This behavior is in contrast to the classical expectation that synchronization is strongest on resonance and it is a manifestation of the discrete energy levels with nonequidistant splitting. We now discuss a similar suppression of quantum synchronization on resonance. However, the energy levels of a spin-1 system are equally spaced, therefore, if there is a synchronization blockade, it has to be of a different physical origin than the one discussed by Lörch *et al.* [2017].

Interference-based quantum synchronization blockade is based on the fact that the external signal \hat{H}_{ext} tries to modify the limit-cycle state by transferring population $\rho_{m,m}^{(0)}$ of a spin eigenstate $|m\rangle$ to other states $|n \neq m\rangle$. This generates coherences $\rho_{n,m}^{(1)}$ between the spin eigenstates. Starting from the equatorial state $|0\rangle$, a semiclassical signal has actually two options for population transfer, namely, to the states $|+1\rangle$ or $|-1\rangle$. This corresponds to taking two different paths in an interferometer after passing beam splitter. Since the signal is a coherent interaction, the spin states acquire a fixed phase relation, which is manifested by the buildup of the coherences $\rho_{1,0}^{(1)}$ and $\rho_{0,-1}^{(1)}$ and is a necessary condition to observe phase localization. To determine the phase distribution, only the frequency difference between the spin states matters such that the transitions $|1\rangle \leftrightarrow |0\rangle$ and $|0\rangle \leftrightarrow |-1\rangle$ are identical. This corresponds to recombining the two paths of the interferometer at a second beam splitter and gives rise to an interference between $\rho_{1,0}^{(1)}$ and $\rho_{0,-1}^{(1)}$.

We previously found that for any value of the detuning Δ , there exists a combination of optimal angles (5.46) such that synchronization is maximal. On resonance, $\Delta = 0$, the condition on the relative phase is $\chi^{\text{opt}} = \pi$. On the other hand, shifting the angle to $\chi = 0$ leads to perfect destructive interference, $\mathcal{S}/\eta = 0$. If we keep $\chi = 0$ fixed and increase the detuning, the coherences (5.42) start to rotate clockwise in the complex plane up to an angle of $\pi/2$ for infinitely large detuning. This is shown in Figure 5.10. If the dissipation rates are balanced, $\gamma_g = \gamma_d$, both coherences rotate together and the interference remains destructive regardless of the detuning. However, if one of the dissipation rates dominates, the rotation of the corresponding coherence lags behind such that the destructive interference is suppressed in a transient regime. This leads to the onset of synchronization away from resonance, as illustrated in the main plot of Figure 5.10.

For the equatorial limit cycle discussed in Section 5.5, the synchronization measure has the form

$$\mathcal{S} = \eta \frac{3}{16} \sqrt{1 - \cos \left(\arctan \left[\frac{(\gamma_d - \gamma_g)\Delta}{\gamma_d \gamma_g + \Delta^2} \right] \right)}, \quad (5.54)$$

where the cosine term approaches zero for a strong lag before coming back to unity. Maximum synchronization is achieved at

$$|\Delta| = \sqrt{\gamma_g \gamma_d},$$

where the synchronization measure converges to

$$\lim_{\gamma_d/\gamma_g \rightarrow \infty} \frac{\mathcal{S}}{\eta} \Big|_{\chi=0, \zeta^{\text{opt}}, |\Delta|=\sqrt{\gamma_g \gamma_d}} = \frac{3}{16} \approx 0.188$$

in the limit of strongly imbalanced rates. Note that this value remains below the fundamental limit (5.47) of the equatorial limit cycle, since the detuning is not able to rotate the coherences up to a relative angle of π , which is the condition for constructive interference.

The revival of destructive interference for very large detuning, $\Delta \gg \gamma_d$, is due to the fact that we constantly reoptimize the amplitudes of the two signal components by changing the angle ζ with the detuning. Therefore, both coherences rotate in the complex plane at a constant amplitude and destructive interference is recovered if both coherences have been rotated by $\pi/2$. Interference-based quantum synchronization blockade is also observed if both signal parameters are kept fixed, $\chi = 0$ and $\zeta = \zeta^{\text{opt}}(\Delta = 0)$, and only the detuning is changed. In this case, both the angle and the absolute value of the coherences change and the coherence associated with the smaller dissipation rate decays to zero, whereas the other one rotates and acquires a larger amplitude.

Interference-based quantum synchronization blockade reveals that having the right relative phase between the signal components is crucial to observe quantum synchronization. This disproves the conjecture by Lee *et al.* [2014] that quantum synchronization in a network of two mutually coupled identical vdP oscillators is only possible for dissipative coupling but not for reactive coupling. Instead, the reactive coupling term investigated in Lee and Sadeghpour [2013] happens to build up coherences that interfere destructively to first order in the interaction strength ε . The synchronization effect observed there is a second-order effect in ε that vanishes in the quantum limit. A similar suppression of synchronization has been observed in a network of two reactively coupled identical equatorial limit-cycle oscillators [Roulet and Bruder,

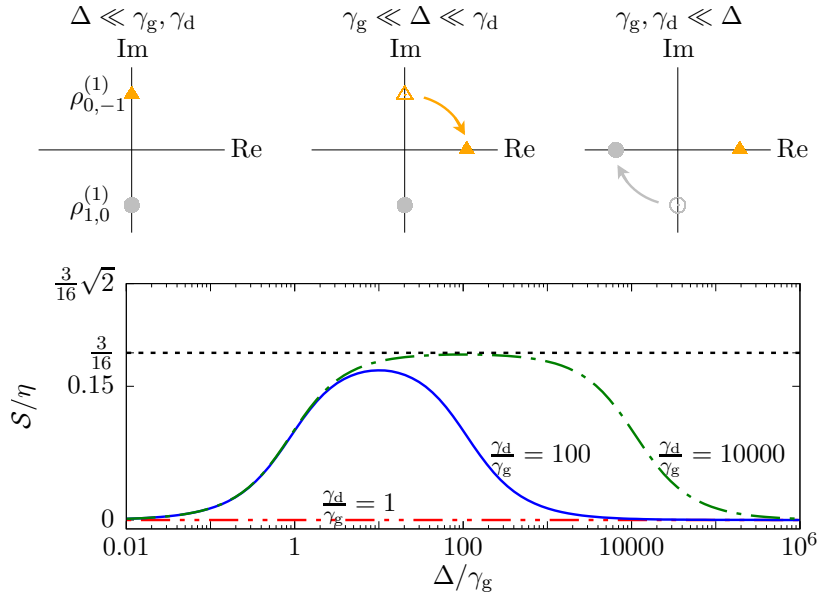


FIGURE 5.10: Illustration of the interference-based quantum synchronization blockade effect for the equatorial limit cycle introduced in Section 5.2.6. The relative phase of the signal components is fixed to $\chi = 0$ and their relative amplitude is chosen according to Equation (5.46). For imbalanced dissipation rates, $\gamma_d \neq \gamma_g$, the coherences $\rho_{0,-1}^{(1)}$ and $\rho_{1,0}^{(1)}$ rotate by different angles if the detuning is in the range $\gamma_g \lesssim \Delta \lesssim \gamma_d$, as indicated by the sketches in the upper row. Therefore, their destructive interference is partially lifted and synchronization is obtained as shown by the lower plot of \mathcal{S}/η . For strong asymmetries $\gamma_d \gg \gamma_g$, the maximum synchronization converges to $\mathcal{S}/\eta = 3/16$, which is indicated by the dotted black line. This is smaller than the maximum synchronization possible for this limit cycle, $3\sqrt{2}/16$, because the detuning cannot fully align the coherences to interfere constructively. The threshold parameter is $\eta = 0.1$.

2018b].

5.8 Experimental implementation of quantum synchronization

Demonstrating quantum synchronization in an experiment remains challenging despite the existence of proposals with trapped ions [Lee and Sadeghpour, 2013] and optomechanical oscillators [Walter *et al.*, 2014]. A significant part of the challenge lies in the specific limit cycle that was envisioned at the time, namely the vdP oscillator, which requires to engineer a single-photon gain and a damping where photons decay in pairs.

Our findings reveal that one actually has a lot of freedom in tailoring a quantum system that is able to synchronize, opening the realm of possibilities. Not only the signal [Sonar *et al.*, 2018] but also the limit cycle itself can be modified, which offers a large and hitherto unexplored choice of both limit-cycle states and methods to stabilize them without imposing a phase preference. When aiming for the first observation of quantum synchronization, this freedom can be leveraged to devise the best strategy to accommodate experimental constraints such as the natural relaxation of the system, which is typically considered as an undesired source of noise. Shifting

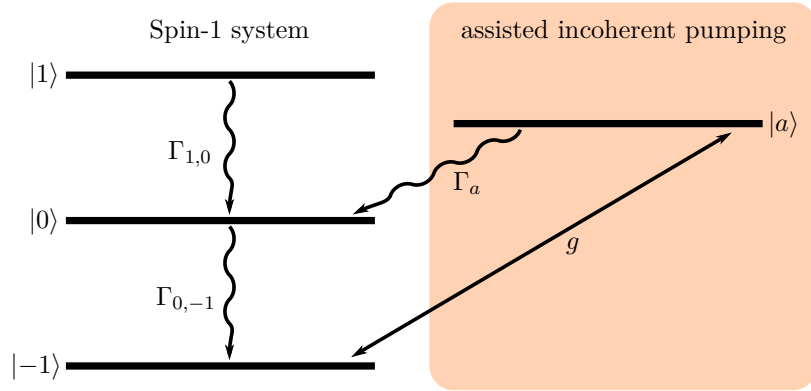


FIGURE 5.11: Experimental proposal to sustain self-oscillations in a spin-1 system. The damping is realized by the natural relaxation of the spin ladder, while the incoherent gain is engineered by coherently driving the $|-1\rangle \leftrightarrow |a\rangle$ transition and exploiting the spontaneous relaxation of the ancillary state $|a\rangle$ to the equatorial state $|0\rangle$.

the paradigm, we now show that this natural relaxation can in fact be exploited as a useful contribution to the stabilization of the limit cycle, reducing the experimental complexity of implementing a quantum self-sustained oscillator.

We now consider a spin-1 system that dissipates energy to its environment at rates $\Gamma_{1,0}$ and $\Gamma_{0,-1}$, as illustrated in Figure 5.11. This system is realized in a variety of experimental platforms, such as trapped ions [Cohen and Retzker, 2014; Senko *et al.*, 2015], nitrogen-vacancy centers [Stark *et al.*, 2018], and superconducting transmons [Neeley *et al.*, 2009; Bianchetti *et al.*, 2010]. Given that we explicitly include the natural dissipative dynamics into the limit cycle stabilization, the only engineering challenge that is left is to stabilize the oscillator away from its ground state by incoherently pumping the transition between the ground state $|-1\rangle$ and the equatorial state $|0\rangle$. This is feasible with current technology, and as an example we consider a scheme that has been demonstrated experimentally with superconducting circuits [Leek *et al.*, 2009, 2010]. There, the working principle is to assist the incoherent transfer from the ground state by driving a transition to an ancillary level, which decays spontaneously into the excited state of interest. This scheme is sketched in the orange box in Figure 5.11 and has been used to efficiently achieve population inversion of up to 93% in the steady-state [Leek *et al.*, 2010]. Such a pumping scheme, supplemented by the natural relaxation of the system, thus successfully establishes a quantum limit cycle.

We now go beyond the proof-of-concept approach and assess the performance of this minimalistic limit-cycle oscillator, benchmarking against the optimal limit cycle derived in Section 5.6. In the regime of interest $\Gamma_{0,-1} \ll \Gamma_a$ where the population in the ancillary state is negligible, $(\Gamma_{0,-1}/\Gamma_a)/(1 + 1/4\mathcal{C}) \ll 1$, the steady state of the spin-1 system is given by

$$\hat{\rho}^{(0)} = \begin{pmatrix} 0 & & \\ & \frac{4\mathcal{C}}{1+4\mathcal{C}} & \\ & & \frac{1}{1+4\mathcal{C}} \end{pmatrix}, \quad (5.55)$$

where we introduced the cooperativity of the pumping process,

$$\mathcal{C} = \frac{g^2}{\Gamma_{0,-1}\Gamma_a}. \quad (5.56)$$

The larger the cooperativity, the more efficiently the pumping acts against the natural relaxation. In practice, the population of the equatorial state $|0\rangle$ can be varied from zero to close to unity by adjusting the cooperativity \mathcal{C} . A value of $\mathcal{C} = 1/8$ implements a vdP-type occupation distribution, whereas a large cooperativity $\mathcal{C} \gg 1$ implements a limit-cycle state that is mostly the equatorial state $|0\rangle$. Remarkably, any finite cooperativity will inevitably lead to an asymmetry between the empty state $|1\rangle$ and the nearly-empty ground state $|-1\rangle$, which is exactly the requirement we derived for optimizing synchronization deep in the quantum regime. This implies that the experimental scheme proposed here is actually able to implement the optimal limit cycle provided that the cooperativity is large enough. The experimental demonstration of the pumping scheme reported a decade ago [Leek *et al.*, 2010] corresponds to $\mathcal{C} \approx 3$. This achievement is already large enough to implement the first observation of quantum synchronization, and sets the optimal limit cycle within reach of state-of-the-art experiments.

5.9 Summary

In this chapter, we have developed a framework to study synchronization in the quantum regime based on the perturbative nature of the phenomenon. This allowed us to identify the coherences between energy eigenstates as the resource of quantum synchronization. We have found that interference effects between coherences that transform identically under rotations may either enhance or hinder synchronization. This result allowed us to explain previous observations and led us to identify a novel interference-based quantum synchronization blockade that does not rely on anharmonicity in the energy levels.

Our framework contains a rule how to choose the signal strength such that the signal stays within the perturbative regime of synchronization and the integrity of the limit cycle is guaranteed to be preserved. The resulting maximum signal strength is a function of the detuning, such that the classical Arnold tongue can be extended for nonzero detuning and becomes a snake-like split tongue.

Focusing on the smallest quantum system that can be synchronized, namely a spin-1 system, we applied the formalism to compare the synchronization of different combinations of limit cycles and signals. To this end, we have demonstrated that the vdP model can be faithfully represented in the spin-1 platform even though the planar position-momentum phase space of the oscillator is replaced by the spherical phase space of a spin. Exploiting the low-dimensional Hilbert space, we have been able to provide an analytical description of previous numerical studies and to derive the optimized signal for this specific limit cycle. We compared the performance to an equatorial limit cycle, which we found to synchronize better despite being insensitive to squeezing.

Furthermore, the analytical understanding gained along the way led us to derive a fundamental bound on the maximum synchronization that can be achieved in the spin-1 system. This result also applies to the quantum vdP oscillator and other limit-cycle oscillators that can be restricted to the lowest three levels in the quantum regime. The bound has been shown to be tight by explicitly constructing a limit cycle that reaches the bound asymptotically for an optimized signal. Moreover, we have motivated that this limit cycle is actually within experimental reach of current technology by proposing a practical stabilization scheme. With this limit-cycle oscillator at hand, quantum synchronization could be readily observed by applying standard coherent (laser) signals that are routinely used in most experimental platforms.

Our findings pave the way to study synchronization of spin-based networks. Since the spin-1 system has the smallest Hilbert space that is able to capture all features of a vdP oscillator deep in the quantum regime, it is a promising candidate to study networks both in terms of numerical efficiency and analytical accessibility.

Finally, our result on the fundamental limit to the synchronization of a spin-1 system constitutes the first step towards understanding the quantum-to-classical transition in synchronization. It provides a reference point to study how this fundamental limit evolves for higher spin numbers, particularly for half-integer spins which do not have access to an equatorial pure-state limit cycle.

The results and figures presented in this chapter have been published in parts in [Koppenhöfer and Roulet, 2019].

Chapter 6

Digital Quantum Simulation of Quantum Synchronization

The results presented in this chapter have been published in:

M. Koppenhöfer, C. Bruder, and A. Roulet,
Quantum Synchronization on the IBM Q System,
Physical Review Research **2**, 023026 (2020).

6.1 Motivation

Synchronization, *i.e.*, the adjustment of the rhythm of a self-sustained oscillation to a weak perturbation, is a universal feature of many complex dynamical systems [Pikovsky *et al.*, 2003]. Classical synchronization has been demonstrated in a variety of very different setups ranging from electrical circuits to biological neuron systems [Adler, 1946; Pecora and Carroll, 1990; Chagnac-Amitai and Connors, 1989]. Several proposals have been made to study quantum effects of synchronization in superconducting circuits [Zhirov and Shepelyansky, 2006; Nigg, 2018], optomechanical systems [Ludwig and Marquardt, 2013; Walter *et al.*, 2014], trapped ions [Lee and Sadeghpour, 2013; Hush *et al.*, 2015], and nanomechanical oscillators [Holmes *et al.*, 2012]. However, all experimental demonstrations of synchronization reported to date on these platforms were operating in the classical regime [Zalalutdinov *et al.*, 2003; Hossein-Zadeh and Vahala, 2008; Zhang *et al.*, 2015b; Bagheri *et al.*, 2013; Shlomi *et al.*, 2015; Seitner *et al.*, 2017; Gil-Santos *et al.*, 2017; Bekker *et al.*, 2017; Toth *et al.*, 2018; Huang and Hossein-Zadeh, 2018] because of the challenge to combine coherent control and engineered nonlinear dissipation in a single experimental platform in the quantum regime.

In the previous chapter, we introduced a theoretical framework for quantum synchronization. The comparison of different limit-cycle oscillators and signals using this framework led us to an alternative way to stabilize a limit-cycle oscillator in the quantum regime, which is expected to be feasible with current technology. Here, we choose yet another approach to implement a quantum limit-cycle oscillator, namely, we experimentally demonstrate quantum synchronization by a digital quantum simulation. The quantum limit-cycle oscillator is realized in a single spin-1 system, the smallest possible system that can host a limit-cycle oscillator [Roulet and Bruder, 2018a]. We use two qubits of a quantum processor to implement the desired spin-1 system while the remaining qubits play the role of the environment sustaining the oscillation. The advantage of this approach is that the nonlinear dissipation required

to study quantum synchronization corresponds to easily engineered single-qubit relaxation. With this mapping in place, we perform a digital quantum simulation [Nielsen and Chuang, 2011; Lloyd, 1996] of spin-1 synchronization dynamics on the publicly available few-qubit quantum processors at the IBM Q System [IBM, 2019a].

The ongoing efforts to build a quantum computer have resulted in noisy intermediate-scale quantum (NISQ) devices [Preskill, 2018], which are constantly improving in terms of decoherence and relaxation times, gate fidelities, and readout fidelities [Corcoles *et al.*, 2019]. NISQ devices have become a highly relevant platform for simulating realistic physical problems and they have already been used to find quantum ground states [Peruzzo *et al.*, 2014; Kandala *et al.*, 2017; Reiner *et al.*, 2019] and to simulate closed-system quantum many-body dynamics [Smith *et al.*, 2019a,b]. Moreover, it has been shown that they can in principle be used to simulate the dynamics of dissipative quantum systems [Lloyd and Viola, 2001; Bacon *et al.*, 2001; Kliesch *et al.*, 2011; García-Pérez *et al.*, 2020]. Our results demonstrate that state-of-the-art NISQ devices are indeed able to study complex dissipative quantum systems that were not realized experimentally before.

This chapter is structured as follows. We introduce the spin-1 limit-cycle oscillator considered in this chapter in Section 6.2. In Section 6.3, we derive a quantum algorithm that implements its dynamics on a quantum computer. Information on the quantum processors of the IBM Q System, on their simulation on classical hardware, and on the quantum state tomography used to reconstruct the state of the spin-1 system are given in Section 6.4. In Section 6.5, we test parts of the quantum algorithm on an actual quantum processor and we identify obstacles imposed by current hardware. Modifications of the quantum circuit in reaction to these obstacles are introduced in Section 6.6. With these modifications, we are able to demonstrate quantum synchronization on the quantum processors of the IBM Q System. The corresponding experimental results are presented in Section 6.7 before we conclude in Section 6.8.

6.2 Spin-1 limit-cycle oscillator

Building on the insight into the physics of quantum synchronization obtained in Chapter 5, we now design a quantum limit-cycle oscillator that is adapted to current NISQ hardware. We focus on the smallest quantum system that can be synchronized, *i.e.*, a single spin 1 [Roulet and Bruder, 2018a], and on the least complex dissipative limit-cycle stabilization mechanism, namely, the dissipative mechanism stabilizing the equatorial limit-cycle state $|0\rangle$ shown in Figure 5.2(a). To study quantum synchronization, an external signal of strength ε is applied to the limit-cycle oscillator, which generates coherent transitions between the spin-1 states and is described by a Hamiltonian \hat{H}_{ext} . As discussed in Section 5.2, the dynamics in a frame rotating at the signal frequency and under a rotating wave approximation is given by the QME

$$\frac{d}{dt}\hat{\rho} = -\frac{i}{\hbar} \left[\Delta\hat{S}_z + \varepsilon\hat{H}_{\text{ext}}, \hat{\rho} \right] + \Gamma_{-1,0}\mathcal{D}[\hat{S}_+\hat{S}_z]\hat{\rho} + \Gamma_{1,0}\mathcal{D}[\hat{S}_-\hat{S}_z]\hat{\rho}. \quad (6.1)$$

Here, $\Delta = \omega_0 - \omega_{\text{ext}}$ is the detuning between the spin precession frequency ω_0 and the signal frequency ω_{ext} . Without loss of generality, we have chosen the z -axis as the spin quantization axis, and \hat{S}_z is the corresponding spin-component operator introduced in Appendix A.2. By \hat{S}_{\pm} we denote the spin raising and lowering operators, $\Gamma_{-1,0}$ and $\Gamma_{1,0}$ are the decay rates towards the state $|0\rangle$, and \mathcal{D} is a Lindblad dissipator of the form (2.12). We consider a general signal Hamiltonian \hat{H}_{ext} of the form (5.7), which describes coherent transitions between the spin-1 eigenstates. For the sake of

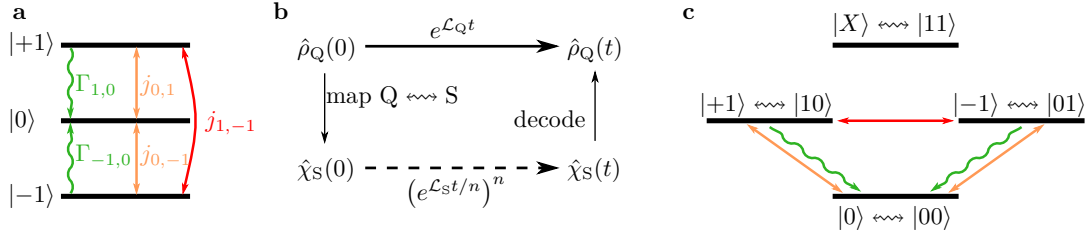


FIGURE 6.1: **(a)** Energy level diagram of a spin-1 system hosting a limit-cycle oscillator. The limit cycle is stabilized by dissipative transitions towards the spin-1 state $|0\rangle$ at rates $\Gamma_{\pm 1,0}$ and is subjected to an external signal that drives transitions $j_{k,l}$ between the spin-1 states. **(b)** Working principle of a digital quantum simulation. Instead of evolving the initial state $\hat{\rho}_Q(0)$ of a quantum system Q , the state is mapped onto a state $\hat{\chi}_S(0)$ of the quantum simulator S . Likewise, the time evolution of Q is expressed in terms of quantum gates of the simulator S . The time evolution is performed on the simulator S up to the final state $\hat{\chi}_S(t)$, which is measured and decoded. **(c)** Spin-1 energy level diagram shown in (a) expressed in terms of two-qubit states according to the mapping (6.3). The surplus state $|X\rangle$ must be isolated from the spin-1 states.

as a compact notation of the subsequent results, we redefine the complex coefficients $t_{i,j}$ that determine the relative amplitude and phase of the three possible transitions as follows:

$$\begin{aligned} t_{0,1} &= \frac{j_{0,1}}{\sqrt{2}}, \\ t_{-1,0} &= \frac{j_{0,-1}^*}{\sqrt{2}}, \\ t_{-1,1} &= \frac{j_{-1,1}}{2}. \end{aligned} \quad (6.2)$$

This gives rise to the signal Hamiltonian

$$\hat{H}_{\text{ext}} = \hbar \left(\frac{j_{0,1}}{\sqrt{2}} \hat{S}_z \hat{S}_+ - \frac{j_{0,-1}^*}{\sqrt{2}} \hat{S}_z \hat{S}_- + \frac{j_{-1,1}}{2} \hat{S}_+^2 + \text{H.c.} \right).$$

For instance, the combination $j_{0,1} = j_{0,-1}^*$ and $j_{-1,1} = 0$ corresponds to a semiclassical signal, while the choice $j_{0,1} = j_{0,-1} = 0$ and $j_{-1,1} \neq 0$ corresponds to a squeezing signal. A sketch of the coherent and dissipative transitions in the spin-1 system and their associated rates is shown in Figure 6.1(a).

6.3 Mapping to a quantum computer

To implement the spin-1 synchronization dynamics (6.1) on a quantum computer, we use the technique of quantum simulation introduced in Section 2.7.2. Quantum simulation means that a quantum system Q – the spin-1 limit-cycle oscillator – is implemented by means of another quantum system S – the quantum simulator – which is experimentally well controllable.

As a quantum simulator, we use the publicly available quantum computers at the IBM Q System, which are a NISQ version of a universal quantum computer. Consequently, we will implement a *digital* quantum simulation, whose working principle is sketched in Figure 6.1(b). In a first step, we define a mapping from the spin-1 Hilbert

space onto the Hilbert space $\mathcal{H}^{(N)}$ of the quantum computer. For reasons that will become clear in Section 6.3.2, we choose to represent the three spin-1 states in terms of the two-qubit states

$$|+1\rangle \longleftrightarrow |1\rangle_{q_1} \otimes |0\rangle_{q_0} \equiv |10\rangle , \quad (6.3a)$$

$$|0\rangle \longleftrightarrow |0\rangle_{q_1} \otimes |0\rangle_{q_0} \equiv |00\rangle , \quad (6.3b)$$

$$|-1\rangle \longleftrightarrow |0\rangle_{q_1} \otimes |1\rangle_{q_0} \equiv |01\rangle . \quad (6.3c)$$

Note that this encoding gives rise to a fourth state

$$|X\rangle \longleftrightarrow |1\rangle_{q_1} \otimes |1\rangle_{q_0} \equiv |11\rangle \quad (6.4)$$

outside the spin-1 Hilbert space, which needs to be isolated from the spin states. The spin-1 level diagram expressed in terms of these two-qubit states is shown in Figure 6.1(c).

6.3.1 Unitary time evolution

Having defined the mapping between the spin-1 system and the quantum computer, we must translate the continuous time evolution (6.1) to the level of qubits, to which we can only apply a finite set of discrete unitary gates summarized in Appendix C. As described in Section 2.7.2, the exact time evolution is approximated by a series of many transformations that propagate the system's state for a small time step dt . Trotter [1959] and Suzuki [1976] have developed formal ways to decompose the unitary part of Equation (6.1). Here, we choose a symmetric decomposition that is exact up to third-order corrections in terms of the small time step dt [Nielsen and Chuang, 2011],

$$e^{i(\hat{A}+\hat{B})dt} = e^{i\hat{A}dt/2} e^{i\hat{B}dt} e^{i\hat{A}dt/2} + \mathcal{O}(dt^3) .$$

Applying this rule to the unitary part of Equation (6.1), we obtain the decomposition

$$\begin{aligned} & e^{-i(\Delta\hat{S}_z + \varepsilon\hat{H}_{\text{ext}})dt/\hbar} \\ &= \hat{U}_0\left(\frac{dt}{2}\right) \hat{U}_{1,0}\left(\frac{dt}{2}\right) \hat{U}_{-1,0}\left(\frac{dt}{2}\right) \hat{U}_{1,-1}(dt) \hat{U}_{-1,0}\left(\frac{dt}{2}\right) \hat{U}_{1,0}\left(\frac{dt}{2}\right) \hat{U}_0\left(\frac{dt}{2}\right) \\ &+ \mathcal{O}(dt^3) , \end{aligned} \quad (6.5)$$

where

$$\hat{U}_0(t) = e^{-i\Delta\hat{S}_z t/\hbar} , \quad (6.6a)$$

$$\hat{U}_{1,0}(t) = e^{-i\varepsilon(j_{0,1}\hat{S}_z\hat{S}_+/\sqrt{2}+\text{H.c.})t/\hbar} , \quad (6.6b)$$

$$\hat{U}_{-1,0}(t) = e^{+i\varepsilon(j_{0,-1}\hat{S}_z\hat{S}_-/\sqrt{2}+\text{H.c.})t/\hbar} , \quad (6.6c)$$

$$\hat{U}_{1,-1}(t) = e^{-i\varepsilon(j_{-1,1}\hat{S}_+^2/2+\text{H.c.})t/\hbar} . \quad (6.6d)$$

To translate these unitary time-evolution operators to a corresponding transformation of the encoded states in the quantum computer, we define the spin-1/2 operators $\hat{\tau}_x = \hat{\sigma}_x/2$, $\hat{\tau}_y = \hat{\sigma}_y/2$, and $\hat{\tau}_z = \hat{\sigma}_z/2$, and the spin-1/2 ladder operators

$$\hat{\tau}_{\pm} = \hat{\tau}_x \pm i\hat{\tau}_y . \quad (6.7)$$

Note that we are using the quantum-information notation, where $|0\rangle$ is the eigenstate of $\hat{\sigma}_z$ with eigenvalue $+1$. Therefore, the raising and lowering operators act counter-intuitively,

$$\begin{aligned}\hat{\tau}_+ |1\rangle &= |0\rangle , \\ \hat{\tau}_- |0\rangle &= |1\rangle .\end{aligned}$$

Using these ladder operators, we construct two-qubit operators that act on the two-qubit subspace $\{|10\rangle, |00\rangle, |01\rangle\}$ in the same way as the corresponding spin-1 operators act on the spin-1 state space $\{|+1\rangle, |0\rangle, |-1\rangle\}$,

$$\begin{aligned}\hat{S}_z \hat{S}_+ / \sqrt{2\hbar} &\leftrightarrow \hat{\tau}_- \otimes \hat{\tau}_+ \hat{\tau}_- , \\ \hat{S}_z \hat{S}_- / \sqrt{2\hbar} &\leftrightarrow \hat{\tau}_+ \hat{\tau}_- \otimes \hat{\tau}_- , \\ \hat{S}_+ \hat{S}_z / \sqrt{2\hbar} &\leftrightarrow \hat{\tau}_+ \hat{\tau}_- \otimes \hat{\tau}_+ , \\ \hat{S}_- \hat{S}_z / \sqrt{2\hbar} &\leftrightarrow \hat{\tau}_+ \otimes \hat{\tau}_+ \hat{\tau}_- , \\ \hat{S}_+^2 / 2\hbar &\leftrightarrow (\hat{\tau}_- \hat{\tau}_+ \otimes \hat{\tau}_+ \hat{\tau}_-) \text{SWAP} , \\ \hat{S}_-^2 / 2\hbar &\leftrightarrow (\hat{\tau}_+ \hat{\tau}_- \otimes \hat{\tau}_- \hat{\tau}_+) \text{SWAP} ,\end{aligned}$$

where SWAP denotes a swap operation of the two qubits in the quantum register. The operator \hat{S}_z can be obtained from the correspondences listed above via the decomposition $\hat{S}_z = (\hat{S}_z \hat{S}_+ + \hat{S}_- \hat{S}_z)^2 - (\hat{S}_z \hat{S}_- + \hat{S}_+ \hat{S}_z)^2$. This mapping allows us to translate the unitary time evolution operators (6.6) of a spin-1 system to the corresponding unitary transformation acting on the encoded states in the quantum computer.

In a final step, these abstract unitary transformations of the two-qubit state must be decomposed in terms of the quantum gates available on the IBM Q System, which are listed in Appendix C. The part of the time evolution stemming from the free Hamiltonian, Equation (6.6a), can be decomposed in terms of two single-qubit phase rotations,

$$\hat{U}_0(t) = \hat{R}_z(-\Delta t) \otimes \hat{R}_z(+\Delta t) .$$

This unitary transformation can be implemented by the following quantum circuit:

$$\begin{array}{c} q_0 : \\ q_1 : \end{array} \begin{array}{c} \boxed{} \\ \boxed{U_0(t)} \\ \boxed{} \end{array} = \begin{array}{c} \boxed{R_z(+\Delta t)} \\ \boxed{R_z(-\Delta t)} \end{array} \quad (6.8)$$

As shown in Figure 6.1, the unitary transformations (6.6b) and (6.6c) describing the signal components $j_{0,1}$ and $j_{0,-1}$ correspond to rotations of the qubits q_1 and q_0 , respectively, provided that the other qubit is in the state $|0\rangle$. These rotations can be expressed in terms of the U_3 basis gate,

$$\hat{U}_{\pm 1,0}(t) = \hat{U}_3 \left(-2\varepsilon |j_{0,\pm 1}| t, \arg(j_{0,\pm 1}) - \frac{3\pi}{2}, -\arg(j_{0,\pm 1}) - \frac{\pi}{2} \right) , \quad (6.9)$$

which is applied to the target qubit q_1 (q_0) as a controlled rotation conditioned on the control qubit q_0 (q_1) being in the state $|0\rangle$. In the *python* API QISKIT [Abraham *et al.*, 2019a], which is used to program the IBM Q System, a controlled \hat{U}_3 operation

Finally, as shown in Figure 6.1, the squeezing signal $j_{1,-1}$ transfers population between the $|01\rangle$ and $|10\rangle$ states, *i.e.*, it corresponds to a partial SWAP operation,

$$\hat{U}_{1,-1}(t) \rightsquigarrow \begin{pmatrix} 1 & 0 & 0 & 0 \\ 0 & \cos(\varepsilon |j_{-1,1}| t) & -ie^{-i \arg(j_{-1,1})} \sin(\varepsilon |j_{-1,1}| t) & 0 \\ 0 & -ie^{i \arg(j_{-1,1})} \sin(\varepsilon |j_{-1,1}| t) & \cos(\varepsilon |j_{-1,1}| t) & 0 \\ 0 & 0 & 0 & 1 \end{pmatrix}.$$

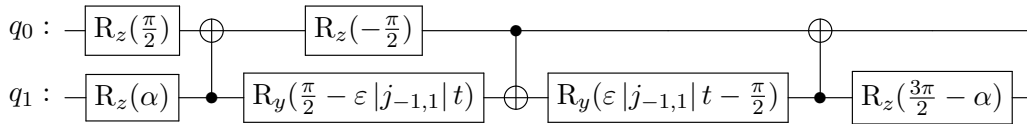
Khaneja *et al.* [2001] and Kraus and Cirac [2001] have shown that every unitary two-qubit transformation \hat{U} can be decomposed into four single-qubit transformations \hat{A}_1 , \hat{A}_2 , \hat{A}_3 , and \hat{A}_4 , and the two-qubit gate

$$\hat{N}(\alpha, \beta, \gamma) = \exp [i (\alpha \hat{\sigma}_x \otimes \hat{\sigma}_x + \beta \hat{\sigma}_y \otimes \hat{\sigma}_y + \gamma \hat{\sigma}_z \otimes \hat{\sigma}_z)]$$

in the following way:

$$\hat{U} = (\hat{A}_1 \otimes \hat{A}_2) \hat{N}(\alpha, \beta, \gamma) (\hat{A}_3 \otimes \hat{A}_4).$$

Vatan and Williams [2004] constructed an optimal implementation of $\hat{N}(\alpha, \beta, \gamma)$ that requires only three CNOT operations. Applying their results, we obtain the following decomposition of the $\hat{U}_{1,-1}$ operation:



where $\alpha = \arg(j_{-1,1})$. A slightly shorter notation of the same circuit in terms of the U_3 basis gate is

$$\begin{array}{c} q_0 : \\ q_1 : \end{array} \begin{array}{c} \boxed{U_{1,-1}(t)} \\ \end{array} = \begin{array}{c} \boxed{U_3(\pi, \alpha', \alpha')} \\ \boxed{U_3(2\varepsilon |j_{-1,1}| t, 0, \pi)} \\ \boxed{U_3(\pi, -\alpha' - \pi, -\alpha')} \end{array} \quad (6.12)$$

where $\alpha' = \arg(j_{-1,1}) - \pi/2$.

These quantum circuits implement the unitary part of the time evolution of a spin-1 system that has been mapped onto a quantum computer according to Equation (6.3).

6.3.2 Dissipative time evolution

Simulating the remaining non-unitary dissipative dynamics may seem challenging given that we can only apply unitary gates on a quantum computer. However, this task can be achieved by simulating discrete-time unitary dynamics on an extended system where ancillary degrees of freedom mimic a dissipative environment. In fact, Lloyd and Viola [2001] have shown that this environment can even be modeled by only a single resettable qubit.

Our mapping (6.3) has the benefit that the limit-cycle state $|0\rangle$ corresponds to the ground state $|0\rangle_{q_1} \otimes |0\rangle_{q_0}$ of the logical qubits. This allows us to implement the required nonlinear limit-cycle stabilization with minimal complexity, since the dissipative stabilization maps onto energy relaxation processes of the two qubits q_0 and q_1 , as shown in Figure 6.1(c). In principle, one could take advantage of the natural energy relaxation of the qubits to stabilize the limit cycle at the hardware-specific relaxation rate Γ_{rel} . However, this is not sufficient if we want to study synchronization

TABLE 6.1: Device parameters of the 5-qubit IBMQX2 processor on September 30, 2019. The exact parameters fluctuate slowly in time and are measured during the daily recalibration of the quantum processor. Qubit 2 is the target qubit of the CNOT gates listed here.

qubit	$T_1/\mu\text{s}$	$T_2/\mu\text{s}$	ν/GHz	errors/ 10^{-2}		
				readout	U_3	CNOT
0	66.4	50.5	5.29	1.0	0.09	1.3
1	66.2	55.5	5.24	1.1	0.10	1.9
2	63.2	75.0	5.03	1.0	0.07	–
3	57.8	29.1	5.30	1.2	0.10	1.7
4	63.6	56.8	5.08	1.4	0.09	1.2

for the following reason. As discussed in Section 5.2, an external signal \hat{H}_{ext} creates coherences between the spin-1 states at a certain rate Γ_{signal} . To satisfy the paradigm of synchronization, Γ_{signal} must be smaller than the rate Γ_{rel} at which the limit cycle is stabilized. On a physical quantum processor, noise and unwanted couplings to the environment will induce decoherence processes that decrease the magnitude of the coherences at a decoherence rate Γ_{dec} . To observe synchronization, the signal must overcome this decoherence, $\Gamma_{\text{signal}} > \Gamma_{\text{dec}}$. However, this is incompatible with the requirement $\Gamma_{\text{rel}} > \Gamma_{\text{signal}}$ since decoherence is typically stronger than energy relaxation, $\Gamma_{\text{dec}} > \Gamma_{\text{rel}}$, as shown in Table 6.1.

Consequently, to study synchronization on a physical quantum processor, the natural energy relaxation rate Γ_{rel} must be artificially increased. This can be achieved by the following circuit [Nielsen and Chuang, 2011]:

$$\begin{array}{c}
 q : \text{---} \bullet \text{---} \oplus \text{---} \\
 a : \text{---} \boxed{U_3(\theta, 0, 0)} \text{---} \bullet \text{---} \boxed{\text{Measurement}} \text{---} |0\rangle \text{---}
 \end{array} \quad (6.13)$$

This quantum circuit maps an initial state $|\psi(0)\rangle_q \otimes |0\rangle_a = (\alpha |0\rangle_q + \beta |1\rangle_q) \otimes |0\rangle_a$ onto the state

$$\left[\alpha |0\rangle_q + \beta \cos\left(\frac{\theta}{2}\right) |1\rangle_q \right] \otimes |0\rangle_a + \beta \sin\left(\frac{\theta}{2}\right) |0\rangle_q \otimes |1\rangle_a$$

immediately before the measurement. If we choose the angle θ such that the condition

$$\sin^2\left(\frac{\theta}{2}\right) = \Gamma dt \ll 1 \quad (6.14)$$

is fulfilled, the measurement projects the qubit q to the state $|\psi(dt)\rangle|_1 = |0\rangle_q$ at a probability $\Gamma |\beta|^2 dt$ if the measurement outcome is 1, or to the state

$$\begin{aligned}
 |\psi(dt)\rangle|_0 &= \alpha \left(1 + \frac{\Gamma}{2} |\beta|^2 dt \right) |0\rangle_q \\
 &+ \beta \left(1 - \frac{\Gamma}{2} dt + \frac{\Gamma}{2} |\beta|^2 dt \right) |1\rangle_q + \mathcal{O}(dt^2)
 \end{aligned}$$

at a probability $1 - \Gamma |\beta|^2 dt$ if the measurement outcome is 0. This is precisely the dissipative dynamics that one obtains from a photon-counting SSE of the form (2.30)

by setting $\hat{o} = \hat{\tau}_+$, $\hat{M} = \Gamma\hat{\tau}_-\hat{\tau}_+/2$, $\xi = 0$, and $\hat{H} = 0$,

$$\begin{aligned} d|\psi\rangle &= \left[-\frac{i}{\hbar} \left(-i\hbar\frac{\Gamma}{2}\hat{\tau}_-\hat{\tau}_+ \right) + \frac{\Gamma}{2} \langle\psi|\hat{\tau}_-\hat{\tau}_+|\psi\rangle \right] |\psi\rangle dt \\ &+ \left[\frac{\hat{\tau}_+|\psi\rangle}{\sqrt{\langle\psi|\hat{\tau}_-\hat{\tau}_+|\psi\rangle}} - |\psi\rangle \right] dN, \end{aligned} \quad (6.15)$$

where $dN \in \{0, 1\}$ is a stochastic Poissonian increment with expectation value

$$\mathbb{E}(dN) = \Gamma \langle\psi|\hat{\tau}_-\hat{\tau}_+|\psi\rangle dt = \Gamma |\beta|^2 dt.$$

The corresponding unconditional QME for the density matrix $\hat{\rho} = \mathbb{E}[|\psi\rangle\langle\psi|]$ is

$$\frac{d}{dt}\hat{\rho} = \Gamma\mathcal{D}[\hat{\tau}_+]\hat{\rho}. \quad (6.16)$$

Note that this equation actually describes single-qubit *relaxation*, because $\hat{\tau}_+$ is a spin-1/2 lowering operator, $\hat{\tau}_+|1\rangle = |0\rangle$.

A controlled unitary gate requires at least two CNOT operations [Barenco *et al.*, 1995; Vatan and Williams, 2004], therefore, the quantum circuit (6.13) contains at least three CNOT gates. However, since the controlled \hat{U}_3 rotation followed by a CNOT gate represents just another two-qubit operation, the circuit could be simplified. Indeed, the following circuit performs exactly the same transformation of the initial state using only two CNOT gates:

$$\begin{array}{c} q \text{ --- } \boxed{U_2(-\pi, 0)} \text{ --- } \oplus \text{ --- } \boxed{U_2(-\frac{\pi}{2}, 0)} \text{ --- } \oplus \text{ --- } \boxed{U_1(-\frac{\pi}{2})} \text{ ---} \\ a \text{ --- } \boxed{U_3(-\frac{\theta}{2}, -\frac{\pi}{2}, \pi)} \text{ --- } \bullet \text{ --- } \boxed{U_3(-\frac{\theta}{2}, \pi, \frac{\pi}{2})} \text{ --- } \bullet \text{ --- } \boxed{U_1(-\frac{\pi}{2})} \text{ --- } \text{Measurement} \text{ --- } |0\rangle \end{array} \quad (6.17)$$

Despite the fact that both circuits describe the same mathematical transformation of an initial state $|\psi(0)\rangle_q \otimes |0\rangle_a$, they will perform differently on a noisy quantum computer. This will be discussed below in Section 6.4.

In conclusion, the quantum circuits (6.13) and (6.17) calculate a single time step of a stochastic photon-counting quantum trajectory starting from an initial state $|\psi(0)\rangle_q$. The ancillary qubit a plays the role of the photon detector and a random detection record is generated by repeatedly measuring its state. The measurement result 1 represents the release of an excitation from the qubit q into the environment and resets the qubit to its ground state. The quantum state along each random trajectory is a pure state, such that it can be described by a state vector $|\psi(t)\rangle_q$ stored in the qubit register. The dissipative dynamics described by the density matrix $\hat{\rho}$ is obtained by averaging over many different quantum trajectories. Technically, this is achieved by executing the quantum circuit many times, each time starting from the same initial state $|\psi(0)\rangle_q$, and tracing over the measurement outcome of the ancillary qubit a .

To construct a single time step of the full dynamics given by Equation (6.1), we combine the circuits (6.8), (6.10), (6.12), and (6.13) or (6.17) to the quantum circuit shown in Figure 6.2(a). The Trotter decomposition (6.5) approximates the exact dynamics to order dt^3 , therefore, we must ensure that the following conditions hold:

$$\begin{aligned} \Delta t &\ll 1, \\ \varepsilon |j_{k,k'}| dt &\ll 1, \\ \Gamma_{k,0} dt &\ll 1. \end{aligned}$$

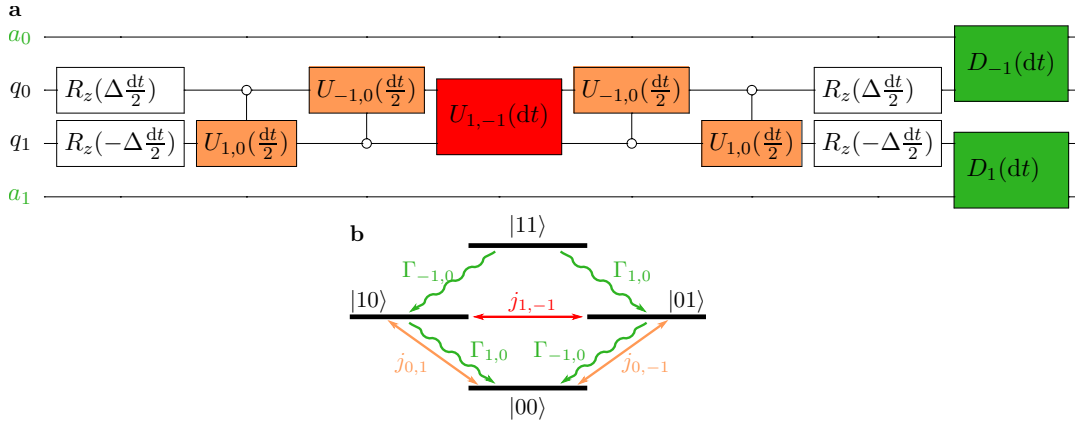


FIGURE 6.2: **(a)** Quantum circuit implementing a single time step dt of the synchronization dynamics given by Equation (6.1). The $U_{k,0}$ gates are defined in Equation (6.10) and the $U_{1,-1}$ gate is defined in Equation (6.12). The D_k gates are chosen from Equations (6.13) and (6.17) depending on the daily calibration of the quantum computer, as discussed in Section 6.4. Note that the two dissipative steps could also be applied sequentially to a single ancillary qubit. **(b)** Sketch of the corresponding dynamics in the two-qubit state space. The gates shown in white in (a) correspond to the free evolution of the limit-cycle oscillator while the other circuit elements implement the transitions of the same color in (b).

Since the dissipative time steps reset the qubits q_0 and q_1 independent of the state of the other qubit, the gates D_k will also induce the transitions $|X\rangle \rightarrow |\pm 1\rangle$, as sketched in Figure 6.2(b). This is actually beneficial on a NISQ computer because these transitions ensure that population cannot be trapped in the state $|X\rangle$. Moreover, since the coherent signal is implemented by controlled gates, the additional level $|X\rangle$ still remains decoupled from the spin-1 system with respect to the unitary part of the dynamics.

6.4 Methods

Having defined the mapping (6.3) and the corresponding quantum circuit to implement the time evolution on the quantum simulator, shown in Figure 6.2, we now discuss technical issues that are related to the execution of the quantum circuit on current hardware. The publicly available NISQ computers at the IBM Q System consist of 5 or 14 fixed-frequency superconducting transmon qubits [IBM, 2019b]. The basis single-qubit gates U_1 , U_2 , and U_3 as well as measurement operations in the \hat{Z} eigenbasis can be applied to each qubit. The qubits are connected according to the connectivity diagram shown in Figures 6.3(a) and (b), and CNOT operations can be applied to pairs of qubits that are connected by lines. Typical hardware parameters of the IBMQX2 quantum computer are summarized in Table 6.1. Since these parameters fluctuate slowly in time, each quantum computer is automatically recalibrated once a day to measure the current hardware parameters and to optimize the microwave pulses that implement quantum gates.

IBM's quantum computers are programmed by defining quantum circuits using the *python* API QISKIT [Abraham *et al.*, 2019a]. To initialize a quantum circuit, the sizes of its quantum register and its classical register are specified. Quantum and classical bits are initialized in the states $|0\rangle$ and 0, respectively. Frequently used

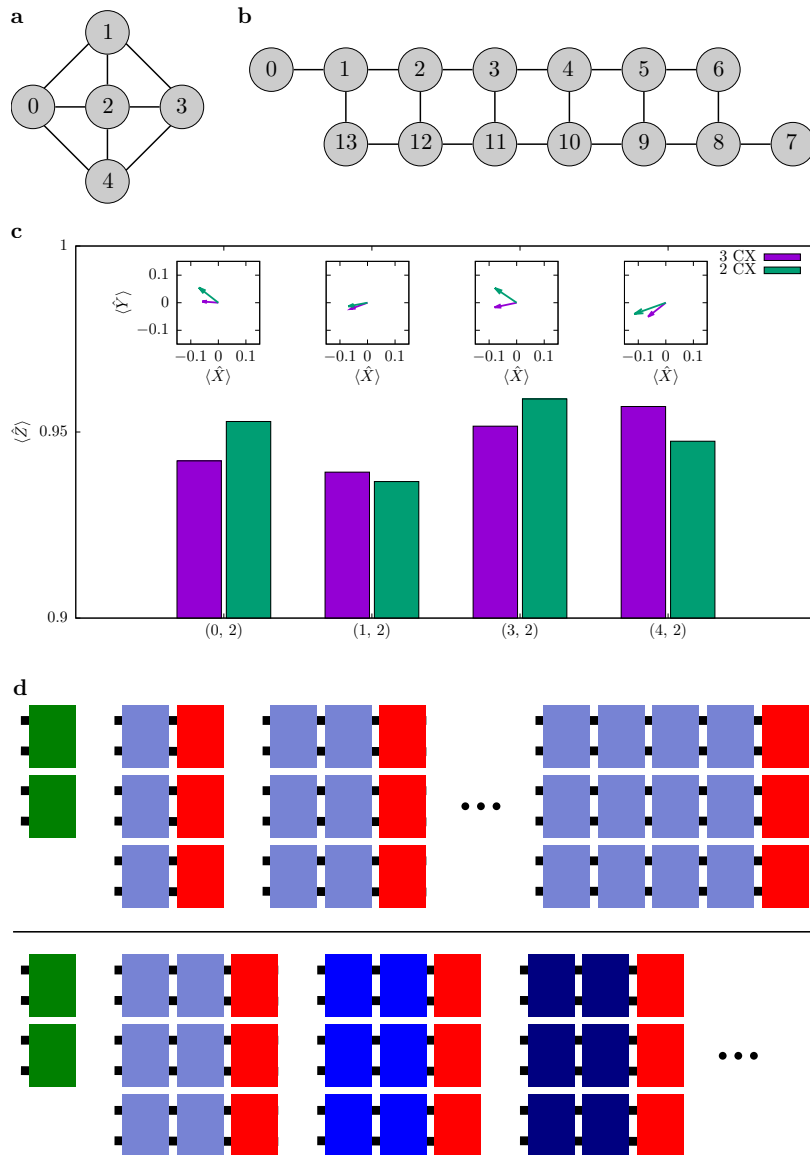


FIGURE 6.3: **(a)** Sketch of the qubit connectivity of the IBMQX2 quantum computer. Each circle represents a qubit. CNOT operations can be applied to the pairs of qubits that are connected by a line. **(b)** Sketch of the qubit connectivity of the IBMQ_16_MELBOURNE quantum computer. **(c)** Comparison of the quantum circuits (6.13) and (6.17) implementing a dissipative time step. **(d)** Sketch how different quantum circuits are grouped into batches. Green boxes represent readout calibration circuits, blueish boxes represent a time step of the quantum simulation, and red boxes represent quantum-state-tomography measurements to reconstruct the final state. Different values of the system parameters are indicated by the shades of blue. The upper row represents a time evolution for fixed system parameters and the lower row represents a scan of a system parameter for a fixed number of time steps.

single and two-qubit gates, measurements operations in the \hat{Z} eigenbasis, and reset operations are predefined in QISKIT and can be applied to the qubits to construct a quantum circuit. This circuit is *virtual* in the sense that it represents an idealized version of the quantum algorithm, which does not account for hardware restrictions such as the set of basis quantum gates and the qubit connectivity scheme shown in Figures 6.3(a) and (b). Therefore, the virtual circuit needs to be mapped onto the quantum hardware in a so-called *transpilation* step. In this process, each virtual qubit is assigned to a physical qubit of the quantum processor, SWAP operations are inserted into the circuit to adapt controlled operations to the connectivity scheme, and all gates are rewritten in terms of the basis gates U_1 , U_2 , U_3 , and CNOT.

To check the functionality of a quantum circuit before executing it on actual hardware, QISKIT provides two types of simulators. The *state vector simulator* tracks the full quantum state $|\psi\rangle$ of the qubit register throughout the quantum circuit, whereas the so-called *QASM simulator* simulates the behavior of actual quantum hardware and returns only binary measurement results. All simulated data presented in this chapter have been obtained using the *QASM simulator*. The *QASM simulator* provides a simple noise model that approximates the behavior of actual quantum hardware and is implemented in the following way: After each single-qubit gate, a single-qubit depolarizing error is applied, *i.e.*, at a probability p the quantum state $\hat{\rho}$ of the processor is replaced by a completely mixed state [Nielsen and Chuang, 2011],

$$\hat{\rho} \rightarrow p \frac{\mathbb{1}}{2} + (1-p)\hat{\rho} = \left(1 - \frac{3}{4}p\right) \hat{\rho} + \frac{p}{4} \left(\hat{X}\hat{\rho}\hat{X} + \hat{Y}\hat{\rho}\hat{Y} + \hat{Z}\hat{\rho}\hat{Z}\right) .$$

This depolarizing error is followed by the simulation of a thermal relaxation error if a gate time and the cryostat temperature of the quantum computer are specified. The probability p of the depolarizing error is chosen such that the overall gate fidelity matches the value determined in the last calibration of the quantum computer. For two-qubit gates, a two-qubit depolarizing error is performed which is followed by the simulation of two single-qubit relaxation errors. If a simulation of readout errors is requested, the state of the qubit is measured and the measurement result is inverted with a certain probability p . Again, p is chosen such that the readout fidelity of the qubit reproduces the value measured in the last calibration.

If a virtual quantum circuit has been transpiled and tested, it can be executed on an actual quantum computer. To this end, the circuit is translated into the *OpenQASM* language [Cross *et al.*, 2017], which is a text-based representation of the quantum circuit that can be added to the job queue of the quantum computer. The user can choose which quantum computer will execute the job and how many repetitions per circuit should be done to collect the statistics of the measurement results. The queuing system restricts the maximum number of repetitions per circuit to 8192.

To choose between the two quantum circuits (6.13) and (6.17) implementing the dissipative time step, we execute both circuits for each possible pair of system and ancillary qubits once after the daily recalibration of the quantum computer. The initial state is $|0\rangle_q \otimes |0\rangle_a$, therefore, both qubits should ideally remain in the state $|0\rangle$ such that the expected measurement results are $\langle \hat{Z} \rangle = 1$ and $\langle \hat{X} \rangle = \langle \hat{Y} \rangle = 0$. Typical results obtained on a NISQ computer are shown in Figure 6.3(c). The final state is found to have a reduced $\langle \hat{Z} \rangle$ expectation value and a preferred phase in the x - y -plane due to gate imperfections and crosstalk between the qubits. This effect is differently pronounced for the two circuits (6.13) and (6.17). To minimize these detrimental effects, we choose for each pair of adjacent qubits the quantum circuit that yields the largest $\langle \hat{Z} \rangle$ expectation value. If the two circuits are equal with respect to this

criterion, we select the circuit that minimizes $\langle \hat{X} \rangle^2 + \langle \hat{Y} \rangle^2$.

The queuing system allows one to group several quantum circuits to a so-called *batch job*. Batch jobs are treated as single tasks such that all contained quantum circuits are executed successively. We grouped quantum circuits that generated the time evolution for different numbers of time steps, or that scanned different values of a parameter, as shown in Figure 6.3(d). At the beginning of each batch job, two calibration circuits have been added to measure the readout errors of the qubits q_0 and q_1 . These circuits initialize the qubits in the states $|0\rangle$ or $|1\rangle$, respectively, and measure the qubit in the \hat{Z} eigenbasis directly after the initialization. The measurement results give an estimate of each qubit's current readout fidelity and QISKIT provides methods to mitigate the readout errors of all subsequent measurements based on this data. The following circuits of each batch job are used to calculate the time evolution of the system or to scan a parameter. Here, the quantum computer is initialized in the state joint ground state $|00\dots 0\rangle$ and a sequence of time steps, shown in blueish colors in Figure 6.3(d), is applied until the desired final time is reached. Then, the state of the quantum processor is determined using a quantum state tomography, shown in red. To calculate a time evolution for fixed system parameters, we vary the number of time steps in each circuit, as shown in the upper part of Figure 6.1(d). To scan the impact of a system parameter, such as the signal strength, we fix the number of time steps per circuit and vary the system parameter, as shown in the lower part of Figure 6.1(d).

To determine the final state of the time evolution, we perform a quantum state tomography of the two qubits q_0 and q_1 encoding the spin-1 system [Altepeter *et al.*, 2004; Nielsen and Chuang, 2011]. The two-qubit state is decomposed in terms of tensor products of Pauli matrices,

$$\hat{\rho} = \frac{1}{4} \sum_{j,k=0}^3 \alpha_{j,k} \hat{\sigma}_j \otimes \hat{\sigma}_k , \quad (6.18)$$

$$\alpha_{j,k} = \text{Tr} [(\hat{\sigma}_j \otimes \hat{\sigma}_k) \hat{\rho}] , \quad (6.19)$$

where $\hat{\sigma}_0 = \hat{\mathbb{1}}$, $\hat{\sigma}_1 = \hat{X}$, $\hat{\sigma}_2 = \hat{Y}$, and $\hat{\sigma}_3 = \hat{Z}$. The coefficient $\alpha_{0,0} = 1$ is fixed by the normalization of the quantum state $\hat{\rho}$. The remaining coefficients $\alpha_{j,k}$ can be determined by measuring the qubits q_0 and q_1 with respect to all nine combinations of measurement bases $\{x, y, z\} \times \{x, y, z\}$. To derive the connection between the measurement results and the coefficients $\alpha_{j,k}$, we rewrite each operator as follows:

$$\hat{\sigma}_j = |+_j\rangle \langle +_j| + \eta_j |-_j\rangle \langle -_j| , \quad (6.20)$$

where $j \in \{0, 1, 2, 3\}$, $\eta_0 = +1$, and $\eta_{1,2,3} = -1$. The state $|\pm_j\rangle$ denotes an eigenstate of the measurement in the $\hat{\sigma}_j$ eigenbasis with eigenvalue ± 1 . For $j = 0$, the measurement basis is the \hat{Z} eigenbasis. Measuring each combination $\{x, y, z\} \times \{x, y, z\}$ of measurement directions N times, we can estimate the probabilities $0 \leq P_{j,k}^{\pm,\pm} \leq 1$ to obtain the eigenvalues ± 1 in a measurement in the $\hat{\sigma}_j$ and $\hat{\sigma}_k$ eigenbases on the qubits q_1 and q_0 , respectively. The standard deviation of the estimate will decrease proportional to $1/\sqrt{N}$, *i.e.*, we can determine $P_{j,k}^{\pm,\pm}$ to arbitrary precision by increasing the number of measurements. Inserting Equation (6.20) into Equation (6.19), we find a relation between the expansion coefficients $\alpha_{j,k}$ and the probabilities $P_{j,k}^{\pm,\pm}$,

$$\alpha_{j,k} = P_{j,k}^{+,+} + \eta_k P_{j,k}^{+,-} + \eta_j P_{j,k}^{-,+} + \eta_j \eta_k P_{j,k}^{-,-} .$$

In the case of noisy measurements, the state $\hat{\rho}$ must be estimated from the measurement results using a maximum likelihood method which ensures that $\hat{\rho}$ is a physical positive-semidefinite density matrix normalized to unit trace. This has been discussed by Smolin *et al.* [2012] and the corresponding algorithm is already implemented in QISKIT.

All data presented in the following sections have been collected on the publicly accessible NISQ processor IBMQX2 between September 30 and October 7, 2019. Each batch job has been executed with the maximum possible number of 8192 repetitions per circuit and, unless stated otherwise, it has been repeated three times to rule out drifts of the device parameters during data collection. The corresponding standard deviation is indicated by the error bars, which are smaller than the plot markers. Note that these error bars capture only statistical measurement errors and the short-term stability of the device parameters on a timescale of hours. Since the parameters of the quantum computer vary on a timescale of days, the quantum computers are recalibrated on a daily basis. Therefore, numerical changes of the results obtained for a small signal strength $\varepsilon \rightarrow 0$ are expected if data obtained on different days are compared. Simulations of the exact dynamics given by Equation (6.1) have been performed using the *python* package QUTIP [Johansson *et al.*, 2012].

6.5 Device characterization

We now study the quantum circuit shown in Figure 6.2(a) on actual quantum hardware. In theory, one can iteratively apply the quantum circuit N times to evolve the initial state of the quantum simulation to the correct final state at time $T = Ndt$ up to corrections of $\mathcal{O}(dt^3)$. We now check whether this is also the case on an actual NISQ computer by testing the different elements of the circuit. In a first step, we will switch off the dissipative stabilization of the limit cycle and we will focus only on the coherent signal. In a second step, we will investigate the performance of the dissipative time evolution in the absence of an applied signal. Our findings will reveal restrictions imposed by the limited capabilities of state-of-the-art quantum computers that require a modification of the quantum circuit shown in Figure 6.2(a). These modifications will be discussed in Section 6.6.

Figure 6.4(a) shows the time evolution of the initial state $|0\rangle$ under the signal components $j_{0,\pm 1}$ on a NISQ computer together with the corresponding result expected for an ideal noise-free quantum computer. Controlled two-qubit gates are found to induce strong depolarization errors that evolve the initial state $|0\rangle$ to a completely mixed state after only a few Trotter steps. This result is also confirmed by simulations taking into account the noise model of the IBM quantum processors provided in the *python* API QISKIT, which are not shown here. We can check that the strong depolarizing errors indeed stem from controlled two-qubit operations by replacing all controlled rotations with the corresponding uncontrolled single-qubit rotation. The corresponding results obtained for local single-qubit rotations are shown in Figure 6.4(b). Since the single-qubit error rates are about an order of magnitude smaller than the two-qubit CNOT error rate [Corcoles *et al.*, 2019], the implementation of the signal using only uncontrolled single-qubit rotations reproduces the expected ideal noise-free result almost perfectly over a much larger range of Trotter steps.

Moving on to multiple dissipative time steps in a row, we encounter another technical restriction of IBM's quantum processors. Currently, measurement operations can only be performed at the end of a quantum computation, *i.e.*, the measurement and subsequent reset operations of the ancillary qubits a_j , which are contained in the

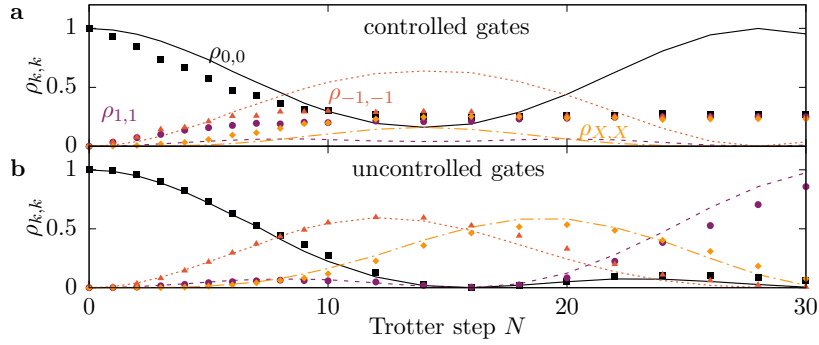


FIGURE 6.4: Time evolution of the state $|0\rangle$ under the semiclassical signal components $j_{0,\pm 1}$ (markers) on a noisy intermediate-scale quantum computer and ideal noise-free time evolution (lines). **(a)** For *controlled* two-qubit $\hat{U}_{\pm 1,0}$ gates as used in the quantum circuit shown in Figure 6.2(a), the state quickly evolves to a completely mixed state. **(b)** For *uncontrolled* single-qubit $\hat{U}_{\pm 1,0}$ gates, the theoretically expected oscillations of the populations is well reproduced experimentally. Parameters are $\varepsilon dt = 0.1$, $j_{-1,0} = 0.5 \times e^{-\pi i/6}$, $j_{1,0} = 1 \times e^{5\pi i/6}$, $j_{-1,1} = 0$, and $\Delta/\varepsilon = 0$. The data have been collected on the IBMQX2 processor on qubits $q_0 = 4$ and $q_1 = 2$.

D_k gates shown in Figure 6.2(a), are not permitted in the middle of a quantum circuit. We can react to this restriction by using a new ancillary qubit in each time step and by measuring all ancillary qubits at the end of the time evolution. As a consequence, the maximum number of Trotter steps is bounded by the number of available ancillary qubits on the quantum computer. Even worse, since SWAP operations are composed of three CNOT gates and suffer strong depolarizing errors, we can only use ancillary qubits that are adjacent to the system qubit q_j , which limits us to at most four time steps. At the moment, this technical constraint on the measurement and reset operations is the most severe limitation for the simulation of dissipative quantum systems on IBM's quantum processors. We expect that it will be lifted in the near future.

To identify suitable system and ancillary qubits, we search for groups of connected qubits that perform well in the test of the dissipative time step discussed in Section 6.4. The qubit with the highest connectivity is used as the system qubit and the other ones serve as ancillary qubits. On the 5-qubit IBMQX2 device, the system qubit is the central qubit 2 and its ancillary qubits are 0, 1, 3, and 4. On the 14-qubit IBMQ_16_MELBOURNE device, the system qubits are either qubit 8 or qubit 11 and the corresponding ancillary qubits are either 6, 7, and 9 or 3, 10, and 12, respectively. The order in which the ancillary qubits interact with the system qubit is determined by the test of the dissipative circuit shown in Figure 6.3(c): The ancillary qubits are sorted in descending order with respect to the measured $\langle \hat{Z} \rangle$ expectation value such that the smallest depolarizing errors are introduced in the first time step. Towards the end of the time evolution, larger depolarizing errors can be tolerated since the signal has already built up coherences. The order of the ancillary qubits is redetermined each day after the recalibration of the quantum computer.

Figure 6.5 demonstrates the dissipative stabilization of the limit-cycle state $|0\rangle$ if no signal is applied, $j_{\pm 1,0} = j_{1,-1} = 0$. As expected, the population of the target state $|0\rangle$ dominates at the end of the time evolution independent of the chosen initial state. However, the controlled two-qubit operations in the circuits (6.13) and (6.17) implementing the dissipative time steps induce depolarizing errors that reduce the population of the limit-cycle state $|0\rangle$ and will evolve the system to a completely

mixed state in the long-time limit. As shown in Figure 6.4(a), this effect is small on the considered timescale since we carefully select the ancillary qubits. In agreement with the observation made in Figure 6.3(c), the noise induced by the dissipative limit-cycle stabilization induces coherence in the limit-cycle state. The magnitude of this noise is indicated by the gray circle. Note that this effect is not captured by the simple noise model provided in QISKIT.

6.6 Dealing with hardware constraints

The main findings of Section 6.5 are that controlled two-qubit operations induce strong depolarizing errors and that the current hardware does not allow measurement and reset operations in the middle of a quantum circuit. Both effects are severe obstacles to a digital quantum simulation of dissipative quantum systems. Luckily, the paradigm of quantum synchronization allows us to adapt the quantum circuit shown in Figure 6.2(a) to circumvent the limitations of IBM's quantum processors.

Figure 6.4(a) shows that it is not feasible to perform the time evolution shown in Figure 6.2(a) on a current NISQ computer because already the implementation of the signal induces strong depolarizing errors already after a few time steps. However, in the synchronization regime, most of the population remains in the limit-cycle state $|0\rangle$ even though a signal is applied to the limit-cycle oscillator. Therefore, it is possible to consider a modified circuit where the controlled $\hat{U}_{\pm 1,0}$ gates are replaced by the corresponding uncontrolled single-qubit rotations. If we additionally decide not to use the squeezing signal, $j_{-1,1} = 0$, we obtain the quantum circuit shown in Figure 6.6(a) which implements the signal without any controlled operations.

The transitions induced by this modified circuit are sketched in Figure 6.6(b). At first sight, Figures 6.6(b) and the original transition scheme shown in Figure 6.2(b) seem to represent completely different dynamics. However, we will now show that both transition schemes are actually equivalent in the regime of synchronization on a noisy quantum computer. The key point is that the signal strength in the regime of synchronization is linearly proportional to a small dimensionless parameter $0 \leq \eta \ll 1$ as discussed in Section 5.2.6, which ensures that the signal \hat{H}_{ext} is only a small perturbation to the limit-cycle state. Thus, the amplitudes of the coherences $\rho_{\pm 1,0}$ are of order η and the populations of the states $|\pm 1\rangle$ are of order η^2 . Therefore, they are strongly suppressed as compared to the limit-cycle state $|0\rangle$ having a population of the order of unity. Under these conditions, we can replace the controlled two-qubit gates $\hat{U}_{\pm 1,0}$ by uncontrolled single-qubit rotations. In principle, the signal will now build up coherences $\rho_{k,X}$ between the spin-1 states and the state $|X\rangle$ and it will transfer population to the state $|X\rangle$. However, both effects can be safely ignored, in particular on a noisy system, because the coherences $\rho_{k,X}$ and the population $\rho_{X,X}$ are only of order η^3 and η^4 , respectively. Moreover, since the relaxation mechanism $D_{\pm 1}$ takes the state $|X\rangle$ back to $|\mp 1\rangle$, there is no risk to trap population in $|X\rangle$.

Having eliminated all controlled gates from the part of the circuit that implements the signal, we are only left with a few controlled two-qubit gates in the dissipative time steps. These gates cannot be replaced since it is unavoidable to entangle the system qubit with the ancillary qubits to induce non-unitary dynamics. However, since we chose to switch off the squeezing drive, the system qubits q_0 and q_1 can now be assigned independently to different physical qubits of the quantum processor. This allows us to map the system qubits to spatially separated groups, *e.g.*, the groups $\{6, 7, 8, 9\}$ and $\{3, 10, 11, 12\}$ on the `IBMQ_16_MELBOURNE` device. On the 5-qubit `IBMQX2`,

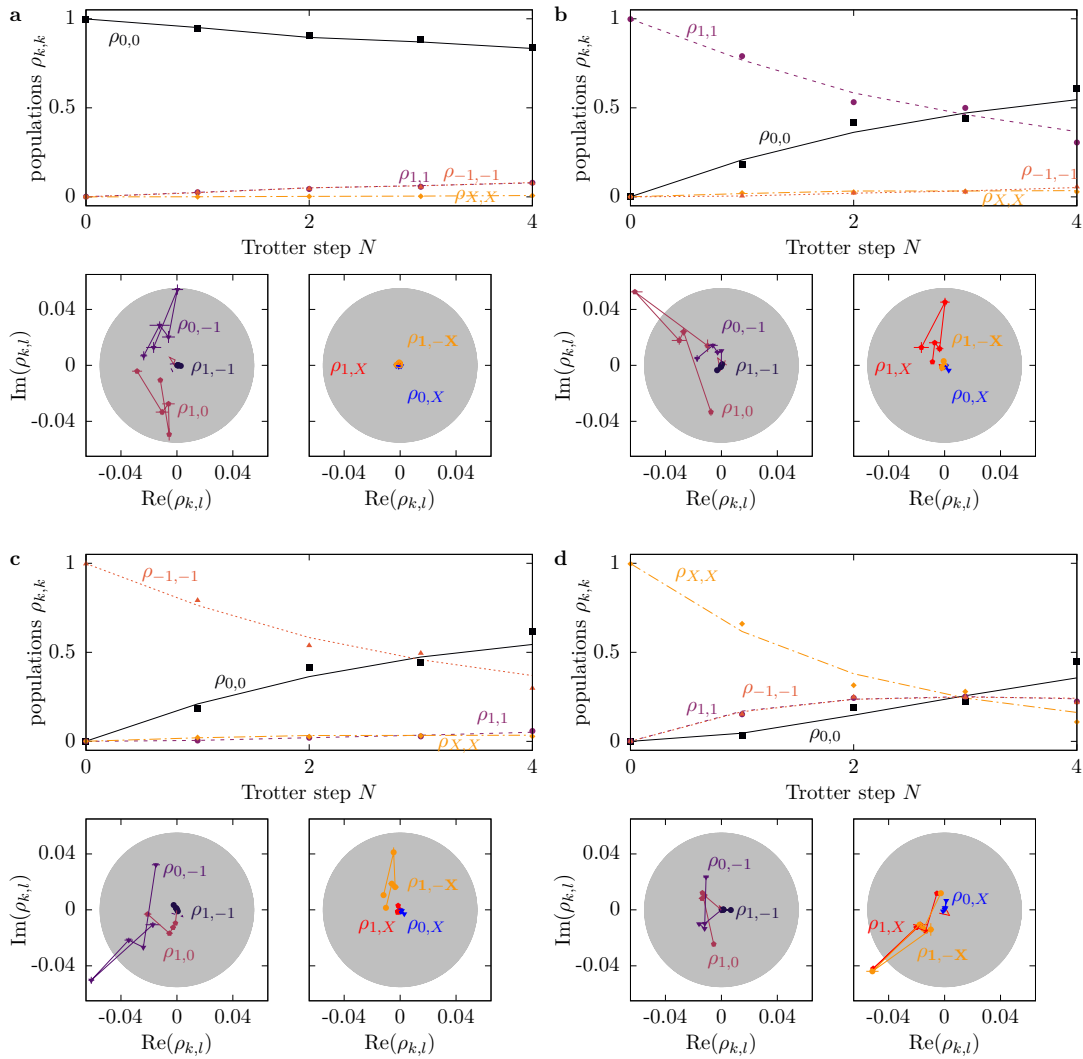


FIGURE 6.5: Characterization of the dissipative stabilization of the limit-cycle state $|0\rangle$ if the signal is switched off, $j_{\pm 1,0} = j_{-1,1} = 0$, on a NISQ computer (markers) and theoretical expectation taking into account noise (lines). The initial state is (a) $|0\rangle$, (b) $|+1\rangle$, (c) $|-1\rangle$, and (d) $|X\rangle$. The gray circle defines the noise level of the coherences due to the gate imperfections in the dissipative limit-cycle stabilization. Parameters are $\Gamma_{1,0}dt = 0.2$, $\Delta/\Gamma_{1,0} = 0$, and $\Gamma_{-1,0}/\Gamma_{1,0} = 1$. Data have been collected on IBMQX2 on qubits $q_0 = 2$ and $q_1 = 2$ in sequential runs.

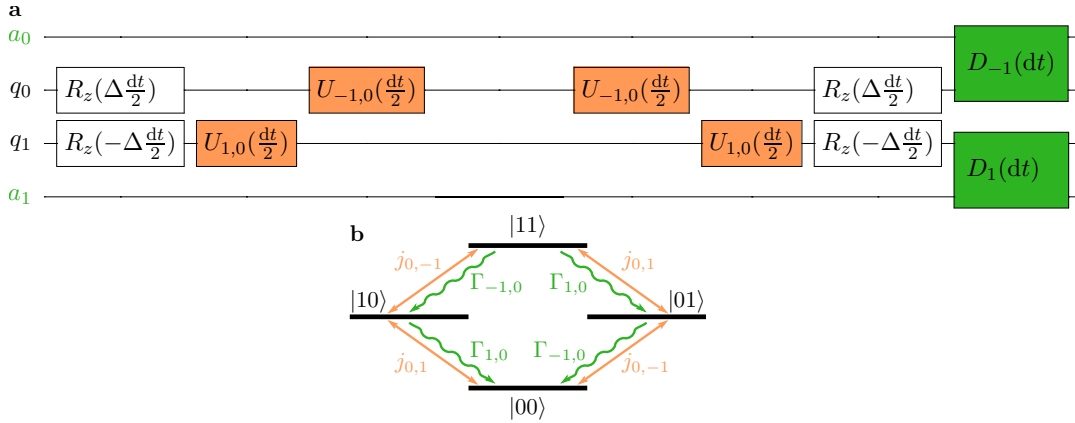


FIGURE 6.6: **(a)** Modified quantum circuit that uses only local single-qubit rotations to implement the signal. In contrast to the ideal circuit shown in Figure 6.2(a), this modified circuit is compatible with the limited capabilities of current NISQ computers. **(b)** Sketch of the dynamics generated by the modified circuit. In the regime of synchronization, this dynamics is equivalent to the one shown in Figure 6.2(b) for $j_{-1,1} = 0$, because of the hierarchy $\rho_{X,X} \ll \rho_{\pm 1, \pm 1} \ll \rho_{0,0}$.

the system qubits q_0 and q_1 can be sequentially assigned to the central physical qubit 2 in two consecutive runs.

Given the fixed qubit connectivity and the low SWAP fidelities of IBM's current quantum computers, the limit on the available Trotter steps imposed by the device connectivity cannot be evaded. As a consequence, a quantum simulation of the steady-state solution of Equation (6.1) is out of reach, but we are able to demonstrate the transient buildup of synchronization, as shown in Figure 6.7.

The data show the time evolution of the populations and coherences if both a signal and the dissipative limit-cycle stabilization are switched on. Comparing this result to Figure 6.5(a), we find that the signal builds up the populations $\rho_{0,-1}$ and $\rho_{1,0}$ well beyond the noise level of the limit-cycle state. At the same time, the population $\rho_{0,0}$ is slightly reduced since the signal transfers population to the states $|\pm 1\rangle$. Other coherences are built up due to higher-order effects, but they remain below the noise level of the limit-cycle state. In particular, the coherences $\rho_{k,X}$ remain well below this threshold, which justifies the replacement of controlled gates in the signal by uncontrolled ones.

6.7 Experimental demonstration of quantum synchronization

Figure 6.7 demonstrates that the modified quantum circuit shown in Figure 6.6(a) is compatible with the technical restrictions of current NISQ computers. Using this circuit, we now perform a digital quantum simulation of quantum synchronization dynamics on the IBM Q System and we experimentally demonstrate typical features of quantum synchronization. In a first step, we measure the final state $\hat{\rho}$ after 3 time steps as a function of the detuning Δ and we reconstruct the phase distribution $S_{\hat{\rho}}(\phi)$

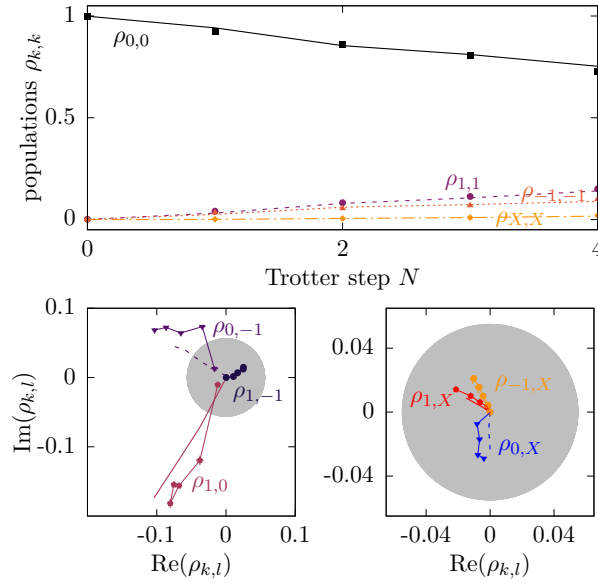


FIGURE 6.7: Demonstration of the onset of synchronization if both a signal and the dissipative stabilization of the limit-cycle state are switched on, $j_{-1,0} = 1 \times e^{2\pi i/6}$, $j_{1,0} = 2 \times e^{-\pi i/6}$, and $j_{-1,1} = 0$. The signal builds up the coherences $\rho_{1,0}$ and $\rho_{0,-1}$ well beyond the noise level of the limit cycle, indicated by the gray circle. The coherences $\rho_{k,X}$ remain well below the noise level, which justifies to use the simplified circuit shown in Figure 6.6(a). Parameters are $\Gamma_{1,0}dt = 0.2$, $\Delta/\Gamma_{1,0} = 0$, $\varepsilon/\Gamma_{1,0} = 0.25$, and $\Gamma_{-1,0}/\Gamma_{1,0} = 1$. Data have been collected on the IBMQX2 quantum computer on the qubits $q_0 = 2$ and $q_1 = 2$ in sequential runs.

using Equation (5.20),

$$S_{\hat{\rho}}(\phi) = \frac{3}{8\sqrt{2}} |\rho_{1,0} + \rho_{0,-1}| \cos[\phi + \arg(\rho_{1,0} + \rho_{0,-1})] + \frac{1}{2\pi} |\rho_{1,-1}| \cos[2\phi + \arg(\rho_{1,-1})] . \quad (6.21)$$

The results are shown in Figure 6.8(a). For a detuned signal, $|\Delta| > 0$, synchronization decreases since we keep the overall signal strength ε fixed. At the same time, the relative phase ϕ between the limit-cycle oscillator and the signal changes. The measurement results agree well with the theoretical prediction of the position of the peak of Equation (6.21), which is indicated by the dashed black line. The small deviations of the expected position of the maximum stems from a detuning dependence of the limit-cycle stabilization mechanism due to device imperfections.

As discussed in Section 5.2.6, a nonzero phase distribution $S_{\hat{\rho}}(\phi)$ is only a necessary condition for quantum synchronization since it could be caused by a signal that is forcing the limit-cycle oscillator. Given a nonzero phase distribution, a sufficient condition for the demonstration of quantum synchronization is that the coherences of the density matrix increase linearly with the signal strength. To check this, we vary the signal strength ε and reconstruct the final state $\hat{\rho}$ by a quantum state tomography. The corresponding results are shown in Figure 6.8(b). The coherences $\rho_{1,0}$ and $\rho_{0,-1}$ are built up proportional to ε , as one expects from a signal that contains only the semiclassical signal components $j_{\pm 1,0}$. Moreover, the limit-cycle population remains

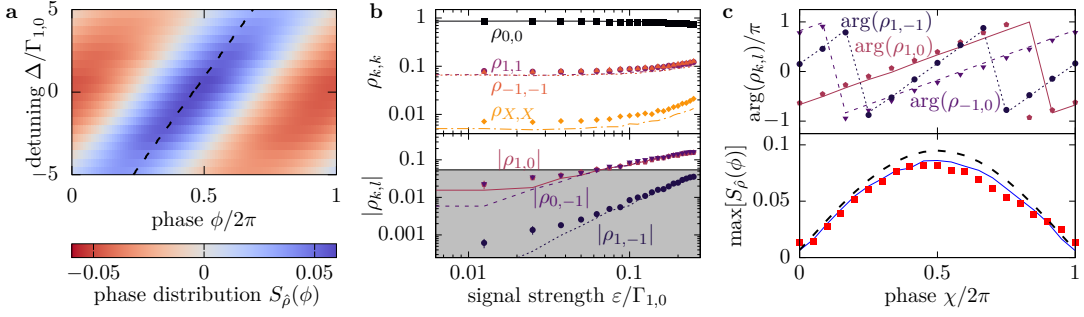


FIGURE 6.8: **(a)** Phase distribution $S_{\hat{\rho}}(\phi)$ of the spin-1 limit-cycle oscillator as a function of the detuning Δ between its natural frequency and the signal frequency after $N = 3$ time steps. The solid line indicates the theoretical expectation of the position of the maximum of $S_{\hat{\rho}}(\phi)$, obtained by combining Equations (6.1) and (6.21). Parameters are $\Gamma_{-1,0}/\Gamma_{1,0} = 1$, $\Gamma_{1,0}dt = 0.2$, $\varepsilon/\Gamma_{1,0} = 0.25$, $j_{-1,0} = 2 \times e^{2\pi i/6}$, $j_{1,0} = 2 \times e^{-\pi i/6}$, and $j_{-1,1} = 0$. **(b)** Populations and coherences as a function of the signal strength ε for $\Delta/\Gamma_{1,0} = 0$. The gray background indicates the noise level of the coherences introduced in Figure 6.5. **(c)** Upper panel: Phase of the coherences if the overall phase χ of the signals, $j_{\pm 1,0}e^{i\chi}$, is varied for $\Delta/\Gamma_{1,0} = 0$ and $\varepsilon/\Gamma_{1,0} = 0.25$. Lower panel: Demonstration of an interference-based quantum synchronization blockade if the phase of only one of the signals is varied, $j_{-1,0} = e^{i\chi} \times 2 \times e^{-2\pi i/6}$ and $j_{1,0} = 2 \times e^{-2\pi i/6} = \text{const}$. Red data points are the result obtained on a NISQ device, the solid blue line corresponds to a simulation taking into account noise, and the dashed black line describes the theory result. Parameters are $\Gamma_{-1,0}/\Gamma_{1,0} = 1.25$, $\Gamma_{1,0}dt = 0.2$, $\varepsilon/\Gamma_{1,0} = 0.25$, and $j_{-1,1} = 0$. All data of this figure have been collected on the IBMQX2 processor on qubits $q_0 = 2$ and $q_1 = 2$ in sequential runs.

mostly in the state $|0\rangle$ and the populations $\rho_{0,0}$, $\rho_{1,1}$, and $\rho_{-1,-1}$ change only quadratically in the signal strength ε . Therefore, the applied signal perturbs the limit-cycle state only weakly and we operate in the regime of quantum synchronization.

The population $\rho_{X,X}$ is strongly suppressed as compared to the spin-1 coherences, which justifies our approximation to replace controlled gates by uncontrolled ones in the quantum circuit implementing the signal. The coherence $\rho_{1,-1}$ is build up quadratically in the signal strength ε , which is a higher-order effect. Indeed, using Equation (5.13), we find that the nonzero first-order coherences $\rho_{\pm 1,0}$ give rise to a nonzero coherence $\rho_{1,-1}$ in a second-order process,

$$\langle 1 | \mathcal{L}_{\text{ext}} \hat{\rho}^{(1)} | -1 \rangle = -i \left[\langle 1 | \hat{H}_{\text{ext}} | 0 \rangle \rho_{0,-1}^{(0)} - \rho_{1,0}^{(0)} \langle 0 | \hat{H}_{\text{ext}} | -1 \rangle \right] \propto \varepsilon^2 .$$

Note that the magnitude $|\rho_{1,-1}|$ remains below the noise level of the limit-cycle state, as shown in Figure 6.7.

Having verified that we operate in the regime of synchronization, we demonstrate in the upper panel of Figure 6.8(c) that we can tune the phase of the coherences by changing the phase of the signal components. A global phase χ of the signal coefficients,

$$j_{\pm 1,0} \rightarrow e^{i\chi} j_{\pm 1,0} ,$$

rotates the phase of the coherences as expected from theory. This allows us to experimentally demonstrate the effect of interference-based quantum synchronization

blockade, which has been introduced in Section 5.7. By rotating only the phase of one of the signal components,

$$\begin{aligned} j_{-1,0} &\rightarrow e^{i\chi} j_{-1,0} , \\ \dot{j}_{1,0} &= \text{const} , \end{aligned}$$

the relative phase between the coherences $\rho_{1,0}$ and $\rho_{0,-1}$ is changed. As shown in Equation (6.21), synchronization will be strongly suppressed if the two coherences interfere destructively, which is shown in Figure 6.8(c) for $\chi = 0$ and $\chi = 2\pi$. This result is the first experimental demonstration of a genuinely quantum effect in synchronization.

6.8 Summary

Our results demonstrate that state-of-the-art NISQ computers enable the study of realistic dissipative quantum systems. Despite the fact that quantum algorithms to simulate dissipative quantum systems have been discussed for quite some time [Lloyd and Viola, 2001; Bacon *et al.*, 2001; Kliesch *et al.*, 2011], actual quantum hardware was not powerful enough to implement them successfully. Therefore, only isolated subproblems could be tested experimentally by García-Pérez *et al.* [2020]. We encountered obstacles to the simulation of the ideal quantum circuit shown in Figure 6.2(a), too, namely,

- (i) the two-qubit gate fidelities [Corcoles *et al.*, 2019] are still at least an order of magnitude too low,
- (ii) missing qubit reset operations complicate the quantum circuit, and
- (iii) the effective connectivity of the device is too low to compensate point (ii), mainly because of point (i).

However, we were able to react to these limitations since we implemented quantum synchronization dynamics. The perturbative structure of synchronization allowed us to modify the quantum circuit to the form shown in Figure 6.6(a), which is compatible with current NISQ computers.

In this way, we were able to experimentally demonstrate quantum synchronization and, in particular, interference-based quantum synchronization blockade. A key element to our success was the freedom to choose a limit-cycle stabilization mechanism that is less complicated than the one of the quantum vdP oscillator and, in particular, can be mapped to simple single-qubit relaxation processes on a quantum computer. In this way, we solved the experimental challenge to implement both a highly nonlinear dissipation mechanism and coherent control of the signal in a single experimental platform.

Understanding dissipative quantum systems is of high relevance for quantum sensing [Wiersig, 2016], quantum information processing [Metelmann and Clerk, 2015], and quantum state preparation [Poyatos *et al.*, 1996]. Simulating dissipative quantum systems is much harder than simulating a comparable closed system since one has to account for environmental degrees of freedom. For instance, even for a moderate network size of approximately 20 limit-cycle oscillators, classical simulation approaches will fail. Our results reveal that current algorithms to simulate dissipative quantum systems will not be suited to study more complex dissipative quantum systems in the near future. The perturbative structure of synchronization and our choice to switch off

the squeezing drive put us into the special situation to be able to remove all controlled operations from the implementation of the signal. In general, controlled operations will constitute a crucial part of the time evolution, in particular in networks of dissipative quantum systems, where exchange interactions such as the $\hat{U}_{1,-1}$ gate, will be indispensable. In this context, our results provide a guideline for the development of novel quantum computers and novel algorithms enabling the study of dissipative quantum systems on current NISQ devices.

The results and figures presented in this chapter have been published in parts in [Koppenhöfer *et al.*, 2020b].

Chapter 7

Conclusion and Outlook

In recent years, significant experimental progress has been made to engineer micro- and nanoscale systems that require a quantum-mechanical description of their dynamics. In this thesis, we investigated the generation of nonclassical states in dissipative quantum systems by continuous measurements, and we discussed quantum synchronization phenomena in limit-cycle oscillators.

Nonclassical state generation

In the first part of this thesis, we studied how continuous measurements of dissipative quantum systems, *i.e.*, photon counting or homodyne detection, can be used to generate nonclassical states. The key element of our approach was to infer the current state of a quantum system from the record of previous measurement results, which allows one to perform a postselection of interesting nonclassical states.

In the case of an optomechanical system driven into mechanical limit-cycle motion, discussed in Chapter 3, the continuous measurement of the radiation leaking out of the optical cavity allows one to track mechanical amplitude fluctuations. This decreases the amplitude uncertainty of the mechanical state such that the mechanical oscillation has a nonclassical sub-Poissonian phonon-number distribution. Our findings complement previous studies that focused on the unconditional dynamics in the absence of continuous measurements and predicted nonclassical mechanical states only in the resolved-sideband regime $\kappa \ll \Omega_{\text{mech}}$. We showed that adding a continuous detection significantly enlarges the range of parameters where nonclassical states can be observed. Using our approach, nonclassical mechanical states can be generated even in the unresolved-sideband regime $\kappa > \Omega_{\text{mech}}$. Optomechanical limit-cycle motion has already been demonstrated in experiments, but it has not been possible to enter parameter regimes where nonclassical limit cycles could be experimentally observed. Our numerical study predicts a significant reduction of the mechanical amplitude fluctuations particularly in parameter regimes that are inspired by typical experimental values. Consequently, inducing nonclassical states by continuous measurements may pave an experimentally feasible way to generate and observe nonclassical mechanical limit-cycle motion in state-of-the-art optomechanical systems.

In Chapter 4, we took a broader view and investigated continuously monitored quantum systems whose time evolution can be modeled by a piecewise-deterministic stochastic process. The continuous deterministic part of the time evolution and the stochastic quantum jump process define two competing time scales, $1/\Gamma_{\text{rel}}$ and $1/\Gamma_{\text{jump}}$, respectively. We showed that the continuous time evolution induces a relaxation process towards well-defined states. By tuning the system parameters such that the condition $\Gamma_{\text{rel}} \geq \Gamma_{\text{jump}}$ holds, the continuous time evolution can be made dominant. Using this effect, we proposed a heralded state-preparation protocol to generate deterministic quantum states. Focusing on a generic model of a nonclassical system, the Kerr nonlinear oscillator, we demonstrated that the protocol enables

the generation of states with a negative Wigner function. This is an important result because the Wigner function of the Kerr oscillator in the absence of a continuous measurement must be strictly positive. Since an ensemble average over many quantum trajectories reproduces the steady-state result, the nonclassicality of the target state stabilized by the state generation protocol is carefully balanced by all other quantum states that are explored along the stochastic quantum trajectory. We demonstrated that small Schrödinger cat states can be generated by our protocol without the need for feedback.

In the projects presented in Chapters 3 and 4, we chose a specific dissipative quantum system and characterized the nonclassical states that can be generated by a continuous measurement. An interesting open question is the reverse problem, namely, given a certain quantum state, which system and which continuous measurement generate this state? This question is highly relevant to quantum-enhanced metrology [Pezzè *et al.*, 2018; Degen *et al.*, 2017], quantum information processing [Stahlke, 2014; Rahimi-Keshari *et al.*, 2016; Veitch *et al.*, 2012], and quantum error correction in continuous-variable systems [Michael *et al.*, 2016; Braunstein and van Loock, 2005], which require various types of nonclassical states as a resource.

The nonlinear continuous part of the time evolution in the presence of a photon-counting measurement is characterized by an effective non-Hermitian Hamiltonian. Recently, non-Hermitian Hamiltonians attracted significant attention because of the presence of exceptional points in their complex eigenvalue spectrum. At a n -th order exceptional point, $n + 1$ eigenvalues and eigenvectors of the non-Hermitian Hamiltonian coalesce and the Hamiltonian becomes non-diagonalizable [Moiseyev, 2011]. This effect can be used to induce topological energy transfer between the coalescing eigenmodes if the parameters of the Hamiltonian are varied along a closed loop in parameter space that encircles the exceptional point [Heiss, 1999; Xu *et al.*, 2016]. Close to the exceptional point, the energy splitting of the eigenmodes scales proportional to the $n + 1$ -th root of these parameters. Wiersig [2016] suggested that this scaling gives rise to an enhanced measurement sensitivity close to the exceptional point. Whether this will also lead to an enhanced measurement precision for realistic measurement protocols is the subject of a current controversy [Langbein, 2018; Lau and Clerk, 2018; Chen *et al.*, 2019; Zhang *et al.*, 2019]. Effective non-Hermitian dynamics can be engineered by balancing coherent interactions and dissipation in multimode systems, *e.g.*, in photonic systems [Makris *et al.*, 2008; Regensburger *et al.*, 2012], cold atoms [Hang *et al.*, 2013], coupled optomechanical devices [Jing *et al.*, 2014], and ferromagnets in a microwave cavity that are driven by two phase-shifted magnetic fields [Grigoryan *et al.*, 2018; Soykal and Flatté, 2010]. Our results suggest that continuous measurements of dissipative quantum systems in the regime $\Gamma_{\text{rel}} \gg \Gamma_{\text{jump}}$ may provide another experimentally feasible way to induce and investigate non-Hermitian dynamics.

Quantum synchronization

Our growing abilities to fabricate and control micro-, nano-, and optomechanical systems open the exciting possibility to study nonlinear dynamics in the quantum regime. In the second part of this thesis, we focused on a particular effect in nonlinear dynamics, namely, synchronization. Powerful mathematical methods have been developed to formalize and study the problem of classical synchronization, *e.g.*, two-timing methods to derive approximate equations of motion for the slowly varying amplitude and phase of the oscillation, linear stability analysis, and bifurcation theory to classify and graphically represent transitions between different types of oscillatory dynamics. The

case of quantum synchronization, however, is much less understood. Different proposals for quantum limit-cycle oscillators have been put forward, which were guided by an analysis of the semiclassical equations of motion that reproduce a classical limit-cycle oscillator. Similarly, quantum synchronization measures have been proposed to generalize different aspects of classical synchronization to the quantum regime.

In Chapter 5, we developed a framework for quantum synchronization with the aim to provide a universal platform to study and classify quantum synchronization phenomena. The framework is based on a quantum master equation approach to model dissipative quantum systems, and on the perturbative nature of the synchronization problem. It applies both to oscillator-based and spin-based quantum limit-cycle oscillators. We identified the coherences between the energy eigenstates as the quantum-mechanical resource of synchronization and found that coherences which transform identically under phase rotations contribute collectively to phase localization. This gives rise to an interference-based quantum synchronization blockade effect, which complements a previously reported quantum synchronization blockade based on the anharmonicity of the energy spectrum of a quantum limit-cycle oscillator.

An important building block of our framework is a rule how to choose the overall signal strength such that the signal remains a small perturbation to the limit cycle. This rule enables the comparison of different quantum limit-cycle oscillators and led to the following results. First, we were able to derive an analytical formula describing the upper boundary of the synchronization region in parameter space. Thereby, we extended the well-known Arnold tongue to a snake-like split tongue. Second, we put recent numerical studies into a broader picture and showed analytically that there is an optimal amplitude of the squeezing signal beyond which squeezing does no longer improve quantum synchronization. However, synchronization can still be further increased by modifying the components of the semiclassical signal. Third, we derived a tight upper bound on the maximum degree of quantum synchronization that is achievable in the quantum regime and we constructed a limit cycle that reaches this bound asymptotically. Finally, we proposed a practical scheme to stabilize this limit cycle, which promises to be experimentally less challenging than the dissipative transition scheme that stabilizes the quantum van der Pol oscillator.

The framework developed in this thesis can be applied to a variety of open questions in the field of quantum synchronization. First, one may exploit the perturbative nature of the synchronization problem to relate the quantum synchronization measure $S_{\hat{\rho}}(\varphi)$ to other synchronization measures, such as the ones reviewed in Section 2.6.4. In particular, it is desirable to establish an analytical connection with the power spectrum $S_{\hat{a}^\dagger\hat{a}}(\omega)$ of the limit-cycle oscillator because power spectra can be easily measured in experiments whereas the evaluation of the relative phase distribution $S_{\hat{\rho}}(\varphi)$ requires a rather complex quantum state tomography.

Second, our framework can be easily generalized to the case of mutually coupled limit-cycle oscillators. The definition of a weak signal will then be replaced by a condition on the strength of the mutual coupling, which ensures that the coupling is only a small perturbation to the limit-cycle dynamics of the oscillators. This will open the exciting possibility to revisit the controversy on the interplay of entanglement, quantum discord, and quantum synchronization. The publications reviewed in Section 2.6.4 consider very different limit-cycle oscillators and parameter regimes, ranging from the equatorial spin-1 limit cycle and the van der Pol oscillator in the quantum regime to an optomechanical limit cycle at large mechanical amplitudes. Moreover, even limit-cycle oscillators implemented on the same experimental platform will differ in their degree of entanglement depending on the structure of their limit cycles.

Thus, to put these very different results into a broader picture, a universal framework is needed that allows one to compare synchronization across very different platforms.

Third, a framework for quantum synchronization of coupled limit-cycle oscillators will be a useful starting point to construct a theory of quantum chimera states. Kuramoto and Battogtokh [2002] discovered that synchronized and incoherent subpopulations can coexist in networks of identical classical limit-cycle oscillators. Abrams and Strogatz [2004] proposed to call these hybrid states *chimera states* in allusion to a famous monster in Greek mythology, which is composed of a lion, a goat, and a snake. First attempts to study chimera states in the quantum regime have been made, which are mainly based on a discussion of the semiclassical equations of motion [Bastidas *et al.*, 2015; Viennot and Aubourg, 2016]. However, a quantum chimera state could be defined independently of the classical limit of the equations of motion by considering the relative phase distributions between different pairs of limit-cycle oscillators in the network. The dynamics of chimera states in a network and its change as a function of external parameters may have applications in quantum sensing. Spin-1 systems will be an ideal platform to study networks of quantum limit-cycle oscillators since they minimize the Hilbert-space dimension and provide a universal model for different limit-cycle oscillators in the quantum regime. Using the perturbative structure of the synchronization problem, even analytical calculations could be feasible for small network sizes.

Finally, it will be interesting to generalize the bound on the maximum synchronization derived in Section 5.6 to larger spin systems. This will shed light on the transition from quantum synchronization, where noise plays a crucial role, to classical synchronization. Moreover, it will allow one to establish a link between the discussion of optimal synchronization in the quantum regime, presented in this thesis, and the discussion of optimal synchronization in classical nonlinear dynamics [Harada *et al.*, 2010; Zlotnik and Li, 2012; Zlotnik *et al.*, 2013; Tanaka, 2014; Hasegawa and Arita, 2014; Pikovsky, 2015]. The case of half-integer spin systems is particularly interesting since these systems have an even number of levels and, thus, do not feature an equatorial pure-state limit cycle.

Digital quantum simulation of dissipative quantum systems

In Chapter 6, we used digital quantum simulation to implement quantum synchronization on a current quantum computer. We mapped the Hilbert space of a spin-1 system to a two-qubit register and constructed a quantum circuit that evolves the two-qubit state according to the spin-1 synchronization dynamics. Testing this circuit on an actual quantum computer, we identified several technical constraints of state-of-the-art quantum hardware that hinder the digital quantum simulation of arbitrary dissipative quantum systems. Nevertheless, the perturbative nature of synchronization allowed us to simplify the quantum circuit such that we could circumvent the hardware constraints. We experimentally demonstrated quantum synchronization dynamics and a genuinely quantum effect in synchronization, namely, quantum interference-based synchronization blockade. On one hand, these results demonstrate that current quantum computers have become powerful enough to study realistic dissipative quantum systems if these systems provide suitable symmetries to adapt the quantum algorithm to the technical restrictions of current hardware. On the other hand, they also reveal that digital quantum simulation of arbitrary complex dissipative quantum systems is still out of reach.

Consequently, an important task for future research on quantum simulation of dissipative quantum systems is to develop novel algorithms that are adapted to current quantum hardware. A promising way is to generalize existing hybrid quantum-classical algorithms, such as the variational quantum eigensolver [Peruzzo *et al.*, 2014; Kandala *et al.*, 2017], used to calculate ground states of closed quantum systems, or the quantum approximate optimization algorithm [Farhi *et al.*, 2014], used to solve optimization problems. These algorithms are based on the variational principle, *i.e.*, they minimize the expectation value of an observable with respect to a set of parameters that characterize a class of quantum states. The algorithms are called *hybrid* because most of the calculation is performed on classical hardware and the quantum computer is only used to generate the quantum state and to efficiently evaluate its expectation value. These tasks can be implemented by very short quantum circuits that are compatible with current hardware. Importantly, the steady state of a quantum master equation can be rephrased as a variational problem, too [Weimer, 2015]. Generalizations [Yoshioka *et al.*, 2019] of these hybrid quantum-classical algorithms for closed systems will open a way to study complex dissipative quantum systems, such as large networks of limit-cycle oscillators, on current NISQ computers.

Acknowledgements

Finally, I would like to thank all the people whose help was indispensable for my scientific work that led to this thesis.

First of all, I thank my supervisor Professor Christoph Bruder for accepting me as a PhD student in his group, and for his guidance and support of my research. I highly appreciate the great freedom I had to choose and pursue my research projects, and the possibility to engage in side activities such as organizing a conference. Besides giving me the chance to attend numerous schools, workshops, and conferences around the world, he also pointed out many scientific opportunities and cultural events in and around Basel. I am deeply grateful for all I learned and discovered in the last years, and for all chances that he opened up.

I also thank my co-supervisor Professor Philipp Treutlein for his interest in my research, and his constructive feedback on progress reports and seminar talks.

Many thanks go to Professor Rosario Fazio, who kindly agreed to referee this work. I appreciate the effort and time he invested into this process, despite the current uncertainties, travel restrictions, and other technical obstacles.

I thank Professor Stefan Goedecker for chairing my PhD defense.

I would also like to thank my collaborators Niels Lörch, Alexandre Roulet, Ehud Amitai, and Aaron Daniel, who challenged me in discussions and brought new ideas to my attention. I am very grateful for all I learned from them both on science and on other topics. Moreover, I thank all current and previous group members for the excellent group spirit, fruitful discussions, cheerful activities, and a most enjoyable time. Special thanks to Tibor Sekera, who was the driving force of the rooftop table-tennis sessions, and to all players, in particular Ehud Amitai, Aaron Daniel, Tomoki Hiro-sawa, Michal Kloc, Alexandre Roulet, Frank Schäfer, Christoph Orth, and Gaomin Tang.

I am grateful to our PhD school *Quantum Computing and Quantum Technology* and its coordinator Thilo Glatzel for many interesting soft-skill and networking events, company excursions, and the financial support by an Excellence Fellowship.

Many thanks to Axel Lode for technical support and a comprehensive introduction to the duties of a computer manager, and to the sciCORE staff for troubleshooting and maintenance of the computing cluster. I am also grateful to the IBM Q System team for making their quantum computers accessible via the internet, and for the great QISKIT hackathon. Moreover, I would like to express my gratitude to our assistants Aicha Lang, Astrid Kalt, and Barbara Kammermann for their support in various administrative tasks.

I profited a lot from discussions on my research projects with Andrew Armour, Aashish Clerk, Sebastián Díaz, Liang Jiang, Manuel Grimm, Klemens Hammerer, Paul Magnard, Michael Marthaler, Matthias Mergenthaler, Fabio Pistolesi, and James Wootton. A special thanks goes to Charles D. Brown for valuable advice on the English language.

Last but not least, I am deeply grateful to my family and my wife Claudia for all support, patience, and trust that I received during the time of my PhD. I also thank her for valuable feedback on this thesis.

Appendix A

Definitions and Conventions

In this appendix, we review the basic properties of the quantum harmonic oscillator and of spin systems to define the notation used in this thesis.

A.1 Quantum harmonic oscillator

A.1.1 Operators

The Hamiltonian of a quantum harmonic oscillator is given by

$$\hat{H}_{\text{QHO}} = \frac{1}{2m}\hat{P}^2 + \frac{1}{2}m\omega^2\hat{X}^2 ,$$

where m and ω denote the mass of the oscillator and its natural frequency of oscillation, respectively. The position and momentum operators, \hat{X} and \hat{P} , satisfy the commutation relation $[\hat{X}, \hat{P}] = i\hbar$. Since position and momentum do not commute, the eigenstates of the quantum harmonic oscillator must fulfill the Heisenberg uncertainty relation

$$\langle (\Delta\hat{X})^2 \rangle \langle (\Delta\hat{P})^2 \rangle \geq \frac{\hbar^2}{4} ,$$

where

$$\langle (\Delta\hat{O})^2 \rangle = \langle (\hat{O} - \langle \hat{O} \rangle)^2 \rangle \tag{A.1}$$

denotes the variance of the observable \hat{O} . For the ground state of the quantum harmonic oscillator, the Heisenberg uncertainty relation turns into an equality since its position and momentum variances are given by

$$\begin{aligned} \langle (\Delta\hat{X})^2 \rangle_{\text{gs}} &= x_{\text{zpf}}^2 = \frac{\hbar}{2m\omega} , \\ \langle (\Delta\hat{P})^2 \rangle_{\text{gs}} &= p_{\text{zpf}}^2 = \frac{\hbar m\omega}{2} . \end{aligned} \tag{A.2}$$

The positive quantities x_{zpf} and p_{zpf} are called the zero-point fluctuations and can be used to introduce new dimensionless position and momentum operators

$$\hat{x} = \frac{1}{\sqrt{2}x_{\text{zpf}}}\hat{X} \quad \text{and} \quad \hat{p} = \frac{1}{\sqrt{2}p_{\text{zpf}}}\hat{P} ,$$

which fulfill the commutation relation $[\hat{x}, \hat{p}] = i$. The Hamiltonian can be expressed in terms of \hat{x} and \hat{p} in a symmetric form,

$$\hat{H}_{\text{QHO}} = \frac{\hbar\omega}{2}(\hat{x}^2 + \hat{p}^2) .$$

The dimensionless position and momentum operators can be combined to the annihilation and creation operator

$$\hat{a} = \frac{1}{\sqrt{2}}(\hat{x} + i\hat{p}) \quad \text{and} \quad \hat{a}^\dagger = \frac{1}{\sqrt{2}}(\hat{x} - i\hat{p}) , \quad (\text{A.3})$$

respectively, which fulfill the commutation relation $[\hat{a}, \hat{a}^\dagger] = 1$. The inverse relations are given by

$$\hat{x} = \frac{1}{\sqrt{2}}(\hat{a}^\dagger + \hat{a}) \quad \text{and} \quad \hat{p} = \frac{i}{\sqrt{2}}(\hat{a}^\dagger - \hat{a}) .$$

Using these annihilation and creation operators, we can rewrite the Hamiltonian of the quantum harmonic oscillator once again and obtain

$$\hat{H}_{\text{QHO}} = \hbar\omega \left(\hat{a}^\dagger \hat{a} + \frac{1}{2} \right) .$$

In the following, we will ignore the constant energy shift $\hbar\omega/2$. As a short-hand notation, we introduce the operator $\hat{n} = \hat{a}^\dagger \hat{a}$. Obviously, the commutation relation $[\hat{H}_{\text{QHO}}, \hat{n}] = 0$ holds, *i.e.*, we can classify the eigenstates of the quantum harmonic oscillator by the occupation number n ,

$$\hat{n} |n\rangle = n |n\rangle .$$

The states $|n\rangle$ are called the *Fock states*. Finally, the commutation relations of \hat{a} and \hat{a}^\dagger with the occupation-number operator \hat{n} are

$$[\hat{n}, \hat{a}] = -\hat{a} \quad \text{and} \quad [\hat{n}, \hat{a}^\dagger] = \hat{a}^\dagger .$$

These commutation relations imply the properties

$$\hat{a}^\dagger |n\rangle = \sqrt{n+1} |n+1\rangle \quad \text{and} \quad \hat{a} |n\rangle = \sqrt{n} |n-1\rangle ,$$

which justify to call \hat{a} and \hat{a}^\dagger annihilation and creation operators, respectively.

A.1.2 Coherent states

The eigenstates $|\alpha\rangle$ of the annihilation operator, $\hat{a}|\alpha\rangle = \alpha|\alpha\rangle$ are called *coherent states*. They can be expressed in terms of Fock states as follows:

$$|\alpha\rangle = e^{-|\alpha|^2/2} \sum_{n=0}^{\infty} \frac{\alpha^n}{\sqrt{n!}} |n\rangle = e^{-|\alpha|^2/2} e^{\alpha \hat{a}^\dagger} |0\rangle . \quad (\text{A.4})$$

Coherent states can be obtained by displacing the vacuum state $|0\rangle$,

$$|\alpha\rangle = \hat{D}(\alpha) |0\rangle ,$$

where the displacement operator $\hat{D}(\alpha)$ is defined in Equation (2.45).

A.2 Spin system

A.2.1 Operators

The spin-component operators \hat{S}_x , \hat{S}_y , and \hat{S}_z of a spin system are defined by the algebra

$$[\hat{S}_j, \hat{S}_k] = i\hbar \sum_l \epsilon_{jkl} \hat{S}_l ,$$

where the indices take a value in $\{x, y, z\}$ and ϵ_{jkl} is the Levi-Civita symbol defined by

$$\epsilon_{jkl} = \begin{cases} +1 & \text{if } (j, k, l) \text{ is an even permutation of } (x, y, z), \\ -1 & \text{if } (j, k, l) \text{ is an odd permutation of } (x, y, z), \\ 0 & \text{else.} \end{cases}$$

The Hermitian operators \hat{S}_x , \hat{S}_y , and \hat{S}_z describe the spatial components of the spin and can be combined to the operator

$$\hat{S}^2 = \hat{S}_x^2 + \hat{S}_y^2 + \hat{S}_z^2 .$$

The eigenstates of a spin system are characterized by the quantum numbers S and m , which are the eigenvalues associated with the operator \hat{S}^2 and one of the spin-component operators, *e.g.*, the \hat{S}_z operator:

$$\hat{S}^2 |S, m\rangle = \hbar^2 S(S+1) |S, m\rangle , \quad (\text{A.5})$$

$$\hat{S}_z |S, m\rangle = \hbar m |S, m\rangle . \quad (\text{A.6})$$

The quantum number S can take integer or half-integer numbers, $S = 0, \frac{1}{2}, 1, \frac{3}{2}, \dots$, and m takes the values $-S, -S+1, \dots, S-1, S$. By linear combination of the \hat{S}_x and \hat{S}_y operators, one can construct the ladder operators

$$\hat{S}_\pm = \hat{S}_x \pm i\hat{S}_y ,$$

which fulfill the commutation relations

$$\begin{aligned} [\hat{S}^2, \hat{S}_\pm] &= 0 , \\ [\hat{S}_z, \hat{S}_\pm] &= \pm\hbar \hat{S}_\pm , \end{aligned}$$

and act on the states $|S, m\rangle$ as follows:

$$\hat{S}_\pm |S, m\rangle = \hbar \sqrt{S(S+1) - m(m \pm 1)} |S, m \pm 1\rangle . \quad (\text{A.7})$$

Equations (A.6) and (A.7) allow one to construct a matrix representation of the spin operators. In this thesis, we represent the spin-1 states by the Euclidean basis vectors in the following way:

$$|1, +1\rangle \leftrightarrow \begin{pmatrix} 1 \\ 0 \\ 0 \end{pmatrix} , \quad |1, 0\rangle \leftrightarrow \begin{pmatrix} 0 \\ 1 \\ 0 \end{pmatrix} , \quad |1, -1\rangle \leftrightarrow \begin{pmatrix} 0 \\ 0 \\ 1 \end{pmatrix} .$$

With this convention, the spin-1 operators have the matrix representation

$$\hat{S}_x \rightsquigarrow \frac{\hbar}{\sqrt{2}} \begin{pmatrix} 0 & 1 & 0 \\ 1 & 0 & 1 \\ 0 & 1 & 0 \end{pmatrix}, \quad \hat{S}_y \rightsquigarrow \frac{\hbar}{\sqrt{2}} \begin{pmatrix} 0 & -i & 0 \\ i & 0 & -i \\ 0 & i & 0 \end{pmatrix}, \quad \hat{S}_z \rightsquigarrow \hbar \begin{pmatrix} 1 & 0 & 0 \\ 0 & 0 & 0 \\ 0 & 0 & -1 \end{pmatrix},$$

and the two ladder operators are represented by

$$\hat{S}_+ \rightsquigarrow \hbar \begin{pmatrix} 0 & \sqrt{2} & 0 \\ 0 & 0 & \sqrt{2} \\ 0 & 0 & 0 \end{pmatrix}, \quad \hat{S}_- \rightsquigarrow \hbar \begin{pmatrix} 0 & 0 & 0 \\ \sqrt{2} & 0 & 0 \\ 0 & \sqrt{2} & 0 \end{pmatrix}.$$

A.2.2 Spin-coherent states

To define spin-coherent states, we follow the procedure outlined in [Radcliffe, 1971]. The ground state $|0\rangle$ of a harmonic oscillator is identified with the spin state $|S, +S\rangle$.¹ The spin states $|S, m\rangle$ are relabeled according to the deviation of their \hat{S}_z eigenvalue from the maximum eigenvalue $+S$,

$$|p\rangle \equiv |S, S - p\rangle,$$

In analogy to the occupation-number operator \hat{n} of a harmonic oscillator, we define a spin-deviation operator

$$\hat{N} = S - \hat{S}_z/\hbar,$$

which fulfills $\hat{N}|p\rangle = p|p\rangle$. The spin-lowering operator $\hat{S}_- = \hat{S}_x - i\hat{S}_y$ is the creation operator for spin deviations and corresponds to the creation operator \hat{a}^\dagger of a harmonic oscillator, with the restriction that the spin system only features a finite number of $2S + 1$ eigenstates,

$$(\hat{S}_-)^p |0\rangle = \begin{cases} \hbar^p \sqrt{\frac{(2S)!p!}{(2S-p)!}} |p\rangle & \text{if } 0 \leq p \leq 2S, \\ 0 & \text{if } p > 2S. \end{cases}$$

This behavior is reproduced by the following expression for the spin-lowering operator in terms of the creation and annihilation operators of a harmonic oscillator [Holstein and Primakoff, 1940]:

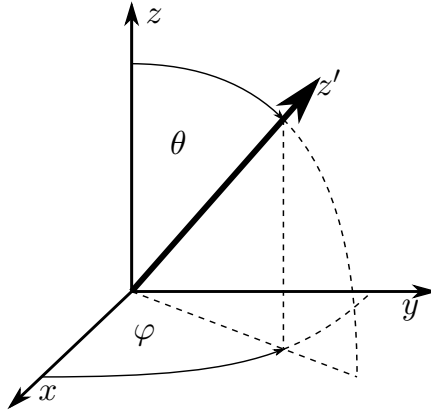
$$\hat{S}_- = \hbar\sqrt{2S}\hat{a}^\dagger \sqrt{1 - \frac{\hat{a}^\dagger\hat{a}}{2S}}.$$

In analogy to Equation (A.4), a spin-coherent state is defined as the normalized exponential of the spin-lowering operator,

$$|\mu\rangle = \frac{1}{(1 + |\mu|^2)^S} e^{\mu\hat{S}_-/\hbar} |0\rangle = \frac{1}{(1 + |\mu|^2)^S} \sum_{p=0}^{2S} \sqrt{\frac{(2S)!}{p!(2S-p)!}} \mu^p |p\rangle. \quad (\text{A.8})$$

This definition of a spin-coherent state converges to the coherent state of a harmonic oscillator in the limit of a large spin, $S \gg 1$, where we have $\hat{S}_- \rightarrow \hbar\sqrt{2S}\hat{a}^\dagger$. Rescaling

¹ Note that the convention of identifying the state $|S, +S\rangle$ with the ground state $|0\rangle$ of a harmonic oscillator is compatible with the Holstein-Primakoff transformation [Holstein and Primakoff, 1940]. However, one could equally well identify the state $|S, -S\rangle$ with the ground state $|0\rangle$ [Arecchi *et al.*, 1972].

FIGURE A.1: Definition of the rotated quantization axis z' .

the parameter $\mu = \alpha/\sqrt{2S}$ appropriately, we obtain

$$\lim_{S \rightarrow \infty} |\mu\rangle = e^{-|\alpha|^2/2} e^{\alpha \hat{a}^\dagger} |0\rangle .$$

The spin-coherent states satisfy the completeness relation [Radcliffe, 1971]

$$\frac{2S+1}{\pi} \int d^2\mu \frac{1}{(1+|\mu|^2)^2} |\mu\rangle \langle \mu| = \sum_{p=0}^{2S} |p\rangle \langle p| = \mathbf{1} .$$

To interpret the parameter μ in Equation (A.8), it is instructive to investigate the effect of changing the spin quantization axis by a spatial rotation

$$\hat{R}(\alpha, \beta, \gamma) = e^{-i\alpha \hat{S}_z} e^{-i\beta \hat{S}_y} e^{-i\gamma \hat{S}_z} ,$$

where α , β , and γ are the Euler angles [Brink and Satchler, 1968]. We consider a rotated reference frame whose quantization axis z' points along the original (θ, φ) direction, as shown in Figure A.1, where the angles are defined on the intervals $\theta \in [0, \pi)$ and $\varphi \in [0, 2\pi)$. The overlap between a state $|\mu\rangle = |\tan(\theta/2)e^{i\varphi}\rangle$ in the original reference frame and the ground state $|0\rangle'$ of the rotated reference frame is found to be [Radcliffe, 1971]

$$\langle \mu | 0 \rangle' = \langle \tan(\theta/2)e^{i\varphi} | \hat{R}(\varphi, \theta, 0) | 0 \rangle = e^{-i\varphi S} .$$

Hence, the state $|\mu\rangle = |\tan(\theta/2)e^{i\varphi}\rangle$ is equivalent to the ground state $|0\rangle'$ in the rotated reference frame up to an irrelevant global phase factor. We can use this property to redefine spin-coherent states as follows:

$$|\theta, \varphi\rangle = \hat{R}(\varphi, \theta, 0) |S, S\rangle = e^{-i\varphi \hat{S}_z} e^{-i\theta \hat{S}_y} |S, S\rangle . \quad (\text{A.9})$$

The corresponding completeness relation reads as

$$\frac{2S+1}{4\pi} \int d\varphi d\theta \sin(\theta) |\theta, \varphi\rangle \langle \theta, \varphi| = \mathbf{1} .$$

Expanding Equation (A.9) in the spin basis $|S, m\rangle$, we find

$$|\theta, \varphi\rangle = \sum_{m=-S}^S |S, m\rangle D_{m,S}^S(\varphi, \theta, 0) ,$$

where $D_{m,n}^S(\varphi, \theta, 0) = \langle S, m | \hat{R}(\varphi, \theta, 0) | S, n \rangle$ are the matrix elements of the rotation operator \hat{R} and are tabulated, *e.g.*, in the book by Brink and Satchler [1968].

In conclusion, a spin-coherent state $|\theta, \varphi\rangle$ is the spin- S eigenstate $|S, +S\rangle$ with respect to a quantization axis pointing along the spatial direction (θ, φ) in polar coordinates. It converges to a coherent state in the large-spin limit, which allows one to identify the latitude angle θ (North–South direction) with the amplitude degree of freedom and the longitude angle φ (East–West direction) with the phase degree of freedom. Alternatively, one can characterize a spin-coherent state by the complex parameter $\mu = \tan(\theta/2)e^{i\varphi}$, which is related to the angles (θ, φ) by a stereographic projection.

Appendix B

Quantum Synchronization Formalism for Oscillator-Based Systems

In this appendix, we provide a summary of the most important formulas if the framework for quantum synchronization developed in Section 5.2 is applied to limit-cycle oscillators, which are defined on the infinite-dimensional Hilbert space of a harmonic oscillator. An example of such a limit-cycle oscillator is the quantum van der Pol (vdP) oscillator introduced in Section 2.6.3.

Using the Equations (5.1) and (5.5), one defines a quantum limit-cycle oscillator by specifying its free Hamiltonian,

$$\hat{H}_{\text{sys}} = \hbar\omega_0 \hat{a}^\dagger \hat{a} ,$$

and a set of Lindblad operators \hat{O}_j that describe suitable dissipative transitions to stabilize the limit cycle. In the case of a vdP oscillator, these operators are $\hat{O}_g = \hat{a}^\dagger$ and $\hat{O}_d = \hat{a}^2$, but one could also consider other sets of operators, *e.g.*, the combination of transitions between single Fock states $\hat{O}_n = |n\rangle \langle n-1|$ suggested by Lörch *et al.* [2017].

The phase-space picture of a quantum state can be obtained by calculating the Husimi function $\mathcal{Q}(\alpha)$ defined in Section 2.3,

$$\mathcal{Q}_{\hat{\rho}}(\alpha) = \frac{1}{\pi} \langle \alpha | \hat{\rho} | \alpha \rangle ,$$

where $|\alpha\rangle$ denotes a coherent state (A.4) of a harmonic oscillator. Its complex argument α can be rewritten in polar form, $\alpha = r e^{i\phi}$, where r corresponds to the classical amplitude of oscillation and ϕ is the phase relevant for the quantum synchronization formalism. Integrating out the amplitude r , we find

$$\begin{aligned} P_{\hat{\rho}}(\phi) &= \int_0^\infty dr r \mathcal{Q}_{\hat{\rho}}(r e^{i\phi}) \\ &= \frac{1}{2\pi} \left[1 + \sum_{n \neq n'=0}^\infty \Gamma\left(\frac{n+n'}{2} + 1\right) \frac{e^{i(n-n')\phi}}{\sqrt{n!n'}} \rho_{n',n} \right] , \end{aligned} \quad (\text{B.1})$$

where we introduced the notation $\rho_{n',n} = \langle n' | \hat{\rho} | n \rangle$ for the matrix elements of the density matrix with respect to Fock states. The Gamma function is denoted by $\Gamma(x)$. Deep in the quantum regime, we can restrict Equation (B.1) to the three lowest Fock

states and obtain

$$P_{\hat{\rho}}(\phi) = \frac{1}{2\pi} \left[1 + \frac{\sqrt{\pi}}{2} \left(\rho_{1,0} + \frac{3}{2\sqrt{2}} \rho_{2,1} \right) e^{-i\phi} + \frac{1}{\sqrt{2}} \rho_{2,0} e^{-2i\phi} + \text{H.c.} \right] .$$

Note that the notion of a phase is not uniquely defined [Lynch, 1995]. Alternative approaches to define the notion of a phase are based on the Susskind-Glogower formalism [Susskind and Glogower, 1964] or on choosing alternative phase-space quasiprobability distributions, *e.g.*, the Wigner function [Lee and Sadeghpour, 2013; Walter *et al.*, 2014]. In the Susskind-Glogower formalism, one defines a phase state as follows:

$$|\phi\rangle = \sum_{n=0}^{\infty} e^{in\phi} |n\rangle .$$

The corresponding phase distribution is then given by

$$P_{\hat{\rho}}^{\text{SG}}(\phi) = \frac{1}{2\pi} \langle \phi | \hat{\rho} | \phi \rangle = \frac{1}{2\pi} \left[1 + \sum_{n \neq n'=0}^{\infty} e^{i(n-n')\phi} \rho_{n',n} \right] .$$

Restricting the Hilbert space to the three lowest levels, we find

$$P_{\hat{\rho}}^{\text{SG}}(\phi) = \frac{1}{2\pi} \left[1 + (\rho_{1,0} + \rho_{2,1}) e^{-i\phi} + \rho_{2,0} e^{-2i\phi} + \text{H.c.} \right] .$$

The same result is obtained in the formalism by Barnett and Pegg [1986]. Alternatively, one could replace the Husimi function by the Wigner function $\mathcal{W}(\alpha)$ defined in Section 2.3, decompose again its complex argument $\alpha = r e^{i\phi}$ in polar coordinates, and integrate out the radial direction r . The corresponding result is

$$\begin{aligned} P_{\hat{\rho}}^{\text{W}}(\phi) &= \int_0^{\infty} dr r \mathcal{W}_{\hat{\rho}}(r e^{i\phi}) \\ &= \frac{1}{2\pi} \left[1 + 4 \sum_{n \neq m=0}^{\infty} \sum_{k=0}^{\min\{m,n\}} e^{i(n-m)\phi} \frac{(-1)^{\min\{m,n\}-k} \sqrt{m!n!}}{k!(n-k)!(m-k)!} \right. \\ &\quad \left. \times |n-m| 2^{(n+m)/2-k-3} \Gamma\left(\frac{m+n}{2} - k\right) \rho_{m,n} \right] . \end{aligned}$$

Restricting again the Hilbert space to the three lowest levels, we obtain

$$P_{\hat{\rho}}^{\text{W}}(\phi) = \frac{1}{2\pi} \left[1 + \frac{\sqrt{\pi}}{\sqrt{2}} \left(\rho_{1,0} + \frac{1}{\sqrt{2}} \rho_{2,1} \right) e^{-i\phi} + \sqrt{2} \rho_{2,0} e^{-2i\phi} + \text{H.c.} \right] .$$

For all of these different methods to introduce a phase distribution, the phase-rotation operator is given by

$$\hat{R}(\alpha) = e^{i\alpha \hat{a}^\dagger \hat{a}} .$$

The system Hamiltonian \hat{H}_{sys} is obviously invariant under phase rotations,

$$\hat{R}(\alpha) \hat{H}_{\text{sys}} \hat{R}^\dagger(\alpha) = \hat{H}_{\text{sys}} .$$

To ensure that Equation (5.1) is invariant under phase rotations, the Lindblad operators \hat{O}_j must satisfy the condition

$$\hat{R}(\alpha)\hat{O}_j\hat{R}^\dagger(\alpha) = e^{i\nu_j(\alpha)}\hat{O}_j,$$

where $\nu_j(\alpha)$ is a real phase. If this condition is satisfied, the limit cycle will be a statistical mixture of Fock states,

$$\begin{pmatrix} \rho_{0,0} & & & \\ & \rho_{1,1} & & \\ & & \rho_{2,2} & \\ & & & \ddots \end{pmatrix},$$

where the conditions $1 \geq \rho_{k,k} \geq 0$ and $\sum_k \rho_{k,k} = 1$ hold.

Finally, we require that the signal Hamiltonian \hat{H}_{ext} is completely off-diagonal in the Fock basis,

$$\langle m | \hat{H}_{\text{ext}} | m' \rangle \propto 1 - \delta_{m,m'}.$$

If this condition is satisfied, the calculation presented in Section 5.2.4 and below can be straightforwardly generalized to the case of an oscillator-based system.

Appendix C

Basis Gates of the IBM Q System

In this appendix, we define the basis gates of the IBM Q System and their matrix representation. We choose to represent the single-qubit basis states $|0\rangle$ and $|1\rangle$ by the following vectors:

$$|0\rangle \leftrightarrow \begin{pmatrix} 1 \\ 0 \end{pmatrix}, \quad |1\rangle \leftrightarrow \begin{pmatrix} 0 \\ 1 \end{pmatrix}.$$

The IBM Q System provides four basis quantum gates, namely, a two-qubit CNOT gate and the three single-qubit gates U_1 , U_2 , and U_3 . The single-qubit gates have the following matrix representation [Abraham *et al.*, 2019b]:

$$\begin{aligned} \hat{U}_3(\theta, \varphi, \lambda) &\leftrightarrow \begin{pmatrix} \cos(\theta/2) & -e^{i\lambda} \sin(\theta/2) \\ e^{i\varphi} \sin(\theta/2) & e^{i\lambda+i\varphi} \cos(\theta/2) \end{pmatrix}, \\ \hat{U}_2(\varphi, \lambda) = U_3(\pi/2, \varphi, \lambda) &\leftrightarrow \frac{1}{\sqrt{2}} \begin{pmatrix} 1 & -e^{i\lambda} \\ e^{i\varphi} & e^{i\lambda+i\varphi} \end{pmatrix}, \\ \hat{U}_1(\lambda) = U_3(0, 0, \lambda) &\leftrightarrow \begin{pmatrix} 1 & 0 \\ 0 & e^{i\lambda} \end{pmatrix}. \end{aligned}$$

As described in Section 6.4, a quantum circuit is *transpiled*, *i.e.*, rewritten in terms of these four basis gates, before it is executed by the quantum computer. For instance, rotations around the x , y , and z axis are rewritten as follows:

$$\begin{aligned} \hat{R}_x(\theta) &= \hat{U}_3(\theta, -\pi/2, \pi/2), \\ \hat{R}_y(\theta) &= \hat{U}_3(\theta, 0, 0), \\ \hat{R}_z(\theta) &= \hat{U}_1(\theta). \end{aligned}$$

The Pauli operators \hat{X} , \hat{Y} , and \hat{Z} as well as the Hadamard gate \hat{H} and the $\pi/8$ -gate \hat{T} introduced in Section 2.7.1 are rewritten as follows:

$$\begin{aligned} \hat{X} &= \hat{U}_3(\pi, 0, \pi), \\ \hat{Y} &= \hat{U}_3(\pi, \pi/2, \pi/2), \\ \hat{Z} &= \hat{U}_3(0, \pi, 0), \\ \hat{H} &= \hat{U}_3(\pi/2, 0, \pi), \\ \hat{T} &= \hat{U}_1(\pi/4). \end{aligned}$$

Finally, the matrix representation of the two-qubit operation $\hat{U}_{1,-1}(t)$ discussed in Section 6.2 is based on the following representation of the two-qubit basis states:

$$\begin{aligned}
 |00\rangle &\equiv |0\rangle_{q_1} \otimes |0\rangle_{q_0} \longleftrightarrow \begin{pmatrix} 1 \\ 0 \\ 0 \\ 0 \end{pmatrix}, & |01\rangle &\equiv |0\rangle_{q_1} \otimes |1\rangle_{q_0} \longleftrightarrow \begin{pmatrix} 0 \\ 1 \\ 0 \\ 0 \end{pmatrix}, \\
 |10\rangle &\equiv |1\rangle_{q_1} \otimes |0\rangle_{q_0} \longleftrightarrow \begin{pmatrix} 0 \\ 0 \\ 1 \\ 0 \end{pmatrix}, & |11\rangle &\equiv |1\rangle_{q_1} \otimes |1\rangle_{q_0} \longleftrightarrow \begin{pmatrix} 0 \\ 0 \\ 0 \\ 1 \end{pmatrix}.
 \end{aligned}$$

List of Symbols

SYMBOL	MEANING	DEFINED IN
$\mathbb{1}$	identity superoperator	
$\hat{\mathbb{1}}$	identity operator	
\longleftrightarrow	mapping between different representations of an operator or state	
$\mathcal{PV} \int$	Cauchy principal value integral	
LATIN SYMBOLS		
\hat{a}	bosonic annihilation operator of optical mode	Eq. (A.3)
A	slowly-varying complex amplitude of vdP oscillator	Eq. (2.95)
\hat{b}	bosonic annihilation operator of mechanical mode	Eq. (A.3)
B	amplitude of optomechanical limit-cycle oscillation	Eq. (2.63)
\tilde{B}	rescaled optomechanical amplitude B	Eq. (2.65)
B_{ss}	steady-state value of optomechanical amplitude B	
c_{μ}	expansion coefficient of state $\hat{\rho}$	Eq. (4.15)
	expansion coefficient of state $ \psi\rangle$	Eq. (4.30)
$C_{\hat{\rho}}(\lambda, s)$	s -parametrized characteristic function of the state $\hat{\rho}$	Eq. (2.44)
\mathcal{C}	optomechanical cooperativity	Eq. (2.61)
	cooperativity of assisted incoherent pumping process	Eq. (5.56)
$ \mathcal{C}_{\pm}(\alpha)\rangle$	Schrödinger cat state of amplitude α	Eq. (2.91)
d_{μ}	expansion coefficient of perturbation $\hat{\sigma}$	Eq. (4.22)
	expansion coefficient of perturbation $ \sigma\rangle$	Eq. (4.35)
dN	stochastic Poissonian increment	Eq. (2.23)
dW	stochastic Wiener increment	Eq. (2.37)
$\hat{D}(\lambda)$	displacement operator	Eq. (2.45)
\mathcal{D}	Lindblad dissipator	Eq. (2.12)
\hat{e}_j	environmental operators that couple to a quantum system	Eq. (2.8)
\hat{E}_r	effect of a POVM	Eq. (2.16)
$\mathbb{E}(x)$	ensemble-average of a stochastic process x	
F	Fano factor	Eq. (2.74)
F_{cond}	average Fano factor of conditional state	Sec. 3.3
F_{ss}	Fano factor of unconditional steady state	Sec. 3.3
g	cavity-enhanced optomechanical coupling strength	Eq. (2.60)
	coherent drive of assisted incoherent pumping process	Fig. 5.11
g_0	bare optomechanical coupling strength	Eq. (2.55)
g_l	expansion coefficient of $\mathcal{L}_{\text{ext}}\hat{\rho}^{(0)}$	Eq. (5.27)
h_{μ}	eigenvalue of non-Hermitian Hamiltonian $\hat{H} - i\hbar\hat{M}$	Eq. (4.28)
\hat{H}	Schrödinger-picture Hamiltonian	
	Hadamard gate	Eq. (2.106)
\tilde{H}	interaction-picture Hamiltonian	Eq. (2.2)
\hat{H}_0	Hamiltonian of a Kerr oscillator	Eq. (2.78)

$\hat{H}'_0(\alpha)$	Hamiltonian of a Kerr oscillator in a displaced frame	Eq. (2.89)
\hat{H}_{ext}	Hamiltonian of external signal in synchronization	Eq. (5.7)
\hat{H}_{lin}	linearized optomechanical Hamiltonian	Eq. (2.59)
\hat{H}_{OM}	optomechanical Hamiltonian	Eq. (2.56)
\hat{H}_{sys}	free Hamiltonian of a limit-cycle oscillator	Eq. (5.2)
\mathcal{H}	nonlinear Hamiltonian	Eq. (4.25)
$\mathcal{H}^{(N)}$	Hilbert space of a N -qubit register	Eq. (2.103)
$j_{k,l}$	rescaled parameters $t_{k,l}$ of the external signal \hat{H}_{ext}	Eq. (6.2)
$J_k(x)$	k -th Bessel function of the first kind	
K	Kerr nonlinearity parameter	Eq. (2.78)
k_B	Boltzmann constant	
\mathcal{L}	unitary and unmonitored dissipative dynamics in SME	Eq. (2.26)
$\bar{\mathcal{L}}$	nonlinear continuous time evolution in SME	Eq. (4.3)
\mathcal{L}_0	superoperator defining the QME of the Kerr oscillator	Eq. (4.1)
	superoperator defining the QME of a spin-1 system	Eq. (5.5)
\mathcal{L}_{ext}	superoperator of the external signal in synchronization	Eq. (5.12)
\hat{M}	correction to Hamiltonian due to continuous measurement	Eq. (2.28)
n_{ph}	mechanical th. occ. number in optomechanical system	Eq. (2.58)
n_{th}	thermal occupation number	Eq. (2.14)
	optical th. occ. number in optomechanical system	Eq. (2.58)
	thermal occupation number of Kerr oscillator	Eq. (2.80)
$N(\hat{\rho})$	negativity measure based on Wigner function $\mathcal{W}_{\hat{\rho}}(\alpha)$	Eq. (4.38)
N_{max}	maximum observable value of $N(\hat{\rho})$	Sec. 4.5
N_{opt}	photon number in optomechanical cavity	Eq. (2.69)
N_u	number of unmonitored Lindblad terms	Eq. (2.19)
\mathcal{N}	correction to \mathcal{L} due to continuous measurement	Eq. (2.27)
\hat{o}	perfectly monitored Lindblad operator	Eq. (2.19)
\hat{O}_{d}	Lindblad operator describing a dissipation process	Eq. 5.2
\hat{O}_{g}	Lindblad operator describing a energy gain process	Fig. 5.2
\hat{O}_j	Lindblad operator stabilizing the limit cycle	Eq. (5.5)
$\hat{O}_{r,k}$	measurement operator of a POVM	Sec. 2.2.1
\mathcal{O}_r	operation of a POVM	Eq. (2.18)
$\mathcal{O}(x)$	order of x	
$p(F)$	probability distribution of the Fano factor	Sec. 3.4
$p_{\text{avg}}(\varepsilon)$	deformation measure of limit cycle	Eq. (5.22)
$p_{\text{bare}}(n)$	average phonon-number distribution of mechanical state	Sec. 3.5
$p_{\text{fluc}}(n)$	distribution of mechanical amplitude fluctuations	Sec. 3.5
$p_{\text{max}}(\varepsilon)$	deformation measure of limit cycle	Eq. (5.23)
$p_{\text{ss}}(n)$	optomechanical steady-state phonon-number distribution	Sec. 3.5
p_{zpf}	quantum zero-point fluctuation of momentum	Eq. (A.2)
P	dimensionless drive power of Kerr oscillator	Eq. (2.84)
$P_{\hat{\rho}}(\phi)$	phase distribution	Eq. (5.3)
$\hat{P}_{ \psi\rangle}$	projector on subspace of $ \psi\rangle$	Eq. (4.33)
$\hat{P}_{\perp \psi\rangle}$	projector on subspace perpendicular to $ \psi\rangle$	Eq. (4.34)
P	momentum quadrature in a displaced or rotating frame	
$\mathcal{P}_{\hat{\rho}}(\alpha)$	Glauber-Sudarshan \mathcal{P} function	Eq. (2.46)
$\mathcal{P}_{\hat{\rho}}$	projector on subspace of $\hat{\rho}$	Eq. (4.19)
$\mathcal{P}_{\perp\hat{\rho}}$	projector on subspace perpendicular to $\hat{\rho}$	Eq. (4.20)
q_0, q_1	system qubits	Chap. 6
q_1, q_2	numerical prefactors of the phase distribution $S_{\hat{\rho}}(\phi)$	Sec. 5.6

Q	position quadrature in a displaced or rotating frame	
$Q_{\hat{\rho}}(\alpha)$	Husimi Q function for continuous-variable systems	Eq. (2.48)
$Q_{\hat{\rho}}(\theta, \varphi)$	Husimi Q function for spin systems	Eq. (2.53)
$\hat{R}(\alpha)$	phase-rotation operator	Eq. (5.4)
\hat{s}_j	system ladder operators that couple to the environment	Eq. (2.8)
$S_{\hat{\rho}}(\phi)$	shifted phase distribution $P_{\hat{\rho}}(\phi)$	Eq. (5.20)
S_{cond}	average von Neumann entropy along a quantum trajectory	Eq. (3.11)
$S_{\hat{e}_j \hat{e}_k}$	spectral function	Eq. (2.11)
$S_{\hat{e}_j \hat{e}_k}^{\pm}$	half-sided spectral function	Eq. (2.10)
S_{vN}	von Neumann entropy	Eq. (3.10)
$\hat{S}_{x,y,z,\pm}$	spin operators	App. A.2
$S(\hat{\rho})$	synchronization measure based on maximum of $S_{\hat{\rho}}$	Eq. (5.21)
$t_{i,j}$	coefficients of signal components of external signal \hat{H}_{ext}	Eq. (5.7)
\hat{T}	$\pi/8$ gate	Eq. (2.107)
\hat{u}_j	unmonitored Lindblad operator in continuous measurement	Eq. (2.19)
$\hat{U}_0(t)$	free time evolution of the limit-cycle oscillator	Eq. (6.6)
$\hat{U}_{1,2,3}$	basis gates of the IBM Q System	App. C
$\hat{U}_{k,l}(t)$	time evolution generated by signal components $t_{k,l}$	Eq. (6.6)
$\mathcal{W}_{\hat{\rho}}(\alpha)$	Wigner function	Eq. (2.47)
x_{zpf}	quantum zero-point fluctuation of position	Eq. (A.2)
\hat{X}	Pauli $\hat{\sigma}_x$ operator	Eq. (2.105)
$ X\rangle$	surplus state of the two-qubit register	Eq. (6.4)
\hat{Z}	Pauli $\hat{\sigma}_z$ operator	Eq. (2.102)

GREEK SYMBOLS

α	complex argument of a coherent state	Eq. (A.4)
	optical amplitude $\langle \hat{a} \rangle$ in semiclassical approximation	
α_0	rescaled steady-state amplitude α_{ss} of Kerr oscillator	Eq. (2.85)
α_1	semiclassical drive of Kerr oscillator	Eq. (2.78)
α_2	squeezing drive of Kerr oscillator	Eq. (2.78)
α_{laser}	laser drive of optomechanical system	Eq. (2.56)
α_{ss}	steady-state value of α	
β	mechanical amplitude $\langle \hat{b} \rangle$ in semiclassical approximation	
	parameter determining amplitude of classical vdP oscillator	Eq. (2.94)
$\bar{\beta}$	offset of optomechanical limit-cycle oscillation	Eq. (2.63)
β_{ss}	steady-state value of β	
γ	rate of dissipative transition	Eq. (2.13)
γ_{d}	dissipative rate of damping process described by \hat{O}_{d}	Fig. 5.2
γ_{g}	dissipative rate of gain process described by \hat{O}_{g}	Fig. 5.2
Γ_{asy}	jump-rate asymmetry between pseudosteady states	Eq. (4.40)
Γ_{BA}	backaction damping rate in optomechanical system	Eq. (2.70)
Γ_{jump}	average detection rate in photon-counting measurement	Eq. (4.9)
$\Gamma_{k,0}$	dissipative transition rates $ k\rangle \rightarrow 0\rangle$ in spin-1 system	Eq. (6.1)
Γ_{mech}	mechanical damping rate in optomechanical system	Eq. (2.58)
Γ_{rel}	mech. amplitude relaxation rate in optomechanical system	Eq. (3.6)
	relaxation rate towards pseudosteady state	Sec. 4.3
δ	dimensionless detuning of Kerr oscillator	Eq. (2.83)
$\delta\Omega$	mechanical frequency shift due to optical spring effect	Eq. (2.71)
$\delta\Omega_{\text{ss}}$	steady-state value of $\delta\Omega$	

Δ	detuning between optomechanical system and laser drive	Eq. (2.57)
	detuning between Kerr oscillator and drive	Eq. (2.79)
	detuning $\Delta_{1:1}$ between limit-cycle oscillator and signal	Eq. (5.9)
$\Delta_{m:n}$	detuning in $m : n$ synchronization	Eq. (2.99)
$\langle\langle(\Delta\hat{O})^2\rangle\rangle$	variance of the observable \hat{O}	Eq. (A.1)
ϵ	accuracy of a digital quantum simulation	Eq. (2.111)
	nonlinearity of the classical vdP oscillator	Eq. (2.94)
ε	coupling strength for mutual synchronization	Sec. 2.6
	signal strength for unidirectional synchronization	Eq. (5.1)
	small parameter of perturbation in stability analysis	Eq. (4.18)
ζ	angle of relative strength of semiclassical signal components	Eq. (5.39)
η	overall detection efficiency of a continuous measurement	Sec. 3.3
	dimensionless expansion parameter in synchronization	Eq. (5.25)
θ	latitude angle of a spin-coherent state	Eq. (A.9)
θ_k	parameter of circuit D_k implementing single-qubit relaxation	Eq. (6.14)
$ \theta, \varphi\rangle$	spin-coherent state	Eq. (2.52)
$\Theta(x)$	Heaviside theta function	
κ	energy decay rate of optical cavity in optomechanical system	Eq. (2.58)
	energy decay rate of Kerr oscillator	Eq. (2.80)
λ_μ	eigenvalue of superoperator $\mathcal{L} + \mathcal{N}$	Eq. (4.11)
ξ	LO signal in homodyne detection	Eq. (2.35)
$\hat{\Pi}$	parity operator	Eq. (2.49)
$\hat{\rho}$	density matrix in Schrödinger picture	
$\tilde{\rho}$	density matrix in interaction-picture	Eq. (2.1)
$\hat{\rho}'$	density matrix in a displaced frame	Eq. (2.88)
$\hat{\rho}^{(j)}$	expansion coefficient of the density matrix	Eq. (5.10)
$\rho_{j,k}$	matrix element $\langle j \hat{\rho} k \rangle$ of $\hat{\rho}$	
$\hat{\rho}_\mu$	right eigenstate of a superoperator	Eq. (4.11)
$\check{\rho}_\mu$	left eigenstate of a superoperator	Eq. (4.12)
$\hat{\rho}_{\text{ps}}$	pseudosteady state	Eq. (4.10)
$\hat{\sigma}$	perturbation to state $\hat{\rho}$	Eq. (4.18)
$ \sigma\rangle$	perturbation to state $ \psi\rangle$	Eq. (4.32)
$\tau_{i,j}$	rescaled signal coefficient $t_{i,j}$ of \hat{H}_{ext}	Eq. (5.31)
τ_{ratio}	ratio between squeezing and semiclassical amplitude	Eq. (5.37)
$\hat{\tau}_{x,y,z,\pm}$	spin-1/2 operators	Eq. (6.7)
φ	phase variable along limit cycle	Eq. (2.93)
	longitude angle of spin-coherent state	Eq. (A.9)
	phase of the measured quadrature in homodyne detection	Eq. (2.35)
φ_{opt}	phase in homodyne detection that minimizes F_{cond}	Sec. 3.4
φ_{ss}	phase of the steady-state solution α_{ss} of Kerr oscillator	Eq. (2.82)
ϕ	phase of mechanical oscillation in optomechanical system	Eq. (2.63)
	relative phase $\phi_{1:1}$ between limit-cycle oscillator and signal	Eq. (2.98)
$\phi_{m:n}$	relative phase in $m : n$ synchronization	Eq. (2.98)
χ	relative phase between the semiclassical signal components	Eq. (5.39)
$\hat{\chi}$	perturbed density matrix	Eq. (4.18)
$ \chi\rangle$	perturbed state vector	Eq. (4.32)
$ \psi\rangle$	state vector	
$ \psi'\rangle$	state vector in a displaced frame	Eq. (4.39)
$ \psi_\mu\rangle$	right eigenstate of non-Hermitian Hamiltonian $\hat{H} - i\hbar\hat{M}$	Eq. (4.28)
$ \bar{\psi}_\mu\rangle$	left eigenstate of non-Hermitian Hamiltonian $\hat{H} - i\hbar\hat{M}$	Eq. (4.29)

$ \psi\rangle_{\text{ps}}$	pseudosteady state of a SSE	Eq. (4.26)
ω_0	natural frequency of oscillation of self-sustained oscillator	Eq. (2.93)
ω_{cav}	optical frequency of optomechanical cavity	Eq. (2.54)
ω_{har}	frequency of a harmonic drive applied to Kerr oscillator	Eq. (2.76)
ω_{laser}	frequency of optomechanical laser drive	Eq. (2.57)
ω_{par}	frequency of parametric drive applied to Kerr oscillator	Eq. (2.77)
Ω_{mech}	mechanical frequency of the optomechanical system	Eq. (2.56)

Bibliography

- Abraham, H., I. Y. Akhalwaya, G. Aleksandrowicz, T. Alexander, G. Alexandrowics, E. Arbel, A. Asfaw, C. Azaustre, P. Barkoutsos, G. Barron, L. Bello, Y. Ben-Haim, L. S. Bishop, S. Bosch, D. Bucher, *et al.* (2019a): *Qiskit: An Open-source Framework for Quantum Computing*, <https://www.doi.org/10.5281/zenodo.2562110>.
- Abraham, H., I. Y. Akhalwaya, G. Aleksandrowicz, T. Alexander, G. Alexandrowics, E. Arbel, A. Asfaw, C. Azaustre, P. Barkoutsos, G. Barron, L. Bello, Y. Ben-Haim, L. S. Bishop, S. Bosch, D. Bucher, *et al.* (2019b): *Qiskit User Guide*, https://qiskit.github.io/ibmqx-user-guides/full-user-guide/002-The_Weird_and_Wonderful_World_of_the_Qubit/004-advanced_qubit_gates.html.
- Abrams, D. M. and S. H. Strogatz (2004): *Chimera States for Coupled Oscillators*. Phys. Rev. Lett. **93**, 174102.
- Adler, R. (1946): *A Study of Locking Phenomena in Oscillators*. P. IRE **34**, 351.
- Agarwal, G. S. (1981): *Relation between atomic coherent-state representation, state multipoles, and generalized phase-space distributions*. Phys. Rev. A **24**, 2889.
- Agrawal, D. K., J. Woodhouse, and A. A. Seshia (2013): *Observation of Locked Phase Dynamics and Enhanced Frequency Stability in Synchronized Micromechanical Oscillators*. Phys. Rev. Lett. **111**, 084101.
- Alsing, P. and H. J. Carmichael (1991): *Spontaneous dressed-state polarization of a coupled atom and cavity mode*. Quantum Opt. **3**, 13.
- Altepeter, J. B., D. F. V. James, and P. G. Kwiat (2004): *Quantum State Estimation*. In: Paris, M. and J. Rehacek (editors), *Qubit Quantum State Tomography* (Springer Verlag, Berlin Heidelberg), pages 113–145.
- Ameri, V., M. Eghbali-Arani, A. Mari, A. Farace, F. Kheirandish, V. Giovannetti, and R. Fazio (2015): *Mutual information as an order parameter for quantum synchronization*. Phys. Rev. A **91**, 012301.
- Anetsberger, G., O. Arcizet, Q. P. Unterreithmeier, R. Riviere, A. Schliesser, E. M. Weig, J. P. Kotthaus, and T. J. Kippenberg (2009): *Near-field cavity optomechanics with nanomechanical oscillators*. Nat. Phys. **5**, 909.
- Arcizet, O., P.-F. Cohadon, T. Briant, M. Pinard, and A. Heidmann (2006): *Radiation-pressure cooling and optomechanical instability of a micromirror*. Nature **444**, 71.
- Arecchi, F. T., E. Courtens, R. Gilmore, and H. Thomas (1972): *Atomic Coherent States in Quantum Optics*. Phys. Rev. A **6**, 2211.
- Armour, A. D. and D. A. Rodrigues (2012): *Quantum dynamics of a mechanical resonator driven by a cavity*. Comptes Rendus Physique **13**, 440.

- Arute, F., K. Arya, R. Babbush, D. Bacon, J. C. Bardin, R. Barends, R. Biswas, S. Boixo, F. G. S. L. Brandao, D. A. Buell, B. Burkett, Y. Chen, Z. Chen, B. Chiaro, R. Collins, *et al.* (2019): *Quantum supremacy using a programmable superconducting processor*. *Nature* **574**, 505.
- Aschoff, J. (1965): *Circadian Rhythms in Man*. *Science* **148**, 1427.
- Aspelmeyer, M., T. J. Kippenberg, and F. Marquardt (2014): *Cavity optomechanics*. *Rev. Mod. Phys.* **86**, 1391.
- Bacon, D., A. M. Childs, I. L. Chuang, J. Kempe, D. W. Leung, and X. Zhou (2001): *Universal simulation of Markovian quantum dynamics*. *Phys. Rev. A* **64**, 062302.
- Bagheri, M., M. Poot, L. Fan, F. Marquardt, and H. X. Tang (2013): *Photonic Cavity Synchronization of Nanomechanical Oscillators*. *Phys. Rev. Lett.* **111**, 213902.
- Banaszek, K. and K. Wódkiewicz (1996): *Direct Probing of Quantum Phase Space by Photon Counting*. *Phys. Rev. Lett.* **76**, 4344.
- Bardeen, J. and W. H. Brattain (1948): *The Transistor, A Semi-Conductor Triode*. *Phys. Rev.* **74**, 230.
- Barenco, A., C. H. Bennett, R. Cleve, D. P. DiVincenzo, N. Margolus, P. Shor, T. Sleator, J. A. Smolin, and H. Weinfurter (1995): *Elementary gates for quantum computation*. *Phys. Rev. A* **52**, 3457.
- Barnett, S. M. and D. T. Pegg (1986): *Phase in quantum optics*. *J. Phys. A-Math. Gen.* **19**, 3849.
- Bartolo, N., F. Minganti, W. Casteels, and C. Ciuti (2016): *Exact steady state of a Kerr resonator with one- and two-photon driving and dissipation: Controllable Wigner-function multimodality and dissipative phase transitions*. *Phys. Rev. A* **94**, 033841.
- Bastidas, V. M., I. Omelchenko, A. Zakharova, E. Schöll, and T. Brandes (2015): *Quantum signatures of chimera states*. *Phys. Rev. E* **92**, 062924.
- Bekker, C., R. Kalra, C. Baker, and W. P. Bowen (2017): *Injection locking of an electro-optomechanical device*. *Optica* **4**, 1196.
- Benioff, P. (1980): *The computer as a physical system: A microscopic quantum mechanical Hamiltonian model of computers as represented by Turing machines*. *J. Stat. Phys.* **22**, 563.
- Bennett, C. H. and G. Brassard (2014): *Quantum Cryptography: Public Key Distribution and Coin Tossing*. *Theor. Comput. Sci.* **560**, 7.
- Benz, S. P. and C. J. Burroughs (1991): *Coherent emission from two-dimensional Josephson junction arrays*. *Appl. Phys. Lett.* **58**, 2162.
- Besse, J.-C., S. Gasparinetti, M. C. Collodo, T. Walter, P. Kurpiers, M. Pechal, C. Eichler, and A. Wallraff (2018): *Single-Shot Quantum Nondemolition Detection of Individual Itinerant Microwave Photons*. *Phys. Rev. X* **8**, 021003.
- Bianchetti, R., S. Filipp, M. Baur, J. M. Fink, C. Lang, L. Steffen, M. Boissonneault, A. Blais, and A. Wallraff (2010): *Control and Tomography of a Three Level Superconducting Artificial Atom*. *Phys. Rev. Lett.* **105**, 223601.

- Bimbard, E., N. Jain, A. MacRae, and A. I. Lvovsky (2010): *Quantum-optical state engineering up to the two-photon level*. Nat. Photonics **4**, 243.
- Bishop, R. F. and A. Vourdas (1994): *Displaced and squeezed parity operator: Its role in classical mappings of quantum theories*. Phys. Rev. A **50**, 4488.
- Boccaletti, S., J. Kurths, G. Osipov, D. Valladares, and C. Zhou (2002): *The synchronization of chaotic systems*. Phys. Rep. **366**, 1.
- Bose, S., P. L. Knight, M. B. Plenio, and V. Vedral (1999): *Proposal for Teleportation of an Atomic State via Cavity Decay*. Phys. Rev. Lett. **83**, 5158.
- Braunstein, S. L. and P. van Loock (2005): *Quantum information with continuous variables*. Rev. Mod. Phys. **77**, 513.
- Breuer, H.-P. and F. Petruccione (2002): *The Theory of Open Quantum Systems* (Oxford University Press, Oxford).
- Briant, T., P. Cohadon, M. Pinard, and A. Heidmann (2003): *Optical phase-space reconstruction of mirror motion at the attometer level*. Eur. Phys. J. D **22**, 131.
- Brif, C. and A. Mann (1999): *Phase-space formulation of quantum mechanics and quantum-state reconstruction for physical systems with Lie-group symmetries*. Phys. Rev. A **59**, 971.
- Brink, D. M. and G. R. Satchler (1968): *Angular momentum* (Clarendon Press, Oxford).
- Brody, D. C. and E.-M. Graefe (2012): *Mixed-State Evolution in the Presence of Gain and Loss*. Phys. Rev. Lett. **109**, 230405.
- Brunelli, M., O. Houhou, D. W. Moore, A. Nunnenkamp, M. Paternostro, and A. Ferraro (2018): *Unconditional preparation of nonclassical states via linear-and-quadratic optomechanics*. Phys. Rev. A **98**, 063801.
- Buck, J. and E. Buck (1968): *Mechanism of Rhythmic Synchronous Flashing of Fireflies*. Science **159**, 1319.
- Buot, F. A. (1974): *Method for calculating $\text{Tr}\mathcal{H}^n$ in solid-state theory*. Phys. Rev. B **10**, 3700.
- Cabrillo, C., J. I. Cirac, P. García-Fernández, and P. Zoller (1999): *Creation of entangled states of distant atoms by interference*. Phys. Rev. A **59**, 1025.
- Caldeira, A. O. and A. J. Leggett (1981): *Influence of Dissipation on Quantum Tunneling in Macroscopic Systems*. Phys. Rev. Lett. **46**, 211.
- Carmichael, H. J. (2002): *Statistical Methods in Quantum Optics 1. Master Equations and Fokker-Planck Equations* (Springer Verlag, Berlin Heidelberg), 1st corrected edition.
- Carmichael, H. J. (2008): *Statistical Methods in Quantum Optics 2. Non-Classical Fields* (Springer Verlag, Berlin Heidelberg), 1st edition.
- Carvalho, A. R. R., M. Busse, O. Brodier, C. Viviescas, and A. Buchleitner (2007): *Optimal Dynamical Characterization of Entanglement*. Phys. Rev. Lett. **98**, 190501.

- Chagnac-Amitai, Y. and B. W. Connors (1989): *Synchronized Excitation and Inhibition Driven by Intrinsically Bursting Neurons in Neocortex*. J. Neurophysiol. **62**, 1149.
- Chan, J., T. P. Mayer Alegre, A. H. Safavi-Naeini, J. T. Hill, A. Krause, S. Gröblacher, M. Aspelmeyer, and O. Painter (2011): *Laser cooling of a nanomechanical oscillator into its quantum ground state*. Nature **478**, 89.
- Chen, C., L. Jin, and R.-B. Liu (2019): *Sensitivity of parameter estimation near the exceptional point of a non-Hermitian system*. N. J. Phys. **21**, 083002.
- Childress, L., M. P. Schmidt, A. D. Kashkanova, C. D. Brown, G. I. Harris, A. Aiello, F. Marquardt, and J. G. E. Harris (2017): *Cavity optomechanics in a levitated helium drop*. Phys. Rev. A **96**, 063842.
- Chiorescu, I., Y. Nakamura, C. J. P. M. Harmans, and J. E. Mooij (2003): *Coherent Quantum Dynamics of a Superconducting Flux Qubit*. Science **299**, 1869.
- Chow, J. and J. Gambetta (2020): *Quantum Takes Flight: Moving from Laboratory Demonstrations to Building Systems*. IBM Research Blog, January 8.
- Chu, Y., P. Kharel, T. Yoon, L. Frunzio, P. T. Rakich, and R. J. Schoelkopf (2018): *Creation and control of multi-phonon Fock states in a bulk acoustic-wave resonator*. Nature **563**, 666.
- Clausen, J., M. Dakna, L. Knöll, and D. G. Welsch (1999): *Conditional quantum-state transformation at a beam splitter*. J. of Opt. B-Quantum S. O. **1**, 332.
- Cohen, I. and A. Retzker (2014): *Proposal for Verification of the Haldane Phase Using Trapped Ions*. Phys. Rev. Lett. **112**, 040503.
- Cohen, J. D., S. M. Meeneha, G. S. MacCabe, S. Gröblacher, A. H. Safavi-Naeini, F. Marsili, M. D. Shaw, and O. Painter (2015): *Phonon counting and intensity interferometry of a nanomechanical resonator*. Nature **520**, 522.
- Cohen, L. and M. O. Scully (1986): *Joint Wigner distribution for spin-1/2 particles*. Found. Phys. **16**, 295.
- Corcoles, A. D., A. Kandala, A. Javadi-Abhari, D. T. McClure, A. W. Cross, K. Temme, P. D. Nation, M. Steffen, and J. M. Gambetta (2019): *Challenges and Opportunities of Near-Term Quantum Computing Systems*. arXiv preprint 1910.02894.
- Cross, A. W., L. S. Bishop, J. A. Smolin, and J. M. Gambetta (2017): *Open Quantum Assembly Language*. arXiv preprint 1707.03429.
- Dalibard, J., Y. Castin, and K. Mølmer (1992): *Wave-function approach to dissipative processes in quantum optics*. Phys. Rev. Lett. **68**, 580.
- Davis-Tilley, C., C. K. Teoh, and A. D. Armour (2018): *Dynamics of many-body quantum synchronisation*. N. J. Phys. **20**, 113002.
- Degen, C. L., F. Reinhard, and P. Cappellaro (2017): *Quantum sensing*. Rev. Mod. Phys. **89**, 035002.
- Deutsch, D. and R. Jozsa (1992): *Rapid solution of problems by quantum computation*. P. R. Soc. Lond. A Mat. **439**, 553.

- Doherty, A. C. and K. Jacobs (1999): *Feedback control of quantum systems using continuous state estimation*. Phys. Rev. A **60**, 2700.
- Dörfler, F., M. Chertkov, and F. Bullo (2013): *Synchronization in complex oscillator networks and smart grids*. P. Natl. Acad. Sci. USA **110**, 2005.
- Drummond, P. D. and D. F. Walls (1980): *Quantum theory of optical bistability. I. Nonlinear polarisability model*. J. Phys. A-Math. Gen. **13**, 725.
- Dum, R., P. Zoller, and H. Ritsch (1992): *Monte Carlo simulation of the atomic master equation for spontaneous emission*. Phys. Rev. A **45**, 4879.
- Eichenfield, M., J. Chan, R. M. Camacho, K. J. Vahala, and O. Painter (2009): *Optomechanical crystals*. Nature **462**, 78.
- Ekinci, K. L. and M. L. Roukes (2005): *Nanoelectromechanical systems*. Rev. Sci. Instrum. **76**, 061101.
- Evers, F. and A. D. Mirlin (2000): *Fluctuations of the Inverse Participation Ratio at the Anderson Transition*. Phys. Rev. Lett. **84**, 3690.
- Fano, U. (1957): *Description of States in Quantum Mechanics by Density Matrix and Operator Techniques*. Rev. Mod. Phys. **29**, 74.
- Farhi, E., J. Goldstone, and S. Gutmann (2014): *A Quantum Approximate Optimization Algorithm*. arXiv preprint 1411.4028.
- Ferrari, F., R. Viana, S. Lopes, and R. Stoop (2015): *Phase synchronization of coupled bursting neurons and the generalized Kuramoto model*. Neural Networks **66**, 107.
- Feynman, R. P. (1982): *Simulating physics with computers*. Int. J. Theor. Phys. **21**, 467.
- Feynman, R. P. (2005): *Negative Probability*. In: Hiley, B. and F. D. Peat (editors), *Quantum Implications: Essays in Honour of David Bohm* (Routledge), pages 235–248.
- Fukuda, D., G. Fujii, T. Numata, K. Amemiya, A. Yoshizawa, H. Tsuchida, H. Fujino, H. Ishii, T. Itatani, S. Inoue, and T. Zama (2011): *Titanium-based transition-edge photon number resolving detector with 98% detection efficiency with index-matched small-gap fiber coupling*. Opt. Express **19**, 870.
- Galetti, D. and A. F. R. de Toledo Piza (1988): *An extended Weyl-Wigner transformation for special finite spaces*. Physica A **149**, 267.
- Galland, C., N. Sangouard, N. Piro, N. Gisin, and T. J. Kippenberg (2014): *Heralded Single-Phonon Preparation, Storage, and Readout in Cavity Optomechanics*. Phys. Rev. Lett. **112**, 143602.
- Galve, F., G. Luca Giorgi, and R. Zambrini (2017): *Quantum Correlations and Synchronization Measures*. In: Fanchini, F. F., D. d. O. Soares Pinto, and G. Adesso (editors), *Lectures on General Quantum Correlations and their Applications* (Springer International Publishing, Cham), pages 393–420.
- García-Pérez, G., M. A. C. Rossi, and S. Maniscalco (2020): *IBM Q Experience as a versatile experimental testbed for simulating open quantum systems*. npj Quantum Inf. **6**, 1.

- Gardiner, C. W. (1995): *Handbook of Stochastic Methods for Physics, Chemistry and the Natural Sciences* (Springer Verlag, Berlin Heidelberg).
- Gardiner, C. W. and P. Zoller (2000): *Quantum Noise* (Springer Verlag, Berlin Heidelberg).
- Genoni, M. G., J. Zhang, J. Millen, P. F. Barker, and A. Serafini (2015): *Quantum cooling and squeezing of a levitating nanosphere via time-continuous measurements*. N. J. Phys. **17**, 073019.
- Gerry, C. and P. Knight (2005): *Introductory Quantum Optics* (Cambridge University Press, Cambridge).
- Gibbons, K. S., M. J. Hoffman, and W. K. Wootters (2004): *Discrete phase space based on finite fields*. Phys. Rev. A **70**, 062101.
- Gigan, S., H. R. Böhm, M. Paternostro, F. Blaser, G. Langer, J. B. Hertzberg, K. C. Schwab, D. Bäuerle, M. Aspelmeyer, and A. Zeilinger (2006): *Self-cooling of a micromirror by radiation pressure*. Nature **444**, 67.
- Gil-Santos, E., M. Labousse, C. Baker, A. Goetschy, W. Hease, C. Gomez, A. Lemaitre, G. Leo, C. Ciuti, and I. Favero (2017): *Light-Mediated Cascaded Locking of Multiple Nano-Optomechanical Oscillators*. Phys. Rev. Lett. **118**, 063605.
- Gogolin, C. and J. Eisert (2016): *Equilibration, thermalisation, and the emergence of statistical mechanics in closed quantum systems*. Rep. Prog. Phys. **79**, 056001.
- Gradshteyn, I. S. and I. M. Ryzhik (1980): *Table of Integrals, Series, and Products* (Academic Press, San Diego).
- Greiner, M., O. Mandel, T. Esslinger, T. W. Hänsch, and I. Bloch (2002): *Quantum phase transition from a superfluid to a Mott insulator in a gas of ultracold atoms*. Nature **415**, 39.
- Grigoryan, V. L., K. Shen, and K. Xia (2018): *Synchronized spin-photon coupling in a microwave cavity*. Phys. Rev. B **98**, 024406.
- Grover, L. K. (1997): *Quantum Mechanics Helps in Searching for a Needle in a Haystack*. Phys. Rev. Lett. **79**, 325.
- Grudinin, I. S., H. Lee, O. Painter, and K. J. Vahala (2010): *Phonon Laser Action in a Tunable Two-Level System*. Phys. Rev. Lett. **104**, 083901.
- Hang, C., G. Huang, and V. V. Konotop (2013): *\mathcal{PT} Symmetry with a System of Three-Level Atoms*. Phys. Rev. Lett. **110**, 083604.
- Hanson, R., L. P. Kouwenhoven, J. R. Petta, S. Tarucha, and L. M. K. Vandersypen (2007): *Spins in few-electron quantum dots*. Rev. Mod. Phys. **79**, 1217.
- Harada, T., H.-A. Tanaka, M. J. Hankins, and I. Z. Kiss (2010): *Optimal Waveform for the Entrainment of a Weakly Forced Oscillator*. Phys. Rev. Lett. **105**, 088301.
- Hasegawa, Y. and M. Arita (2014): *Circadian clocks optimally adapt to sunlight for reliable synchronization*. J. R. Soc. Interface **11**, 20131018.
- Heikkilä, T. T., F. Massel, J. Tuorila, R. Khan, and M. A. Sillanpää (2014): *Enhancing Optomechanical Coupling via the Josephson Effect*. Phys. Rev. Lett. **112**, 203603.

- Heinrich, G., M. Ludwig, J. Qian, B. Kubala, and F. Marquardt (2011): *Collective Dynamics in Optomechanical Arrays*. Phys. Rev. Lett. **107**, 043603.
- Heiss, W. (1999): *Phases of wave functions and level repulsion*. Eur. Phys. J. D **7**, 1.
- Hofheinz, M., H. Wang, M. Ansmann, R. C. Bialczak, E. Lucero, M. Neeley, A. D. O'Connell, D. Sank, J. Wenner, J. M. Martinis, and A. N. Cleland (2009): *Synthesizing arbitrary quantum states in a superconducting resonator*. Nature **459**, 546.
- Holmes, C. A., C. P. Meaney, and G. J. Milburn (2012): *Synchronization of many nanomechanical resonators coupled via a common cavity field*. Phys. Rev. E **85**, 066203.
- Holonyak, N. and S. F. Bevacqua (1962): *Coherent (visible) light emission from Ga(As_{1-x}P_x) junctions*. Appl. Phys. Lett. **1**, 82.
- Holstein, T. and H. Primakoff (1940): *Field Dependence of the Intrinsic Domain Magnetization of a Ferromagnet*. Phys. Rev. **58**, 1098.
- Home, J. P., D. Hanneke, J. D. Jost, D. Leibfried, and D. J. Wineland (2011): *Normal modes of trapped ions in the presence of anharmonic trap potentials*. N. J. Phys. **13**, 073026.
- Hong, S., R. Riedinger, I. Marinković, A. Wallucks, S. G. Hofer, R. A. Norte, M. Aspelmeyer, and S. Gröblacher (2017): *Hanbury Brown and Twiss interferometry of single phonons from an optomechanical resonator*. Science **258**, 203.
- Hopkins, A., K. Jacobs, S. Habib, and K. Schwab (2003): *Feedback cooling of a nanomechanical resonator*. Phys. Rev. B **68**, 235328.
- Hosseini-Zadeh, M. and K. J. Vahala (2008): *Observation of injection locking in an optomechanical rf oscillator*. Appl. Phys. Lett. **93**, 191115.
- Huang, K. and M. Hossein-Zadeh (2018): *Injection locking of optomechanical oscillators via acoustic waves*. Opt. Express **26**, 8275.
- Hush, M. R., W. Li, S. Genway, I. Lesanovsky, and A. D. Armour (2015): *Spin correlations as a probe of quantum synchronization in trapped-ion phonon lasers*. Phys. Rev. A **91**, 061401(R).
- Huygens, C. (1673): *Horologium oscillatorium, sive De motu pendulorum ad horologia aptato demonstrationes geometricae* (F. Muguet, Paris).
- IBM (2019a): *IBM Q System*, <https://quantum-computing.ibm.com/>.
- IBM (2019b): *IBM Q System User Guide*, <https://quantum-computing.ibm.com/support/guides/user-guide>.
- Iwasawa, K., K. Makino, H. Yonezawa, M. Tsang, A. Davidovic, E. Huntington, and A. Furusawa (2013): *Quantum-Limited Mirror-Motion Estimation*. Phys. Rev. Lett. **111**, 163602.
- Jacobs, K. and A. J. Landahl (2009): *Engineering Giant Nonlinearities in Quantum Nanosystems*. Phys. Rev. Lett. **103**, 067201.

- Jaksch, D., C. Bruder, J. I. Cirac, C. W. Gardiner, and P. Zoller (1998): *Cold Bosonic Atoms in Optical Lattices*. Phys. Rev. Lett. **81**, 3108.
- Jewett, M. E. and R. E. Kronauer (1998): *Refinement of Limit Cycle Oscillator Model of the Effects of Light on the Human Circadian Pacemaker*. J. Theor. Biol. **192**, 455.
- Jiang, X., Q. Lin, J. Rosenberg, K. Vahala, and O. Painter (2009): *High-Q double-disk microcavities for cavity optomechanics*. Opt. Express **17**, 20911.
- Jing, H., S. K. Özdemir, X.-Y. Lü, J. Zhang, L. Yang, and F. Nori (2014): *PT-Symmetric Phonon Laser*. Phys. Rev. Lett. **113**, 053604.
- Johansson, J. R., P. D. Nation, and F. Nori (2012): *QuTiP: An open-source Python framework for the dynamics of open quantum systems*. Comput. Phys. Commun. **183**, 1760.
- Kandala, A., A. Mezzacapo, K. Temme, M. Takita, M. Brink, J. M. Chow, and J. M. Gambetta (2017): *Hardware-efficient variational quantum eigensolver for small molecules and quantum magnets*. Nature **549**, 242.
- Kelly, J. (2018): *A Preview of Bristlecone, Google's New Quantum Processor*. Google AI Blog, March 5.
- Khaneja, N., R. Brockett, and S. J. Glaser (2001): *Time optimal control in spin systems*. Phys. Rev. A **63**, 032308.
- Kheruntsyan, K. V. (1999): *Wigner function for a driven anharmonic oscillator*. J. Opt. B-Quantum S. O. **1**, 225.
- Kheruntsyan, K. V., D. S. Krähmer, G. Y. Kryuchkyan, and K. G. Petrossian (1996): *Wigner function for a generalized model of a parametric oscillator: phase-space tristability, competition and nonclassical effects*. Opt. Commun. **139**, 157.
- Khurgin, J. B., M. W. Pruessner, T. H. Stievater, and W. S. Rabinovich (2012a): *Optically pumped coherent mechanical oscillators: the laser rate equation theory and experimental verification*. N. J. Phys. **14**, 105022.
- Khurgin, J. B., M. W. Pruessner, T. H. Stievater, and W. S. Rabinovich (2012b): *Laser-Rate-Equation Description of Optomechanical Oscillators*. Phys. Rev. Lett. **108**, 223904.
- Kliesch, M., T. Barthel, C. Gogolin, M. Kastoryano, and J. Eisert (2011): *Dissipative Quantum Church-Turing Theorem*. Phys. Rev. Lett. **107**, 120501.
- Kloeden, P. E. and E. Platen (1995): *Numerical solution of stochastic differential equations* (Springer Verlag, Berlin Heidelberg), 2nd corrected edition.
- Ko, T.-W. and G. B. Ermentrout (2008): *Partially locked states in coupled oscillators due to inhomogeneous coupling*. Phys. Rev. E **78**, 016203.
- Kono, S., K. Koshino, Y. Tabuchi, A. Noguchi, and Y. Nakamura (2018): *Quantum non-demolition detection of an itinerant microwave photon*. Nat. Phys. **14**, 546.
- Koppenhöfer, M., C. Bruder, and N. Lörch (2018): *Unraveling nonclassicality in the optomechanical instability*. Phys. Rev. A **97**, 063812.

- Koppenhöfer, M., C. Bruder, and N. Lörch (2020a): *Heralded dissipative preparation of nonclassical states in a Kerr oscillator*. Phys. Rev. Research **2**, 013071.
- Koppenhöfer, M., C. Bruder, and A. Roulet (2020b): *Quantum synchronization on the IBM Q system*. Phys. Rev. Research **2**, 023026.
- Koppenhöfer, M. and A. Roulet (2019): *Optimal synchronization deep in the quantum regime: Resource and fundamental limit*. Phys. Rev. A **99**, 043804.
- Koppens, F. H. L., C. Buizert, K. J. Tielrooij, I. T. Vink, K. C. Nowack, T. Meunier, L. P. Kouwenhoven, and L. M. K. Vandersypen (2006): *Driven coherent oscillations of a single electron spin in a quantum dot*. Nature **442**, 766.
- Koseska, A., E. Volkov, and J. Kurths (2013): *Oscillation quenching mechanisms: Amplitude vs. oscillation death*. Phys. Rep. **531**, 173.
- Kraus, B. and J. I. Cirac (2001): *Optimal creation of entanglement using a two-qubit gate*. Phys. Rev. A **63**, 062309.
- Krauter, H., C. A. Muschik, K. Jensen, W. Wasilewski, J. M. Petersen, J. I. Cirac, and E. S. Polzik (2011): *Entanglement Generated by Dissipation and Steady State Entanglement of Two Macroscopic Objects*. Phys. Rev. Lett. **107**, 080503.
- Kuramoto, Y. (1984): *Chemical Oscillations, Waves and Turbulence* (Springer Verlag, Berlin Heidelberg).
- Kuramoto, Y. and D. Battogtokh (2002): *Coexistence of Coherence and Incoherence in Nonlocally Coupled Phase Oscillators*. Nonl. Phen. Compl. Syst. **5**, 380.
- Lance, A. M., H. Jeong, N. B. Grosse, T. Symul, T. C. Ralph, and P. K. Lam (2006): *Quantum-state engineering with continuous-variable postselection*. Phys. Rev. A **73**, 041801.
- Langbein, W. (2018): *No exceptional precision of exceptional-point sensors*. Phys. Rev. A **98**, 023805.
- Lau, H.-K. and A. A. Clerk (2018): *Fundamental limits and non-reciprocal approaches in non-Hermitian quantum sensing*. Nat. Commun. **9**, 4320.
- Law, C. K. (1995): *Interaction between a moving mirror and radiation pressure: A Hamiltonian formulation*. Phys. Rev. A **51**, 2537.
- Lee, T. E., C.-K. Chan, and S. Wang (2014): *Entanglement tongue and quantum synchronization of disordered oscillators*. Phys. Rev. E **89**, 022913.
- Lee, T. E. and M. C. Cross (2013): *Quantum-classical transition of correlations of two coupled cavities*. Phys. Rev. A **88**, 013834.
- Lee, T. E. and H. R. Sadeghpour (2013): *Quantum Synchronization of Quantum van der Pol Oscillators with Trapped Ions*. Phys. Rev. Lett. **111**, 234101.
- Leek, P. J., M. Baur, J. M. Fink, R. Bianchetti, L. Steffen, S. Filipp, and A. Wallraff (2010): *Cavity Quantum Electrodynamics with Separate Photon Storage and Qubit Readout Modes*. Phys. Rev. Lett. **104**, 100504.
- Leek, P. J., S. Filipp, P. Maurer, M. Baur, R. Bianchetti, J. M. Fink, M. Göppl, L. Steffen, and A. Wallraff (2009): *Using sideband transitions for two-qubit operations in superconducting circuits*. Phys. Rev. B **79**, 180511.

- Li, A. C. Y., F. Petruccione, and J. Koch (2014): *Perturbative approach to Markovian open quantum systems*. *Sci. Rep.* **4**, 4887.
- Linden, N., S. Popescu, A. J. Short, and A. Winter (2009): *Quantum mechanical evolution towards thermal equilibrium*. *Phys. Rev. E* **79**, 061103.
- Lloyd, S. (1996): *Universal Quantum Simulators*. *Science* **273**, 1073.
- Lloyd, S. and L. Viola (2001): *Engineering quantum dynamics*. *Phys. Rev. A* **65**, 010101.
- Lörch, N., E. Amitai, A. Nunnenkamp, and C. Bruder (2016): *Genuine Quantum Signatures in Synchronization of Anharmonic Self-Oscillators*. *Phys. Rev. Lett.* **117**, 073601.
- Lörch, N., S. E. Nigg, A. Nunnenkamp, R. P. Tiwari, and C. Bruder (2017): *Quantum Synchronization Blockade: Energy Quantization Hinders Synchronization of Identical Oscillators*. *Phys. Rev. Lett.* **118**, 243602.
- Lörch, N., J. Qian, A. Clerk, F. Marquardt, and K. Hammerer (2014): *Laser Theory for Optomechanics: Limit Cycles in the Quantum Regime*. *Phys. Rev. X* **4**, 011015.
- Lorenz, E. N. (1963): *Deterministic Nonperiodic Flow*. *J. Atmos. Sci.* **20**, 130.
- Lougovski, P., E. Solano, Z. M. Zhang, H. Walther, H. Mack, and W. P. Schleich (2003): *Fresnel Representation of the Wigner Function: An Operational Approach*. *Phys. Rev. Lett.* **91**, 010401.
- Ludwig, M. and F. Marquardt (2013): *Quantum Many-Body Dynamics in Optomechanical Arrays*. *Phys. Rev. Lett.* **111**, 073603.
- Lund, A. P., H. Jeong, T. C. Ralph, and M. S. Kim (2004): *Conditional production of superpositions of coherent states with inefficient photon detection*. *Phys. Rev. A* **70**, 020101.
- Lynch, R. (1995): *The quantum phase problem: a critical review*. *Phys. Rep.* **256**, 367.
- Ma, R., A. Schliesser, P. Del’Haye, A. Dabirian, G. Anetsberger, and T. J. Kippenberg (2007): *Radiation-pressure-driven vibrational modes in ultrahigh- Q silica microspheres*. *Opt. Lett.* **32**, 2200.
- Machado, J. D. P. and Y. M. Blanter (2016): *Quantum nonlinear dynamics of optomechanical systems in the strong-coupling regime*. *Phys. Rev. A* **94**, 063835.
- Maiman, T. H. (1960): *Stimulated optical radiation in ruby*. *Nature* **187**, 493.
- Makhlin, Y., G. Schön, and A. Shnirman (2001): *Quantum-state engineering with Josephson-junction devices*. *Rev. Mod. Phys.* **73**, 357.
- Makris, K. G., R. El-Ganainy, D. N. Christodoulides, and Z. H. Musslimani (2008): *Beam Dynamics in PT Symmetric Optical Lattices*. *Phys. Rev. Lett.* **100**, 103904.
- Mamaev, M., L. C. Govia, and A. A. Clerk (2018): *Dissipative stabilization of entangled cat states using a driven Bose-Hubbard dimer*. *Quantum* **2**, 58.
- Mancini, S., D. Vitali, and P. Tombesi (1998): *Optomechanical Cooling of a Macroscopic Oscillator by Homodyne Feedback*. *Phys. Rev. Lett.* **80**, 688.

- Mandel, L. (1986): *Non-Classical States of the Electromagnetic Field*. Phys. Scripta **T12**, 34.
- Mari, A. and J. Eisert (2012): *Positive Wigner Functions Render Classical Simulation of Quantum Computation Efficient*. Phys. Rev. Lett. **109**, 230503.
- Mari, A., A. Farace, N. Didier, V. Giovannetti, and R. Fazio (2013): *Measures of Quantum Synchronization in Continuous Variable Systems*. Phys. Rev. Lett. **111**, 103605.
- Marquardt, F., J. P. Chen, A. A. Clerk, and S. M. Girvin (2007): *Quantum Theory of Cavity-Assisted Sideband Cooling of Mechanical Motion*. Phys. Rev. Lett. **99**, 093902.
- Marquardt, F., J. G. E. Harris, and S. M. Girvin (2006): *Dynamical Multistability Induced by Radiation Pressure in High-Finesse Micromechanical Optical Cavities*. Phys. Rev. Lett. **96**, 103901.
- Matheny, M. H., M. Grau, L. G. Villanueva, R. B. Karabalin, M. C. Cross, and M. L. Roukes (2014): *Phase Synchronization of Two Anharmonic Nanomechanical Oscillators*. Phys. Rev. Lett. **112**, 014101.
- McClure, D. and J. Gambetta (2019): *Quantum computation center opens*. IBM Research Blog, September 18.
- Meaney, C. H., H. Nha, T. Duty, and G. J. Milburn (2014): *Quantum and classical nonlinear dynamics in a microwave cavity*. EPJ Quantum Technol. **1**, 7.
- Metelmann, A. and A. A. Clerk (2015): *Nonreciprocal Photon Transmission and Amplification via Reservoir Engineering*. Phys. Rev. X **5**, 021025.
- Michael, M. H., M. Silveri, R. T. Brierley, V. V. Albert, J. Salmilehto, L. Jiang, and S. M. Girvin (2016): *New Class of Quantum Error-Correcting Codes for a Bosonic Mode*. Phys. Rev. X **6**, 031006.
- Minganti, F., N. Bartolo, J. Lolli, W. Casteels, and C. Ciuti (2016): *Exact results for Schrödinger cats in driven-dissipative systems and their feedback control*. Sci. Rep. **6**, 26987.
- Modi, K., A. Brodutch, H. Cable, T. Paterek, and V. Vedral (2012): *The classical-quantum boundary for correlations: Discord and related measures*. Rev. Mod. Phys. **84**, 1655.
- Moiseyev, N. (2011): *Non-Hermitian Quantum Mechanics* (Cambridge University Press, Cambridge).
- Munro, W. J., K. Nemoto, R. G. Beausoleil, and T. P. Spiller (2005): *High-efficiency quantum-nondemolition single-photon-number-resolving detector*. Phys. Rev. A **71**, 033819.
- Nakamura, Y., Y. A. Pashkin, and J. S. Tsai (1999): *Coherent control of macroscopic quantum states in a single-Cooper-pair box*. Nature **398**, 786.
- Nation, P. D. (2013): *Nonclassical mechanical states in an optomechanical micromaser analog*. Phys. Rev. A **88**, 053828.

- Nayfeh, A. H. and D. T. Mook (1995): *Nonlinear Oscillations* (Wiley-VCH Verlag, Weinheim).
- Néda, Z., E. Ravasz, Y. Brechet, T. Vicsek, and A. L. Barabási (2000): *The sound of many hands clapping*. *Nature* **403**, 849.
- Neeley, M., M. Ansmann, R. C. Bialczak, M. Hofheinz, E. Lucero, A. D. O’Connell, D. Sank, H. Wang, J. Wenner, A. N. Cleland, M. R. Geller, and J. M. Martinis (2009): *Emulation of a Quantum Spin with a Superconducting Phase Qudit*. *Science* **325**, 722.
- Nha, H. and H. J. Carmichael (2004): *Entanglement within the Quantum Trajectory Description of Open Quantum Systems*. *Phys. Rev. Lett.* **93**, 120408.
- Nielsen, M. A. and I. L. Chuang (2011): *Quantum Computation and Quantum Information: 10th Anniversary Edition* (Cambridge University Press, Cambridge).
- Nigg, S. E. (2018): *Observing quantum synchronization blockade in circuit quantum electrodynamics*. *Phys. Rev. A* **97**, 013811.
- O’Connell, A. D., M. Hofheinz, M. Ansmann, R. C. Bialczak, M. Lenander, E. Lucero, M. Neeley, D. Sank, H. Wang, M. Weides, J. Wenner, J. M. Martinis, and A. N. Cleland (2010): *Quantum ground state and single-phonon control of a mechanical resonator*. *Nature* **464**, 697.
- Opatrný, T., V. Bužek, J. Bajer, and G. Drobný (1995): *Propensities in discrete phase spaces: Q function of a state in a finite-dimensional Hilbert space*. *Phys. Rev. A* **52**, 2419.
- Ourjoumtsev, A., R. Tualle-Brouri, J. Laurat, and P. Grangier (2006): *Generating Optical Schrödinger Kittens for Quantum Information Processing*. *Science* **312**, 83.
- Palomaki, T. A., J. W. Harlow, J. D. Teufel, R. W. Simmonds, and K. W. Lehnert (2013): *Coherent state transfer between itinerant microwave fields and a mechanical oscillator*. *Nature* **495**, 210.
- Peano, V., C. Brendel, M. Schmidt, and F. Marquardt (2015): *Topological Phases of Sound and Light*. *Phys. Rev. X* **5**, 031011.
- Pecora, L. M. and T. L. Carroll (1990): *Synchronization in chaotic systems*. *Phys. Rev. Lett.* **64**, 821.
- Pednault, E., J. A. Gunnels, G. Nannicini, L. Horesh, and R. Wisnieff (2019): *Leveraging Secondary Storage to Simulate Deep 54-qubit Sycamore Circuits*. arXiv preprint 1910.09534.
- Peruzzo, A., J. McClean, P. Shadbolt, M.-H. Yung, X.-Q. Zhou, P. J. Love, A. Aspuru-Guzik, and J. L. O’Brien (2014): *A variational eigenvalue solver on a photonic quantum processor*. *Nat. Commun.* **5**, 4213.
- Pezzè, L., A. Smerzi, M. K. Oberthaler, R. Schmied, and P. Treutlein (2018): *Quantum metrology with nonclassical states of atomic ensembles*. *Rev. Mod. Phys.* **90**, 035005.
- Pikovskiy, A. (2015): *Maximizing Coherence of Oscillations by External Locking*. *Phys. Rev. Lett.* **115**, 070602.

- Pikovsky, A., M. Rosenblum, and J. Kurths (2003): *Synchronization. A universal concept in nonlinear sciences* (Cambridge University Press, Cambridge).
- Plenio, M. B., S. F. Huelga, A. Beige, and P. L. Knight (1999): *Cavity-loss-induced generation of entangled atoms*. Phys. Rev. A **59**, 2468.
- Polkovnikov, A. (2010): *Phase space representation of quantum dynamics*. Ann. Phys.-New York **325**, 1790.
- Poyatos, J. F., J. I. Cirac, and P. Zoller (1996): *Quantum Reservoir Engineering with Laser Cooled Trapped Ions*. Phys. Rev. Lett. **77**, 4728.
- Preskill, J. (2018): *Quantum Computing in the NISQ era and beyond*. Quantum **2**, 79.
- Purdy, T. P., R. W. Peterson, and C. A. Regal (2013): *Observation of Radiation Pressure Shot Noise on a Macroscopic Object*. Science **339**, 801.
- Qian, J., A. A. Clerk, K. Hammerer, and F. Marquardt (2012): *Quantum Signatures of the Optomechanical Instability*. Phys. Rev. Lett. **109**, 253601.
- Radcliffe, J. M. (1971): *Some properties of coherent spin states*. J. Phys. A-Gen. **4**, 313.
- Rahimi-Keshari, S., T. C. Ralph, and C. M. Caves (2016): *Sufficient Conditions for Efficient Classical Simulation of Quantum Optics*. Phys. Rev. X **6**, 021039.
- Rannacher, R. (2014): *Numerische Mathematik 1. Numerik gewöhnlicher Differentialgleichungen* (Heidelberg University Publishing, Heidelberg).
- Regal, C. A., J. D. Teufel, and K. W. Lehnert (2008): *Measuring nanomechanical motion with a microwave cavity interferometer*. Nat. Phys. **4**, 555.
- Regensburger, A., C. Bersch, M.-A. Miri, G. Onishchukov, D. N. Christodoulides, and U. Peschel (2012): *Parity-time symmetric photonic lattices*. Nature **488**, 167.
- Reiner, J.-M., F. Wilhelm-Mauch, G. Schön, and M. Marthaler (2019): *Finding the ground state of the Hubbard model by variational methods on a quantum computer with gate errors*. Quantum Sci. Technol. **4**, 035005.
- Rigetti (2019): *Rigetti Computing*, <https://www.rigetti.com/>.
- Rimberg, A. J., M. P. Blencowe, A. D. Armour, and P. D. Nation (2014): *A cavity-Cooper pair transistor scheme for investigating quantum optomechanics in the ultra-strong coupling regime*. N. J. Phys. **16**, 055008.
- Rodrigues, D. A. and A. D. Armour (2010): *Amplitude Noise Suppression in Cavity-Driven Oscillations of a Mechanical Resonator*. Phys. Rev. Lett. **104**, 053601.
- Rodrigues, F. A., T. K. D. Peron, P. Ji, and J. Kurths (2016): *The Kuramoto model in complex networks*. Phys. Rep. **610**, 1.
- Rokhsari, H., T. J. Kippenberg, T. Carmon, and K. J. Vahala (2005): *Radiation-pressure-driven micro-mechanical oscillator*. Opt. Express **13**, 5293.
- Rompala, K., R. Rand, and H. Howland (2007): *Dynamics of three coupled van der Pol oscillators with application to circadian rhythms*. Commun. Nonlinear Sci. **12**, 794.

- Roulet, A. and C. Bruder (2018a): *Synchronizing the Smallest Possible System*. Phys. Rev. Lett. **121**, 053601.
- Roulet, A. and C. Bruder (2018b): *Quantum Synchronization and Entanglement Generation*. Phys. Rev. Lett. **121**, 063601.
- Rowat, P. F. and A. I. Selverston (1993): *Modeling the gastric mill central pattern generator of the lobster with a relaxation-oscillator network*. J. Neurophysiol. **70**, 1030.
- Roy, R. and K. S. Thornburg (1994): *Experimental synchronization of chaotic lasers*. Phys. Rev. Lett. **72**, 2009.
- Schreppler, S., N. Spethmann, N. Brahms, T. Botter, M. Barrios, and D. M. Stamper-Kurn (2014): *Optically measuring force near the standard quantum limit*. Science **344**, 1486.
- Seitner, M. J., M. Abdi, A. Ridolfo, M. J. Hartmann, and E. M. Weig (2017): *Parametric Oscillation, Frequency Mixing, and Injection Locking of Strongly Coupled Nanomechanical Resonator Modes*. Phys. Rev. Lett. **118**, 254301.
- Senko, C., P. Richerme, J. Smith, A. Lee, I. Cohen, A. Retzker, and C. Monroe (2015): *Realization of a Quantum Integer-Spin Chain with Controllable Interactions*. Phys. Rev. X **5**, 021026.
- Shahandeh, F. and M. Ringbauer (2019): *Optomechanical state reconstruction and nonclassicality verification beyond the resolved-sideband regime*. Quantum **3**, 125.
- Shalibo, Y., R. Resh, O. Fogel, D. Shwa, R. Bialczak, J. M. Martinis, and N. Katz (2013): *Direct Wigner Tomography of a Superconducting Anharmonic Oscillator*. Phys. Rev. Lett. **110**, 100404.
- Shlomi, K., D. Yuvaraj, I. Baskin, O. Suchoi, R. Winik, and E. Buks (2015): *Synchronization in an optomechanical cavity*. Phys. Rev. E **91**, 032910.
- Shor, P. W. (1997): *Polynomial-Time Algorithms for Prime Factorization and Discrete Logarithms on a Quantum Computer*. SIAM J. Comput. **26**, 1484.
- Smith, A., B. Jobst, A. G. Green, and F. Pollmann (2019a): *Crossing a topological phase transition with a quantum computer*. arXiv preprint 1910.05351.
- Smith, A., M. S. Kim, F. Pollmann, and J. Knolle (2019b): *Simulating quantum many-body dynamics on a current digital quantum computer*. npj Quantum Inf. **5**, 106.
- Smolin, J. A., J. M. Gambetta, and G. Smith (2012): *Efficient Method for Computing the Maximum-Likelihood Quantum State from Measurements with Additive Gaussian Noise*. Phys. Rev. Lett. **108**, 070502.
- Sonar, S., M. Hajdušek, M. Mukherjee, R. Fazio, V. Vedral, S. Vinjanampathy, and L.-C. Kwek (2018): *Squeezing Enhances Quantum Synchronization*. Phys. Rev. Lett. **120**, 163601.
- Sörgel, L. and K. Hornberger (2015): *Unraveling quantum Brownian motion: Pointer states and their classical trajectories*. Phys. Rev. A **92**, 062112.

- Soykal, O. O. and M. E. Flatté (2010): *Strong Field Interactions between a Nanomagnet and a Photonic Cavity*. Phys. Rev. Lett. **104**, 077202.
- Stahlke, D. (2014): *Quantum interference as a resource for quantum speedup*. Phys. Rev. A **90**, 022302.
- Stark, A., N. Aharon, A. Huck, H. A. R. El-Ella, A. Retzker, F. Jelezko, and U. L. Andersen (2018): *Clock transition by continuous dynamical decoupling of a three-level system*. Sci. Rep. **8**, 14807.
- Strogatz, S. H. (2000): *From Kuramoto to Crawford: exploring the onset of synchronization in populations of coupled oscillators*. Physica D **143**, 1.
- Strogatz, S. H. (2015): *Nonlinear Dynamics and Chaos. With Applications to Physics, Biology, Chemistry, and Engineering* (Westview Press, Cambridge), 2nd edition.
- Susskind, L. and J. Glogower (1964): *Quantum mechanical phase and time operator*. Physics Physique Fizika **1**, 49.
- Suzuki, M. (1976): *Generalized Trotter's formula and systematic approximants of exponential operators and inner derivations with applications to many-body problems*. Commun. Math. Phys. **51**, 183.
- Takeda, S., T. Mizuta, M. Fuwa, J.-i. Yoshikawa, H. Yonezawa, and A. Furusawa (2013): *Generation and eight-port homodyne characterization of time-bin qubits for continuous-variable quantum information processing*. Phys. Rev. A **87**, 043803.
- Takeuchi, S., J. Kim, Y. Yamamoto, and H. H. Hogue (1999): *Development of a high-quantum-efficiency single-photon counting system*. Appl. Phys. Lett. **74**, 1063.
- Tanaka, H.-A. (2014): *Optimal entrainment with smooth, pulse, and square signals in weakly forced nonlinear oscillators*. Physica D **288**, 1.
- Teufel, J. D., T. Donner, M. A. Castellanos-Beltran, J. W. Harlow, and K. W. Lehnert (2009): *Nanomechanical motion measured with an imprecision below that at the standard quantum limit*. Nat. Nanotechnol. **4**, 820.
- Teufel, J. D., T. Donner, D. Li, J. W. Harlow, M. S. Allman, K. Cicak, A. J. Sirois, J. D. Whittaker, K. W. Lehnert, and R. W. Simmonds (2011): *Sideband cooling of micromechanical motion to the quantum ground state*. Nature **475**, 359.
- Thompson, J. D., B. M. Zwickl, A. M. Jayich, F. Marquardt, S. M. Girvin, and J. G. E. Harris (2008): *Strong dispersive coupling of a high-finesse cavity to a micromechanical membrane*. Nature **452**, 72.
- Toth, L., N. Bernier, A. Feofanov, and T. Kippenberg (2018): *A maser based on dynamical backaction on microwave light*. Physics Letters A **382**, 2233.
- Trotter, H. F. (1959): *On the product of semi-groups of operators*. Proc. Amer. Math. Soc. **10**, 545.
- van der Pol, B. (1926): *On relaxation oscillators*. Phil. Mag. **2**, 978.
- van der Pol, B. and J. van der Mark (1928): *The heartbeat considered as a relaxation oscillation, and an electrical model of the heart*. Phil. Mag. **6**, 763.

- Vanner, M. R., I. Pikovski, and M. S. Kim (2015): *Towards optomechanical quantum state reconstruction of mechanical motion*. Ann. Phys. **527**, 15.
- Vatan, F. and C. Williams (2004): *Optimal quantum circuits for general two-qubit gates*. Phys. Rev. A **69**, 032315.
- Veitch, V., C. Ferrie, D. Gross, and J. Emerson (2012): *Negative quasi-probability as a resource for quantum computation*. N. J. Phys. **14**, 113011.
- Veitch, V., N. Wiebe, C. Ferrie, and J. Emerson (2013): *Efficient simulation scheme for a class of quantum optics experiments with non-negative Wigner representation*. N. J. Phys. **15**, 013037.
- Verhagen, E., S. Deleglise, S. Weis, A. Schliesser, and T. J. Kippenberg (2012): *Quantum-coherent coupling of a mechanical oscillator to an optical cavity mode*. Nature **482**, 63.
- Viennot, D. and L. Aubourg (2016): *Quantum chimeras states*. Phys. Lett. A **380**, 678.
- Viviescas, C., I. Guevara, A. R. R. Carvalho, M. Busse, and A. Buchleitner (2010): *Entanglement Dynamics in Open Two-Qubit Systems via Diffusive Quantum Trajectories*. Phys. Rev. Lett. **105**, 210502.
- Wallentowitz, S. and W. Vogel (1996): *Unbalanced homodyning for quantum state measurements*. Phys. Rev. A **53**, 4528.
- Walls, D. F. and G. J. Milburn (1994): *Quantum Optics* (Springer-Verlag, Berlin Heidelberg).
- Walter, S., A. Nunnenkamp, and C. Bruder (2014): *Quantum Synchronization of a Driven Self-Sustained Oscillator*. Phys. Rev. Lett. **112**, 094102.
- Wegner, F. (1980): *Inverse participation ratio in $2+\epsilon$ dimensions*. Z. Phys. B Cond. Mat. **36**, 209.
- Weigert, A., H. J. Wendker, and L. Wisotzki (2005): *Astronomie und Astrophysik* (Wiley-VCH Verlag, Weinheim), 4th edition.
- Weimer, H. (2015): *Variational Principle for Steady States of Dissipative Quantum Many-Body Systems*. Phys. Rev. Lett. **114**, 040402.
- Weiss, T., A. Kronwald, and F. Marquardt (2016): *Noise-induced transitions in optomechanical synchronization*. New J. Phys. **18**, 013043.
- Weiss, T., S. Walter, and F. Marquardt (2017): *Quantum-coherent phase oscillations in synchronization*. Phys. Rev. A **95**, 041802(R).
- Wendin, G. (2017): *Quantum information processing with superconducting circuits: a review*. Reports on Progress in Physics **80**, 106001.
- Wieczorek, W., S. G. Hofer, J. Hoelscher-Obermaier, R. Riedinger, K. Hammerer, and M. Aspelmeyer (2015): *Optimal State Estimation for Cavity Optomechanical Systems*. Phys. Rev. Lett. **114**, 223601.
- Wiersig, J. (2016): *Sensors operating at exceptional points: General theory*. Phys. Rev. A **93**, 033809.

- Wigner, E. (1932): *On the Quantum Correction For Thermodynamic Equilibrium*. Phys. Rev. **40**, 749.
- Wilson, D. J., V. Sudhir, N. Piro, R. Schilling, A. Ghadimi, and T. J. Kippenberg (2015): *Measurement-based control of a mechanical oscillator at its thermal decoherence rate*. Nature **524**, 325.
- Wilson-Rae, I., N. Nooshi, W. Zwerger, and T. J. Kippenberg (2007): *Theory of Ground State Cooling of a Mechanical Oscillator Using Dynamical Backaction*. Phys. Rev. Lett. **99**, 093901.
- Winful, H. G. and L. Rahman (1990): *Synchronized chaos and spatiotemporal chaos in arrays of coupled lasers*. Phys. Rev. Lett. **65**, 1575.
- Wiseman, H. M. and G. J. Milburn (1993): *Quantum theory of field-quadrature measurements*. Phys. Rev. A **47**, 642.
- Wiseman, H. M. and G. J. Milburn (2009): *Quantum Measurement and Control* (Cambridge University Press, Cambridge).
- Wootters, W. K. (1987): *A Wigner-function formulation of finite-state quantum mechanics*. Ann. Phys.-New York **176**, 1.
- Würfel, P. and U. Würfel (2016): *Physics of Solar Cells. From Basic Principles to Advanced Concepts* (Wiley-VCH Verlag, Weinheim), 3rd edition.
- Xu, H., D. Mason, L. Jiang, and J. G. E. Harris (2016): *Topological energy transfer in an optomechanical system with exceptional points*. Nature **537**, 80.
- Yoshioka, N., Y. O. Nakagawa, K. Mitarai, and K. Fujii (2019): *Variational Quantum Algorithm for Non-equilibrium Steady States*. arXiv preprint 1908.09836.
- Zalalutdinov, M., K. L. Aubin, M. Pandey, A. T. Zehnder, R. H. Rand, H. G. Craighead, and J. M. Parpia (2003): *Frequency entrainment for micromechanical oscillator*. Appl. Phys. Lett. **83**, 3281.
- Zhang, J., B. Peng, S. K. Özdemir, Y.-x. Liu, H. Jing, X.-y. Lü, Y.-l. Liu, L. Yang, and F. Nori (2015a): *Giant nonlinearity via breaking parity-time symmetry: A route to low-threshold phonon diodes*. Phys. Rev. B **92**, 115407.
- Zhang, M., S. Shah, J. Cardenas, and M. Lipson (2015b): *Synchronization and Phase Noise Reduction in Micromechanical Oscillator Arrays Coupled through Light*. Phys. Rev. Lett. **115**, 163902.
- Zhang, M., W. Sweeney, C. W. Hsu, L. Yang, A. D. Stone, and L. Jiang (2019): *Quantum Noise Theory of Exceptional Point Amplifying Sensors*. Phys. Rev. Lett. **123**, 180501.
- Zhang, M., G. S. Wiederhecker, S. Manipatruni, A. Barnard, P. McEuen, and M. Lipson (2012): *Synchronization of Micromechanical Oscillators Using Light*. Phys. Rev. Lett. **109**, 233906.
- Zhang, X. H. H. and H. U. Baranger (2019): *Heralded Bell State of Dissipative Qubits Using Classical Light in a Waveguide*. Phys. Rev. Lett. **122**, 140502.
- Zhao, M. and D. Babikov (2008): *Coherent and optimal control of adiabatic motion of ions in a trap*. Phys. Rev. A **77**, 012338.

- Zhirov, O. V. and D. L. Shepelyansky (2006): *Quantum synchronization*. E. Phys. J. D **38**, 375.
- Zhu, B., J. Schachenmayer, M. Xu, F. Herrera, J. G. Restrepo, M. J. Holland, and A. M. Rey (2015): *Synchronization of interacting quantum dipoles*. N. J. Phys. **17**, 083063.
- Zlotnik, A., Y. Chen, I. Z. Kiss, H.-A. Tanaka, and J.-S. Li (2013): *Optimal Waveform for Fast Entrainment of Weakly Forced Nonlinear Oscillators*. Phys. Rev. Lett. **111**, 024102.
- Zlotnik, A. and J.-S. Li (2012): *Optimal entrainment of neural oscillator ensembles*. J. Neural Eng. **9**, 046015.
- Zurek, W. H. (2003): *Decoherence, einselection, and the quantum origins of the classical*. Rev. Mod. Phys. **75**, 715.
- Zwanenburg, F. A., A. S. Dzurak, A. Morello, M. Y. Simmons, L. C. L. Hollenberg, G. Klimeck, S. Rogge, S. N. Coppersmith, and M. A. Eriksson (2013): *Silicon quantum electronics*. Rev. Mod. Phys. **85**, 961.